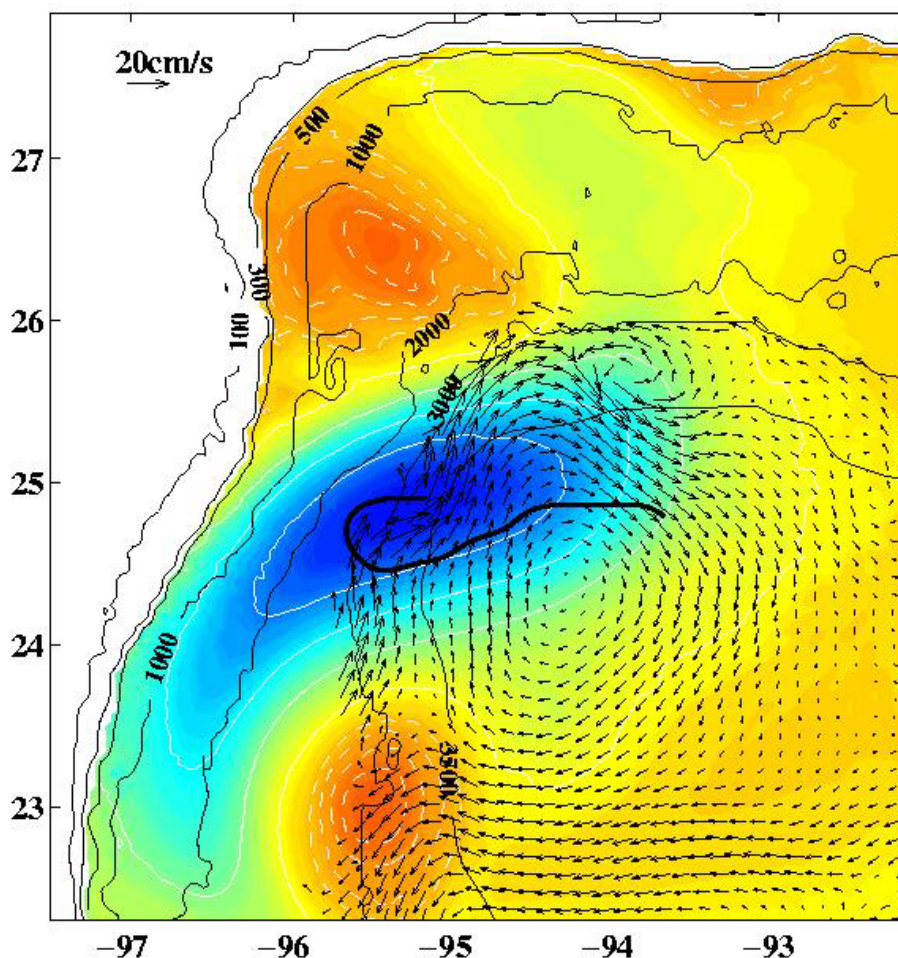




Cross-Shelf Exchange Processes and the Deepwater Circulation of the Gulf of Mexico: Dynamical Effects of Submarine Canyons and the Interactions of Loop Current Eddies with Topography

Final Report



Cross-Shelf Exchange Processes and the Deepwater Circulation of the Gulf of Mexico: Dynamical Effects of Submarine Canyons and the Interactions of Loop Current Eddies with Topography

Final Report

Authors

Sergei A. Frolov
G. Dail Rowe
Lewis M. Rothstein
Isaac Ginis

Prepared under MMS Contract
14-35-01-99-CT-31029
by
Accurate Environmental Forecasting, Inc.
165 Dean Knauss Road
Narragansette, RI 02882

Published by

**U.S. Department of the Interior
Minerals Management Service
Gulf of Mexico OCS Region**

**New Orleans
March 2004**

DISCLAIMER

This report was prepared under contract between the Minerals Management Service (MMS) and Accurate Environmental Forecasting, Inc. This report has been technically reviewed by the MMS, and it has been approved for publication. Approval does not signify that the contents necessarily reflect the views and policies of the MMS, nor does mention of trade names or commercial products constitute endorsement or recommendation for use. It is, however, exempt from review and compliance with the MMS editorial standards.

REPORT AVAILABILITY

Extra copies of this report may be obtained from the Public Information Office (Mail Stop 5034) at the following address:

U.S. Department of the Interior
Minerals Management Service
Gulf of Mexico OCS Region
Public Information Office (MS 5034)
1201 Elmwood Park Boulevard
New Orleans, Louisiana 70123-2394

Telephone: (504) 736-2519 or
1-800-200-GULF

CITATION

Suggested citation:

Frolov, S.A., G.D. Rowe, L.M. Rothstein, and I. Ginis. 2004. Cross-shelf exchange processes and the deepwater circulation of the Gulf of Mexico: Dynamical effects of submarine canyons and the interactions of Loop Current eddies with topography; final report. U.S. Dept. of the Interior, Minerals Mgmt. Service, Gulf of Mexico OCS Region, New Orleans, LA. OCS Study MMS 2004-017 149 pp.

ABOUT THE COVER

Shown on the cover of this report is a numerical simulation of Fast Eddy interacting with the western Gulf of Mexico shelf. Thin black contours indicate depth in meters, arrows indicate velocity at 2,500 meters depth (the scale is shown in the upper left corner), thick black line indicates the trajectory of Fast Eddy center. Depth of 1027 kg/m^3 density surface is shown with white contours and with color. Solid contours and the warmer colors (orange/yellow) correspond to locations where the density surface is elevated over its normal depth indicating cyclonic (counterclockwise) circulation. Dashed contours and the colder colors (blue) correspond to locations where the density surface lies below its normal depth indicating anticyclonic (clockwise) circulation. Interaction of Fast Eddy with the shelf resulted in formation of a surface cyclone north of it and a deep anticyclone east of it.

ACKNOWLEDGMENTS

We would like to thank Dr. Peter Hamilton for being extremely helpful in providing the observational data used in our numerical simulations. We also would like to thank Dr. Wilton Sturges for valuable advise and discussions.

Helpful suggestions and scientific guidance of the Scientific Review Committee, Drs. John Allen and Dong-Ping Wang, throughout the course of the entire four-year program is gratefully acknowledged. Finally, we appreciate the expert guidance of Dr. Alexis Lugo-Fernandez, the COTR over the first three years of this program, and Dr. Carole Current who took over as COTR for the final year.

4.4.4	Idealized Topography Experiments in the Northern GOM	50
4.4.4.1	Experiment Setup	52
4.4.4.2	Results	53
4.4.4.3	Accelerated Westward Eddy Propagation Mode	55
4.4.5	Realistic Topography Experiments	57
4.4.5.1	Western GOM	57
4.4.5.2	Northern GOM	60
4.4.5.3	Northwest Corner of the GOM	60
4.4.6	Fast Eddy Simulation	66
4.4.6.1	Model Configuration and Initialization	66
4.4.6.2	Simulation Results and Comparison with Observations	67
4.4.6.3	Discussion of Dynamical Mechanisms	69
5	DYNAMICAL EFFECTS OF DESOTO CANYON	75
5.1	Introduction	75
5.2	Direct Interaction with Anticyclones	76
5.2.1	Structure of the Anticyclonic Circulation	76
5.2.2	Eastward Propagation of Anticyclones	77
5.2.2.1	Introduction	77
5.2.2.2	Experiment Design	78
5.2.2.3	Results	78
5.2.3	Circulation Within the Canyon	79
5.3	Remote Generation of an Eastward Along-Shelf Current	84
5.3.1	Remote Generation of an Eastward Along-Shelf Current by an LCE	84
5.3.2	Remote Generation of an Eastward Along-Shelf Current by a Cyclone: Conceptual Model	87
5.3.3	Remote Generation of an Eastward Along-Shelf Current by a Cyclone: Nu- merical Simulations	87
5.4	Interaction with Loop Current Frontal Eddies	91
5.4.1	Stability Properties of the Loop Current	95
5.4.1.1	Experiment Design	95
5.4.1.2	Results	105
5.4.2	Realistic Simulations of LCFE's	107
5.4.2.1	PE Model Stability Experiments	107
5.4.2.2	Model Configuration for LCFE Simulations	108
5.4.2.3	Realistic LCFE Simulations	110
6	MIDWATER-COLUMN JETS	119
6.1	Small-Scale Cyclones over Northern Slope Topography	119
6.1.1	Isolated Cyclones	119
6.1.1.1	Experiment Design and Model Setup	119
6.1.1.2	Results	120
6.1.1.3	Conclusions	120
6.1.2	Cyclones Coupled with LCE's	122
6.1.2.1	Experiment Design	122
6.1.2.2	Results	122
6.1.2.3	Conclusions	122

6.2	Mechanisms of Midwater-Column Jet Formation	122
6.2.1	Topography Interactions	126
6.2.1.1	Experiment Design and Numerical Models	126
6.2.1.2	Results	126
6.2.1.3	Conclusions	126
6.2.2	Baroclinic Instability	128
6.2.2.1	Identifying Baroclinically Unstable Frontal Structures	128
6.2.2.2	Baroclinic Instability Confined to the Upper Water Column	129
6.2.2.3	Baroclinic Instability Confined to the Midwater Column	129
6.2.2.4	Conclusions	131
6.3	Other Hypothesis for Midwater-Column Jets	131
7	SUMMARY	135
7.1	Loop Current Eddies	135
7.1.1	Dynamical Mechanisms	135
7.1.2	Interaction of an Isolated LCE with Topography in Various Regions of the GOM	136
7.1.3	Fast Eddy Simulation	138
7.2	Dynamical Effects of DeSoto Canyon	139
7.2.1	Direct Interaction of an Anticyclone with the DeSoto Canyon	140
7.2.2	Remote Generation of Eastward Jets	140
7.2.3	Interaction with Loop Current Frontal Eddies	141
7.3	Small Cyclones in the Northern GOM	144
8	LITERATURE CITED	147

LIST OF FIGURES

	Page
4.1 Initial meridional section of zonal velocity and interface displacement across the eddy center.	18
4.2 Eddy trajectory and eddy shape superimposed upon topography.	19
4.3 Lower layer pressure superimposed by interface displacement and topography at day 30.	20
4.4 Same as Figure 4.2 except for experiment two.	21
4.5 Interface elevations and velocity structure of the idealized vortex initialized in 7-layer IE model.	23
4.6 LCE propagation over flat bottom and shallow slope in 7-layer and 2-layer IE model experiments.	25
4.7 Zonal sections of bathymetry and initial interface displacement for the two IE+ model experiments.	26
4.8 Upper layer interface displacement at 5, 25, 60, and 300 days of integration for the wide shelf experiment.	28
4.9 Comparison of the LCE tracks from the narrow and wide shelf experiments.	29
4.10 Wide shelf topography configuration experiment, day 40 of model integration.	31
4.11 Same as in Figure 4.10 but for narrow shelf experiment.	32
4.12 Modified bottom topography profile compared to the narrow shelf profile.	33
4.13 Hybrid topography experiment compared to the wide shelf experiment.	34
4.14 Example of observed cyclic eddy behavior during its interaction with the GOM western boundary.	35
4.15 Illustration of density and velocity vertical profile transformations during transition from a 2-layer system to continuously stratified system and back to a 3-layer system.	38
4.16 Same as Figure 4.6 but for 7-layer IE and PE models.	40
4.17 23°N topography configuration experiment, day 120 of integration.	43
4.18 Same experiment as in Figure 4.17, but day 40.	44
4.19 Illustration of the mechanism generating the westward-intensified midwater-column circulation.	46
4.20 Same as Figure 4.17 but without stratification below the thermocline.	48
4.21 25°N topography configuration experiment, day 100 of integration.	49
4.22 Same as Figure 4.21 but without stratification below the thermocline.	51
4.23 Domain configuration for simulation of LCE interaction with the GOM northern shelf.	52
4.24 Interaction of an LCE initialized at 87.6°W, 26.8°N with idealized northern shelf topography	54
4.25 Same as in Figure 4.24 but LCE initialized at 87.6°W, 27°N, day 120 of integration.	55
4.26 Summary plot of LCE interaction with idealized northern shelf topography.	56
4.27 Accelerated mode of eddy propagation over the southern edge of the northern slope.	58
4.28 Domain configuration for simulation of LCE interaction with the GOM western shelf.	59
4.29 Simulated interaction of a LCE with the GOM western shelf at 23°N, day 120 of integration.	61
4.30 Simulated interaction of an LCE initialized at 87.6°W, 27°N with the GOM northern shelf, day 250 of integration.	62
4.31 Initial conditions for the simulation of an LCE in the northwest corner.	63

4.32	Simulation of an LCE in the northwest corner after 65 days of integration	65
4.33	Initial conditions for Fast Eddy simulation.	68
4.34	Fast Eddy simulation after 15 days of integration (November 12)	70
4.35	Figure 4.4-17b from SAIC, 1988: Topography of the 15°C isotherm based on the November 1985 AXBT survey.	71
4.36	Fast Eddy simulation, day 55 (December 22).	73
4.37	Same as Figure 4.36 but 60 days of integration.	74
5.1	Interaction of "deep" anticyclonic eddy with the northern shelf west of DeSoto Canyon	80
5.2	Same as in Figure 5.1 but forced with a cyclone.	81
5.3	Realistic simulation of the "deep" anticyclonic eddy interacting with the DeSoto Canyon.	82
5.4	Same as in Figure 5.3 but color code indicates passive tracer concentration.	83
5.5	Schematic diagram of the eastward along-shelf jet generated by a remote LCE interac- tion with the shelf; from Hamilton et al. (2000).	85
5.6	SST image for December 6, 1997.	86
5.7	SSH for October 1, 1997 derived from TOPEX/EPoS-2 plus model mean	88
5.8	Simulation of Eldorado Eddy interacting with the northern shelf.	89
5.9	Schematic illustrating the conceptual model of an eastward along-shelf current by a cyclone.	90
5.10	Simulation of a "shielded" cyclone interacting with the northern shelf west of DeSoto Canyon.	92
5.11	Simulated velocity field at 15- and 300-meter depth.	93
5.12	Velocities at 6- and 300-meter depth observed during the "eastward jet" event in the vicinity of DeSoto Canyon.	94
5.13	Conceptual model of a LCFE flow interaction with the slope in the DeSoto Canyon region; from Hamilton et al. (2000).	96
5.14	Example of a zonal channel stability experiment leading to the formation of frontal cyclones resembling observed LCFE's.	98
5.15	Observed LC cross-section compared to the constructed baseline stream structure. . .	100
5.16	LC stream structure with a narrow cyclonic side compared to the baseline LC stream structure.	101
5.17	Cross-stream PV profiles corresponding to the LC stream structure with narrow cy- clonic side and to the baseline stream structure.	102
5.18	Shallow stream structure with a narrow cyclonic side compared to the regular depth stream structure with a narrow cyclonic side.	103
5.19	Cross-stream PV profiles in each density layer for the shallow and the regular depth LC stream structures.	104
5.20	Summary of zonal channel stability experiments.	106
5.21	Zonal channel stability experiment conducted using a PE model.	109
5.22	PE model configuration and typical initial conditions designed for realistic LCFE sim- ulations.	111
5.23	Same as in Figure 5.22 but with the initial disturbance capable of developing an LCFE.	112
5.24	Same as in Figure 5.23 but after 1 month of integration.	113
5.25	SSH from the realistic LCFE simulation compared to observed SSH.	114
5.26	Velocities produced by the realistic LCFE simulation.	115
5.27	Observed geostrophic velocities corresponding to simulated simulated velocities in Figure 5.26.	116
5.28	Passive tracer distribution at 50-m depth after 2 months of model integration.	117

6.1	PE model simulations of a small and a large isolated cyclones over realistic northern GOM topography.	121
6.2	Illustration of advantages of the PV-based initialization scheme.	123
6.3	PE model simulation of an elliptic LCE interacting with a small-scale cyclone.	124
6.4	Same as in Figure 6.3 but for the isolated elliptic LCE simulation.	125
6.5	Simulation of a cyclone being squeezed between an LCE and topography.	127
6.6	Unstable surface-intensified frontal structure and the PV and velocity fields after 30 days of model integration.	130
6.7	Same as in Figure 6.6 but for midwater-intensified front structure after 60 days of integration.	132

ACRONYMS AND ABBREVIATIONS

AVHRR	Advanced Very High Resolution Radiometry
f	Coriolis parameter
g	Gravitational acceleration
IE	Intermediate Equations
IE+	Extended Intermediate Equations
LC	Loop Current
LCE	Loop Current Eddy
LCFE	Loop Current Frontal Eddy
NCEP	National Center of Environmental
PE	Primitive Equations
POM	Princeton Ocean Model
PT	Potential Thickness
PV	Potential Vorticity
SSH	Sea Surface Height
SST	Sea Surface Temperature
TRW	Topographic Rossby Wave
u, v	Velocity components
ζ	Relative vorticity

1. EXECUTIVE SUMMARY

Synopsis

Accurate Environmental Forecasting, Inc. (AEF) was awarded a four-year contract in 1999 by the Minerals Management Service (MMS) to study the interactions of Gulf of Mexico (GOM) eddies with topography and the dynamical effects of submarine canyons in the GOM. Both of these topics are central towards the more fundamental objective of understanding the cross-shelf exchange processes and the deep-water circulation of the GOM that ultimately determine, for example, the pathways and environmental impacts of pollutants. In addition GOM eddies are quite energetic, so much so that their currents pose a serious hazard to oil and gas operations in the GOM and therefore an understanding of the processes that are associated with these energetic phenomena are essential. The dynamical complexity of the GOM circulation requires that, before an attempt can be made to achieve the ultimate goal of forecasting pollutant dispersal and eddy pathways, we must learn more about the fundamental physical processes that define the cross-shelf and deep circulation in the GOM.

During the four-year program the investigation followed closely the recommendations of the steering committee and focused on two major topics. The first topic was the dynamical processes involved in the interaction of Loop Current Eddies (LCE's) with bottom topography in four regions of the GOM: the central GOM, the northern GOM, the north-east corner of the GOM, and the western GOM. The second topic was the dynamical effects of the DeSoto Canyon on the GOM circulation as well as the circulation within the Canyon induced by large-scale GOM currents. In addition to these two main topics, a brief investigation of the physical processes associated with the evolution of small-scale cyclones over the northern continental slope in the GOM was conducted. The goal of this investigation was to identify potential mechanisms that can lead to the formation of high-intensity midwater-column-intensified currents, which are frequently referred to as midwater-column jets. Below we briefly summarize what we consider to be the most important results from our research program. This is followed by a summary of the next set of scientific questions that resulted from our program.

Important Results

Deep Eddies

Previous idealized (Chassignet and Cushman-Roisin 1991) and more realistic (Welsh and Inoue 2000) numerical studies have demonstrated that LCE's moving over the flat topography that is characteristic of the central GOM can cause formation of large "deep" eddies. The term "deep" is used to reflect the fact that these features, unlike more common surface eddies, have currents that are stronger at depth. Our numerical experiments, while confirming the findings of previous studies, have demonstrated that deep eddies can form not only during LCE propagation in the central GOM but also during their interaction with the western shelf, particularly in the region around 25°W. This region is characterized by a relatively narrow continental slope that causes a substantial portion of those large LCE's that interact with the western shelf to remain over the relatively flat topography area east of the continental slope. Because of this geometry, deep eddies are generated over the flat topography areas as the LCE, interacting with the western shelf, becomes elliptic and rotates clockwise. The deep eddies are characterized by relatively strong currents (up

to 20 cm/s) and large size (200-300 km in diameter) and should have significant impact on the deep local environment. The currents associated with these features are capable of transporting pollutants and any other tracer over large distances making them an important consideration in deep oil spill analysis. Aside from their impact on the deep ocean environment, deep eddies were also shown to significantly affect the evolution of LCE's interacting with the western shelf. In particular, it was demonstrated that a deep cyclone-anticyclone pair might have been responsible for off-shore eastward motion of "Fast Eddy," as observed during its interaction with the western shelf in 1985-1986.

Mechanisms of Cyclone Formation

Numerical simulations of a LCE interacting with a thermocline-penetrating shelf have shown that small to intermediate-scale cyclones form as a result of water advection from the shelf. When a LCE encounters a shelf, its circulation penetrates onto the deeper part of the shelf, advecting the shelf water into deeper ocean. The water mass moving down the topographic slope thus acquires a vertical component to the flow that is further associated with a horizontal convergence due to mass conservation constraints. This horizontal convergence leads to formation of cyclonic vortices in the upper ocean. The cyclones generated by this process can reach considerable strength depending upon the exact shape of the bathymetry and the motion of the LCE. The mechanism is very robust and was identified in numerous numerical simulations, conducted with at least two different models, as well as in observations. We believe that this important result will assist MMS in the analysis and evaluation of general circulation models of the GOM as well as in designing new observational programs.

Dynamical Significance of the Intermediate Layer

The intermediate layer, i.e., the density layer defined with moderate to weak stratification extending from approximately 400 to 1,200 meters, was found to play a central role in the process of LCE-topography interaction. A number of previous studies indicated that many aspects of the circulation in the GOM could be reproduced if the intermediate layer is ignored and the GOM is modeled as a two-layer system, where the bottom of the main thermocline is considered as a dynamical boundary between the stratified upper ocean and the nearly uniform density abyss. Indeed, two-layer numerical simulations conducted during our program show that several aspects of LCE-topography interaction could be reproduced (qualitatively) by a two-layer model. However, our multi-layer and continuously stratified experiments have revealed the importance of the intermediate layer. As a LCE moves onto the continental slope crossing topographic contours an accelerated current (15-20 cm/s) is generated in the mid-water column (intermediate layer) region underneath the eddy. This current is directed along the topography and to the right of the direction of eddy propagation and accelerates in the onshore direction. A slow, broad current recirculating behind the LCE in the opposite direction is generated.

We have demonstrated that the generation mechanism for these currents underneath the eddy is related to water column squashing as the eddy advances onto the topographic slope. This current generation can only occur if stratification exists below the main thermocline. In the absence of stratification the relative vorticity generated by thermocline motions is radiated away as topographic Rossby waves. The stratification enables cross-topographic flow underneath the thermocline allowing the along-shore northward current to recirculate around the eddy. The net effect of the midwater-column currents on the LCE is to deflect its trajectory to the right. Thus, in the process of a LCE interaction with the western shelf, the role of the intermediate layer is to provide

a northward component to the eddy motion. Aside from its influence on LCE evolution the deep cross-topographic flow enabled by the presence of the intermediate layer can play an important role in bringing nutrients from the deeper regions to the surface of the GOM.

Regional Evolution of Isolated LCE's

Potential scenarios describing the evolution of an isolated LCE interacting with bottom topography in various regions of the GOM were identified. The central, the western, and the northern regions of the GOM were studied in isolation. In each region several scenarios of LCE evolution were considered and for each scenario the physical mechanisms involved and their relative importance were identified. Clearly, in reality the behavior of each particular LCE is affected by the history of evolution of earlier LCE's, by other LCE's present in the GOM at the same time, and by other smaller-scale circulation features. However, identifying possible scenarios of evolution of an isolated LCE is critical for designing future observational programs and understanding the complex patterns of real LCE interactions.

In particular, it was found that a large LCE impacting the western GOM shelf in the vicinity of 25°N (a region characterized by a relatively wide shelf and a narrow continental slope) is likely to move away from the shelf after some period of interaction as a result of eastward advection by deep eddies. On the other hand, a LCE impacting the western GOM shelf in the vicinity of 23°N (a region characterized by a relatively narrow shelf and a wide continental slope) is likely to stay at the shelf resulting in prolonged period of interaction and relatively faster decay. Also, a LCE is likely to move northward as it approaches the western shelf as a result of intermediate layer compression. Finally, isolated LCE's moving over the northern continental slope are likely to maintain a steady, nearly westward trajectory until hitting the western boundary in the GOM northwestern corner, where they are likely to remain until their final decay. Interestingly, LCE's moving over the southern end of the northern continental shelf were found capable of moving westward with twice the normal (β -drift) speed due to interaction with a deep cyclone just beneath the LCE.

Dynamical Interpretation of Observations

The dynamical knowledge and intuition developed from our numerical experiments was applied to simulate, in very realistic settings, actual current-topography interaction events observed during several previous MMS-funded studies. These simulations provided better dynamical interpretation of the collected data and allowed for a better understanding of the observed circulation patterns. Current-topography interaction events in two different regions of the GOM were simulated. One region is the western shelf around 25°N, where the interaction of "Fast Eddy" with the shelf observed during the Physical Oceanography Program (1985-1988) was simulated. The other region is the DeSoto Canyon, where circulation patterns observed during the Eddy Intrusion Study (1997-2000) were successfully simulated.

Future Work

LCE/Deep Eddy Vertical Coupling

It was demonstrated in the course of this program that the deep layer, which is often considered as dynamically passive, could provide a strong feedback to LCE's moving over flat topographic

regions. Deep eddies form beneath a moving LCE as the result of stretching and compression of the deep layer. Deep eddies are largely barotropic features and, therefore, have significant surface expression. This represents a serious difficulty for data assimilating general circulation models (GCM), that are commonly used by MMS to make oil spill and other environmental risk assessments. These models attempt to deduce subsurface ocean structures from satellite sea surface height data, however, it is impossible to distinguish deep eddies from regular surface-intensified eddies on the basis of their surface signature alone. Typically, sea surface height anomalies are interpreted by data assimilating models as the signal associated with surface-intensified baroclinic features. This means that these models are likely to overestimate the amount of energy in the upper ocean (particularly cyclonic energy) and underestimate the amount of deep energy. We believe that the results of our research can be used to design new techniques of sea surface height data assimilation that would allow one to distinguish between sea surface height anomalies associated with deep and surface-intensified features on the basis of their time evolution.

Intermediate Layer

Dynamics Multi-layer and continuously stratified experiments conducted during our study indicated that the intermediate layer, i.e., the density layer with moderate to weak stratification extending from approximately 400 to 1,200 meters, can play an important dynamical role. In particular, the effect of northward LCE propagation during its interaction with the western shelf was linked to the existence of the intermediate layer. According to our analysis, the primary dynamical role of the intermediate layer is to allow cross-slope motions below the thermocline. The cross-slope currents below the main thermocline are likely to have important biological implications, i.e. they bring nutrients from deeper regions of the GOM to the surface. Our analysis of the intermediate layer physics in the framework of the current program was somewhat limited due to the time constraints of the program; it was mostly focused on the dynamical role of the intermediate layer in the LCE-topography interaction process. We feel that further investigation will bring much better understanding of the processes that occur in the intermediate layer and its larger role in the GOM circulation.

Cyclone Formation Processes

Our investigation revealed that LCE-topography interactions are frequently associated with generation of small to intermediate scale cyclones via the mechanism of off-shelf advection by LCE currents penetrating onto the shelf. Due to the relatively high frequency of LCE-shelf interaction events the mechanism of cyclone formation via off-shelf advection appears to be an important source of cyclonic activity in the GOM. Consequently, this mechanism must be adequately represented by GCM-type numerical models attempting to simulate the circulation in the GOM in order to produce an adequate amount of upper ocean cyclonic energy. The latter, in turn, is important for accurate predictions of oil spills and other environmental analysis conducted by MMS.

Our investigation during this program was focused on the effects of off-shelf advected cyclones on LCE's, however the large-scale implications of the phenomenon were not addressed. We believe that additional process-oriented studies are needed to investigate the detailed force balance involved in the important process of off-shelf advection and to determine those parameters and conditions that control the amount of cyclonic energy produced. This will allow making more definitive conclusions about the significance of off-shelf advection as a source of surface cyclonic energy in the GOM. Furthermore, it is necessary to investigate the ability of various numerical models currently used for simulating GOM circulation to represent this process.

Non-hydrostatic Physics

Rapidly evolving computer technologies permit numerical ocean models with higher and higher resolution, increasing the realism of the simulations. Horizontal resolution on the order of hundreds of meters or better is already quite feasible for regional simulations. We can expect in the nearest future that the same fine resolution will become possible in large-scale, long-term simulations. Thus, numerical models will soon routinely resolve horizontal scales of 100 meters or less. Unfortunately, the hydrostatic approximation, which is assumed in the majority of numerical models that are currently in use today, is, generally speaking, no longer valid at those scales. Recent depth surveys revealed bathymetric features with horizontal scales less than 1 km. Strong currents associated with LCE's, Loop Current Frontal Eddies, etc. interacting with those bathymetric features are expected to produce rapidly evolving vertical velocities violating the hydrostatic approximation. Investigation of the role of non-hydrostatic physics is thus no longer a curiosity but rather a necessity in order that we better understand relatively high-frequency energetic events in the GOM.

LCE's Over the Northern Slope

Our numerical experiments indicate the possibility that modon-like features exist over the southern edge of the northwestern continental slope. LCE's moving westward along the slope can create a deep cyclone that is permanently coupled to it over flat topography areas adjacent to the slope. We were able to simulate these features in our numerical experiments. The characteristic property of these features is a rapid (twice the speed of the beta-drift) westward propagation. The biological impact of these features (associated upwelling/downwelling) could be important and needs to be further investigated. Also, high intensity currents can be created underneath the southern portion of the LCE (due to the underlying deep cyclone); it is necessary to understand the potential magnitude of these currents and their interaction with the finer-scale topography of the northern slope.

2. INVESTIGATION METHODOLOGY

The overall methodology adopted for this study is based upon a numerical experiment strategy of building model configurations with gradually increasing realism: start with relatively less complex models, which we hypothesize to represent the essential physics of the phenomenon, then gradually transition into a more complete set of physics while still retaining the simplified setting of the problem as much as possible. This methodology enables a clear dynamical analysis of the experiment results and an in-depth understanding of the physics, which is an essential part of this process-oriented study. The final step in this approach is a transition to fully realistic settings capable of reproducing the observed events in significant detail. This dynamical, "bottom-up," process-oriented methodology is markedly different from a "top-down" methodology in which very complex numerical ocean circulation models are run and then diagnosed a-posteriori, with little dynamical guidance and/or understanding. Our "bottom-up" methodology builds dynamical intuition at each step that we believe to be the more appropriate methodology when trying to understand the fundamental dynamics of a particular process.

The approach that was used for designing the numerical experiments at each step of the bottom-up methodology is sometimes called "feature" modeling. The main idea of this approach is to represent the overall ocean circulation as a set of patterns or features that can be initialized within a numerical model using our prior knowledge about the density and velocity structure of these features. This approach works particularly well when the ocean circulation is dominated by strong well-organized patterns like eddies and fronts. An important advantage of this approach is its ability to filter out nonessential components of the circulation that may significantly complicate the experiment analysis.

Following this methodology, a hierarchy of numerical experiments was constructed. The hierarchy is based upon the level of approximation used to derive the differential equations describing the fluid motion in each experiment and upon the degree of realism involved in the experiment design. The hierarchy consisted of four classes of experiments: intermediate equations (IE) experiments, extended intermediate equations experiments (IE+), idealized primitive equations (PE) experiments, and realistic PE experiments. The intermediate equations are a class of approximations to the system of primitive equations, which is similar but generally more accurate than the traditional quasi-geostrophic approximation and remains valid for moderate Rossby and Froude numbers. The particular intermediate approximation that we used in our experiments is called the General Vorticity approximation according to the classification of Allen et al. (1990) who has shown it to be one of the most accurate among its class.

The principal goal of the IE experiments was to develop an initial understanding and intuition of the system's principal dynamics. The computational efficiency and the clarity of the dynamical analysis characteristic of an IE model make it an ideal tool for achieving this goal. Another important goal of IE experiments was the development of initialization techniques for more sophisticated primitive equations models. An initialization technique capable of creating a well-balanced initial state that can be integrated in time without generating strong transient components is crucial for the success of the feature modeling approach. IE models are capable of isolating the balanced component of the flow providing a very useful tool for initialization. IE experiments were conducted with the numerical model of Sutyrin and Yushina (1989).

The goal of the extended intermediate equations experiments was to extend the results of the IE experiments into domain configurations with bottom topography that penetrates the lower layer density interface. A serious limitation of the IE model comes from the requirement for finite isopycnal layer thickness. This requirement does not permit the bottom topography to outcrop into the

upper layer since it would lead to zero lower layer thickness in regions of the outcropping. Consequently, the model is incapable of representing flow interactions with realistic shelf topography. In many cases this limitation can be eliminated by employing another IE model based on the extended set of intermediate equations (Sutyryn, personal communications); we will refer to this model as IE+. The extended intermediate equations include a more realistic representation of the bottom friction and the vertical friction allowing the IE+ model to contain a lower layer with zero thickness under certain conditions. Thus, in many cases the IE+ model allows a significant increase in the realism of numerical experiments, e.g. by including realistic coastal topography, while at the same time retaining the computational efficiency and the clarity of the dynamical analysis of the IE model.

The idealized PE experiments further increase the realism of the numerical simulations by including a realistic continuous stratification and a more complete set physics. Even though the IE+ model significantly increases the realism of the IE model, it does limit the number of isopycnal layers to only two. Also, the intermediate equations approximation used by the model limits the flow parameters to moderate Rossby and Froude numbers that can be violated in strong flows especially during interaction with bottom topography. Both of these limitations are lifted by introduction of a continuously stratified PE model. The PE model used in this class of experiments was the Princeton Ocean Model (POM) configured with high (better than 5 km) horizontal and vertical (50 levels) resolutions. The bottom-following σ -coordinate system employed by this model is perfectly suited for studying the flow interactions with coastal topography. One of the goals of the idealized PE experiment class was to verify the results of the IE and IE+ experiments with the more accurate primitive equations approximation. Consequently, the idealized PE model configurations were selected to be very similar to those of the IE and IE+ experiments.

The final step in the hierarchy of numerical experiments is running the fully realistic PE model simulations. These simulations were designed primarily to verify the results of previous idealized experiments by enabling a direct comparison with observations. The realistic simulations were conducted by initializing the ocean conditions observed prior to the simulated events with a high degree of detail. The POM was configured with a fully realistic topography and background stratification. Another important goal of these simulations was to provide a better dynamical interpretation for some of the observed ocean current events and to improve our understanding of ocean circulation in particular regions of the GOM. This is the ultimate goal of the investigation and it can only be achieved after sufficient intuition and understanding of the dynamics involved has been developed as the result of previous idealized experiments.

3. NUMERICAL TOOLS

3.1 IE Model Formulation

The description of the IE model begins with a scaling analysis that demonstrates the applicability of the intermediate approximation. Then, the derivation of the intermediate equations used in this study is presented. For clarity, the derivation is done for a two-layer system; however, it can be easily expanded to a multi-layer system with an arbitrary number of isopycnal layers. The derivation of the intermediate equations is accompanied by a discussion of the limits of its applicability. Finally, the numerical implementation of the model is described.

3.1.1 Scaling Analysis

Since LCE's represent a typical circulation pattern in the GOM, the scaling analysis presented below is based upon the flow parameters associated with a typical LCE. A typical LCE has maximum velocity $V \approx 1 \text{ m/s}$, and radius $L \approx 150 \times 10^3 \text{ m}$. Choosing $f_0 \approx 4 \times 10^{-5}$, we find that the Rossby number, R_0 , which characterizes eddy strength relative to the planetary vorticity, is

$$R_0 \equiv \frac{V}{f_0 L} \approx 0.2. \quad (3.1)$$

Given a typical reduced gravity in the GOM $g' \approx 0.02 \text{ m/s}^2$, a typical upper layer depth $D_1 \approx 300 \text{ m}$, a typical topographic slope $|\nabla D_2| \approx 0.01$, and assuming the eddies are in geostrophic balance at leading order, we find that the ratio of the interface displacement to the upper layer depth,

$$\frac{f_0 V L}{g' D_1} \approx 1, \quad (3.2)$$

and that the ratio of interface slope to bottom slope,

$$\frac{f_0 V}{g' |\nabla D_2|} \approx 0.2. \quad (3.3)$$

These non-dimensional parameters indicate that the flow is essentially in geostrophic balance, and that depth variations in both layers *cannot be assumed small*. This combination suggests an “intermediate” simplification of the primitive equations, i.e. between quasi-geostrophic and primitive equations.

For this study we choose a specific form of the intermediate equations derived by Sutyrin (1994). This form of the intermediate approximation is also called the General Vorticity approximation according to classification of Allen et al. (1990) who has shown it to be one of the most accurate among its class. Since this approximation is not widely used by the numerical modeling community a quick derivation for the example of a two-layer system is presented below.

3.1.2 Intermediate Equations

We consider a stratified, rotating, hydrostatic, Boussinesq fluid with a rigid-lid on the β -plane. For a two-layer inviscid flow, the momentum and continuity equations are:

$$\partial_t \mathbf{v}_i + (f + \zeta_i) \mathbf{k} \times \mathbf{v}_i = -\nabla(p_i + \frac{\mathbf{v}_i^2}{2}), \quad (3.4)$$

$$\partial_t h_i + \nabla \cdot (h_i \mathbf{v}_i) = 0, \quad (3.5)$$

where the subscript $i = 1(2)$ denotes the upper (lower) layer, $\mathbf{v} = (u, v)$ is the horizontal velocity vector (u is the zonal velocity in the x -direction, v is the meridional velocity in the y -direction), $\zeta = \mathbf{k} \cdot \nabla \times \mathbf{v}$ is the relative vorticity, $f = f_0 + \beta y$ is the Coriolis parameter, ∇ is the horizontal gradient operator, and \mathbf{k} is the vertical unit vector. The layer depths are

$$h_1 = D_1 + \eta, \quad h_2 = D_2(x, y) - \eta, \quad (3.6)$$

where D_1 is the average depth of the upper layer, $D_2(x, y)$ is the depth of the lower layer including topography, and η is the interface displacement. The reduced pressure (p_i , the pressure divided by density) and the interface displacement (η_i) are related by the hydrostatic equation:

$$g' \nabla \eta = \nabla(p_1 - p_2), \quad (3.7)$$

where $g' \equiv g(\rho_2 - \rho_1)/\rho_1$ is the reduced gravity.

The potential vorticity, q_i , of fluid parcels is conserved in each layer - i.e.,

$$(\partial_t + \mathbf{v}_i)q_i = 0; \quad (3.8)$$

$$q_i \equiv \frac{f + \zeta_i}{h_i}. \quad (3.9)$$

Under the intermediate approximation we assume that the leading order flow is geostrophic,

$$v_g = \frac{1}{f_0} \mathbf{k} \times \nabla p, \quad (3.10)$$

and the next order flow is expressed as

$$\mathbf{v} = \frac{1}{f + \zeta_g} \left(\mathbf{k} \times \nabla b - \frac{1}{f_0} \nabla \partial_t p \right), \quad (3.11)$$

where $\zeta_g = \frac{1}{f_0} \nabla^2 p$ is the geostrophic vorticity and $b = p + \frac{1}{2} v_g^2$ is the geostrophic Bernoulli function. Inserting the expression (3.11) into the continuity equation (3.5) yields a predictive system of equations for p that involves only the pressure field,

$$(-1)^i \partial_t (p_1 - p_2) + g' \nabla \cdot \left(\frac{PT_i}{f_0} \nabla \partial_t p_i \right) = g' J(b_i, PT_i), \quad (3.12)$$

where $PT = h/(f + \zeta_g)$ is the potential thickness (inverse potential vorticity) that is also conserved by fluid parcels of the system.

The above derivation indicates the limits of applicability of the intermediate approximation. The Rossby number of the flow has to be “moderate”. Since the higher order terms ($O(R_0)$) are included into the balance equations, the Rossby number does not have to be small ($R_0 \ll 1$) like in the more traditional quasi-geostrophic approximation. However, it does have to be less than ~ 0.5 for $R_0^2 \ll 1$ to be valid. Thus, we expect this approximation to fail for small-scale intense flows.

Another important limitation on the applicability of the above equations comes from the requirement of ellipticity of 3.12. The ellipticity of 3.12 requires the potential layer thickness PT to be positive everywhere. This latter condition is violated if the relative vorticity of the flow ζ is negative and greater than the planetary vorticity f . If one assumes that the initial conditions are such that ζ is small and there is no external forcing, then the relative vorticity of the flow in an isopycnal layer can exceed the planetary vorticity only if variations of the layer interface exceed half of its thickness (from conservation of potential thickness). Thus, to ensure the solvability of

3.12, we have to require that the layer thickness was at least twice the magnitude of the maximum interface elevation. An important implication of this is the requirement for the bottom topography to be confined to the lower layer. The bottom topography cannot intersect the lower layer interface since the lower layer thickness has to remain larger than the interface elevations. This condition significantly limits the applicability of the IE model.

3.1.3 IE Numerical Model

The core of the IE model consists of a custom designed multi-grid elliptic solver capable of solving equations 3.11 and 3.12. The solver is designed for parallel execution on multiple processors with distributed memory architecture. The multi-grid technique allows for fast execution times which scale as $N \log(N)$ with the number of grid points allowing the model to run efficiently even for multi-layer very high resolution configurations. Other notable features of the model include a conservative Arakawa spatial approximation for the Jacobian on the right hand side of equation (3.12), and a second-order Adams-Bashforth approximation for each time step. The model is implemented on a uniform rectangular grid and is configurable with an arbitrary number of isopycnal layers.

3.2 IE+ Model Formulation

The IE+ model is a modified version of the IE mode that extends its applicability to configurations with a bottom topography that intersects the lower layer interface. These configurations, however, are still limited to the cases where the topography is sufficiently steep at the point of intersection with the lower layer interface. The modifications to the IE model include a new extended set of intermediate equations and a new elliptic solver.

3.2.1 Extended Intermediate Equations

To leading order in the Rossby number, the flow is geostrophic,

$$v_g = \frac{1}{f_0} \mathbf{k} \times \nabla p, \quad (3.13)$$

and the next order flow is expressed as

$$\mathbf{v} = \frac{1}{f + \zeta_g} \left(\mathbf{k} \times (\nabla b - \frac{\mathbf{F}}{h}) - \frac{1}{f_0} \nabla \partial_t p \right), \quad (3.14)$$

where $\zeta_g = \frac{1}{f_0} \nabla^2 p$ is the geostrophic vorticity and $b = p + \frac{1}{2} v_g^2$ is the geostrophic Bernoulli function, and \mathbf{F} is the frictional momentum flux. Inserting the expression (3.14) into the continuity equation (3.5) yields a predictive system of equations for p that involves only the pressure field (Sutyrin 1994),

$$\frac{(-1)^i}{g'} \partial_t (p_1 - p_2) + \nabla \cdot \left(\frac{PT_i}{f_0} \nabla \partial_t p_i \right) = J(b_i, PT_i) + M_i + Q_i, \quad (3.15)$$

where $PT = h/(f + \zeta_g)$ is the potential thickness (inverse potential vorticity) that is conserved in fluid parcels if $\mathbf{F} = 0$ and $M = 0$, and

$$Q_i = \partial_x \left\{ \frac{A}{f + \zeta_g} \nabla \left(\frac{h}{f_0} \nabla \partial_x p \right) \right\} + \partial_y \left\{ \frac{A}{f + \zeta_g} \nabla \left(\frac{h}{f_0} \nabla \partial_y p \right) \right\}.$$

This expression suggest a simplified form for the effect of momentum diffusion

$$Q_i = \frac{A_i}{f_0} \nabla^2 (PT_i \nabla^2 p_i),$$

where A_i are horizontal friction coefficients in different layers. The version of the model used in this study employs the latter form of the momentum diffusion equation. The diapycnal mass flux is modeled by the Ekman boundary layer either in the lower layer: $M_2 = h_E \nabla^2 p_2$, or in the upper layer: $M_1 = h_E \nabla^2 p_1$, over the shelf where $h_2 = 0$.

These modified intermediate equations (IE+) are uniformly valid for arbitrary layer depth perturbations, including diabatic processes, and permit the interface to intersect the bathymetry. However, an important restriction on the form of the bathymetry applies: the point of the intersection of the bathymetry and the layer interface has to be restricted to a single grid point during the entire integration.

3.2.2 IE+ Numerical Model

Instead of the multi-grid elliptic solver used in the implementation of the IE model an over-relaxation iterative solver is applied for solving the extended intermediate equations 3.14 and 3.15. The solver is capable of restricting the area where the solution is calculated to the grid points with finite layer thickness. This feature allows the solver to deal with situations where the lower layer thickness vanishes due to the topography penetrating through the layer interface. This solver, however, is less efficient and currently limits the model to only two isopycnal layers.

3.3 Primitive Equations Model

The primitive equations model used in this study is the Princeton Ocean Model (POM). Originally developed by Blumberg and Mellor (1987) the POM is widely distributed to the academic community and industry and is run operationally as a part of the Coastal Ocean Forecast System (COFS) at the National Center for Environmental Predictions. The latest version of the model is described in detail by Mellor (1998). The POM is a fully three-dimensional, primitive equation model with complete thermohaline dynamics. The model equations are solved in a curvilinear coordinate system. In this study the model is configured with a spherical coordinate system in the horizontal and with a σ -coordinate system, i.e., following the ocean bottom and the free surface, in the vertical. The bottom following coordinate system allows for better representation of the current-topography interactions. A second order turbulence closure scheme (Mellor and Yamada 1982) is embedded in the model to provide vertical mixing parameters. The horizontal diffusion terms are calculated using the scales of motion resolved by the model and the local deformation field (Smagorinsky 1963). The density is calculated using the modified UNESCO equation of state (Mellor 1998).

For this study the model was configured with horizontal resolution of at least 5 km. Primarily the minimum viscosity necessary to maintain the numerical stability of the model dictates the

requirement for the high resolution. The viscosity levels necessary to maintain the numerical stability at coarser resolutions lead to excessive eddy dissipation rates.

The model was configured with 50 σ -levels distributed so as to provide a vertical resolution reaching a maximum of 35 meters in the thermocline and a minimum of 180 meters near the bottom at 3,500 meters. The vertical resolution is uniform in the upper 500 meters and decreases linearly below that point. This configuration was carefully selected to minimize the well-known pressure gradient error associated with the σ -coordinate system. Removing the basin-averaged density distribution from the time-dependent density field before evaluating the pressure gradient terms further reduces the pressure gradient error in the model.

4. LCE INTERACTIONS WITH TOPOGRAPHY

4.1 Introduction

Large, baroclinic, anti-cyclonic eddies (LCE's) formed in the eastern GOM typically propagate south-westward from their formation region until reaching the western boundary where their continued evolution and motion are strongly influenced by interactions with the continental slope and shelf. Observations of LCE interactions with the slope and shelf do not lend themselves to a canonical description of either the interaction process or its results. LCE's may remain near the slope or move offshore; they may move north or south; and there may be significant modification of the shelf water mass. The only consistently observed characteristic of LCE interactions with the slope and shelf are weakening of the LCE and formation of other (smaller) eddy-like features (Vukovich and Crissman 1986; Kirwan et al. 1988; Lewis et al. 1989; Vukovich and Waddel 1991; Vidal et al. 1992; Hamilton et al. 1999).

This variability in outcomes of LCE interaction with the slope and shelf indicates that there must be a number of variables that govern these interactions, and a number of authors have contributed theoretical insight likely to be relevant in explaining the myriad observed behaviors. Some of the earliest studies of eddy-topography interaction were those of Smith and O'Brien (1983) and Smith (1986). In a series of numerical experiments in a primitive equation two layer model, they showed that β (both planetary and topographic) induced dispersion leads to asymmetric eddy structure which then gives the eddy a nonlinear self-advective tendency, and that eddies with weak lower layer expression evolve quickly to upper layer features in the presence of topography due to dispersion of the lower layer feature by TRW's. These eddies then propagate independently of topography. Grimshaw et al. (1994) also showed that eddies in contact with the bottom rapidly disperse under the influence of TRW's when they encounter strongly sloped topography. In contrast to the above authors, who focus on eddy interactions with sloping topography, Shi and Nof (1994) discuss the dynamics of eddy interactions with boundaries. They show that the propagation and evolution of eddies encountering walls is dominated by the "image" effect which drives anti-cyclones rapidly northward along a western boundary.

In this study, we conduct a series of numerical experiments to identify physical mechanisms controlling LCE interaction with topography representative of the northern and western regions of the GOM. A typical experiment consists of an isolated anticyclonic eddy representative of an LCE that is initialized in the upper ocean away from the coast, the lower layer is initially at rest. The eddy is allowed to evolve freely driven primarily by β -effect which generally tends to push the eddy against the continental shelf.

Following the investigation methodology described in Section 2 a hierarchy of numerical experiments was constructed. The hierarchy is based upon the level of approximation used to derive the differential equations describing the fluid motion in each experiment and upon the degree of realism involved in the experiment design. The hierarchy consisted of four classes of experiments: intermediate equations (IE) experiments, extended intermediate equations experiments, idealized primitive equations experiments, and realistic primitive equations experiments.

The principal goal of the IE experiments was to develop an initial understanding and intuition of the system principal dynamics. The computational efficiency and the clarity of the dynamical analysis characteristic to an IE model make it an ideal tool for achieving this goal. Another important goal of the IE experiments was the development of initialization techniques for more sophisticated primitive equations models. An initialization technique capable of creating a well-balanced initial

state, which can be integrated in time without generating strong transient components, is crucial for the success of the feature modeling approach. IE models are capable of isolating the balanced component of the flow providing a very useful tool for initialization.

The goal of the extended intermediate equations experiments was to extend the results of the IE experiments into domain configurations with bottom topography penetrating the lower layer density interface. A serious limitation of this IE model comes from the requirement for finite isopycnal layer thickness. This requirement does not permit the bottom topography to outcrop into the upper layer since it would lead to zero lower layer thickness in regions of the outcropping. Consequently, the model is incapable of representing flow interactions with realistic shelf topography. In many cases this limitation can be eliminated by employing another IE model (IE+ model) based on the extended set of intermediate equations (see Section 3.2). The extended intermediate equations include more realistic representation of the bottom friction and the vertical friction allowing the IE+ model to permit lower layer with zero thickness under certain conditions. Thus, in many cases IE+ model allows to significantly increase the realism of numerical experiments (i.e. by including realistic coastal topography) while retaining the computational efficiency and the clarity of the dynamical analysis of the IE model.

The idealized PE experiments further increase the realism of the numerical simulations by including a realistic continuous stratification and a more accurate set of equations. Even though the IE+ model significantly increases the realism of the IE model, it does limit the number of isopycnal layers to only two. Also, the intermediate equations used by this model limit the flow parameters to moderate Rossby and Froude numbers, a condition that can be violated in strong flows especially during interactions with bottom topography. Both of these limitations are lifted by introducing a continuously stratified PE model.

The final step in the hierarchy of numerical experiments is a sequence of fully realistic PE model simulations. These simulations were designed primarily to verify the results of previous idealized experiments by enabling a direct comparison with observations. The realistic simulations were conducted by initializing the ocean conditions observed prior to the simulated events with a high degree of detail. Another important goal of these simulations was to provide a better dynamical interpretation for some of the observed ocean current events and to improve our understanding of ocean circulation in particular regions of the GOM. This is the ultimate goal of the investigation and it can only be achieved after sufficient intuition and understanding of the dynamics involved has been developed as the result of previous idealized experiments.

4.2 Intermediate Equations Experiments

The principal goal of the IE experiments was to develop an initial understanding and intuition of the LCE principal dynamics. Due to finite layer thickness limitation of the IE model these initial experiments are restricted to the areas of the GOM where the bottom topography does not penetrate into the main thermocline, i.e., the abyssal plane in the central GOM and the western and northern continental slopes. We initialize an anticyclone resembling a LCE over either the abyssal plane away from the topography or over the northern continental slope and simulate its evolution on the β -plane.

The majority of the experiments are performed with the 2-layer IE model (see Section 3.1). In the 2-layer configuration the upper layer represents the main thermocline and the lower layer represents the deep weakly stratified ocean. The anticyclone is initialized in the upper layer while the lower layer is initially at rest. Then, 7-layer IE experiments are conducted as an intermediate

step between 2-layer IE and the σ -coordinate PE model. In the 7-layer formulation the density variation between isopycnal layers is limited to 0.75 (versus 2.0 in the 2-layer case). This allows fitting of a linear density profile without significant potential thickness distortions (see PE model initialization section below). Conveniently, the 7-layer formulation can be easily converted back to two layers as we will demonstrate below. Intercomparison experiments between 2-layer and 7-layer versions of the IE model are conducted. Some preliminary conclusions about the effect of the finer vertical resolution are made.

4.2.1 2-Layer Experiments

4.2.1.1 Model Configuration and Initialization

The IE model was configured for a rectangular domain of $1,600 \times 1,280$ km with a 10 km grid resolution. No flux boundary conditions were prescribed on the western, eastern, and northern boundaries; the southern boundary was left open to allow TRW's and other waves to propagate out of the domain.

Topography included a linearly sloping bottom at both northern and western boundaries, so that the resulting lower layer thickness was prescribed as

$$D_2 = D_{2min} + \min(x\partial_x D_2, (y - L_y)\partial_y D_2, D_{2max} - D_{2min}) \quad (4.1)$$

where the shallowest lower layer depth, $D_{2min} = 200$ m, the slope, $\partial_x D_2 = -\partial_y D_2 = 0.01$, and the deepest lower layer depth, $D_{2max} = 3,200$ m. With the upper layer thickness $D_1 = 300$ m, the maximum ocean depth was 3,500 m. L_y is the meridional width of the domain. This topography is an idealized representation of the northern and western continental slopes in the GOM. Vertical walls along the western and the northern boundaries represent the shelf break. The shelf itself cannot be realistically represented due to the limitation of the model on the thickness of the lower layer.

The vortex was initialized with a circular potential vorticity perturbation in the upper layer,

$$q_1 = \frac{f}{D_1 + Z(r)}, \quad (4.2)$$

$$Z = Z_c \frac{1 + \tanh(1 - r^2)}{2}, \text{ and} \quad (4.3)$$

$$r = \frac{\sqrt{(x - x_0)^2 + (y - y_0)^2}}{L_c}, \quad (4.4)$$

where the vortex core parameters: $Z_c = 900$ m and $L_c = 80$ km were chosen to initialize the upper layer eddy with maximum velocity of 1 m/s and maximum interface slope of 0.003 at 100 km radius. This corresponds to an eddy diameter of about 400 km as shown in Figure 4.1. The lower layer was initially at rest.

This approach to initialization is sometimes called ‘‘feature modeling.’’ The main idea is to construct a circulation feature by prescribing its shape and velocity with an analytical function. The free parameters of the analytical function are specified to produce a feature of the required size and intensity. In this case, instead of prescribing the density and velocity structure of the feature, we prescribe its potential vorticity signature.

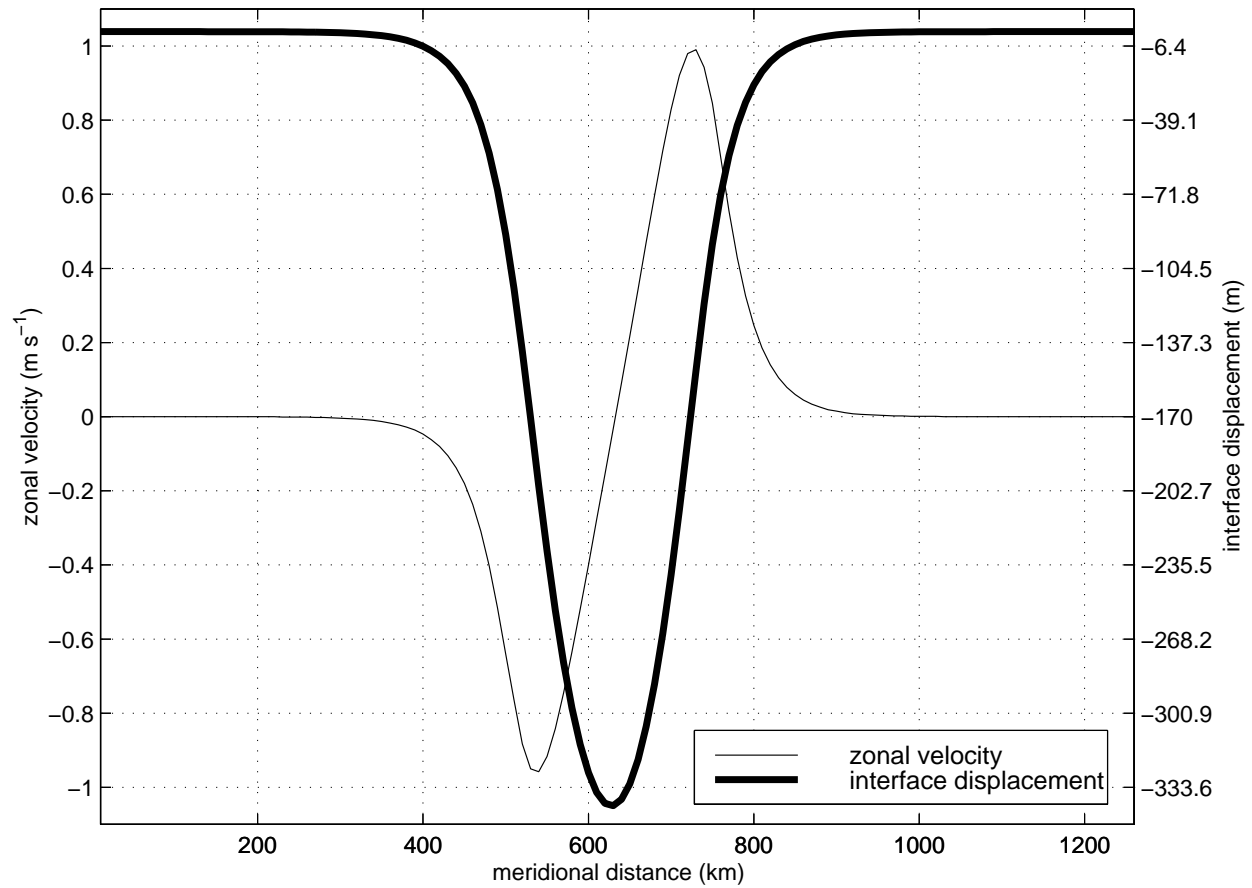


Figure 4.1. Initial meridional section of zonal velocity and interface displacement across the eddy center.

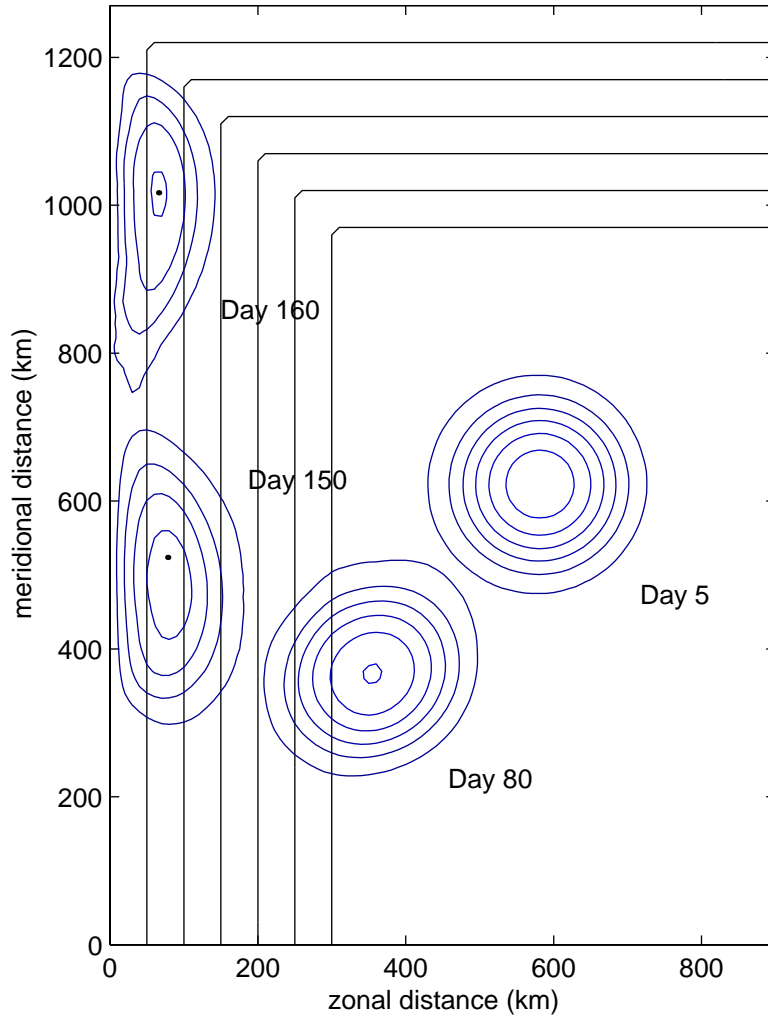


Figure 4.2. Eddy trajectory (dots mark the eddy center each day) and eddy shape (interface displacement; contour interval is 50 m) superimposed upon topography.

4.2.1.2 Numerical Experiments

Two experiments were conducted with the model configured as described in the previous section. Experiment 1 depicts the evolution of an LCE-like eddy and the associated lower layer flow when the eddy is initialized over a flat bottom and interacts with a western continental slope and boundary (Figure 4.2). This experiment shows four distinct phases of evolution that are fundamental to eddy propagation and development. First, over the flat bottom, the eddy drifts southward until it encounters the western continental slope. Second, over the slope, the eddy's southward speed decreases as the eddy continues its westward drift towards the shelf break. Third, the eddy's meridional speed changes sign when the eddy approaches the boundary. Finally, the eddy moves rapidly northward along the boundary and develops an elongated shape.

During the first stage, the eddy's westward drift remains about 3 km/day which is only slightly less than in a reduced-gravity model (Nof 1983; Nycander and Sutyrin 1992). The most dramatic effect that inclusion of dynamics in the lower layer produces is a substantial southward translation, not present in reduced-gravity models of similar eddies, that reaches ≈ 3.5 km/day, which is in

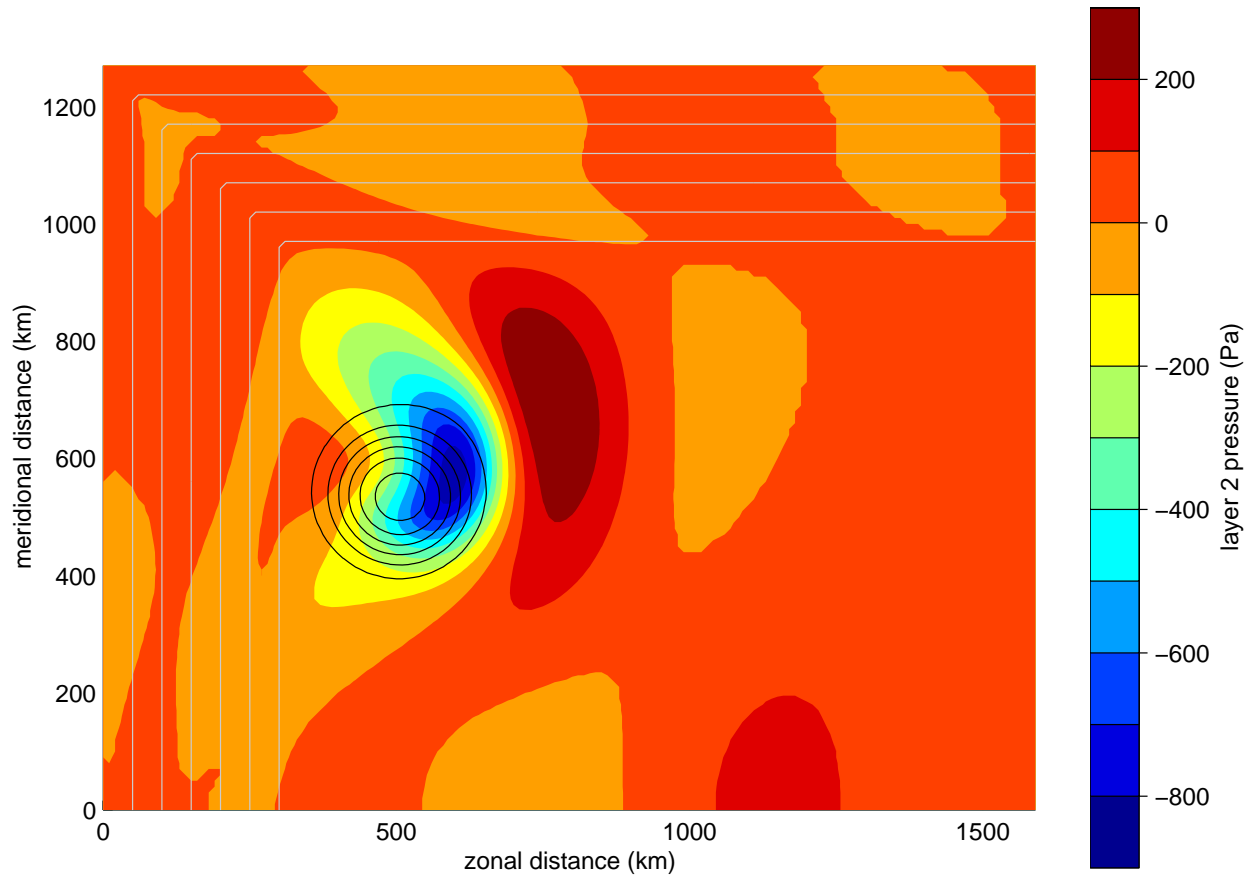


Figure 4.3. Lower layer pressure (shaded) superimposed by interface displacement (contour interval is 50m) and topography at day 30.

qualitative agreement with previous numerical simulations over a flat bottom (e.g., Chassignet and Cushman-Roisin (1991)). The physical mechanism of the southward drift is related to the development of a cyclonic circulation in the lower layer slightly to the east of the vortex center as shown in Figure 4.3. This cyclonic circulation penetrates the upper layer due to the hydrostatic relation and advects the eddy center southward - providing a southward motion in addition to the westward drift which is mostly due to the beta-effect.

The vortex begins to feel the image vortex effect at about 160 km from the western boundary where the meridional eddy motion turns northward. The eddy center continues to approach the western boundary with decreasing zonal speed as it accelerates to the north. The eddy shape becomes elongated as seen at day 150 in Figure 4.2. Such a “wodon”-like eddy structure was described by Shi and Nof (1994) who considered vortex interaction with a vertical wall.

Experiment 2 is configured identically to Experiment 1 with the single exception that the eddy is initialized over the northern continental slope instead of the flat abyssal plane. In this case, three stages of evolution are present: an initial westward drift, a movement towards the northern boundary, and an eastward zonal drift along the northern boundary (Figure 4.4).

During the first stage, TRW dispersion in the lower layer prevents the development of the deep cyclone found in the flat bottom region, and the eddy consequently propagates almost due west in qualitative agreement with the quasi-geostrophic simulations of Theirry and Morel (1999) and the theoretical analysis of Sutyrin (2001). The southward drift speed remains below 0.2 km/day, and

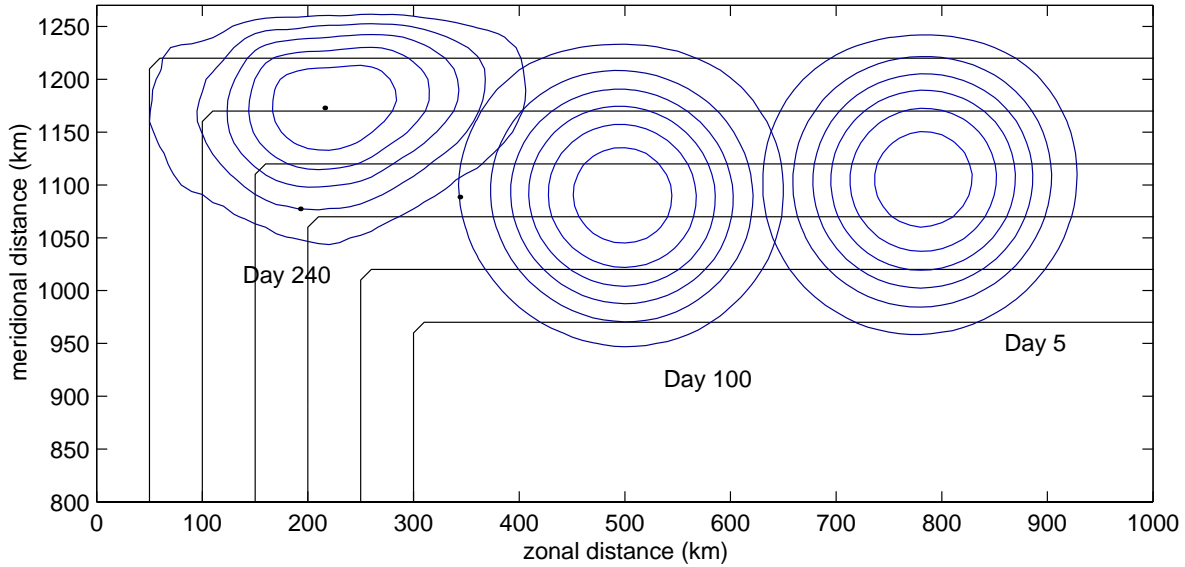


Figure 4.4. Same as Figure 4.2 except for experiment two.

the westward speed of 3 km/day is slightly smaller than in the reduced-gravity model. The TRW's generated in the lower layer have maximum velocity of about 5 cm/s near the northern boundary.

4.2.1.3 Discussion

Large upper-ocean eddies, of which LCE's are examples, drive characteristic deep flow as the β -effect pushes them westward. This deep flow then adds a significant southerly component to the upper-ocean eddy's propagation. The actual magnitude of this deep-flow-induced southerly propagation is dependent upon the depth of the underlying water; lower layer flow in deeper oceans induces weaker southerly propagation.

The fact that the β -induced westward drift of upper-ocean eddies like LCE's drives characteristic deep circulation deserves special commentary for at least three reasons. First, the myth that LCE's are only upper-ocean features needs to be dispelled. All observational descriptions of LCE's (e.g., Kirwan et al. (1988), Lewis et al. (1989), Vukovich and Waddel (1991), Vidal et al. (1992), and Glenn and Ebbesmeyer (1993)) have focused on the vigorous upper-ocean circulation associated with LCE's as they propagate in the GOM and interact with the continental slope and shelf. While these studies have contributed mightily to our understanding of these eddy features, our work and that of others (Welsh and Inoue 2000) makes it clear that there are characteristic deep flows associated with LCE's. Second, the propagation of upper-ocean LCE's is significantly impacted by the accompanying deep circulation. Comparison of the propagation of LCE-like eddies in numerical experiments with and without deep circulation (full versus reduced-gravity models) shows that the inclusion of the deep circulation adds a southerly component to the LCE's propagation in excess of 3 km/day over the abyssal interior – a speed that is approximately equivalent to the LCE's β -induced westward drift. The importance of the lower layer circulation is magnified during LCE-topography interactions involving wide shelves such as those found in the northwestern and northern GOM. During these LCE-topography interactions, the strength of the lower layer circulation is enhanced because the lower layer vortex tube stretching associated with LCE propagation is a larger fraction of the total water column height. This more vigorous lower layer circulation

leads to rapid – as much as 10 km/day in our experiments – southward translation along the shelf-break. Finally, the interaction of the deep circulation driven by LCE’s with the continental slope is a significant source of TRW energy in our simulations. It seems plausible to suggest that bursts of TRW energy are likely to be generated as the deep eddies which develop in the abyss as the LCE propagates disperse into TRW’s as the LCE approaches the continental slope.

When an eddy is initialized over the northern shelf, TRW dispersion prevents development of significant lower layer flows. This implies that the only source of cross-isobath (southerly) movement is self-advection of the surface eddy through nonlinear steepening. In our experiments, southward propagation of the surface eddy never exceeds 0.2 km/day in these circumstances, and the upper-layer eddy propagates essentially zonally until it encounters the bathymetry in the north-west corner.

4.2.2 7-Layer vs. 2-Layer IE Model Intercomparison Experiments

4.2.2.1 Experiment Design

The 7-layer model subdivides the upper layer of the 2-layer model into 6 layers. The layer subdivision was chosen to represent the realistic stratification of the GOM. The typical density profile in the GOM was modified slightly to have the same average density that was used in our previous 2-layer IE experiments. This permits direct comparison of PE and multi-layer IE experiments with our previous results.

The vortex is initialized with a circular PV perturbation specified separately for each layer except the lower layer which is initially assumed motionless. The form of the PV perturbation in i -th layer (PV-based feature model of an LCE) is the same that was used in the 2-layer IE experiments:

$$q_i = \frac{f}{D_i + Z_i(r)}, \quad Z_i = Zc_i \frac{1 + \tanh(1 - r^2)}{2}, \quad r = \frac{\sqrt{(x - x_0)^2 + (y - y_0)^2}}{L_c}, \quad (4.5)$$

the amplitude of the disturbance Zc_i varies from layer to layer while the radius and the width of the transition zone L_c remain the same. This is done to allow a straightforward intercomparison between 2-layer and 7-layer IE model experiments. Amplitudes of PV disturbances in each layer are chosen to produce the stratification in the center of the vortex similar to what is observed in LCE’s. The resulting vortex density, i.e., interface elevations, and velocity structure is shown on Figure 4.5.

The experiment design is similar to the one that was used in our previous 2-layer IE model. The domain is a rectangular $1,600 \times 1,300$ km with 3,500 m depth everywhere except near the northern and western boundaries where it is sloping outwards at 0.01 rate representing the continental rise in GOM. The slope is smoothed in the northwest corner to allow for free propagation of TRW’s. Sponge BCs are applied along southern and eastern boundaries to allow energy propagation out of the domain. The exact form of the bottom topography is shown on Figure 4.6. A uniform 10 km resolution is used.

The 2-layer IE model was initialized by transferring the initial balance solution from 7-layer model:

$$D_1 = \sum_{n=1}^6 \widetilde{D}_n, \quad D_2 = D_7, \quad \rho_1 = \frac{\sum_{n=1}^6 \widetilde{\rho}_n \widetilde{D}_n}{D_1}, \quad \rho_2 = \widetilde{\rho}_7, \quad q_1 = \sum_{n=1}^6 \widetilde{q}_n, \quad q_2 = \widetilde{q}_7,$$

i.e., the unperturbed depth of the upper layer in 2-layer model is taken to be the sum of depths of the upper 6 layers in 7-layer model, the density of the upper layer is taken to be the average

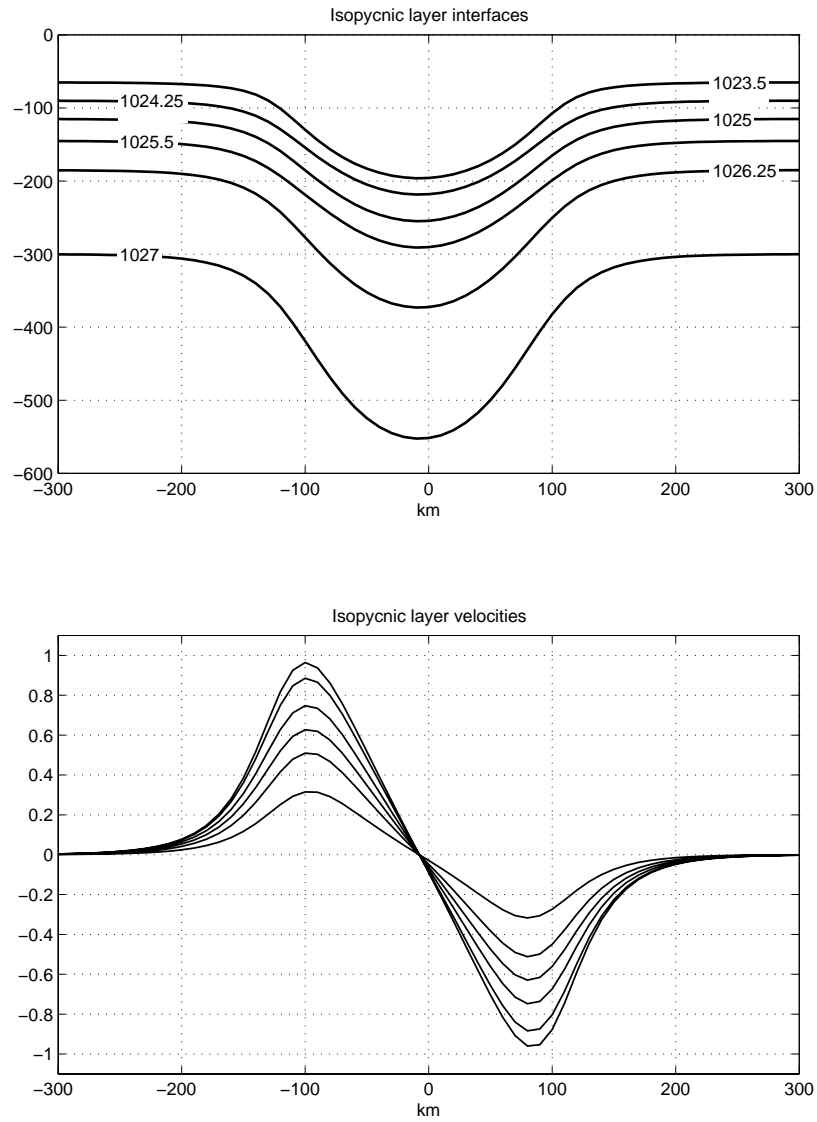


Figure 4.5. Interface elevations and velocity structure of the idealized vortex initialized in 7-layer IE model.

density of the upper 6 layers, and the potential thickness anomaly associated with the vortex is taken to be the sum of anomalies in the 6 upper layers. Note that the resulting eddy structure, as it is prescribed by the potential thickness anomaly, is different from the structure used in our previous experiments.

4.2.2.2 Results

Figure 4.6 shows the vortex propagation over flat bottom and shallow slope in 7-layer (left panel) and 2-layer (right panel) experiments. Thick contours indicate the bottom topography, thin contours indicate lower interface displacements caused by the vortex every 70 days of model integration, blue line indicate continuous vortex trajectory. The general pattern of vortex evolution is very similar in both models and essentially repeats what was previously reported. Initially the vortex propagates south-west over flat bottom region with average speed of 3 km/day being propelled by β -effect and deep cyclonic circulation penetrating to the upper layer. Once it encounters the sloping region the southward component of its propagation speed rapidly decreases due to dispersion of the deep circulation over the topographic slope. The vortex then moves westward until it encounters the boundary wall after which it starts moving rapidly northward due to the image effect with the wall.

The most significant difference between the two experiments is the direction of the vortex propagation. The propagation speed of the vortex simulated in 7-layer model has substantially greater southward component than the propagation speed of the vortex in 2-layer case. The point where the vortex center reaches 2,500 meters isobath, which is approximately the point where it starts turning north, is about 200 km further south in 7-layer case. Since the southward component of the vortex propagation speed is largely due to its advection by deep cyclonic circulation, the accelerated southward motion of the vortex in 7-layer case implies stronger interaction between the vortex and the deep cyclones. However, differences in amplitude of the deep cyclonic circulation between 2-layer and 7-layer cases cannot account for the observed differences in the vortex southward propagation speed. This seems to suggest that in the case of well resolved thermocline structure the interaction of the vortex with deep cyclones can lead to distortion of vortex vertical structure, which produces additional vortex advection.

4.3 IE+ Model Experiments

The IE+ model was used to conduct several idealized experiments simulating interaction of LCE's with western GOM topography. These simulations provided the first insight into the mechanism of LCE interaction with thermocline-penetrating topography. An important finding of the 2-layer IE+ experiments was that the eddy-shelf interaction produces off-shore advection of high PV water from shallow regions over the shelf. The subsequent formation of surface-intensified cyclones associated with positive PV anomalies advected off the shelf was identified as one of the key physical mechanisms controlling the behavior of LCE's. The interaction of a LCE with off-shelf advected cyclones results in a looping southward motion of the eddy.

We also have found that a LCE interacting with the continental shelf can generate bottom-intensified eddies beneath the main thermocline over regions of flat topography. The net effect of these eddies is to amplify the cyclic motions of the LCE. Moreover, it was established that the effect of bottom-intensified eddies on the trajectory of the LCE is substantially stronger than the effect of the surface-intensified cyclonic eddies; this effect is responsible for the large amplitude cyclic motion of LCE's during their interaction with the GOM western shelf at 25°N.

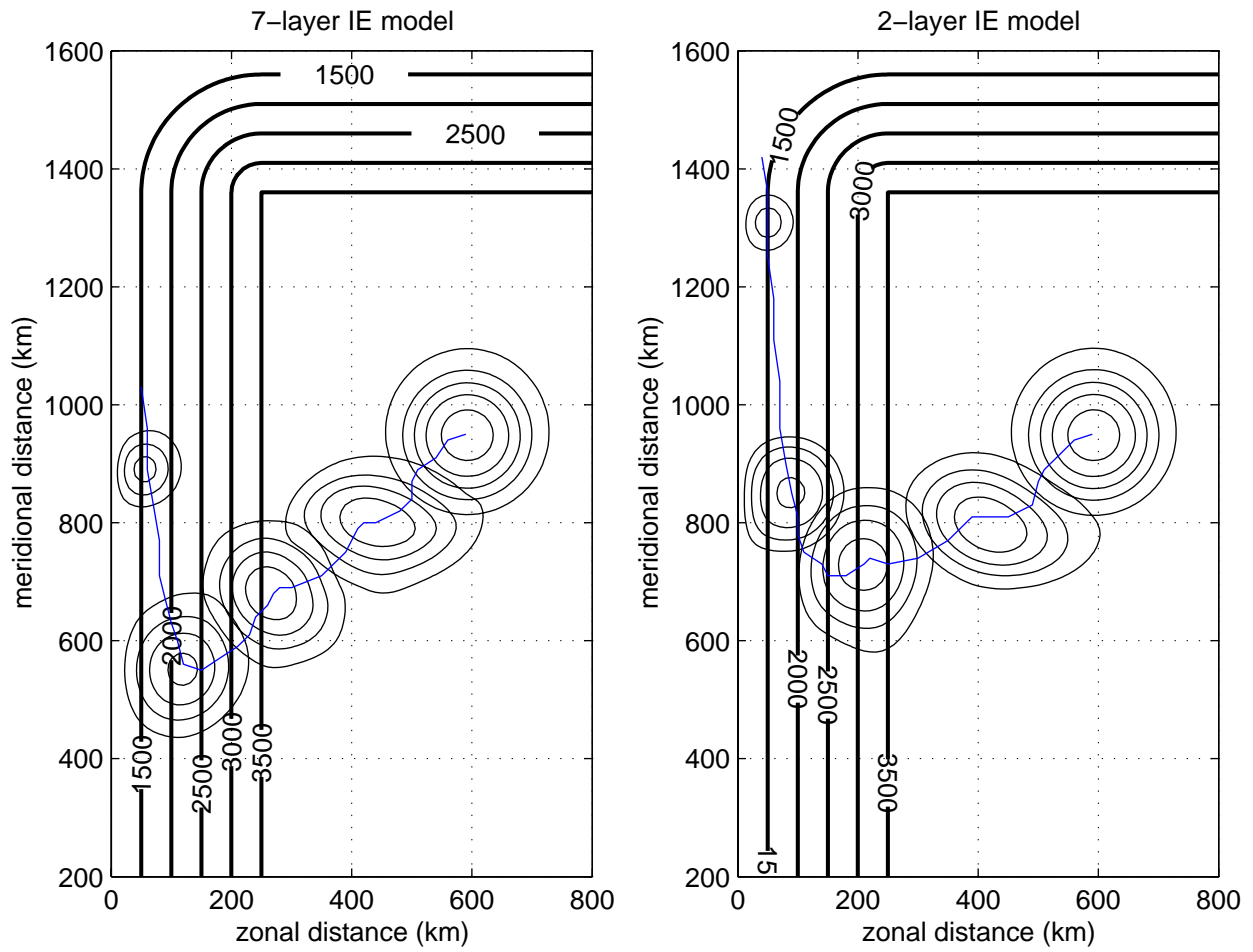


Figure 4.6. LCE propagation over flat bottom and shallow slope in 7-layer (left panel) and 2-layer (right panel) IE model experiments. Thick contours indicate the bottom topography, thin contours indicate lower interface displacements caused by the vortex every 70 days of model integration, blue line indicate continuous vortex trajectory.

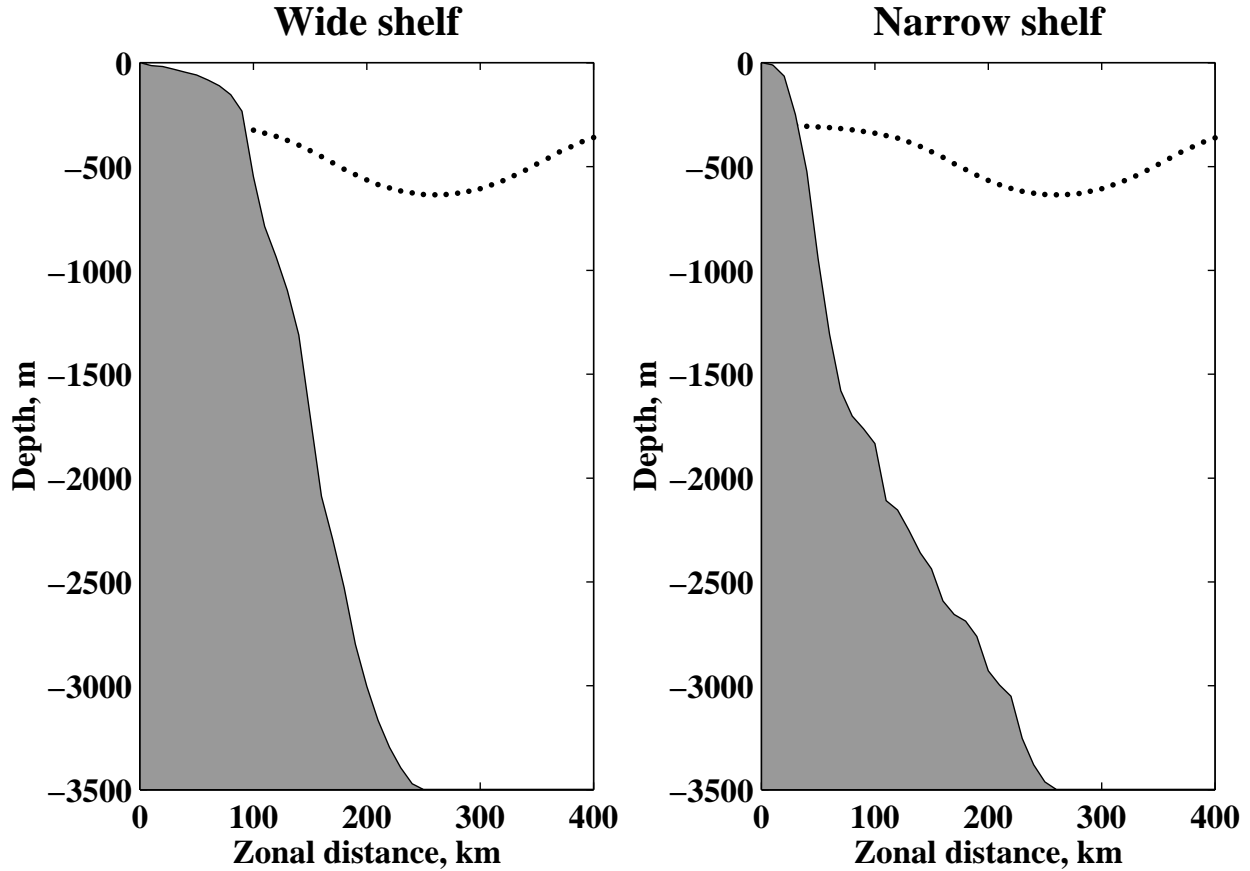


Figure 4.7. Zonal sections of bathymetry and initial interface displacement for the two IE+ model experiments. The wide shelf bathymetry is from 25°N, and the narrow shelf bathymetry is from 23°N. The initial interface displacement is shown with the dotted line.

4.3.1 Experiment Design

The model was configured for a rectangular, $540 \times 1,000$ km, basin with a uniform 10 km horizontal resolution. No flux boundary conditions were assigned on the western, eastern, and northern boundaries; open boundary conditions were assigned on the southern boundary to allow TRW's to propagate out of the domain. The bottom topography in the eastern part of the domain is flat (3,500 m) representing the bathymetry of the central GOM. A meridionally uniform slope is introduced along the western boundary representing the western shelf.

Two types of shelf configuration were simulated. In the first configuration, which corresponds to the GOM coastal topography profile at 25°N, the shelf is relatively wide while the continental slope is relatively narrow. In the second configuration, which corresponds to the GOM topography profile at 23°N, the shelf is relatively narrow while the continental slope is relatively wide. The prescribed basin margin bathymetry included vertical walls on the northern and eastern boundaries. The exact bottom topography profiles were prescribed as specific cross-sections from the ETOPO5 bathymetric database and are shown in Figure 4.7.

The vortex was initialized with the same circular PV perturbation in the upper layer as in our previous IE experiments (Section 4.2.1): where the vortex core parameters: $Z_c = 900$ m and

$L_c = 80$ km are chosen to initialize the upper layer eddy with maximum velocity 1 m/s and maximum interface slope 0.003 at 100 km radius. This corresponds to an eddy diameter of about 400 km. The lower layer is initially at rest. The initial distribution of the interface is shown in Figure 4.7.

4.3.2 Results

Both the narrow (23°N) and wide (25°N) shelf experiments exhibit the same qualitative evolution of the LCE and the associated eddy features during interactions with the bathymetry. We will focus on the wide shelf case in exploring the qualitative behavior of the system. The analysis of important differences between the two experiments is presented in Section 4.3.3.

Figure 4.8 shows the simulated interface displacement at 5, 25, 60, and 300 days of integration for the wide shelf experiment. After the LCE encounters the shelf, water masses are exchanged across the shelf break. On the northern side of the LCE, water is advected from the shelf onto the slope; water is advected from the slope to the shelf on the LCE's southern side. As the shelf water is advected eastward into deeper regions, the water column stretches and acquires cyclonic relative vorticity. This forms a "lopsided" dipole in which the LCE is the much stronger member (day 25). The dipole moves slightly out to sea, leading to the "loopy" character of the LCE track, until the cyclone is swept around the LCE's periphery into the shelf where it dissipates as a packet of topographic Rossby waves (day 60). After this time, the LCE moves back into the slope, and the entire process begins again. This process continues until the LCE weakens so that the cyclone and LCE are of comparable strength (day 300). This more stable dipole structure self advects away from the shelf and to the north.

As indicated above, the behavior in the narrow shelf case is qualitatively similar to the wide shelf case discussed above, but the LCE track resulting from the interaction with the basin margin bathymetry is different (Figure 4.9). In particular, the "loopiness" of the narrow shelf track is less than that of the wide shelf case, and the southward propagation is also substantially reduced.

4.3.3 Experiment Analysis

The numerical simulations indicated that two different shelf configurations produce two types of LCE behavior. In the first configuration, which corresponds to the GOM coastal topography profile at 25°N , the LCE propagates southward following a cyclic trajectory with large (~ 100 km) cycles. In the second configuration, which corresponds to the GOM topography profile at 23°N , the LCE also propagates southward along a cyclic trajectory, but the amplitude of the cycles is substantially smaller (~ 20 km) and the resulting southward propagation speed is slower. The analysis presented below indicates that an additional dynamical process is present in the system controlling LCE interaction with coastal topography. This process is associated with formation of bottom-intensified eddies beneath the LCE via the mechanism of vortex tube stretching/squashing in the lower layer. Furthermore, by conducting additional experiments with modified topography we were able to demonstrate conclusively that this process is responsible for differences in LCE behavior in the 23°N and 25°N topography configurations.

A closer look at the results of the experiment reveals that in some cases bottom-intensified cyclones and anticyclones can form beneath the LCE. An example of bottom-intensified eddy formation beneath an LCE can be seen in Figure 4.10. Shown in the figure is day 40 of the integration in the wide shelf topography configuration. The thick contours indicate the interface displacement and the vectors indicate the velocity in the lower layer. By day 40 the LCE has

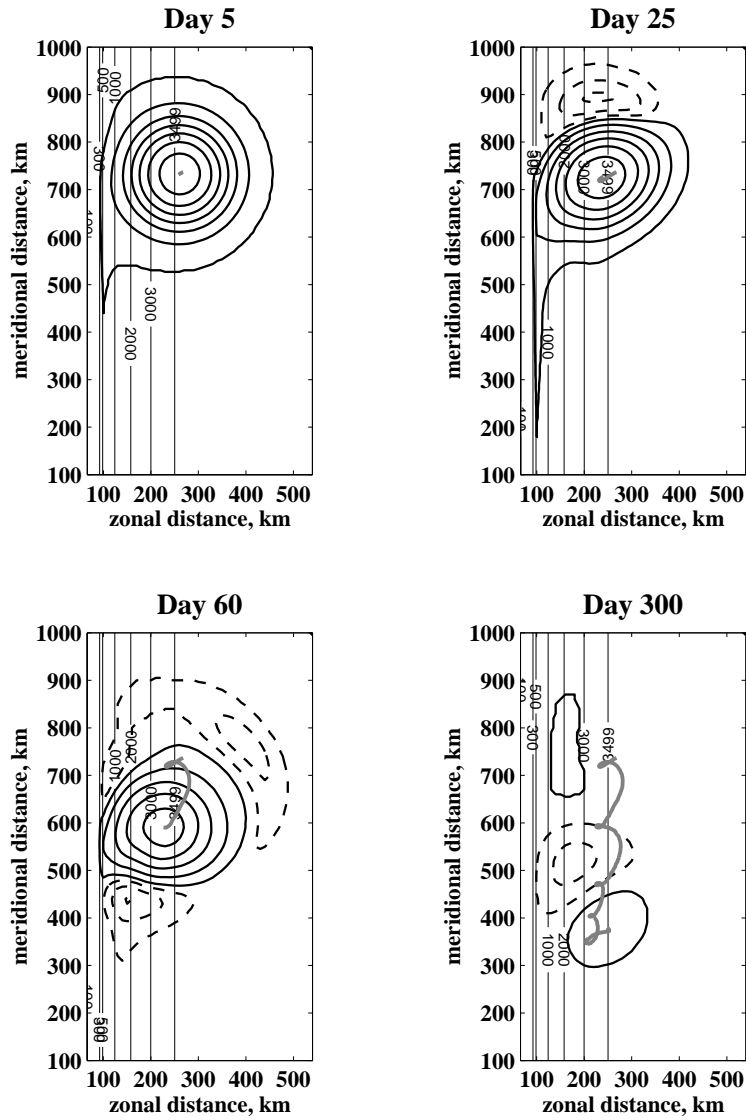


Figure 4.8. Upper layer interface displacement at 5, 25, 60, and 300 days of integration for the wide shelf experiment. Positive displacement is shown with thick solid contours; negative displacement is shown with dashed contours. The gray line indicates the LCE track. Bathymetry is contoured with thin lines.

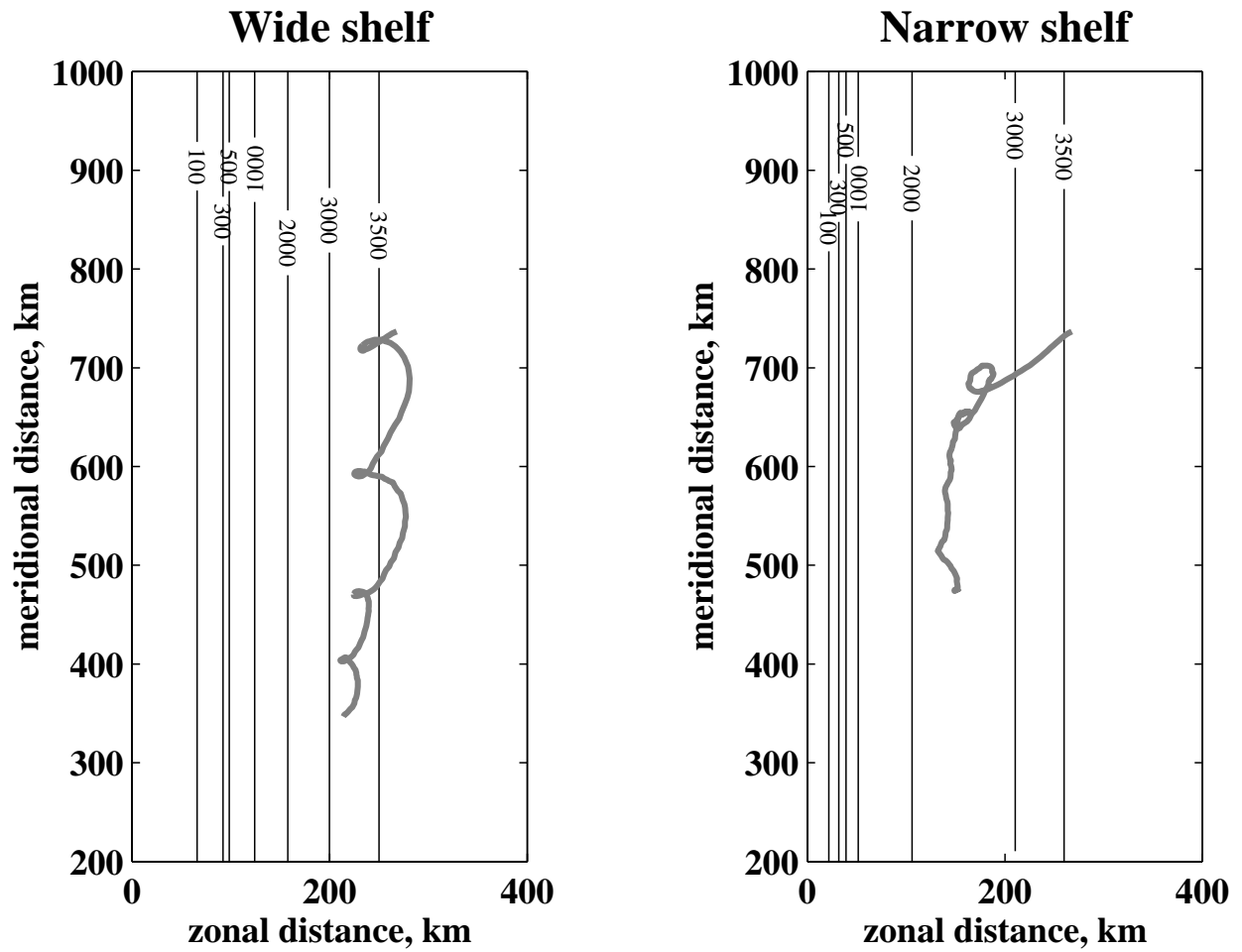


Figure 4.9. Comparison of the LCE tracks from the narrow and wide shelf experiments. Zonal oscillatory motion of the eddy as well as the southward propagation are substantially reduced in the narrow shelf case.

already generated a surface-intensified cyclone via the process of off-shelf PV advection. As a result of cyclone-anticyclone interaction, both the LCE and the cyclone have become elliptic and the pair is rotating clockwise.

A rotating elliptic eddy causes compression of the lower layer water columns in front (in the rotational sense) of the eddy and stretching behind the eddy. The process of water column squashing (stretching) in the lower layer generates anticyclonic (cyclonic) relative vorticity. The bottom slope west of the LCE leads to radiation of the lower layer relative vorticity in the form of topographic Rossby waves. On the other hand, the eastern part of the LCE is located over a flat bottom, allowing the relative vorticity generated in the lower layer to form a bottom-intensified cyclone-anticyclone pair. As one can see from the figure, the net effect of the bottom-intensified pair on the LCE is to push it eastward - i.e., away from the shelf.

The mechanism of bottom-intensified eddy generation described above can only work when a substantial portion of the surface eddy is located over flat topography. Figure 4.11 shows the same IE+ simulation of eddy-shelf interaction but for the 23°N topography configuration. As one can see the LCE is located almost entirely over the sloping bottom which prevents the formation of bottom-intensified eddies.

To demonstrate that the bottom-intensified eddy mechanism is responsible for the different LCE behavior in the 23°N and 25°N topography configurations, a hybrid topography IE+ experiment similar to those described in the previous section was conducted. The coastal topography profile from 25°N was combined with the profile from 23°N . The hybrid profile (Figure 4.12) was constructed to contain the shallow part (shallower than 1000 m) from 23°N (narrow shelf) and the deep part from 25°N (narrow continental slope). The resulting topography has the same configuration in the upper layer as in the narrow shelf experiment, however the narrow continental slope in the lower layer allows the generation of bottom-intensified eddies similar to the wide shelf experiment.

The resulting LCE trajectory in this hybrid experiment was found to be very similar to the trajectory in the 25°N (wide shelf, narrow slope) experiment (see Figure 4.13) - i.e., it had amplified cyclic motion - proving that the large amplitude cyclic motion of the LCE at 25°N is related to the bottom-intensified eddies. The resulting LCE behavior indicates that the effect of bottom-intensified eddies (when they can be generated) on the LCE trajectory is substantially stronger than the effect of the off-shelf-advected surface-intensified eddies.

Observational evidence was found to demonstrate that the anticyclonic eddy behavior seen in the 25°N (wide shelf, narrow slope) experiment can be seen in the western GOM. Figure 4.14 taken from Lewis et al. (1989) shows a drifter trajectory observed in 1985-86. The drifter was seeded in the so-called "Fast Eddy" on July 18, 1985 and tracked the eddy until June 26, 1986 throughout the process of eddy interaction with the western shelf. The eddy was observed to reflect back (move eastward) from the shelf and propagate southward following the same cyclic motion that we see in our experiments.

4.4 PE Experiments

The class of PE experiments is the next step in the hierarchy of numerical experiments with increasing realism. In these experiments the level of realism is increased by introducing a realistic continuous stratification, realistic bottom topography, and more accurate primitive equations into numerical simulations. In following the overall methodology of a gradual increase of realism, the entire set of PE experiments was subdivided into several sets of experiments with gradually

Deep circulation underneath LCE-cyclone pair in IE+ model

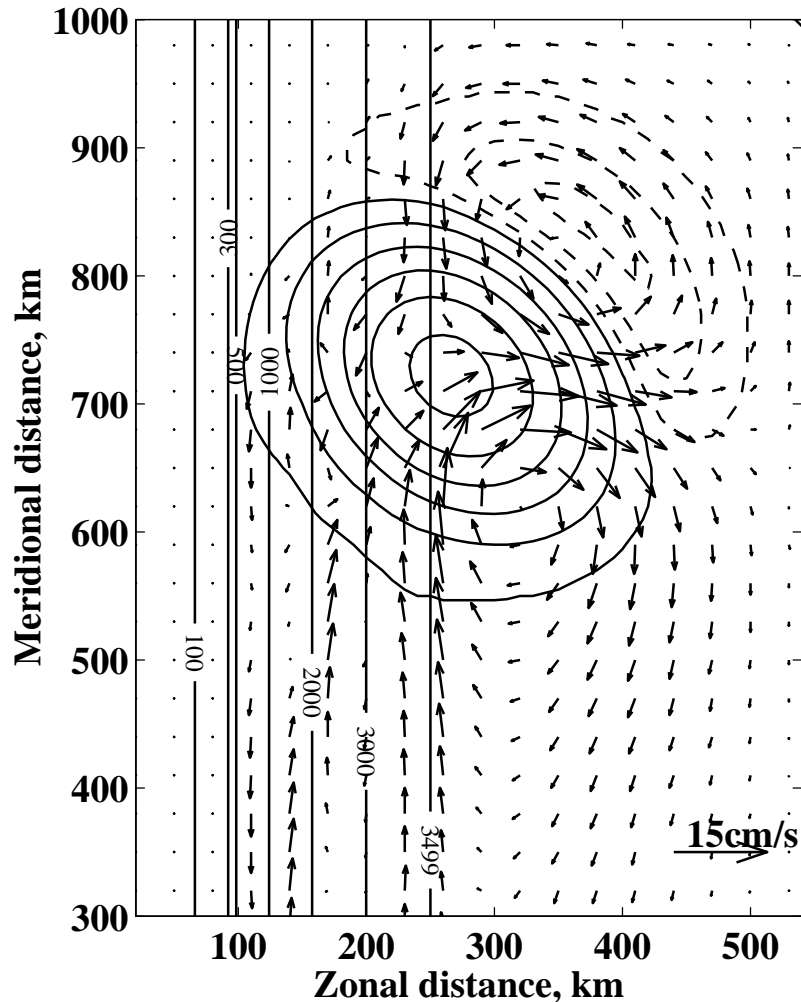


Figure 4.10. Wide shelf topography configuration experiment, day 40 of model integration. Thick contours indicate pressure in the upper layer; and vectors show the velocity in the lower layer. A bottom-intensified cyclone-anticyclone pair is formed underneath the surface eddy over flat topography. The net effect of the deep circulation is to push the surface eddy away from the shelf.

Deep circulation underneath LCE–cyclone pair, "narrow shelf"

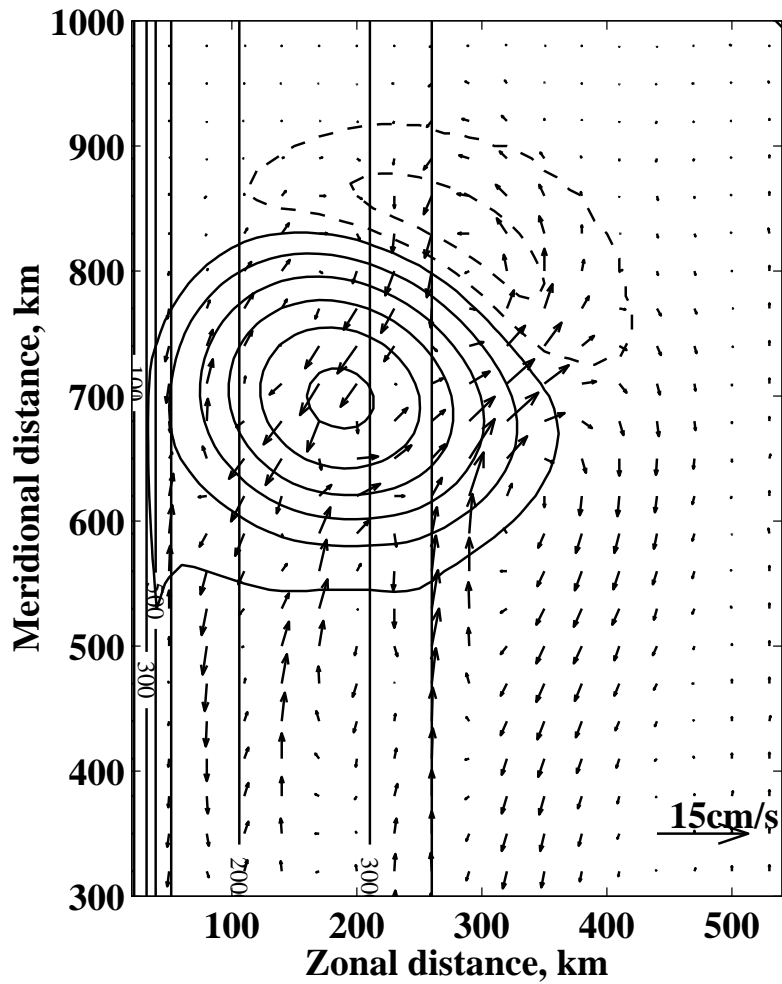


Figure 4.11. Same as in Figure 4.10 but for narrow shelf experiment. The wide continental slope prevents the formation of a bottom-intensified cyclone-anticyclone pair underneath the surface eddy.

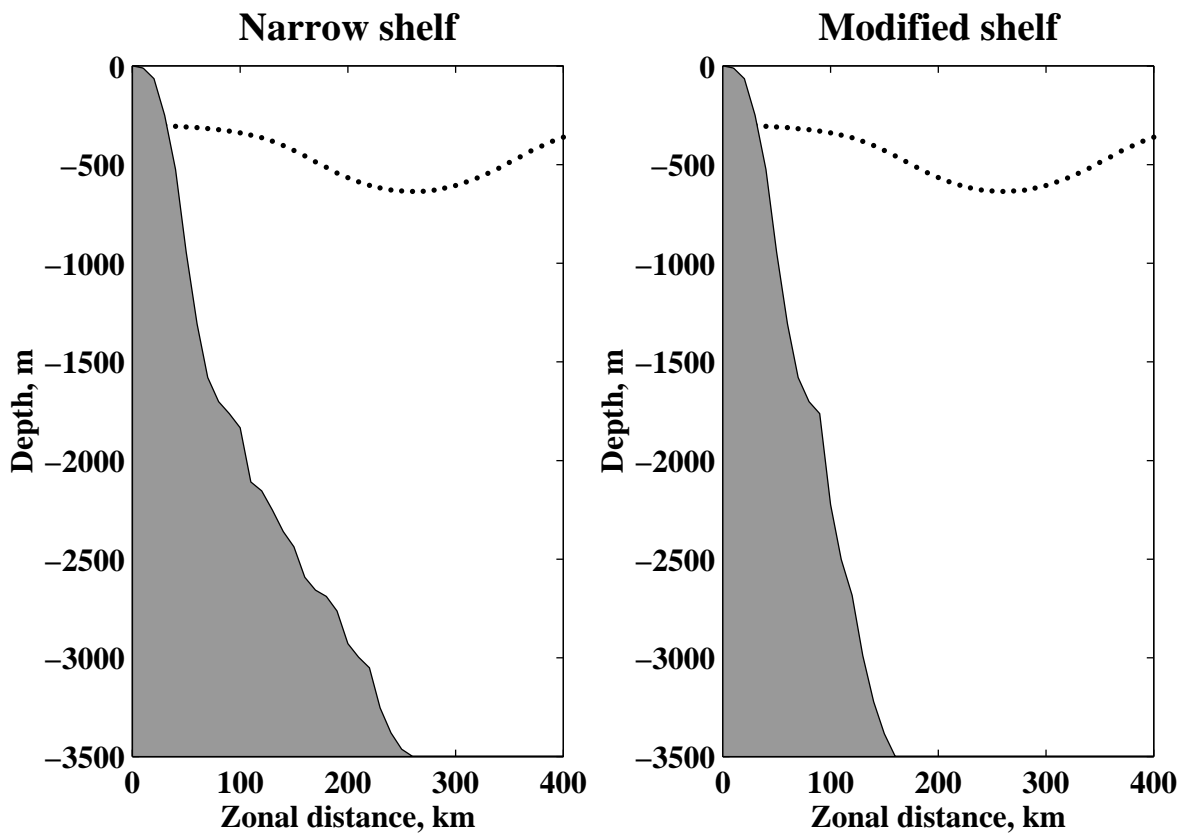


Figure 4.12. Modified bottom topography profile (right panel) compared to the narrow shelf profile (left panel).

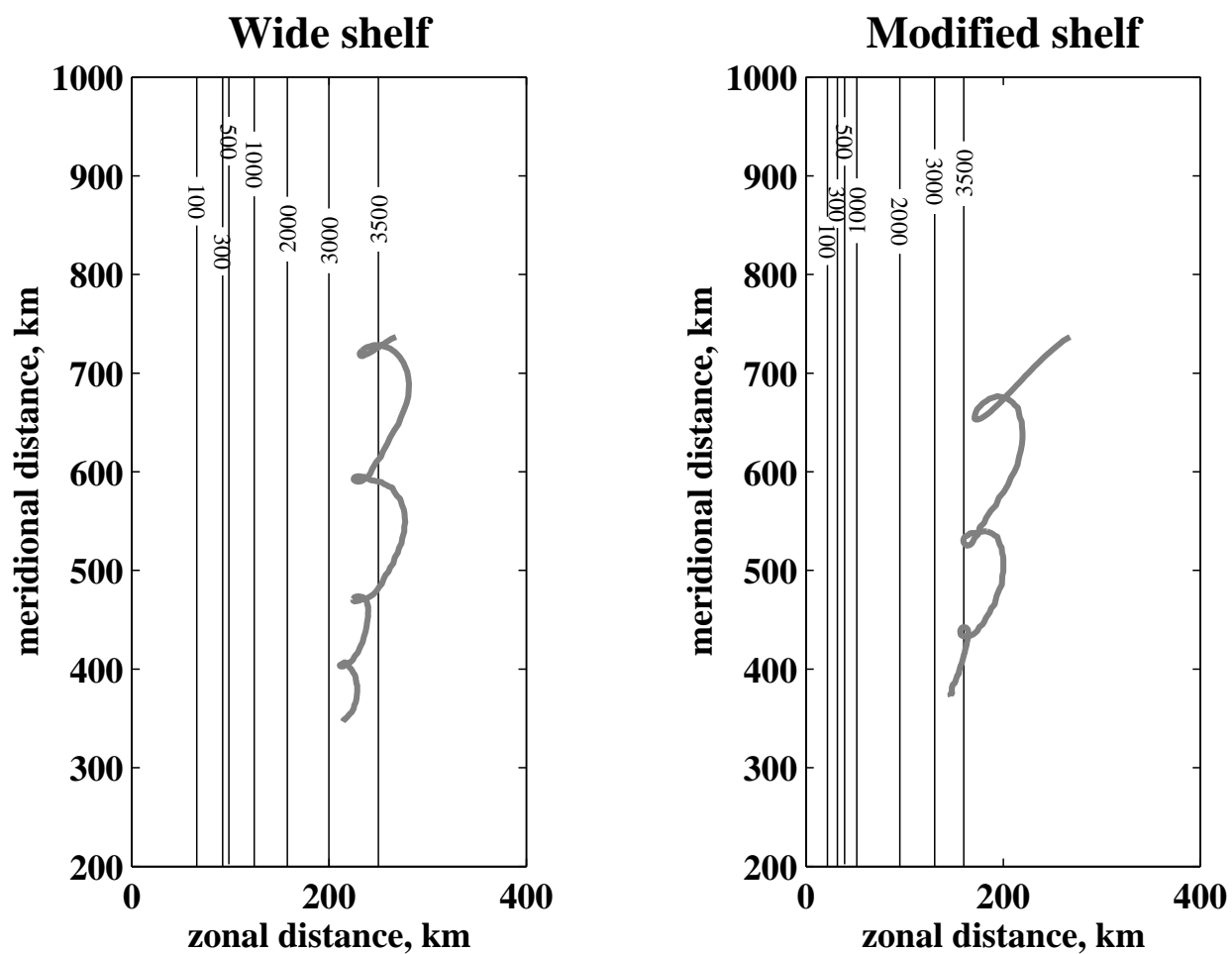
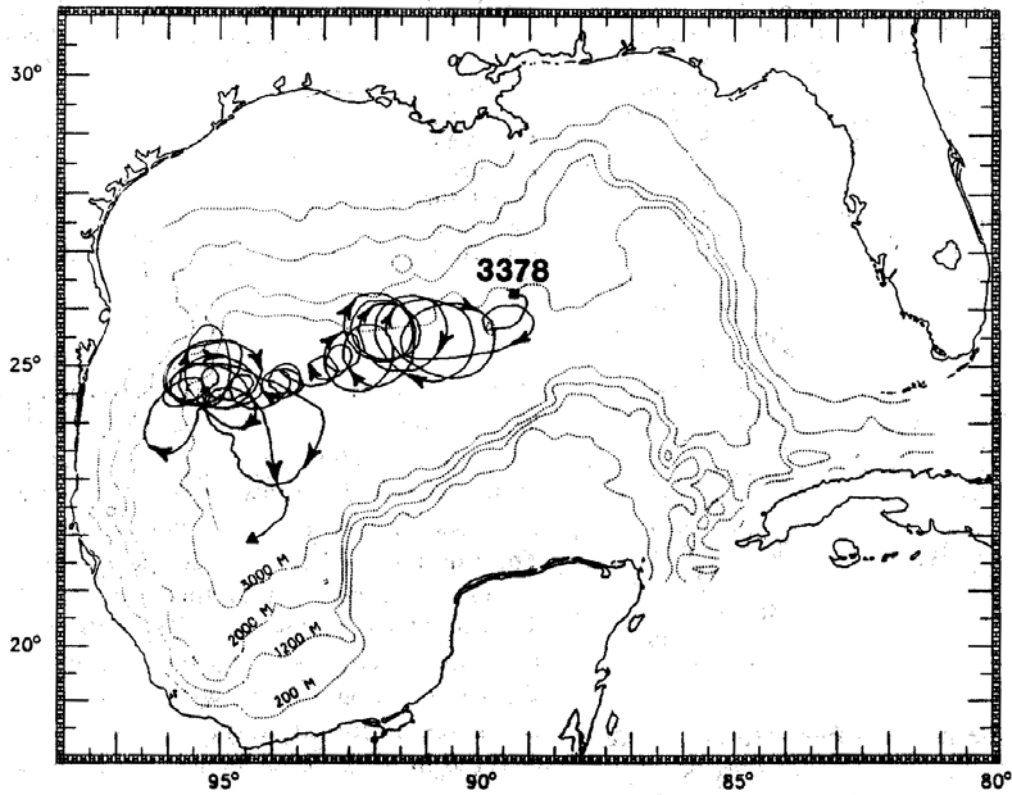


Figure 4.13. Hybrid topography experiment (right panel) compared to the wide shelf experiment (left panel). Trajectory of the anticyclonic eddy is very similar to the trajectory in the wide shelf (25°N) configuration.

LEWIS ET AL.: LAGRANGIAN OBSERVATIONS OF A WARM-CORE RING



Trajectory for drifter 3378. Depth contours are in meters. Squares denote the beginning positions of the drifter trajectories, and triangles denote the end positions.

Figure 4.14. Example of observed cyclic eddy behavior during its interaction with the GOM western boundary.

increasing complexity to provide a smooth transition from IE and IE+ experiments to real event simulations.

We start with developing an initialization procedure which allows for creating a balanced initial conditions in the PE model and enables direct comparison between the PE model and the IE model experiments. Then, the PE model is compared against the IE model in simple configurations to ensure the correctness of the initialization procedure and to verify the IE model results with the more trustworthy primitive equations. Once the confidence in the initialization technique and in previous IE results is reached we proceed with increasing the realism of the PE simulations. The first incremental step is introduction of realistic continuous stratification. The next step is introduction of fully realistic topography. As the result of this incremental process a new dynamical mechanism affecting LCE behavior is revealed. Finally, we simulate several potential scenarios of an isolated LCE evolution during its interaction with coastal topography in the western and the northern GOM and in the northwest corner.

4.4.1 Initialization Procedure

The PE model was initialized by transferring the initial balanced solution from the IE model. The first step in transferring the initial solution from isopycnal layers into the σ -coordinate system is to form a continuous vertical density profile from a set of discrete densities. In order to accomplish this task while preserving the initial balance, the continuous profile is calculated by interpolating linearly between the density layers, i.e. the density in each layer is assumed to change linearly with depth instead of being constant. *Note that the assumption of linear density variation is crucial because it allows for an exact correspondence between fully 3-dimensional PE equations and isopycnal layer shallow water equations which are the basis for the IE model (this can be demonstrated by averaging PE equations vertically within layers).* The linear profiles in each layer are fixed according to two criteria: density values at the layer interfaces have to match, so that the individual profiles form a continuous vertical profile throughout the entire water column (continuity requirement), and the mean density in each layer has to be equal to the density assigned to that particular layer. The second requirement guarantees that the initial balanced solution remains exact after the process of interpolation. Since there is no continuity requirement at the bottom and at the surface, these two criteria are insufficient to uniquely determine the vertical density profile. An additional requirement of constant density in the lower layer is used to eliminate the remaining degree of freedom. This additional requirement has proven to produce the most realistically looking density profiles.

Once a continuous vertical density profile is constructed it is interpolated into the σ -coordinate system. The next step is to convert the obtained density field into three dimensional temperature and salinity fields. This is accomplished using typical salinity profiles in the greater GOM and in LCE's. The salinity is calculated as a mixture of these two profiles. The mixture ratio is chosen to be proportional to the normalized dynamic pressure field in each layer. The mixture ratio is one, i.e., consisting only of the LCE salinity profile, at the center of the vortex. As the dynamic pressure decreases in the radial direction, the mixture ratio decreases as well becoming zero, i.e., consisting only of the GOM salinity profile, outside of the vortex. Thus, the salinity is determined for every point, defining a unique mapping from the density field onto the temperature and salinity fields.

Unfortunately, the velocity field calculated in isopycnal layer coordinates cannot be transferred directly into the PE model coordinate system in the same way as the density. The interpolation process introduces errors into the velocity field that are large enough to bring the initial solution out of balance, therefore, the velocity field has to be recalculated on the grid that is used in the PE

model. In addition, the initial balance in the PE model has to be derived from the specific form of primitive equations written for the coordinate system employed by this particular model, which is different from the intermediate form of balance used in the IE model. It should be emphasized here that switching to a different form of balance does not significantly affect the velocity structure of the vortex; it merely introduces small changes to the velocity field to provide better balanced initial conditions.

The specific procedure that was used to calculate the initial balance in the PE model consists of two steps. First the initial geostrophic balance is calculated using the PE model equations. The obtained geostrophic velocities are then used to calculate the nonlinear momentum advection terms (centrifugal terms). The geostrophic balance is then recalculated taking into account those terms. The procedure may be repeated to improve the balance, however, in practice, a single iteration has proven to be sufficient.

4.4.1.1 2-Layer Initialization

Our initial attempts to initialize the PE model from the 2-layer IE initial balanced solution failed to produce a stable vortex. Our analysis indicates that potential vorticity gradient inversions generated during the transfer of the 2-layer IE solution into σ -coordinates are responsible for the instabilities in the vortex.

The easiest way to see this is to consider a thick isopycnal layer with monotonically varying potential thickness corresponding to a typical stable vortex. During the transition to a σ -coordinate model the originally uniform density layer is represented as a linearly stratified water column. Because of the linear stratification the velocity associated with the potential thickness gradient also has linear vertical shear as follows from the thermal wind relationship. Consider the same layer reverted back to isopycnal coordinates only now we evenly split the original layer into two layers by introducing a new isopycnal surface with the density value equal to the mean density of the original layer. This sequence of transformations is illustrated in Figure 4.15.

For the sake of argument we approximate potential thickness of a layer using quasi-geostrophic approximation (QG):

$$Q = \frac{H + \eta}{f + \zeta} \simeq \frac{H}{f} + \frac{1}{f}\eta - \frac{H}{f^2}\zeta, \quad (4.6)$$

where η is the perturbation layer thickness and ζ is the later relative vorticity. The QG approximation is only used here for illustrative purposes; the same argument can be made for the full form of the shallow water potential thickness. Even though the potential thickness of the original layer is monotonic, the corresponding relative vorticity ζ can have local extrema. In fact, in a typical LCE ζ has a local maximum and a minimum. The non-monotonic character of relative vorticity in the LCE leads to a sharpening of the potential vorticity front associated with the eddy. The initial perturbation layer thickness is split equally between two sub-layers as the result of the layer transformation procedure, i.e., $\eta_1 = \eta_2 = \eta/2$. Since relative vorticity is proportional to velocity (which is 2 times larger in the upper sublayer), we also have $\zeta_1 = 2\zeta_2$. This means that the non-monotonic component of potential thickness associated with relative vorticity (see 4.6) doubles in the upper sublayer, which, in turn, can lead to non-monotonic character of potential thickness of this layer.

As can be seen from the above illustration the process of transferring the initial idealized vortex structure into σ -coordinates can produce potential thickness gradient inversions leading to instability of the vortex initialized in primitive equations model. The inversion is more likely to occur if the density difference between adjacent isopycnal layers is large leading to high vertical velocity shear in those layers.

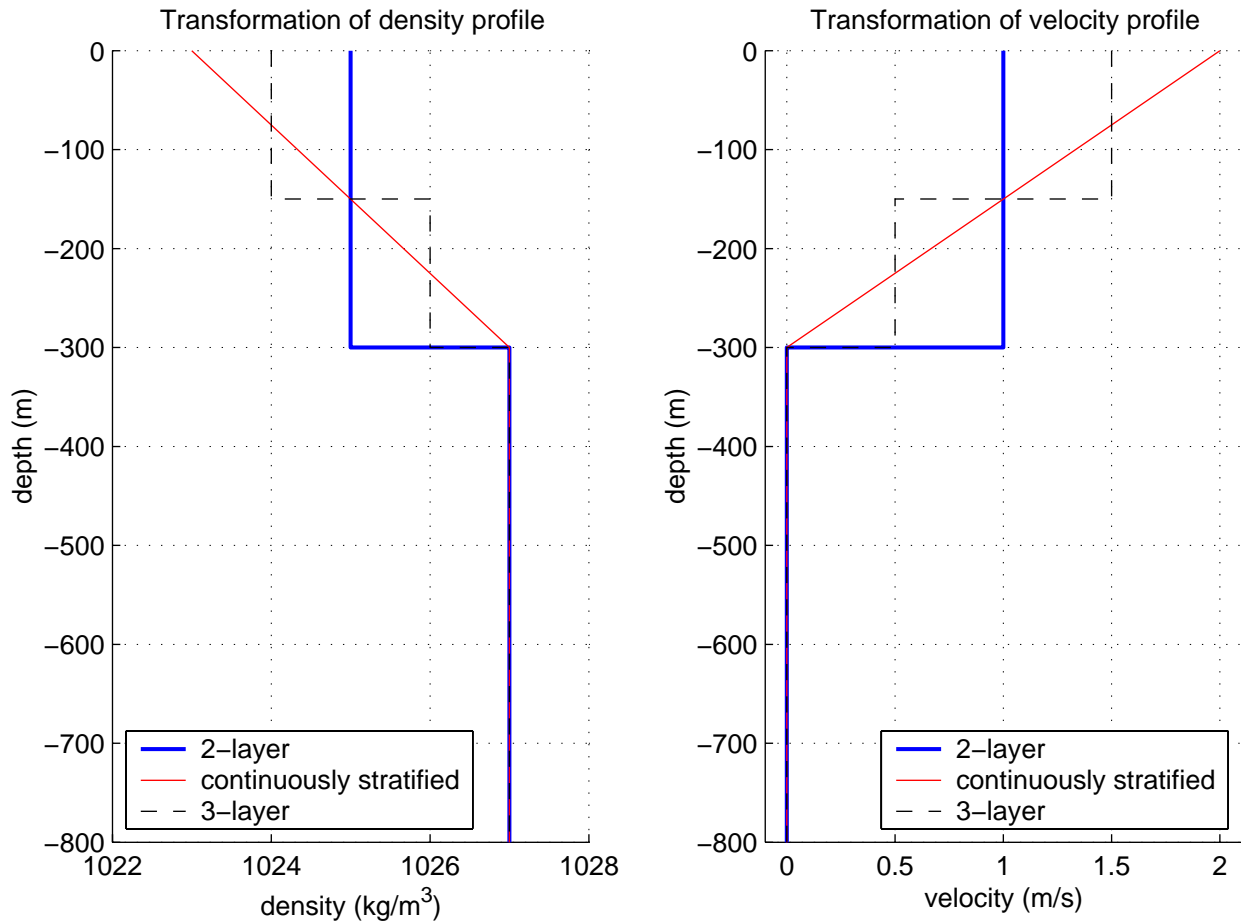


Figure 4.15. Illustration of density and velocity vertical profile transformations during transition from a 2-layer system to continuously stratified system and back to a 3-layer system.

4.4.1.2 7-Layer Initialization

The potential vorticity gradient inversion problem was resolved by using a 7-layer IE model as an intermediate step between two-layer IE and the σ -coordinate PE model. In the 7-layer formulation the density variation between isopycnal layers is limited to 0.75 (versus 2.0 in the 2-layer case). This allows fitting of a linear density profile without significant potential thickness distortions. The initialization of an anticyclonic vortex in a 7-layer IE model was described in Section 4.2.2. The PE model is initialized by transferring the initial balanced solution from the 7-layer IE model using the technique described above.

4.4.2 Intercomparison with the 7-Layer IE Model

4.4.2.1 Experiment Design

The experiment design is the same one that was used for the intercomparison between 2-layer and 7-layer IE models. The domains are rectangular, $1,600 \times 1,300$ km in the case of IE model and $1,500 \times 1,100$ km in the case of PE model. The depth is 3,500 m everywhere in the domain except near the northern and western boundaries where it is sloping outwards at a rate of 0.01, representing the continental rise in GOM. The slope is smoothed in the northwest corner to allow for free propagation of TRW's. Sponge BCs are applied along southern and eastern boundaries to allow energy propagation out of the domain. The exact form of the bottom topography is shown in Figure 4.16. The western wall in the PE model is represented by a steep (0.04) slope.

PE model was initialized by transferring the 7-layer IE initial balance solution into PE model grid. The vortex in IE model is initialized 350 km off the western slope and 400 km off the northern slope. In the PE model the vortex is initialized 250 km off the western slope and 200 km off the northern slope, the differences are associated with the differences in domain size.

4.4.2.2 Results

The results of the intercomparison are shown in Figure 4.16. The left panel of the figure shows the eddy evolution in the 7-layer IE model (identical to the right panel of Figure 4.6), the right panel shows the eddy evolution in the PE model. Even though the details of the solutions differ the direction and speed of the vortex propagation are almost identical in both models indicating that the physical process controlling the vortex propagation seem to be adequately represented in the IE context. One of the most notable differences is the rate of the vortex decay. The vortex intensity, as judged by the magnitude of vertical displacement of the thermocline, is substantially weaker in the PE model by the time the vortex reaches the slope (approximately day 140 of model integration). This result is not very surprising since PE models are notorious for requiring high friction in order to remain computationally stable.

Significant differences occur when the vortex is approaching the western wall. In the 7-layer IE solution the vortex starts rapidly propagating north as soon as its center reaches the 2,000-m isobath. In the PE solution the vortex is gradually turning north after crossing the 2,000-m isobath and soon stalls. The differences are most likely to be associated with the way each model treats the closed western boundary. The IE model implements free-slip boundary conditions along all closed boundaries which naturally facilitate the image effect when the vortex approaches the western wall. The PE model does not provide an option for free-slip closed BCs. The free-slip boundary conditions at the western wall are emulated using steep slope that, combined with a σ -coordinates system, allows one to replace high horizontal friction with a relatively small vertical

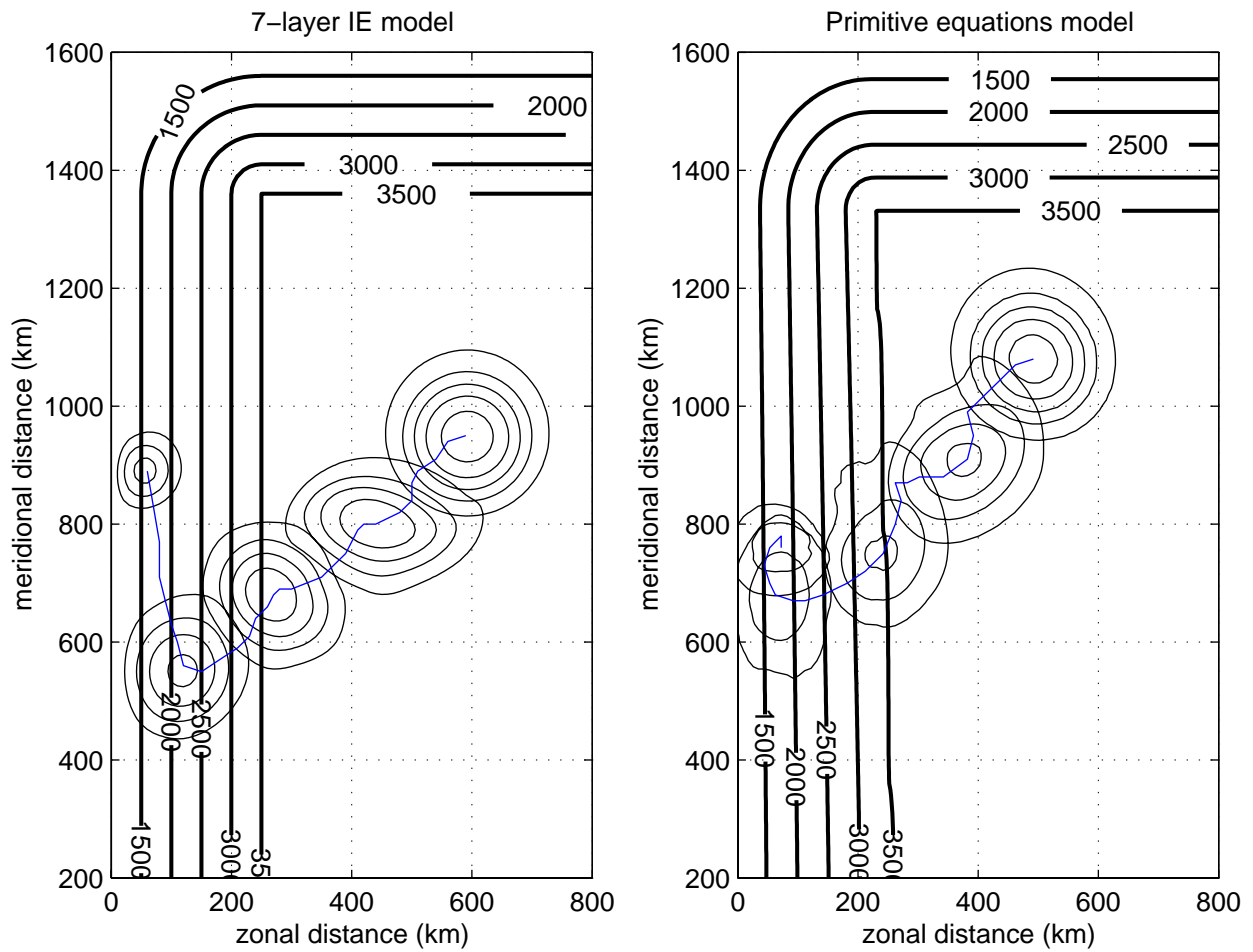


Figure 4.16. Same as Figure 4.6 but for 7-layer IE and PE models. Left panel shows the results of 7-layer IE model experiment and right panel shows the results of PE model experiment.

friction along the slope. The emulated free-slip BCs in PE model do create some image effect, which accounts for the northward motion of the vortex, however the steep slope introduces regions of high potential vorticity at the western boundary. High PV in the region over the steep slope is being advected by the vortex off the boundary, leading to creation of cyclonic circulation north of the vortex and stalling its northward motion. This process is similar to the one that occurs during vortex interaction with the shelf that is described below.

4.4.3 Idealized Topography Experiments in the Western GOM

In this set of experiments the level of realism is further increased as compared to the previous set of PE experiments by updating the LCE initialization technique. The same initialization method, i.e. the method of using a PV-based feature model of the LCE, is applied, however, the vertical resolution of the PV feature model is increased to 8 layers and the parameters of the feature model are calibrated to match real observations.

The experiments simulate the interaction of an isolated LCE with idealized topography representative of the western GOM topography at 23°N and 25°N, similar to the IE+ experiments. Just like in the IE+ experiments an LCE is initialized away from the coastal topography with no motion in the lower layer. The LCE starts moving westward driven by the β -effect and interacts with topography. The main goal of these experiments is to establish the effect of realistic continuous stratification on LCE-topography interaction.

4.4.3.1 Initialization of Realistic Eddy Structure and Background Stratification

A substantial effort has been made to increase the realism for representing the initial conditions for both LCE's and the background ocean stratification. An 8-layer PV-based LCE feature model calibrated to be representative of a typical LCE in the western GOM was created. A procedure was also developed to derive a background vertical density profile representative of the western GOM from climatological data.

Section 4.2.2 describes an initialization procedure based on the multi-layer PV feature model designed to initialize eddies representative of LCE's in our numerical experiments. In the PV feature model framework an LCE is represented by its PV anomalies in the upper layers; the lower layer is assumed at rest and, therefore, the PV anomaly there is determined in the process of calculating the eddy density structure. The i -th layer PV anomaly was prescribed with equation (4.5). Following the procedure described in Section 4.2.2 an 8-layer PV-based LCE feature model calibrated against observations was created. Free parameters L_i and Z_i in (4.5) were determined by prescribing the depth of layer interfaces at the center and the periphery of the eddy, and the velocity peak in each layer. The peak velocity in each layer is determined from the observed vertical velocity profiles in two warm-core rings in the GOM (Cooper et al. 1990). The depth of layer interfaces at the eddy center and periphery is taken to be representative of a typical LCE in the western GOM and was derived from the Levitus 1994 atlas climatological data.

Gridded climatological fields are constructed via the process of horizontal and temporal averaging. The non-selective averaging process mixes together the measurements taken within warm and cold-core eddies as well as those outside of eddies. Therefore, the background stratification extracted from gridded climatological data cannot be considered representative of the background stratification of the GOM. For this reason, a special procedure was designed to construct a vertical density profile representative of the western GOM density structure directly from individual observed profiles.

Historical hydrographic measurements from quadrants 7208 and 7209 of the Levitus 1994 atlas were first filtered to select only profiles which have both temperature and salinity data and extend deeper than 500 meters. These profiles were then converted into potential density profiles. Out of the remaining profiles only those which have 15°C temperatures shallower than 220 meters were selected. The rest of the profiles were assumed to be observed within cold-core eddies and discarded. The above criteria was derived from the analysis of hydrographic maps of eddies in the western GOM (Vukovich and Crissman 1986). A typical vertical density profile for a resting western GOM was derived by fitting a curve into the less-dense side of the envelope of the remaining profiles. Correspondingly, the profile representative of the density structure at the center of a typical warm-core eddy was derived by fitting a curve into the denser side of the envelope of the remaining profiles.

Figure ?? illustrates this procedure. Density profiles from quadrants 7208 and 7209 of the Levitus 1994 atlas which were assumed to be observed within cold-core rings are plotted with dark lines. The rest of the profiles are plotted with light lines. The fitted 8-point curve (each point represents a density layer interface) representing the stratification in the resting western GOM is shown with a thick black line. The profile representative of the density structure at the center of a typical warm-core eddy is shown with a thick gray line. The resulting layer configuration is shown in the table below.

Layer #	1	2	3	4	5	6	7	8
Layer density, kg/m^3	23.5	24.0	25.0	26.0	26.75	27.25	27.625	27.75
Layer thickness, m	20	20	30	100	180	350	800	2,000

4.4.3.2 23°N Topographic Configuration

Figure 4.17 shows day 120 of the new high resolution PE model integration with the 23°N topographic configuration. Shading on the figure represents the PV^1 in the main thermocline calculated using the total depth of the thermocline and the velocity vertically averaged over this depth. The initial anticyclonic eddy approaches the shelf moving in a south-west direction and turns rapidly to the north. After a period of cyclic motion with decaying amplitude combined with slow northward propagation, the eddy stalls. Further integration (not shown) predicts subsequent slow southward eddy drift and dissipation.

The well-defined cyclic motion and the relatively slow dissipation rate are the features of the eddy evolution consistent with the results of the 2-layer IE+ model experiments. This agreement between IE+ and high resolution PE model results increases substantially the level of confidence in the validity of both numerical simulations. The initial northward eddy propagation that can be seen in Figure 4.17, however, is not predicted by the 2-layer IE+ model experiment. Thus, it appears to be a unique feature of the continuously stratified primitive equation physics.

By conducting an in-depth analysis of the idealized PE experiments we were able to identify the physical mechanism responsible for this northward LCE propagation during its interaction with the western shelf. This new mechanism is associated with vortex tubes stretching/squashing

¹Potential vorticity (PV) and velocity in all of our primitive equations model results is defined in the two-layer sense. The two-layer PV and velocity are calculated by first finding the $27\text{kg}/\text{m}^3$ isopycnal surface in the continuously stratified density field. This isopycnal surface roughly corresponds to the bottom of the main thermocline. The velocity is then averaged vertically over the upper and the lower layers, i.e., in the thermocline and below the thermocline. This vertically averaged velocity combined with layer thickness is used to calculate layer PV. Even though the layer PV defined above is not strictly conserved in the PE framework, it provides a very good dynamical tracer and allows for direct comparisons with two-layer IE experiments.

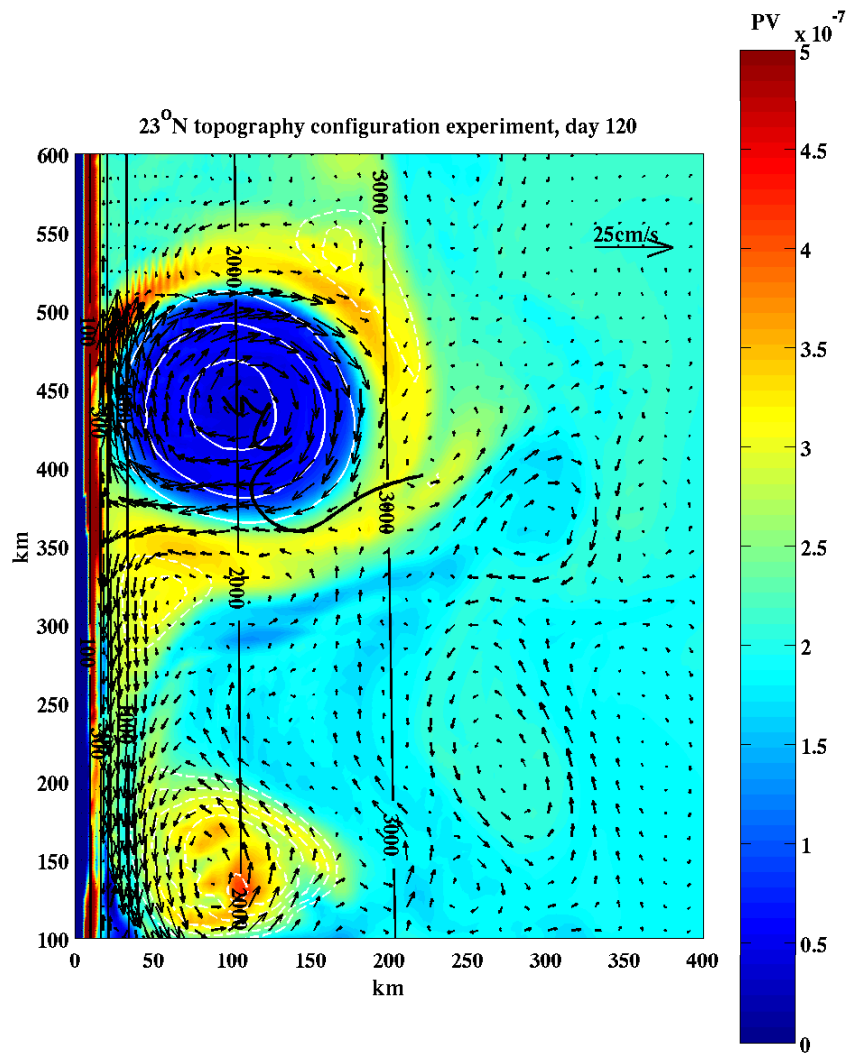


Figure 4.17. 23°N topography configuration experiment, day 120 of integration. Color coded is PV in the main thermocline; white contours indicate the thermocline displacement; and black contours indicate topography. Eddy trajectory is shown with a thick black line. Vectors show the velocity vertically averaged below the thermocline.

23°N topography configuration experiment, day 40

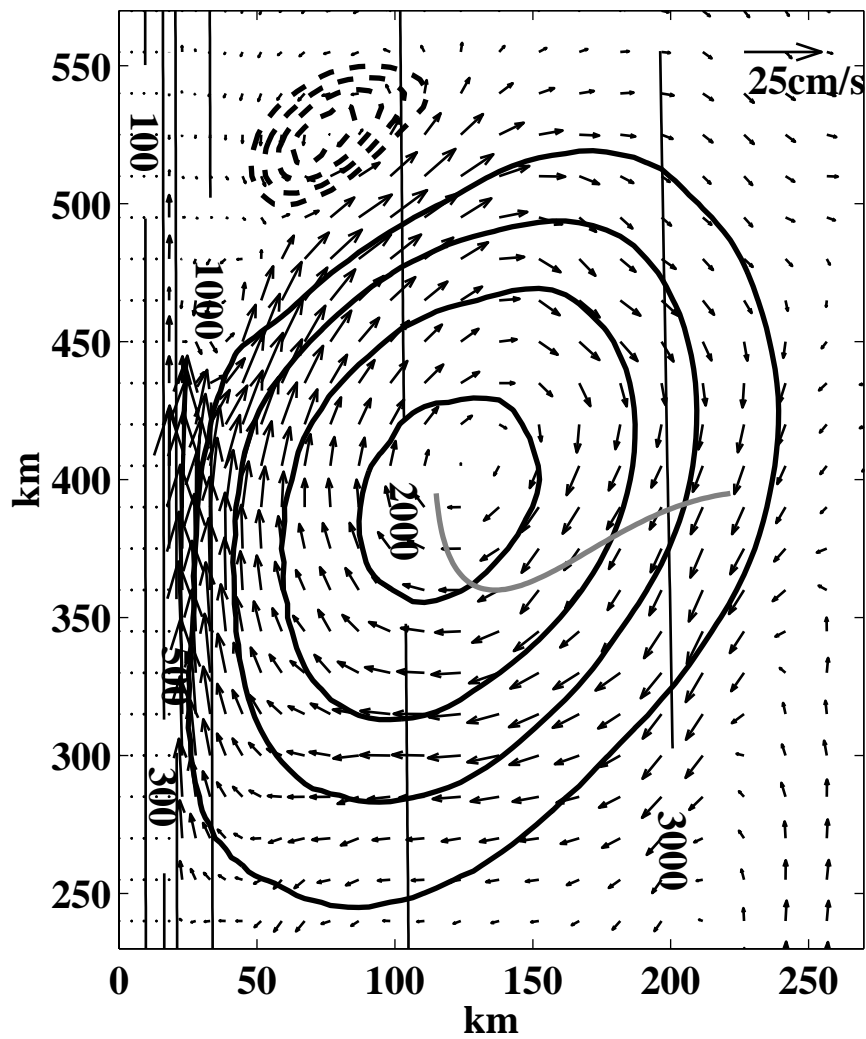


Figure 4.18. Same experiment as in Figure 4.17, but day 40. Thick solid contours indicate a depressed thermocline (anticyclonic features); and thick dashed contours indicate a raised thermocline (cyclonic features). The eddy trajectory is shown with a thick gray line. Vectors show the velocity vertically averaged below the thermocline.

in the midwater column and is described in detail below. The rest of this section is organized as follows: first we describe the mechanism of northward LCE propagation, then we illustrate it in a simpler physical framework, and finally we verify it by comparing appropriately configured PE experiments.

Mechanism of northward LCE propagation near the western shelf

The source of the northward LCE propagation seen in PE model experiments can be identified in Figure 4.18 which shows day 40 of the same experiment shown in Figure 4.17. At the time shown the eddy trajectory has just started curving northward. There is a strong northward current beneath the western part of the eddy which intensifies significantly near the shelf reaching about 30 cm/s magnitude. The along-shelf northward current below the thermocline recirculates as a broad southward current away from the shelf thus forming a co-rotating (anticyclonic) circulation beneath the eddy. This circulation is intensified below the thermocline and is decaying toward the bottom, and we will refer to it as *midwater-column circulation*. These midwater-column currents are identified to be responsible for the northward eddy propagation.

The existence of the midwater-column currents beneath the eddy and associated eddy northward propagation are related to the stratification below the main thermocline. As the eddy moves onto the topographic slope the water columns underneath it are being squashed. Squashing of water columns leads to relative vorticity generation below the main thermocline. If there is no stratification below the thermocline, as in 2-layer case, the deep flow is locked by topography, and the relative vorticity that is generated radiates away in the form of topographic Rossby waves. If realistic stratification is present, however, cross-topographic flow underneath the thermocline becomes possible due to the well known JEBAR effect (Mertz and Wright 1992). Consequently, the deep relative vorticity generated by on-slope eddy motion can form a quasi-stationary circulation.

Three-layer illustration of the midwater-column current generation mechanism

The mechanism of midwater-column current generation is illustrated in Figure 4.19. For this illustration a truncated three-layer IE model was used. The third layer is designed to represent the stratification below the main thermocline. The coastal topography is simulated with a linear slope for simplicity. Initially the eddy is located away from the coast in the deep water. The eddy is characterized by its potential vorticity anomaly in the upper layer (shown with color on the right panel), the structure of the PV anomaly is taken from our two-layer IE experiments. There is no PV anomaly associated with the eddy in the intermediate layer (below the thermocline). The eddy density structure, i.e., interface displacement, and velocity structure are calculated by inverting the specified PV anomaly. The interface displacement corresponding to the off-shore eddy location is shown on the left panel with light blue lines.

We further assume (analysis of the intermediate-layer PV in our PE model experiments supports this assumption) that as the eddy advances on-shore, the associated PV anomaly in the upper layer moves with it while the PV in the intermediate and the lower layers remains unchanged. The interface displacements corresponding to the on-shore and the off-shore eddy locations are shown in the left panel of Figure 4.19 with dark and light dotted lines respectively. Overlaying the interface displacements for two eddy locations clearly indicates the compression of the intermediate layer in front of the eddy. Since the PV is assumed to be constant, the layer thickness changes are compensated with generation of relative vorticity.

To illustrate the structure of the circulation corresponding to the generated relative vorticity we calculate the velocity anomaly in the intermediate layer produced by the eddy shift. Since

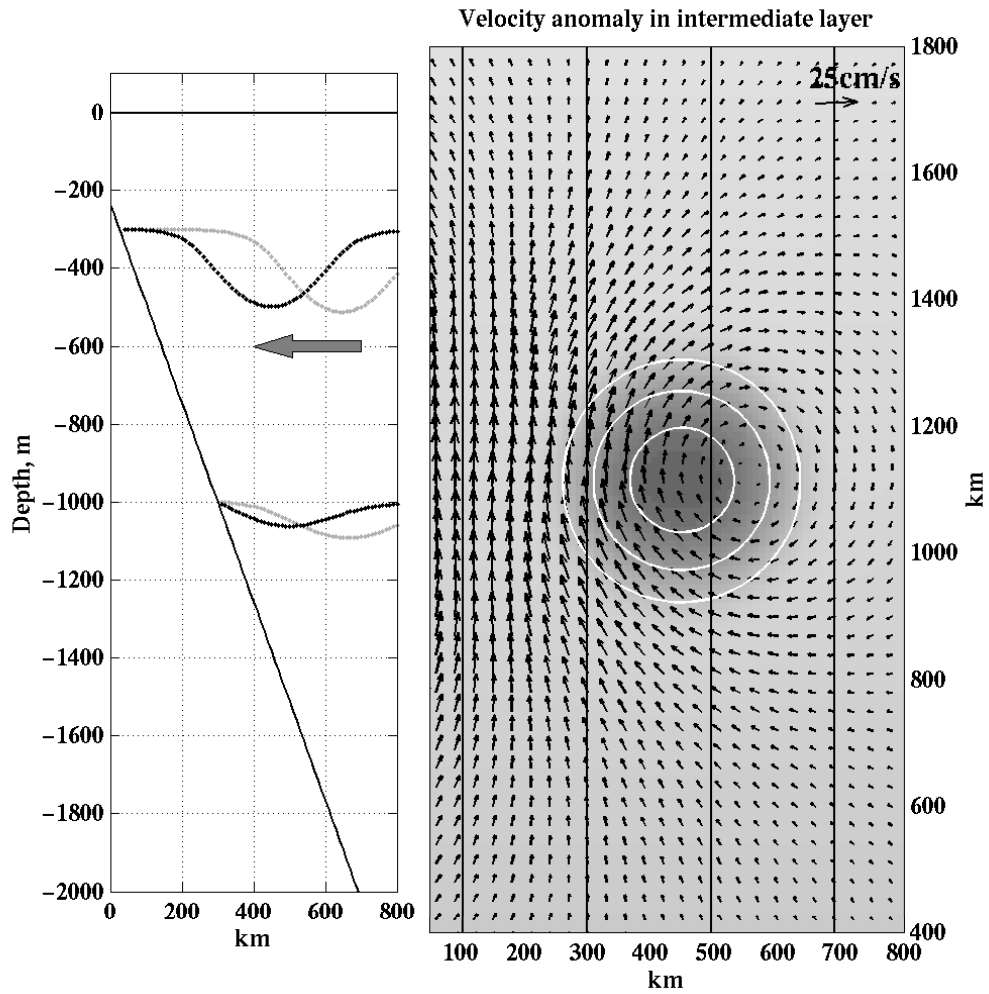


Figure 4.19. Illustration of the mechanism generating the westward-intensified midwater-column circulation. The left panel shows interface displacements associated with two subsequent eddy positions (away from the bottom slope and on the slope). The right panel shows the PV field in the upper layer (shading) and velocity anomaly in the intermediate layer for the on-slope eddy position. White contours indicate the upper layer interface displacement.

the velocity field associated with the eddy itself shifts as the eddy position changes, we shift the velocity calculated for the off-shore eddy location by the distance of the eddy translation prior to the anomaly calculation. The resulting velocity anomaly is shown on the right panel of Figure 4.19. As one can see the circulation generated by the on-shore eddy translation in this simple illustration has the form of an along-shore northward current very similar to the one seen in the PE experiments (Figure 4.18). This circulation is absent in the lower layer corresponding to the downward decay of the midwater-column currents seen in PE model simulations.

Modified Experiment

To demonstrate conclusively that the midwater-column current generation and the associated northward eddy propagation are related to the stratification below the main thermocline, we repeated the same experiment with the deep stratification removed. The result of this modified experiment is shown in Figure 4.20. As one can see, there is no co-rotating circulation beneath the eddy in this case and the northward eddy propagation is very small. In fact, the eddy behavior in this case is very similar to the behavior seen in our 2-layer IE+ model experiment indicating that the key addition to the system in the PE experiments is realistic vertical stratification extending below the main thermocline.

It is interesting to note another effect of the deep stratification revealed by the above experiment inter-comparison. As one can see in Figure 4.18, the off-shelf advected high PV water tends to form relatively strong small-scale cyclones north of the main eddy in the fully stratified case. Another cyclonic eddy is being formed south of the main eddy (Figure 4.17) after the high PV water wraps around and encounters the shelf. In the experiment without the deep stratification the small-scale cyclonic eddies are either weak or do not form at all (see Figure 4.20). Thus, the presence of stratification below the main thermocline seems to facilitate smaller scale eddy formation over the topographic slope. This is most likely due to the fact that the small-scale cyclonic eddies have a significant part of their energy in high wave-number vertical modes which are suppressed when the deep stratification is removed.

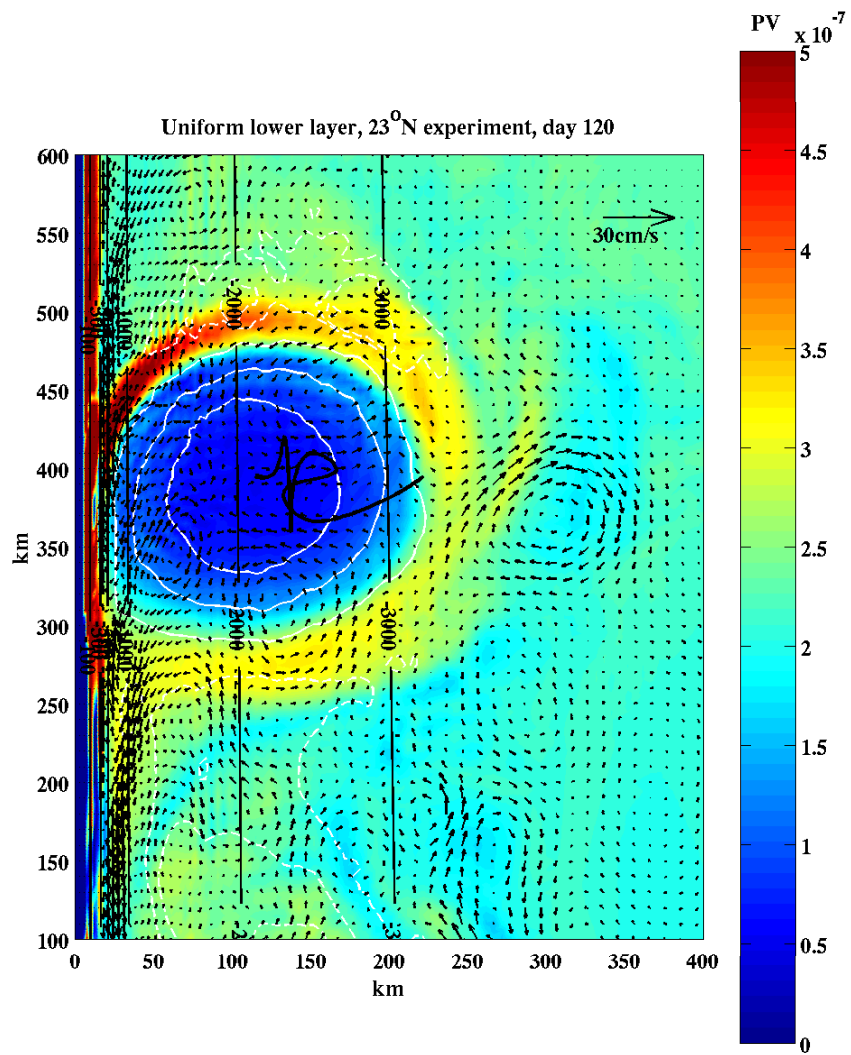


Figure 4.20. Same as Figure 4.17 but without stratification below the thermocline.

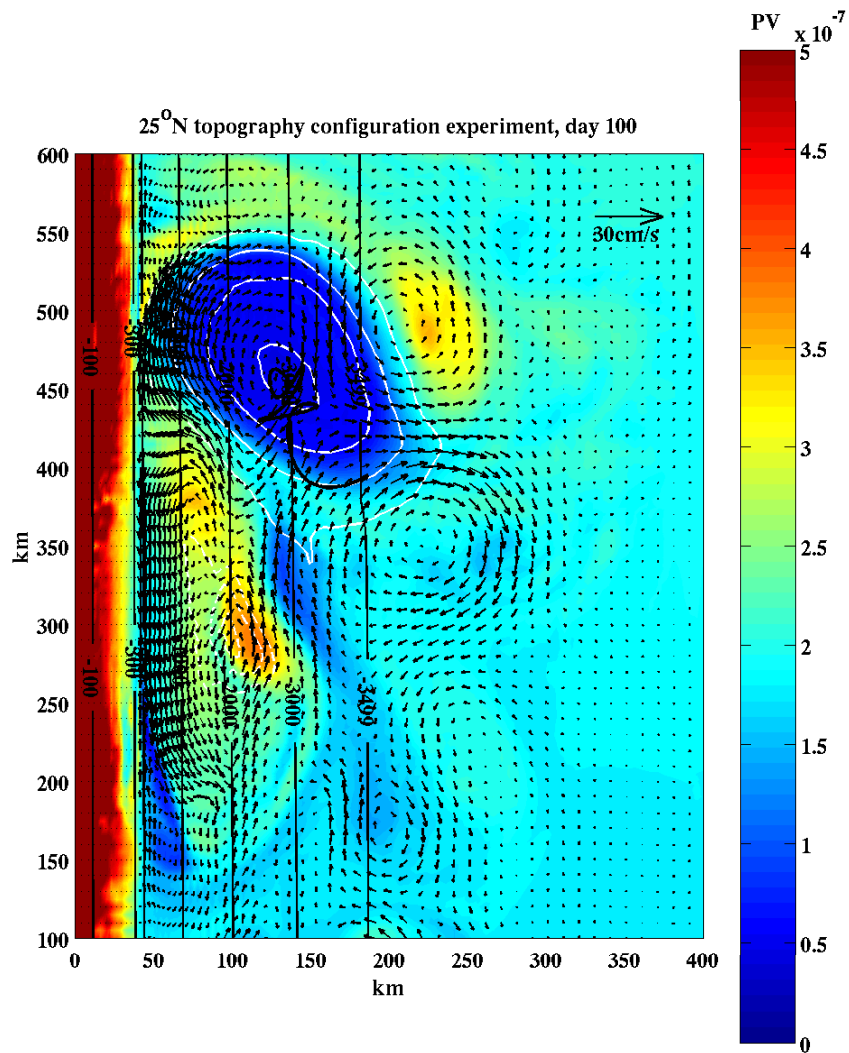


Figure 4.21. 25°N topography configuration experiment, day 100 of integration. Color indicates PV in the main thermocline; white contours indicate the thermocline displacement; and black contours indicate topography. The eddy trajectory is shown with a thick black line. Vectors show the velocity vertically averaged below the thermocline.

4.4.3.3 25°N Topographic Configuration

The mechanism of northward eddy propagation via interaction with midwater-column currents identified in the previous section plays a similar role in the 25°N coastal topographic configuration. Figure 4.21 shows day 100 of model integration with the 25°N (wide shelf, narrow continental slope) configuration. Similar to the 23°N (narrow shelf, wide continental slope) configuration the anticyclonic eddy moves north after encountering the shelf and then follows a cyclic trajectory. In contrast to the 23°N case, however, the amplitude of the cyclic motion is higher and the northward propagation associated with it is smaller (compare Figure 4.17 and Figure 4.21). Zonal amplitudes of the LCE trajectory cycles starting from the first sharp westward turn are ~ 75 km, 50 km, 30 km compared to ~ 50 km, 35 km, 20 km in 23°N case. The resulting northward propagation associated with these cycles is only ~ 40 km compare to ~ 75 km in 23°N case.

The higher amplitude of the cyclic motion and the reduced northward propagation of the LCE in the 25°N topographic configuration compared to the 23°N case is related to the LCE's interaction with bottom-intensified eddies (similar to the 2-layer IE+ model experiment discussed in Section 4.3). The characteristic deep cyclone-anticyclone pair can be identified over the flat topographic region east of the main eddy in Figure 4.21, which is very similar to the deep cyclone-anticyclone pair in Figure 4.10. Similar to the 2-layer IE+ model experiment, the interaction with deep eddies also produces southward motion of the LCE; however, in the PE experiment this motion is countered by the effect of the midwater-column currents that push the LCE northward.

The effect of bottom-intensified eddies on the LCE is noticeably weaker in the PE model experiment compared to the IE+ experiment. This can be seen from the relatively weak amplitude of the cyclic motion. It can be demonstrated that the weakness of LCE interaction with bottom-intensified eddies in the PE experiment is related to the stratification below the main thermocline. Similar to the 23°N case, we repeat the fully stratified experiment with the stratification below the main thermocline removed. The result of this experiment is shown in Figure 4.22. The eddy trajectory simulated in this case is similar to the one in the IE+ experiment and is characterized with high amplitude southward cyclic motion. Thus, the effect of the deep stratification in the 25°N case is to shield the LCE from interaction with bottom-intensified eddies. The exact physical mechanism of this effect is not yet understood.

4.4.4 Idealized Topography Experiments in the Northern GOM

A series of PE numerical experiments similar to those in the western GOM was designed to simulate LCE interaction with coastal topography in the northern GOM. Since a good correspondence was established between IE+ and idealized PE experiments (see Section 4.4.3), we bypass the IE+ modeling step for the northern GOM and proceed directly from our previous 2-layer IE model experiments (Section 4.2.1) to PE experiments. The experiments were conducted using the high resolution PE model with improved eddy initialization applied previously for the western GOM.

The idealized topography is designed to represent the essential features of the coastal topography in the northern GOM while eliminating nonessential complexities introduced by the real topography. The idealized topography experiments simplify the analysis of the model results and allow efficient isolation of different physical mechanisms. This allows one to develop the knowledge and intuition necessary to proceed with understanding the realistic topography experiments.

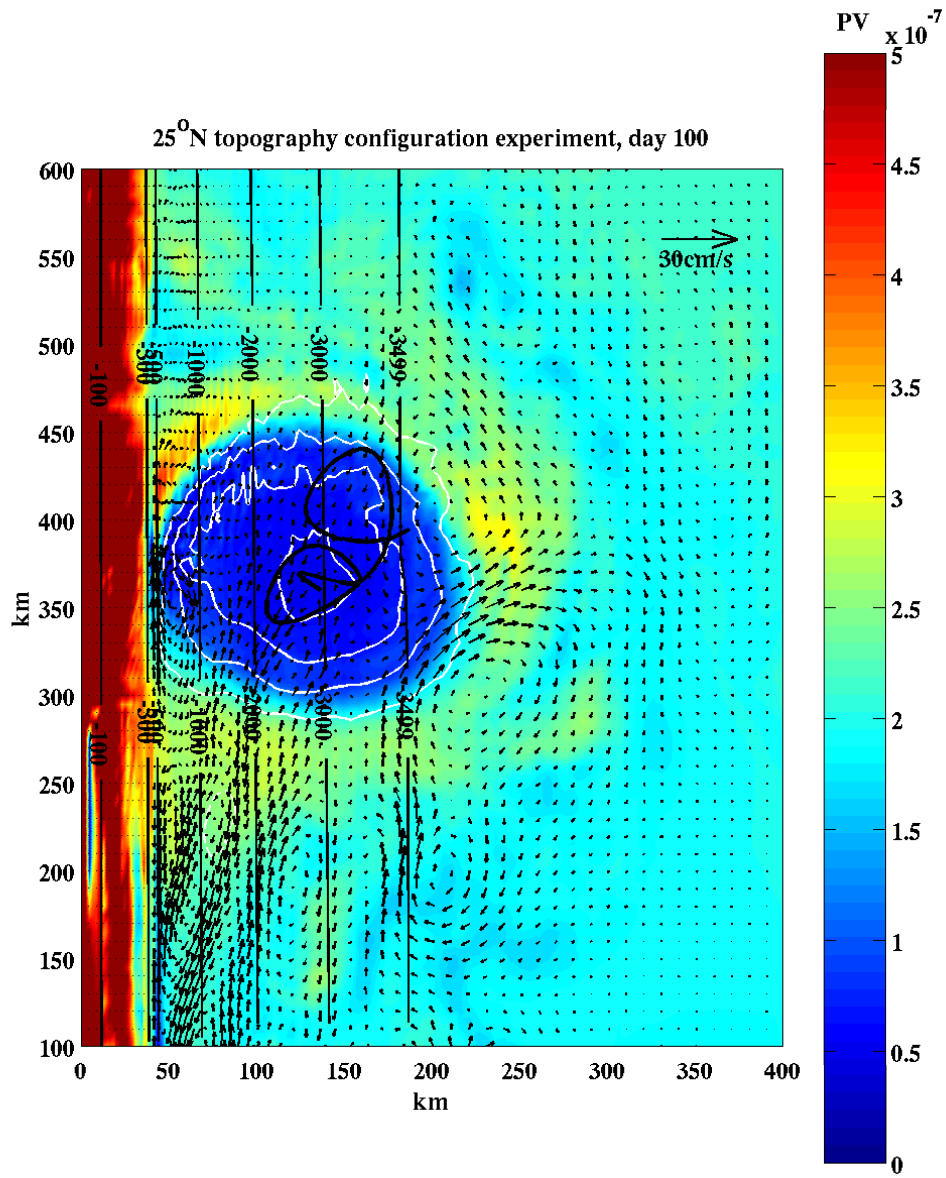


Figure 4.22. Same as Figure 4.21 but without stratification below the thermocline.

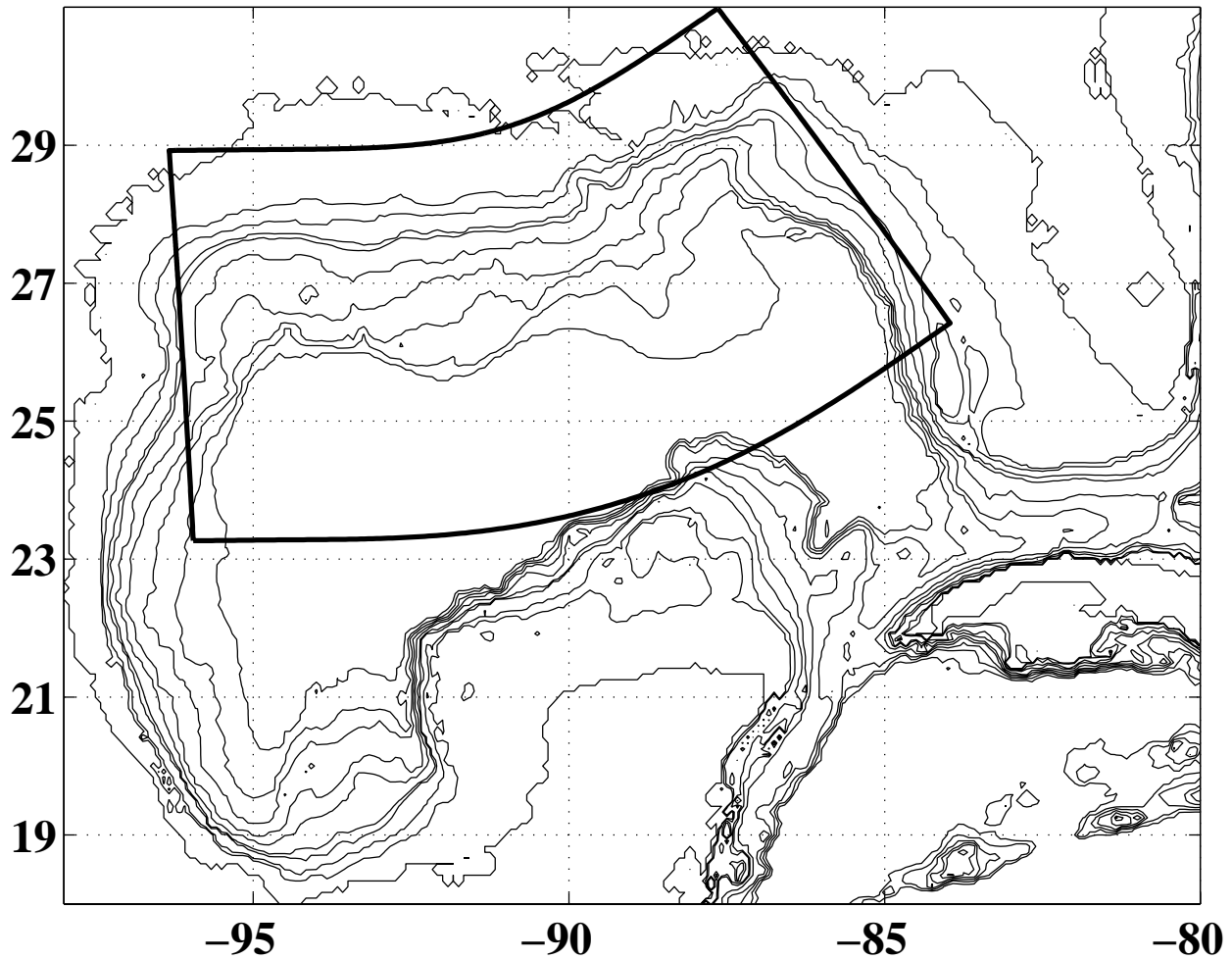


Figure 4.23. Domain configuration for simulation of LCE interaction with the GOM northern shelf.

4.4.4.1 Experiment Setup

The PE model that we used for western GOM experiments described in Section 4.4.3 was reconfigured for the domain shown in Figure 4.23. Closed boundary conditions were applied along the western, northern, and eastern boundaries. Open boundary conditions combined with a sponge layer were applied along the southern boundary.

The model was outfitted with a curvilinear horizontal grid following the northern shelf-break line. This configuration allowed us to increase the resolution in the direction of the strongest topographic gradient - i.e., normal to the shelf break - alleviating the notorious σ -coordinate pressure gradient error. The resolution of the grid varies from ~ 7 km resolution in the south-eastern part of the domain to ~ 3 km in the northeastern part with typical resolution of 5 km. Along the shelf-break line the resolution in the direction of the strongest topographic gradient increases to ~ 2 km.

In order to exclude the complex flow variability introduced by realistic topography and illuminate the effects of separate physical processes, the coastal topography in the northern GOM was represented as a meridional slope uniform along the shelf-break line. For this purpose the shelf-break line was smoothed by fitting a 7-th order polynomial. The slope profile was chosen to represent the real topographic profile at 91°W (a similar approach to that used in the 23°N and 25°N idealized topographic configurations described in Section 4.4.3). The fact that the to-

pographic slope turns north from a nearly zonal direction at approximately 90°W is crucial for facilitating eddy-shelf interactions as will be shown below.

The technology of realistic eddy initialization in high resolution PE models that we previously developed for the western GOM experiments was applied in these experiments for initializing a circular anticyclonic eddy representative of LCE's in the eastern part of the domain. In a typical experiment the eddy is allowed to propagate westward over the topographic slope driven by the β -drift until it encounters the shelf around 90°W .

4.4.4.2 Results

The same fundamental physical mechanisms that control the eddy interaction with coastal topography in the western GOM were shown to work, although in a different fashion, over the northern topography. The off-shelf PV advection mechanism in the northern shelf setting produces small-scale cyclones behind the main eddy similar to the western shelf setting; however, the net effect of these cyclones is to push the main eddy trajectory southward instead of introducing a cyclic motion as we demonstrated for the western shelf. The intensity of the off-shelf advected cyclones and their influence on the LCE trajectory depends upon the distance of the LCE from the northern shelf. LCE's that start far south move westward over the northern continental slope almost unaffected by the presence of the shelf. On the other hand, LCE's that start further north are deflected as far as 25°N after interacting with the off-shelf advected cyclone.

Figure 4.24 shows the result of one of the idealized topography experiments after 250 days of integration. In this particular experiment the eddy was initialized at 87.6°W , 26.8°N , which is relatively far south from the northern shelf. The same analysis that we used in the western GOM experiments has been applied to the model output, converting the 3-d fields on 50 vertical levels into 2 isopycnal layers. The shading in the figure shows the PV in the upper layer (main thermocline) and the vectors show the velocity in the lower layer (vertically averaged below the main thermocline). Contours indicate the bottom topography.

In this experiment the eddy propagation is almost unaffected by the presence of the northern shelf. The eddy trajectory is close to zonal and the propagation speed is ~ 3 km/day, the speed of the β -drift. This is in accord with the results of our previous 2-layer IE model experiments (see Section 4.2.1). In those experiments the northern GOM coastal topography was represented as a linear slope constant in the zonal direction and restricted to the lower layer. An anticyclonic eddy was initialized over the slope in the eastern side of the domain. In this configuration the eddy was shown to propagate westward driven by the β -drift. The lower layer circulation was restricted by the bottom topography and, therefore, had little influence on the eddy propagation.

The presence of a thermocline intersecting the northern shelf in this new experiment does introduce some modifications. The eddy comes close enough to the shelf to generate significant off-shelf advection leading to the formation of a small-scale cyclone. The high PV anomaly created by the off-shelf advection and associated cyclonic eddy can be seen in Figure 4.24 at approximately 91.5°W . Due to the fast westward propagation of the main eddy the off-shelf advected cyclonic eddy is left behind and its influence on the main eddy trajectory is minimal.

Figure 4.25 shows the output of another idealized topography experiment after 120 days of integration. The initial eddy position in this case is 87.6°W , 27.0°N . The off-shelf advection produced by the eddy is substantially stronger than in the previous case, correspondingly, the cyclonic eddy formation is quicker and its intensity is higher. In addition, the westward eddy propagation speed is reduced by half at the point where the eddy encounters the shelf. These two factors lead

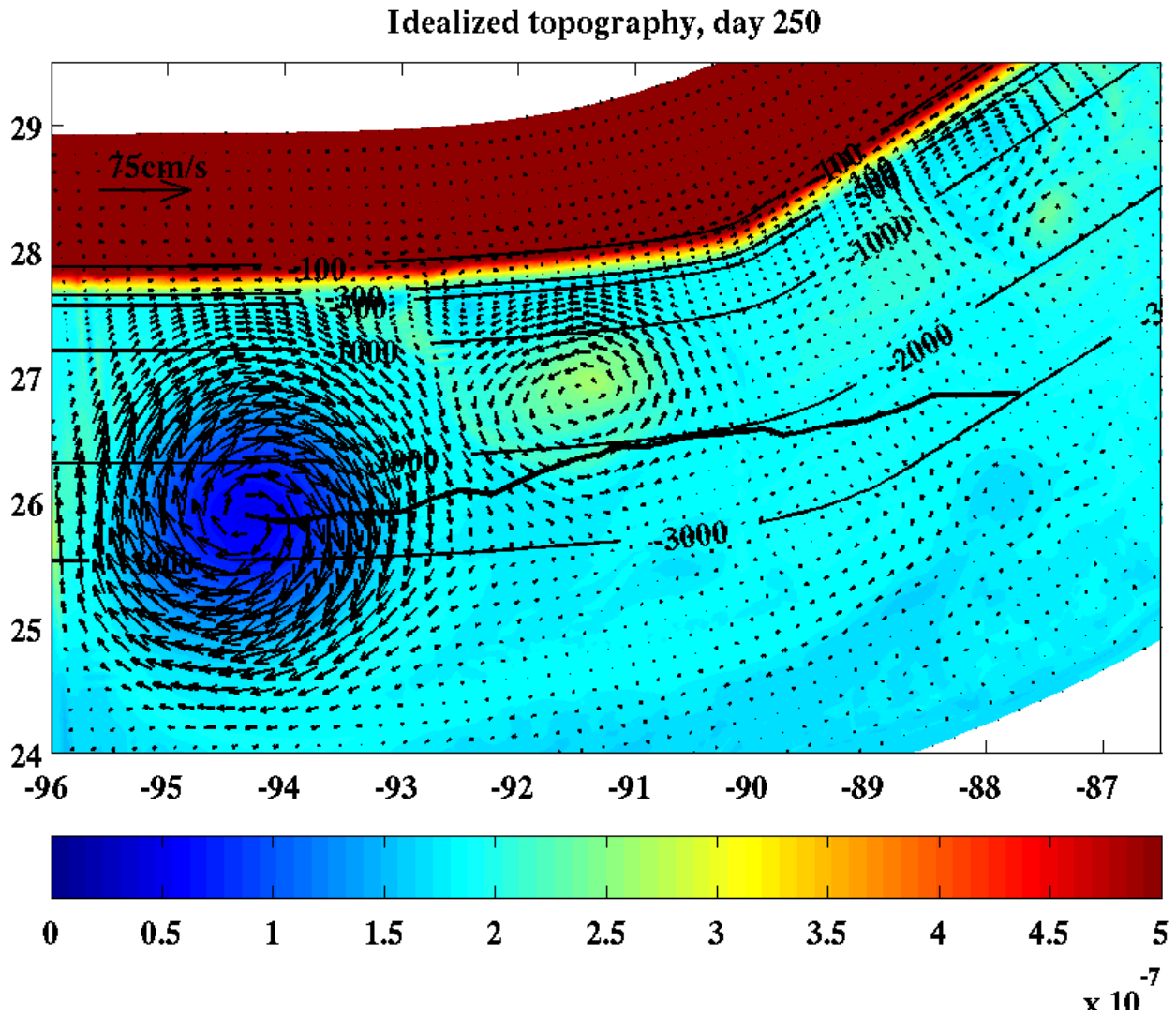


Figure 4.24. Interaction of an LCE initialized at 87.6°W, 26.8°N with idealized northern shelf topography. Day 250 of integration is shown. Color shows PV in the main thermocline; and black contours indicate topography. The eddy trajectory is shown with a thick black line. Vectors show the velocity vertically averaged within the thermocline (upper layer).

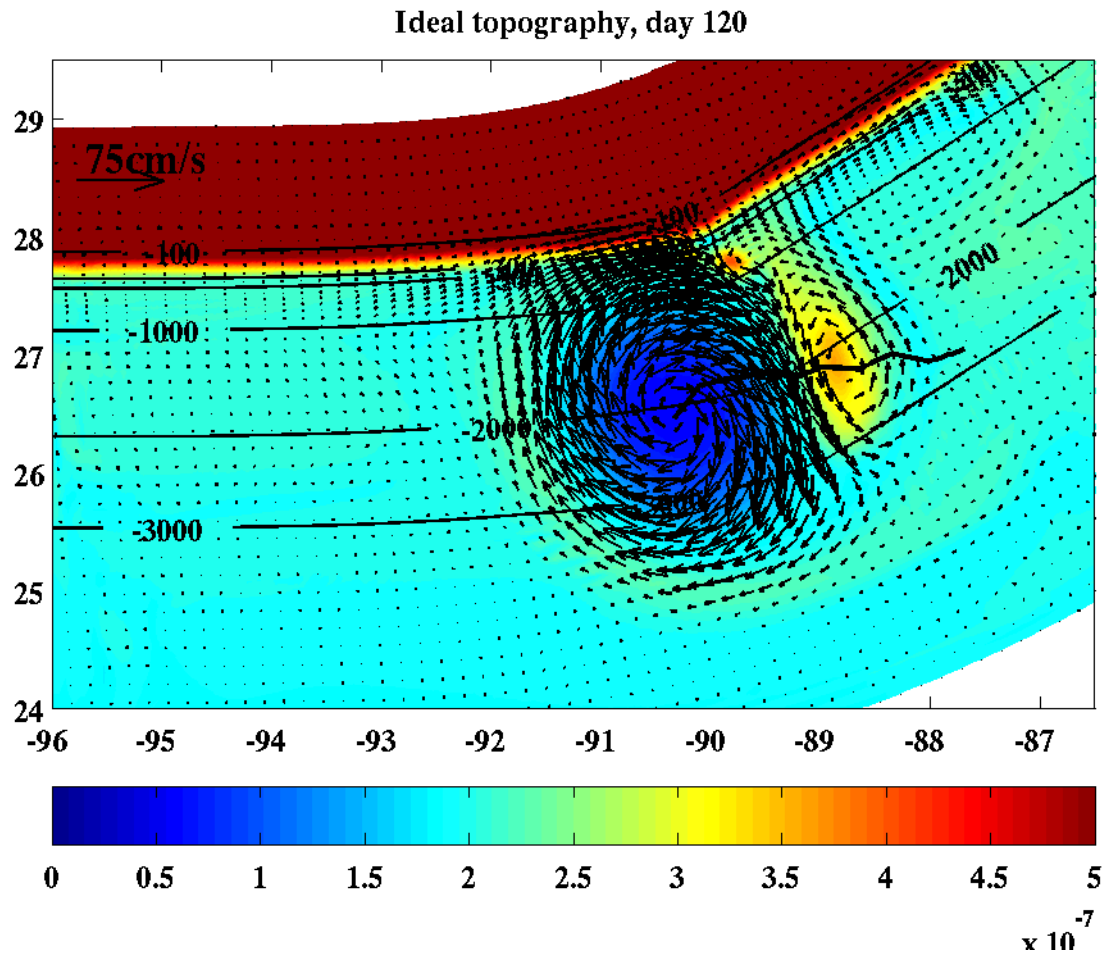


Figure 4.25. Same as in Figure 4.24 but LCE initialized at 87.6°W , 27°N , day 120 of integration.

to much stronger interaction of the off-shelf advected cyclone and the main eddy, which lead to the sharp deflection of the main eddy southward.

Figure 4.26 shows the summary of idealized topography experiments with different initial eddy positions. The obvious general tendency is for the eddy trajectory to deflect more southward as it comes closer to the northern shelf. Another interesting phenomenon can be noticed by following the northernmost trajectory. The initial eddy position in this case is 87.6°W , 27.3°N . After the anticyclone encounters the shelf, its trajectory turns 180° and the eddy moves eastward for a short period of time before turning back westward. This effect has the same origin as the effect of northward eddy propagation that we have seen in the western GOM experiments. As the eddy approaches the shelf, the midwater-column anticyclonic circulation is generated by the mechanism that we identified in Section 4.4.3.2. However, since the shelf is oriented almost zonally in this case, the on-shore intensified along-shelf deep current is directed eastward producing eastward eddy motion.

4.4.4.3 Accelerated Westward Eddy Propagation Mode

Similar to the western GOM, bottom-intensified eddies were shown to form beneath the main eddy on the southern edge of the northern continental slope. However, over the northern GOM

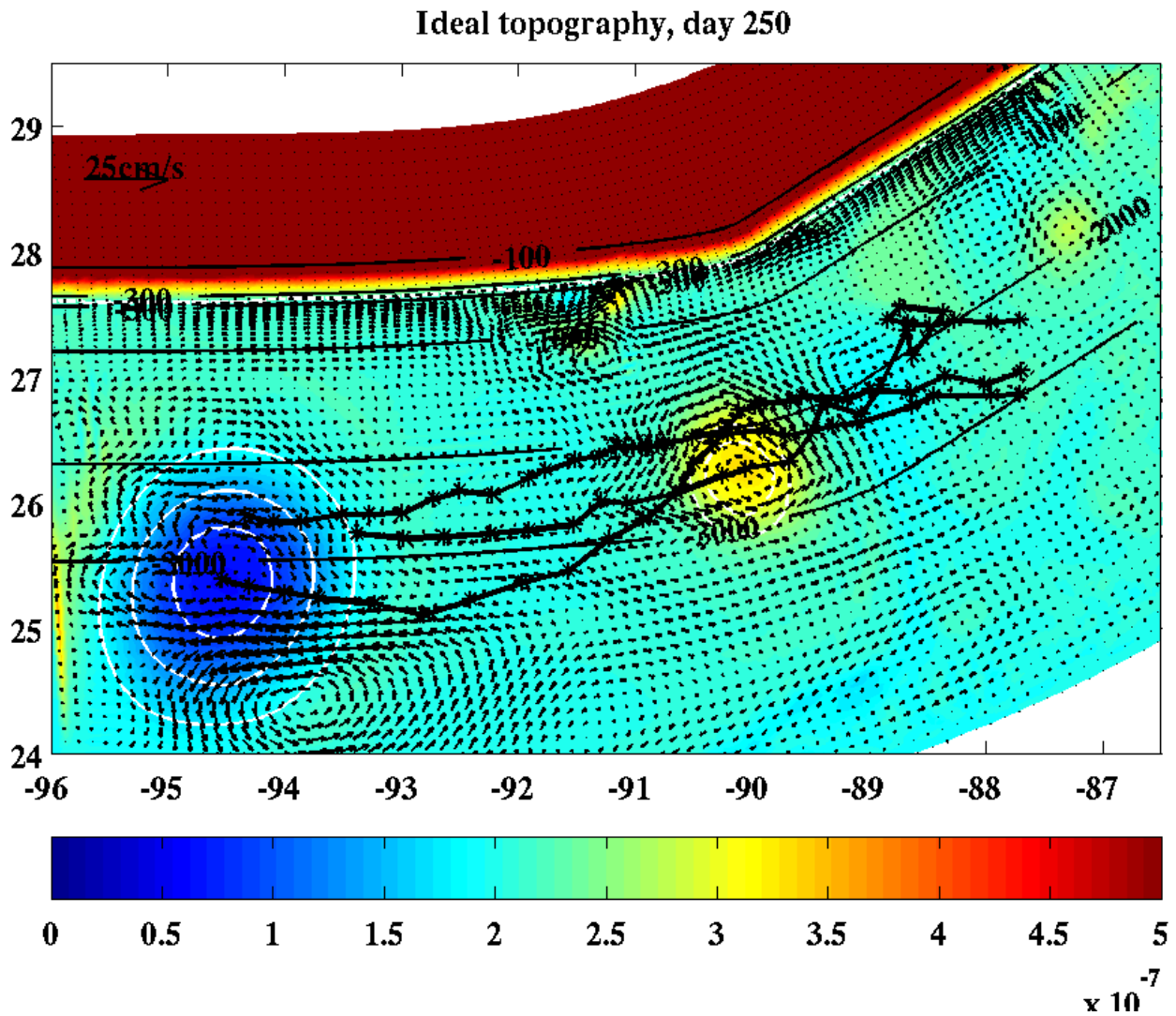


Figure 4.26. Summary plot of LCE interaction with idealized northern shelf topography. Eddy trajectories 250 days long from experiments with different initial LCE locations are shown with thick black lines. Black contours indicate topography.

the effect of these eddies on the surface anticyclone was to accelerate its westward propagation. In the northern GOM setting the preferential direction of deep eddy propagation coincides with the preferential direction of LCE propagation. As a result, LCE's moving along the southern edge of the northern continental slope can form solitary quasi-stationary configurations with bottom-intensified anticyclones. These configurations propagate westward with about twice the speed of the β -drift.

Figure 4.27 shows day 120 of the idealized topography experiment in which a LCE was initialized at 87.6°W , 27.0°N . By the time shown the eddy trajectory has already deflected south after the LCE interaction with the northern shelf. The vectors in the figure indicate velocities in the lower layer (vertically averaged below the thermocline). As one can see, a large bottom-intensified anticyclonic eddy has formed south of the main eddy over the flat topography region. The bottom-intensified anticyclone couples to the surface anticyclone and the pair propagates westward with twice the speed of the β -drift until it reaches the western boundary. This phenomenon appears to be very robust. The simulated LCE track summary shown in Figure 4.26 shows that the eddy westward propagation speed almost doubles as it approaches the southern edge of the continental slope (marks on the eddy trajectories indicate 10 day intervals).

The zonal orientation of the northern slope is the key feature allowing the above effect to exist. The preferential direction of deep eddy propagation created by the bottom slope coincides with the preferential direction of LCE propagation allowing bottom-intensified and surface eddies to interact on a longer time scale. The moving surface eddy causes water column squashing in the lower layer pumping anticyclonic relative vorticity into the deep eddy. In turn, the net effect of the deep anticyclone is to propel the surface eddy westward thus increasing its westward propagation speed.

4.4.5 Realistic Topography Experiments

This set of experiments further increases the level of realism by introducing fully realistic topography of the GOM. The experiment design is very similar to that of the previous set of experiments. An isolated LCE is initialized away from the coast and allowed to propagate freely driven by the β -effect eventually interacting with the coastal topography. The goal of these experiments is to reveal the effects that can potentially be introduced by the realistic topography and that were missed in the previous experiments due to topographic idealizations. Three different regions in the GOM were considered: the western GOM around 23°N , the northern GOM with the focus on the continental shelf and slope west of Mississippi Canyon, and the northwest corner of the GOM.

4.4.5.1 Western GOM

The simulation was performed using the same PE model used before but configured for the real GOM domain shown in Figure 4.28. The model was configured with a uniform 5 km horizontal resolution and 50 vertical levels. All the boundaries were closed and a sponge layer was introduced along the eastern boundary. The model is initialized with horizontally uniform background stratification and a circular anticyclonic eddy just off the western coast. The eddy structure and the background stratification are the same as in the idealized experiments.

The simulated eddy trajectory is shown in Figure 4.29 (only a portion of the domain is shown here). The behavior of the eddy is very similar to that in the idealized 23°N experiment. As the eddy approaches the shelf the off-shelf flux of high PV water leads to formation of small-scale cyclonic eddies. These small-scale cyclonic eddies produce cyclic motion of the main eddy via

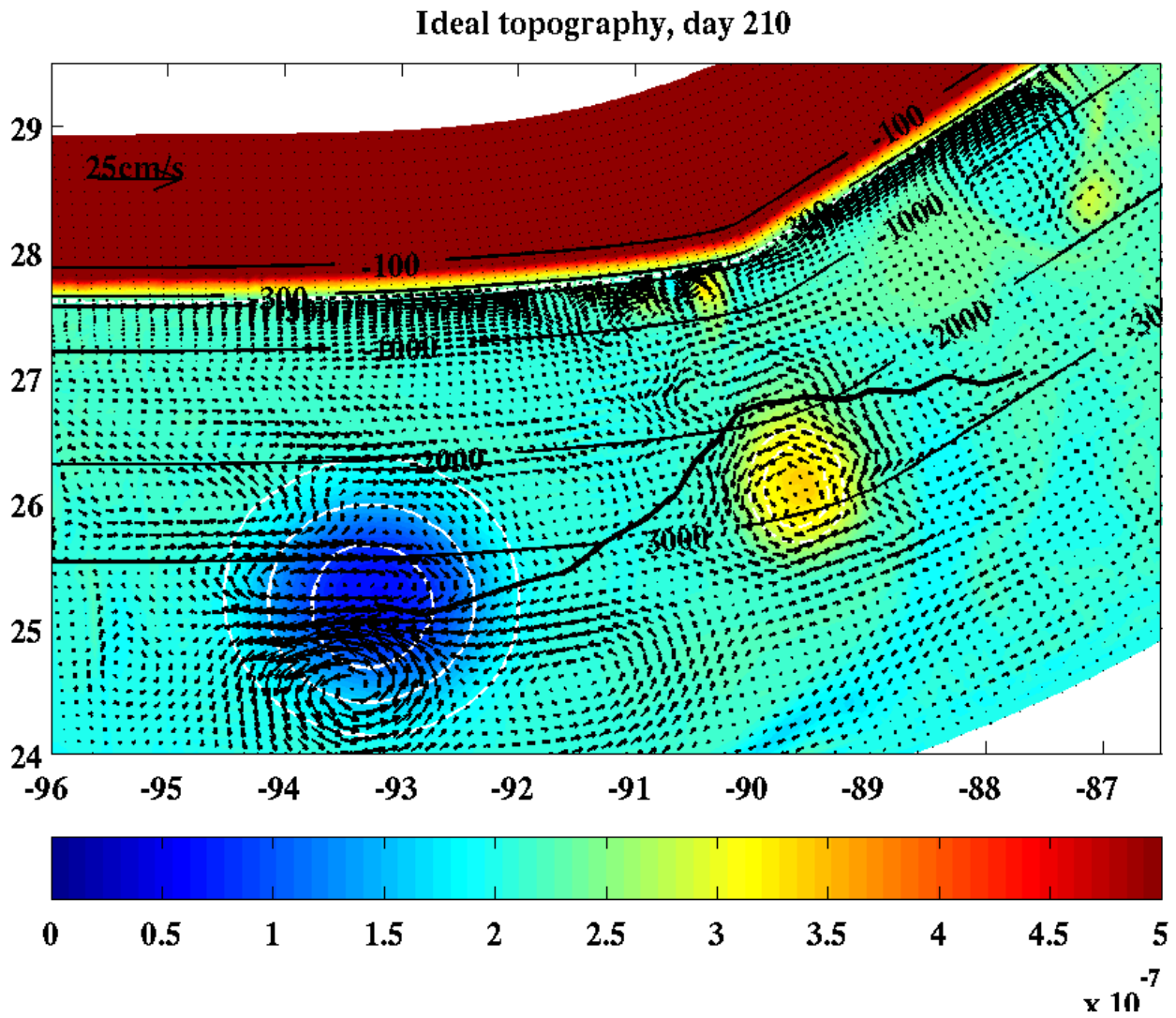


Figure 4.27. Accelerated mode of eddy propagation over the southern edge of the northern slope. Vectors show the velocity averaged vertically below the main thermocline.

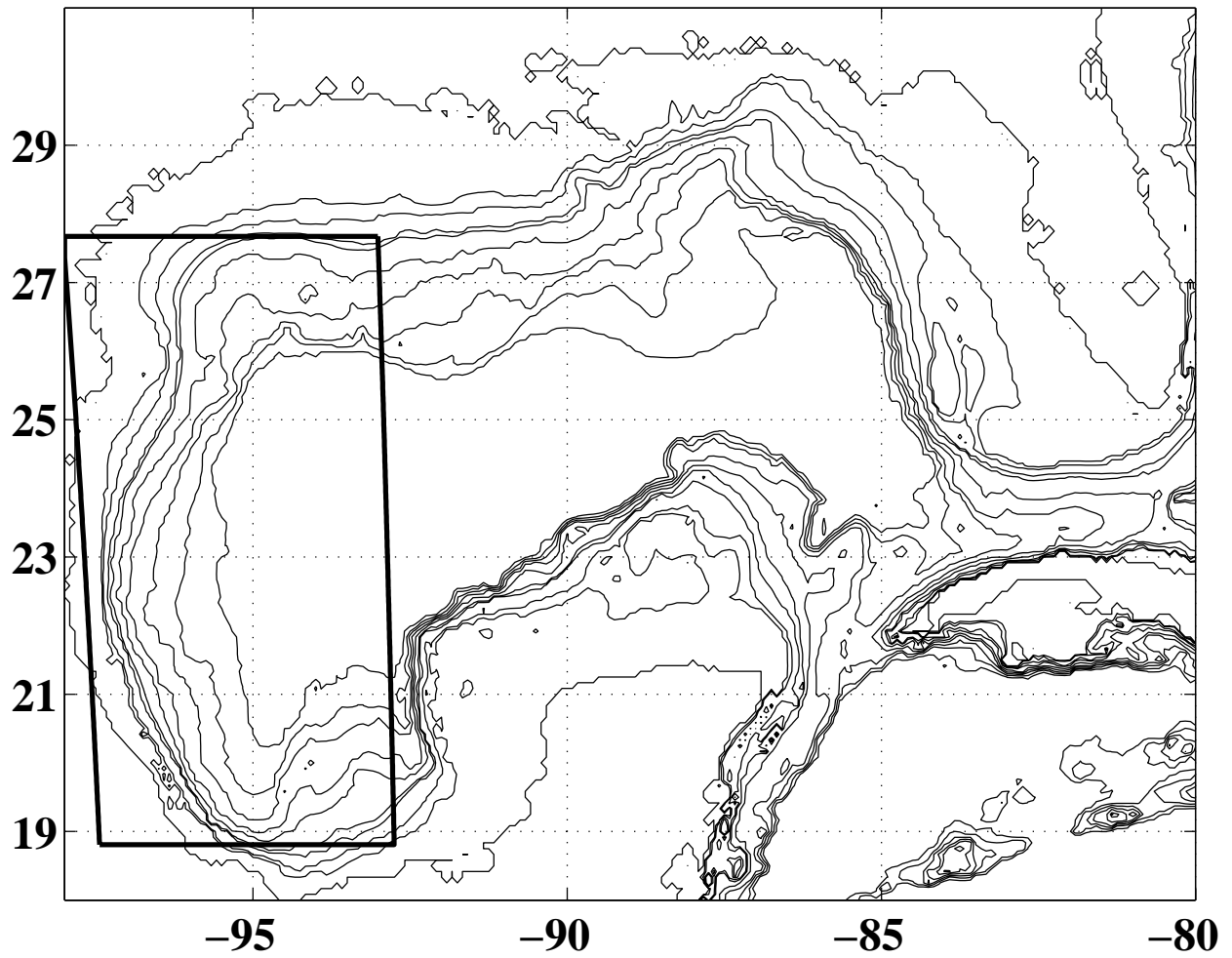


Figure 4.28. Domain configuration for simulation of LCE interaction with the GOM western shelf.

the dipole interaction process. At the same time an initially rapid northward eddy propagation is created by midwater-column currents below the eddy. This northward propagation stalls after 120 days as the eddy stops moving on-shore. The eddy eventually begins slowly migrating southward.

4.4.5.2 Northern GOM

The model domain is shown in Figure 4.23. The simulation employs the same grid configuration and numerical conditions that were used for the idealized experiments. Similar to the western GOM realistic simulation, the model was initialized with horizontally uniform background stratification and a circular anticyclonic eddy at 87.6°W , 27.3°N . The eddy structure and the background stratification were the same as in the idealized experiments.

The results of the simulation is shown in Figure 4.30 after 250 days of integration. The results are very similar to the idealized experiments. The eddy interacts with the northern shelf advecting high PV water off the shelf. A smaller-scale cyclone is formed east of the main eddy that deflects its trajectory southward. As the anticyclonic eddy leaves the off-shelf advected cyclone behind, it resumes its westward zonal propagation. A bottom-intensified anticyclonic eddy south of the main surface eddy, which is the signature of the accelerated westward propagation mode, can be seen in the deep velocity field. This indicates that vertically coupled surface and bottom anticyclones can form a fast propagating solitary solution even over real topography.

4.4.5.3 Northwest Corner of the GOM

In this experiment a LCE was initialized at 94°W , 26.2°N , which places it next to the northern shelf and about 100 km away from the western shelf (see Figure 4.31). The eddy moved westward with a speed typical for β -drift reaching the western shelf (northwest corner) after a month of integration. Approximately at the same time a cyclone formed east of the main eddy adjacent to the northern shelf. The cyclone amplified and started to move south and westward around the eddy. Interaction of the LCE with the cyclone caused it to become elliptic with the minor axis of the ellipse oriented toward the cyclone. The elliptic LCE coupled to the cyclone rotated anticyclonically until the elongated southern part of the LCE encountered the western shelf in the vicinity of Perdido Escarpment ($\sim 25.5^{\circ}\text{N}$). The cyclone continued to move around the center of the LCE squeezing the southern tip of the elliptic LCE between itself and the shelf (Figure 4.32).

By the beginning of the third month of the simulation the portion of the LCE squeezed between the cyclone and the shelf separated completely from the eddy and formed an anticyclonic circulation along the shelf break. At this point the LCE became nearly circular and impinged against the western shelf. The cyclone became nearly stationary and positioned immediately south of the LCE. The pair proceeded to drift slowly southward along the western shelf. The process of squeezing of the elongated portion of the LCE between the cyclone and the shelf created a very intense on-shelf current. After another month of the simulation (day 100) another cyclone formed east of the LCE. The LCE became elliptic again and another portion of it was chopped away squeezed between the cyclone and the shelf. The second cyclone merged with the previous one south of the LCE. The remaining LCE and the cyclone south of it continued to drift southward reaching 25.7°N by the end of the fourth month of simulation. At this point the amplitude of the LCE had decreased by approximately a factor of 3 compared to its original amplitude and the integration was stopped.

Overall, in the absence of background circulation and external forcing, the evolution of an LCE in the northwest corner seems to be characterized by a slow and steady southward drift along the western shelf and a high dissipation rate produced mostly by an ejection of mass. This is in contrast to the LCE evolution pattern identified during our previous experiments simulating

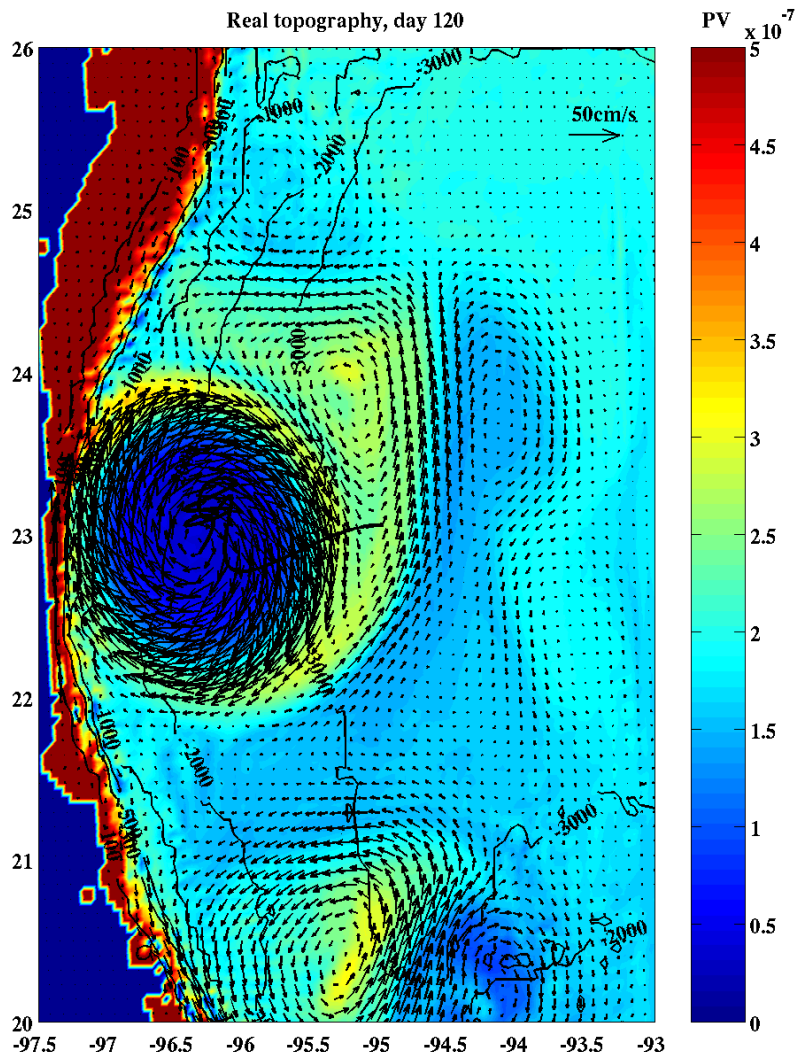


Figure 4.29. Simulated interaction of a LCE with the GOM western shelf at 23°N , day 120 of integration. Color coded is PV in the main thermocline; white contours indicate the thermocline displacement; and black contours indicate topography. The eddy trajectory is shown with the thick black line. Vectors show the velocity vertically averaged above the thermocline.

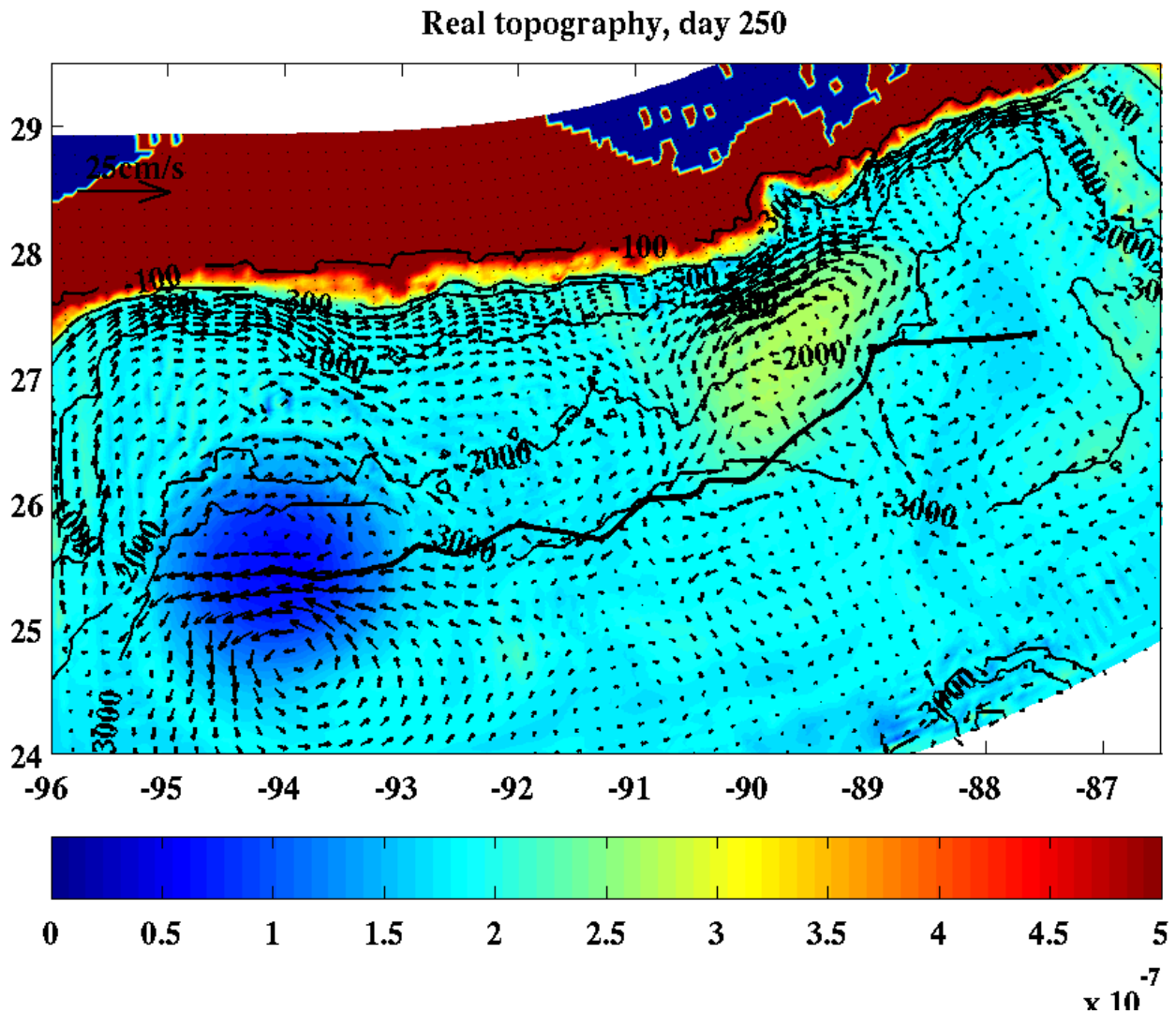


Figure 4.30. Simulated interaction of an LCE initialized at 87.6°W , 27°N with the GOM northern shelf, day 250 of integration. Color coded is PV in the main thermocline, and black contours indicate topography. The eddy trajectory is shown with the thick black line. Vectors show the velocity vertically averaged below the thermocline.

Simulation of an LCE in the northwest corner, initial conditions

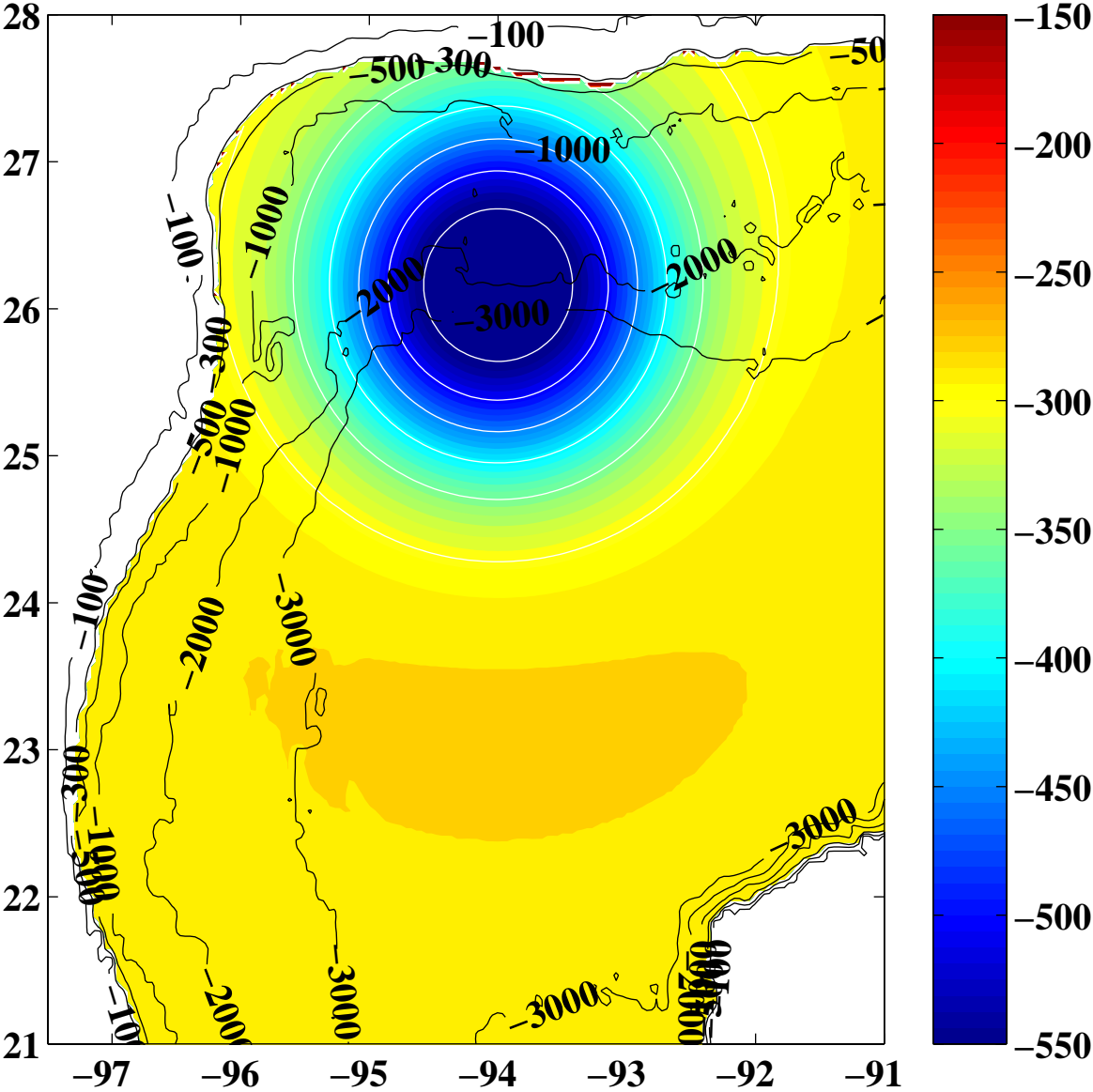


Figure 4.31. Initial conditions for the simulation of an LCE in the northwest corner. Color coded is the height of the 27 kg/m^3 density surface

LCE interactions with the western slope at 25°N and 23°N , which predicted the LCE moving north rapidly while approaching the shelf and then moving southward with unsteady speed along a cyclic trajectory with decaying amplitude. The simulated LCE in the northwest corner dissipates about twice as fast as those interacting with the western shelf.

We further analyze the dynamics controlling the LCE evolution pattern at the northwest corner on the basis of the three dynamical mechanisms identified in our previous idealized experiments. Three dynamical mechanisms were previously identified to be responsible for an LCE behavior during interaction with the shelf: 1) off-shelf PV advection and associated cyclone generation; 2) interaction with deep eddies generated by movements of an LCE over flat topography; 3) interaction with mid-water column currents generated underneath an LCE as it moves onto a continental slope.

The specifics of the topography configuration in the northwest corner create a situation where the last two mechanisms do not have any significant effect on the LCE. The presence of both the northern and the southern continental slopes isolates the LCE from the flat topography region in the central Gulf, preventing deep eddies from forming underneath the LCE. The presence of the northern shelf blocks the northward eddy propagation produced by the interaction with mid-water column currents generated underneath an LCE. Thus, the off-shelf PV advection mechanism and associated cyclone generation is the only remaining mechanism affecting the LCE behavior in the northwest corner. The slow southward drift of the LCE that we see in the northwest corner simulations is produced by its interaction with the cyclonic circulation created east of the eddy via high PV water advection from the northern and western shelves.

The simulated high dissipation rates of the LCE at the northwest corner is associated with the ejection of mass which occurs several times during the simulation. The mass ejection from the LCE is associated with the shelf configuration specific to the Perdido Escarpment region ($\sim 25.5^{\circ}\text{N}$). The shelf break line in this region forms a corner protruding into the Gulf interior. When LCE's located north of Perdido Escarpment interact with cyclones advected off the shelf by the LCE, they become elliptic and form a cyclone-anticyclone pair rotating anticyclonically in a manner very similar to our previous idealized simulations of LCE's interacting with the western shelf. The corner formed by the shelf break line cuts into the southern elongated end of the LCE causing mass ejection. The effect is amplified by the fact that the LCE does not move eastward (off-shore) while interacting with cyclones like it does at 25°N and 23°N . The off-shore LCE motion at 25°N and 23°N is produced by its interaction with off-shelf advected cyclones *north* of the LCE. In the northwest corner case the presence of the northern shelf prevents the cyclones from forming north of the LCE. The process of mass ejection from LCE's in the Perdido Escarpment region creates a very strong on-shelf flow and a 10-20 cm/s southward current along the shelf that extends far south of the LCE. The dynamics of this process is poorly understood and further investigation will be needed.

The above simulation of an LCE interaction with the northwest corner of the GOM reveals the natural tendency of the LCE to drift southward in the absence of a background circulation and other mesoscale features. The southward drift produced by LCE interaction with cyclonic vorticity is relatively weak. If a background circulation and/or other mesoscale features are present the direction of LCE drift can be affected. In particular, an anticyclonic circulation along the perimeter of the GOM, which has been frequently observed (Nowlin et al. 2001), would have a tendency to counteract the natural southward LCE drift and keep it in the northwest corner. The presence of other anticyclones east of the LCE in the northwest corner, which is also often the case, would produce a similar effect.

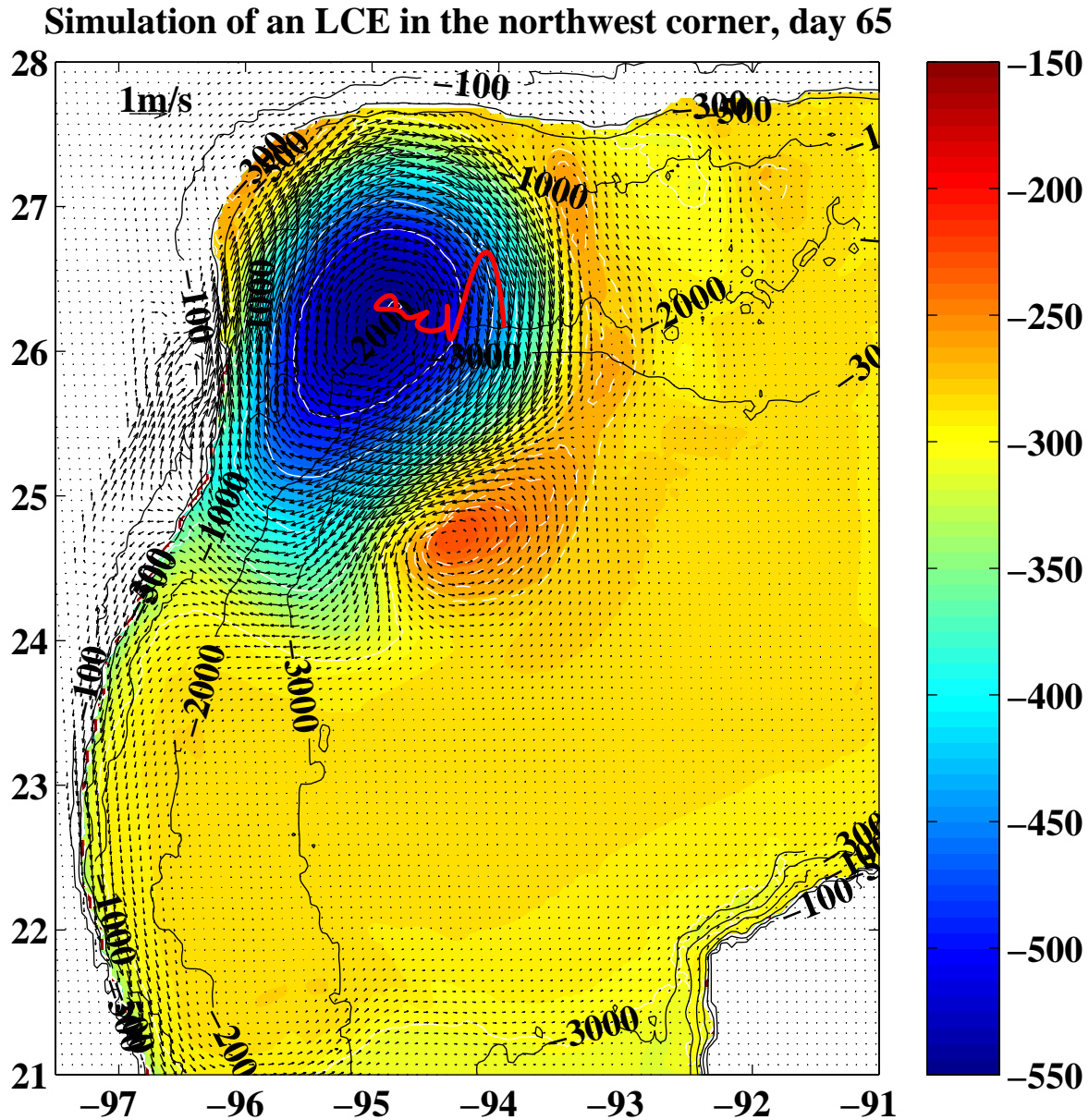


Figure 4.32. Simulation of an LCE in the northwest corner after 65 days of integration. Color-coded is the height of the 27 kg/m^3 isopycnal surface. The thick red line indicates the simulated LCE trajectory. Arrows indicate upper layer velocities calculated by averaging vertically above the 27 kg/m^3 isopycnal surface.

4.4.6 Fast Eddy Simulation

As the final step of the investigation an actual event of an LCE interacting with the western shelf of the GOM was simulated. The event selected for the simulation was the interaction of Fast Eddy with the western shelf at 25°N which started during December 1985 and continued for several months. To our knowledge this event is the best documented example of LCE interaction with the western shelf, which makes it ideal for a numerical simulation. The simulation demonstrated considerable skill in reproducing the observed evolution of Fast Eddy and the surrounding mesoscale features. Results provided a more in-depth understanding of the dynamics associated with the observed sequence of events and a better understanding of the fate of some smaller mesoscale features that were involved.

4.4.6.1 Model Configuration and Initialization

The primitive equations model used in our previous experiments was configured for a rectangular region in the western GOM ($98\text{-}90^{\circ}\text{W}$, $21\text{-}28.5^{\circ}\text{N}$) with uniform 4 km horizontal resolution. The vertical distribution of σ -levels was retained from the previous regional GOM configurations. Closed boundary conditions with a 15 grid point sponge layer at the southern boundary and a 6 grid point sponge layer at the eastern boundary were applied. The topography was derived from the $1/12^{\circ}$ ETOPO5 database. No external forcing was specified.

The model was initialized using the in-house developed initialization technique. The structure and location of Fast Eddy as well as key features of the background circulation in the northwestern GOM on October 28, 1985 were determined from hydrographic surveys and drifter trajectory data. Three mesoscale features were initialized. In addition to Fast Eddy itself, a mid-size cyclone located west of the eddy near the western shelf, and a weak anticyclone located in the northwest corner were initialized (see Figure 4.33). The structure of each feature was prescribed by adjusting the free parameters of the PV-feature model (amplitude and the width of the PV front in each of 8 isopycnal layers) to match the observed feature characteristics.

The structure of Fast Eddy was derived from the hydrographic survey conducted aboard R/V Pelican on October 22-27, 1985 combined with drifter trajectory data from buoy #3378 (SAIC 1988). A procedure has been designed to derive the values of the free parameters of the PV feature model from scattered vertical density profiles. The procedure is based upon the assumptions that the eddy structure does not change significantly during the time of the survey, and that the eddy propagates as a rotating solid body along some trajectory. The position of the eddy at the time of each CTD/XBT measurement is derived from drifter trajectory data. After this, we can calculate the distance to the center of the eddy for each hydrographic measurement. The free parameters of the PV feature model are then adjusted to fit, in a least squares sense, the resulting distribution of density profiles.

The derivation of the eddy position from the drifter trajectory data was done by objectively fitting (in the least square sense) a rotating ellipse solid body model. The model assumes that the drifter is trapped at a constant radius in a translating and rotating elliptic eddy. The radius and the ellipticity of the eddy are assumed to be constant while its speed is allowed to vary. The time interval from October 7 to October 28 (1985) was used for fitting purposes. This interval was selected because the radius of the drifter orbit remained constant during this time, as required by our relatively simple model. The eddy propagation speed is assumed to change linearly within prescribed time intervals; the time intervals are selected subjectively to match the apparent observed variability in eddy motion.

The cyclone over the northern slope was initialized using the PV feature model described in Section 6.1.1. The model was calibrated to match the observed cyclone intensity and ellipticity, which were estimated from the maps of 8°C isotherm depth objectively derived on the basis of hydrographic surveys (SAIC 1988). The position of the cyclone was also subjectively determined from the the maps of 8°C isotherm depth.

The weak anticyclone in the northwest corner was not detected during the R/V Pelican hydrographic survey since the survey did not extend far enough to the north. However, the subsequent AXBT survey on November 11-13, 1985 detected a weak anticyclone at roughly 95.5°W , 26.8°N .

Since weak anticyclonic circulation is frequently observed in the northwest corner of the GOM (Berger et al. 1996), we hypothesized that the anticyclone originated there. In order to represent this feature in the simulation, we initialized an anticyclonic feature at 95.3°W , 26.7°N using our previously developed feature model of a circular anticyclone calibrated to match the observed intensity.

4.4.6.2 Simulation Results and Comparison with Observations

The numerical simulation started on October 28, 1985, when Fast Eddy was approaching the shelf and continued for 6 months. The beginning of the simulation corresponds to the date of the R/V Pelican hydrographic survey, which was used to specify the initial density field in the model as described in the previous section. The results of the simulation were evaluated subjectively by comparing the simulated position and structure of the key mesoscale features with observations. Even though some conclusions regarding the positions of the features can be made on the basis of drifter tracks and satellite data (SAIC 1988), the temperature and salinity data collected during the subsequent three hydrographic surveys present the most useful source of information for verifying the model performance. Consequently, the results of the simulation were evaluated on the dates of the hydrographic surveys: November 11-1, 1985; January 23- February 5, 1986; and April 27-May 14, 1986.

The simulated height of the 27 kg/m^3 isopycnal surface (average depth ~ 300 meters) after 15 days of integration (November 12) is shown on Figure 4.34. Comparison with the map of the depth of the 15°C temperature surface (average depth ~ 200 meters) constructed from the AXBT survey on November 11-13, 1985 (Figure 4.35) demonstrates considerable model skill in reproducing the observed evolution of Fast Eddy and the cyclone initially west of Fast Eddy. In 15 days Fast Eddy moved westward to $\sim 94^{\circ}\text{W}$, while the cyclone was caught in its circulation and advected northeast to $\sim 95.5^{\circ}\text{W}$, 26.3°N .

Further integration shows Fast Eddy approaching the shelf as the cyclone continues to move around it. By the beginning of December the drifter trajectory indicates that Fast Eddy was centered at $\sim 95^{\circ}\text{W}$, 24.5°N , the ratio of its major to minor axes was ~ 2 , and its ellipse was oriented in the northwest direction. This agrees well with the simulated location, ellipticity, and orientation of Fast Eddy after 1 month of integration (beginning of December), demonstrating that at this time the model still has a considerable skill.

Observations available from the beginning of December do not allow us to conclusively determine the location of the cyclone detected in the November hydrographic survey. It was hypothesized that it moved westward together with Fast Eddy and that it was the same eddy detected to the north of Fast Eddy in the January 23- February 5, 1986 (SAIC 1988). Our simulation indicates that this is an unlikely scenario. By mid November the cyclone seems to be well captured within the circulation of Fast Eddy, and only the presence of another strong anticyclonic feature to the north could potentially force the cyclone to move westward. However, there were no traces of such a

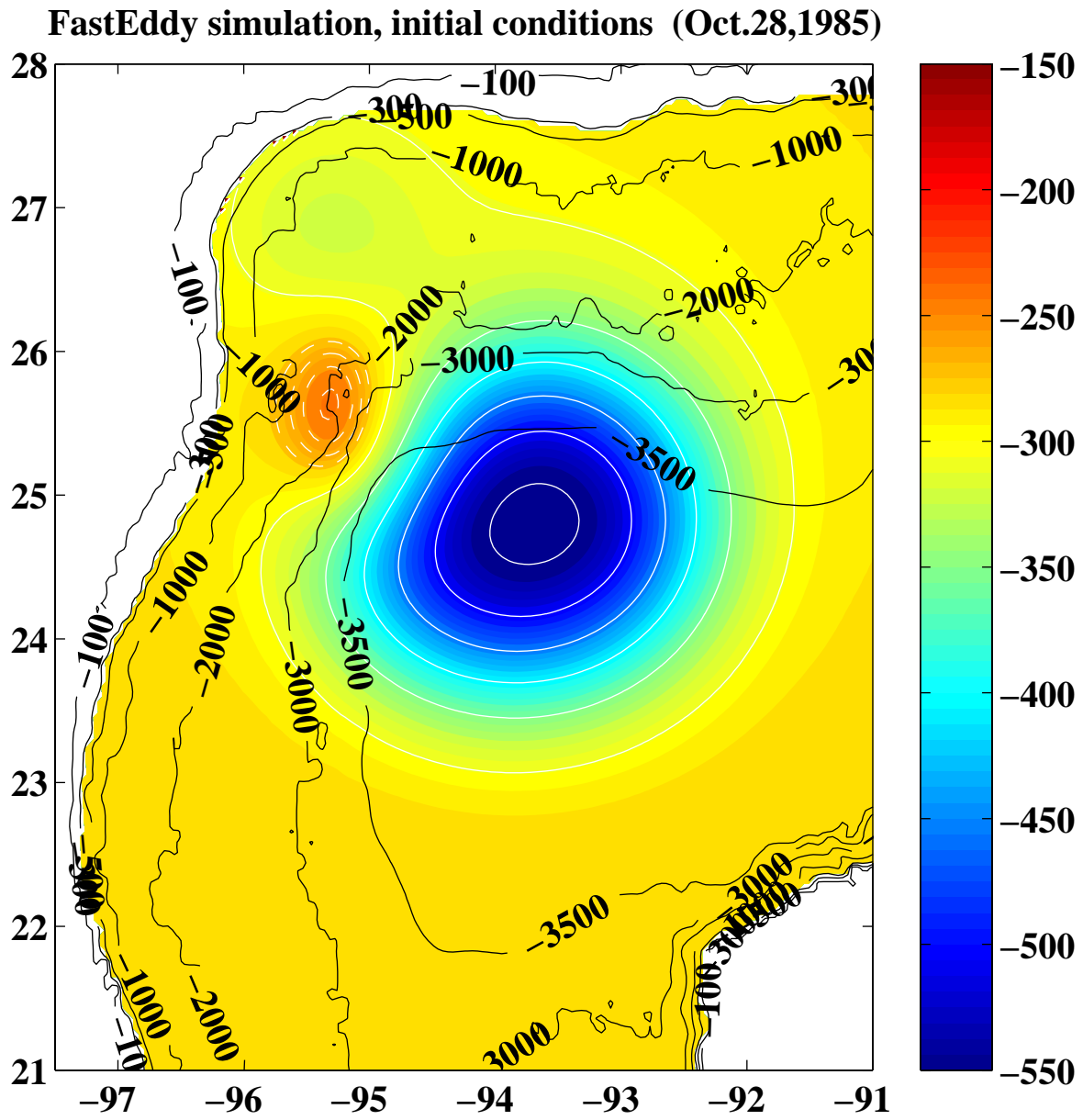


Figure 4.33. Initial conditions for Fast Eddy simulation. Height of the 27 kg/m³ density surface as it is initialized in the model on October 28, 1985.

feature in observations which leads us to believe that the cyclone continued eastward and around Fast Eddy just as depicted in the simulation. This cyclone can be seen around 95°W , 23.5°N in Figure 4.36, which shows the 27 kg/m^3 isopycnal surface after 55 days of integration (December 22). One can also see another cyclone that formed north of Fast Eddy.

During the next month of the simulation (December 1985), Fast Eddy moved in a southwest direction while its northwest portion interacted with the western shelf around 25°N , generating a cyclone around 96°W , 26°N in the process. After the main part of Fast Eddy approached the western shelf (December 22), Fast Eddy moved northward while continuing interactions with the shelf. During this process the cyclone north of Fast Eddy amplified. Immediately after that, Fast Eddy moved eastward toward the deep Gulf and then southward. By the end of January it returned to the shelf at approximately 24.3°N .

The simulated sequence of events after the beginning of December described above closely resembles the sequence reconstructed from observations (SAIC 1988), however, the timing is substantially different. According to the trajectory data of drifter #3378, Fast Eddy approached the western shelf and moved northward as in the simulation; however, the actual time of this event was the end of December, which is half a month later than simulated. Also, the simulated eddy encountered the shelf approximately a half of a degree further south than was observed. In January-February 1986 Fast Eddy was interacting with the western shelf. During this time a cyclone of increasing amplitude was observed north of the Eddy. The simulation also reproduced the cyclone generation process but the duration of the eddy-shelf interaction was substantially shorter. In the simulation Fast Eddy remained at the shelf for several days only, in contrast to 2.5 months in observations. Finally, by the end of February 1986, Fast Eddy was observed to move off-shore and southward, returning back to the shelf around April. The same event, even though it occurred more than two months earlier, was reproduced in the simulation.

The fact that the model was capable of qualitatively reproducing the actual sequence of events during the interaction of Fast Eddy with the shelf demonstrates that the physical mechanisms controlling the eddy-shelf interaction are well represented. This allows us to make conclusions about the dynamics controlling the evolution of temperature and velocity fields during the event on the basis of the model dynamics, which are well understood as the result of our previously conducted idealized studies.

4.4.6.3 Discussion of Dynamical Mechanisms

The analysis of the simulated sequence of events provided more in-depth understanding of the dynamics associated with the observed sequence of events during Fast Eddy interaction with the western shelf. In particular, three elements of the observed (and simulated) event sequence were considered. These elements are the northward shift of the eddy track as it approached the western shelf, the development of a cyclone north of the eddy after its interaction with the shelf, and the abrupt off-shore motion of the eddy after interacting with the shelf.

The northward shift of Fast Eddy as it approached the shelf can be attributed to the interaction of the eddy with northward currents generated in the mid-water column underneath the eddy as the result of its on-slope motion (see Section 4.4.3.2). The characteristic signature of this dynamical mechanism is mid-water column currents underneath the eddy directed northward along the shelf and intensifying in the on-shore direction. These currents can be seen underneath Fast Eddy as it approaches the western shelf in the simulation (Figure 4.36).

The formation and further amplification of a cyclone north of Fast Eddy during its interaction with the shelf is the result of off-shelf PV advection induced by Fast Eddy, similar to the idealized

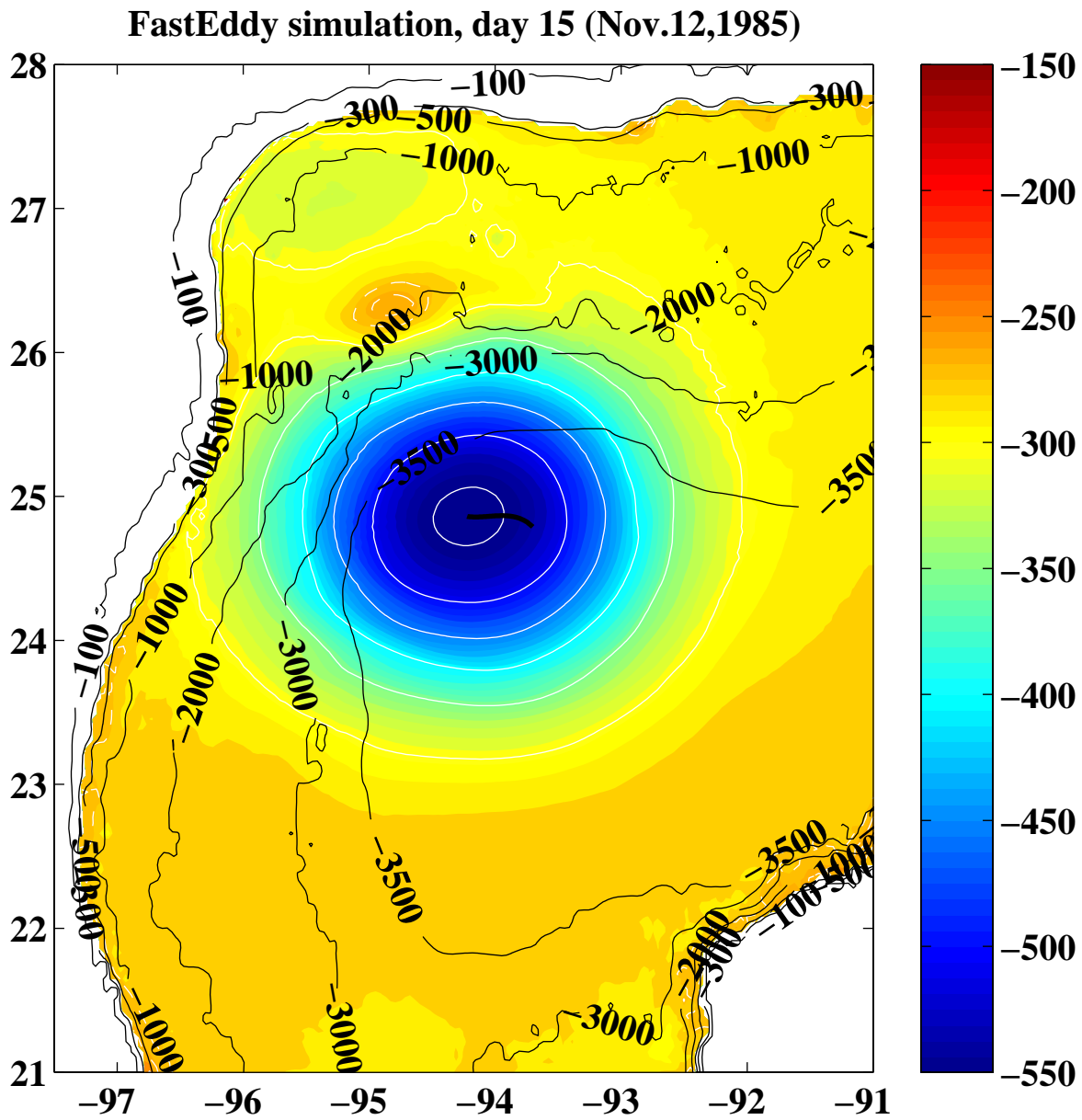


Figure 4.34. Fast Eddy simulation after 15 days of integration (November 12). Colorcoded is the simulated height of the 27 kg/m^3 density surface (average depth ~ 300 meters), thick solid line indicates the simulated Fast Eddy trajectory.

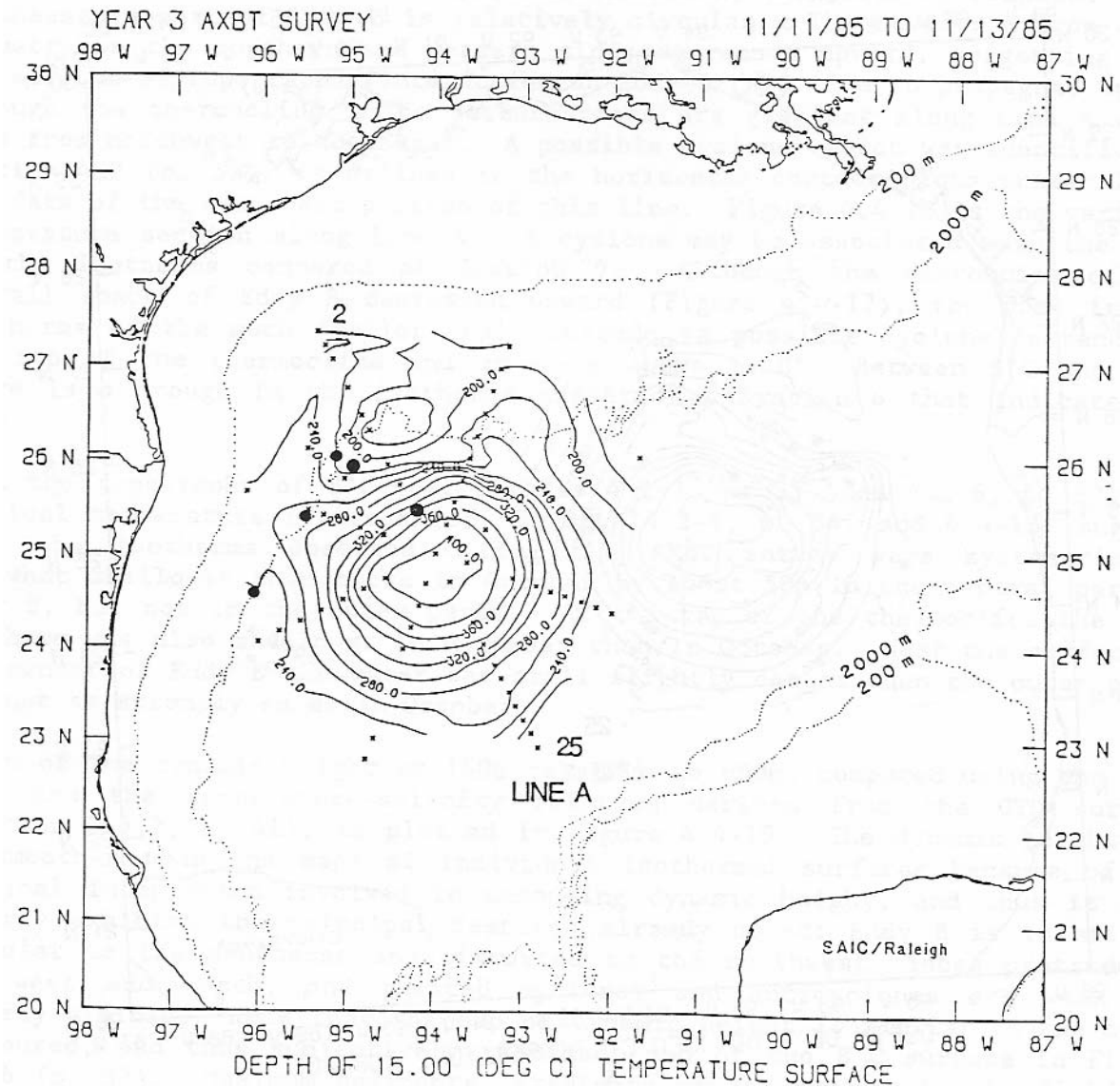


Figure 4.35. Figure 4.4-17b from SAIC, 1988: Topography of the 15°C isotherm based on the November 1985 AXBT survey.

experiments in Section 4.4.3. It is interesting to note the role of the weak anticyclone that was initialized in the northwest corner of the GOM in the beginning of the simulation. Our additional numerical simulations initialized without this anticyclone indicate that the presence of an anticyclonic circulation in the northwest corner facilitates the generation of a more intense cyclone north of Fast Eddy via the process of off-shelf PV advection. Without the anticyclonic circulation in the northwest corner, the high PV water advected off the shelf tends to move around Fast Eddy into the deep Gulf. The presence of the anticyclonic circulation north of the main eddy creates a weak on-shore advection which keeps the high PV water at the shelf allowing it to form a more intense cyclone.

The off-shore excursion of Fast Eddy and subsequent return back to the shelf is caused by its interaction with a deep anticyclone which formed underneath the Eddy as it rotated over the flat topography adjacent to the western continental slope. The deep anticyclone centered at the south-eastern edge of the Eddy around 94.5°W , 24.5°N can be clearly seen in the deep velocity field (Figure 4.37). This mechanism was analyzed in detail in Section 4.3.3 and is related to the squashing and stretching of water columns underneath an LCE moving over a flat bottom. The fact that the off-shore eddy motion in the simulation occurred over 2 months earlier than it was observed is related to the premature formation of the deep anticyclone underneath the off-shore portion of Fast Eddy. The simulated unrealistic southward Fast Eddy propagation in December seems to be related to the same problem. Figure 4.36 shows that a large deep cyclone forms underneath the surface cyclone as it is being advected over the flat topography by the Fast Eddy circulation. This deep cyclone induces southward Fast Eddy propagation which was not observed in the drifter data. Thus, the two biggest inaccuracies in the simulation seem to be related to the same problem of overactive deep eddy formation.

We hypothesize that during the real events some deep circulation was present prior to October 28 which prevented deep eddies from forming. The presence of a strong deep circulation prior to October 28 is supported by the observed abrupt motion of Fast Eddy. Drifter trajectory data indicate that in the beginning of October 1985 Fast Eddy stalled around 93°W and then rapidly moved southwest. It was demonstrated in our LCE propagation experiments (Section 4.3) that this type of behavior is associated with LCE interaction with deep eddies. Deep circulation, when present has a tendency to disrupt the vertical coupling between surface and deep layers thus inhibiting the growth of deep eddies. This is only a preliminary hypothesis and some further studies are necessary to understand exactly how deep circulation disrupts the formation of new deep eddies. Thus we attribute the differences between the simulation and observations to deficiencies of deep circulation initialization in the model related to the lack of appropriate observations.

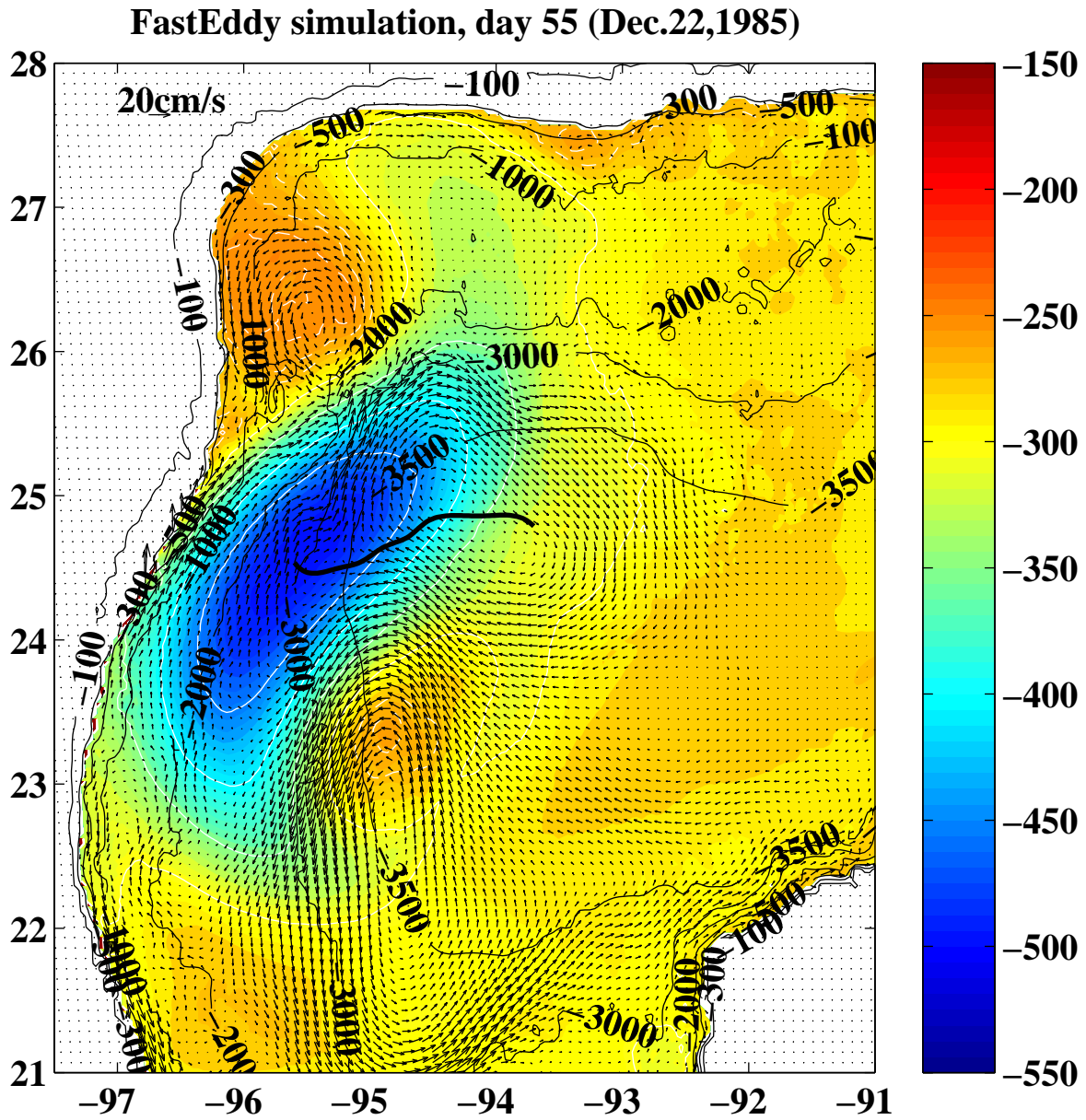


Figure 4.36. Fast Eddy simulation, day 55 (December 22). Color coded is the height of 27 kg/m^3 isopycnal surface. The thick solid line indicates the simulated Fast Eddy trajectory. Arrows indicate deep velocities calculated by averaging vertically below the isopycnal surface.

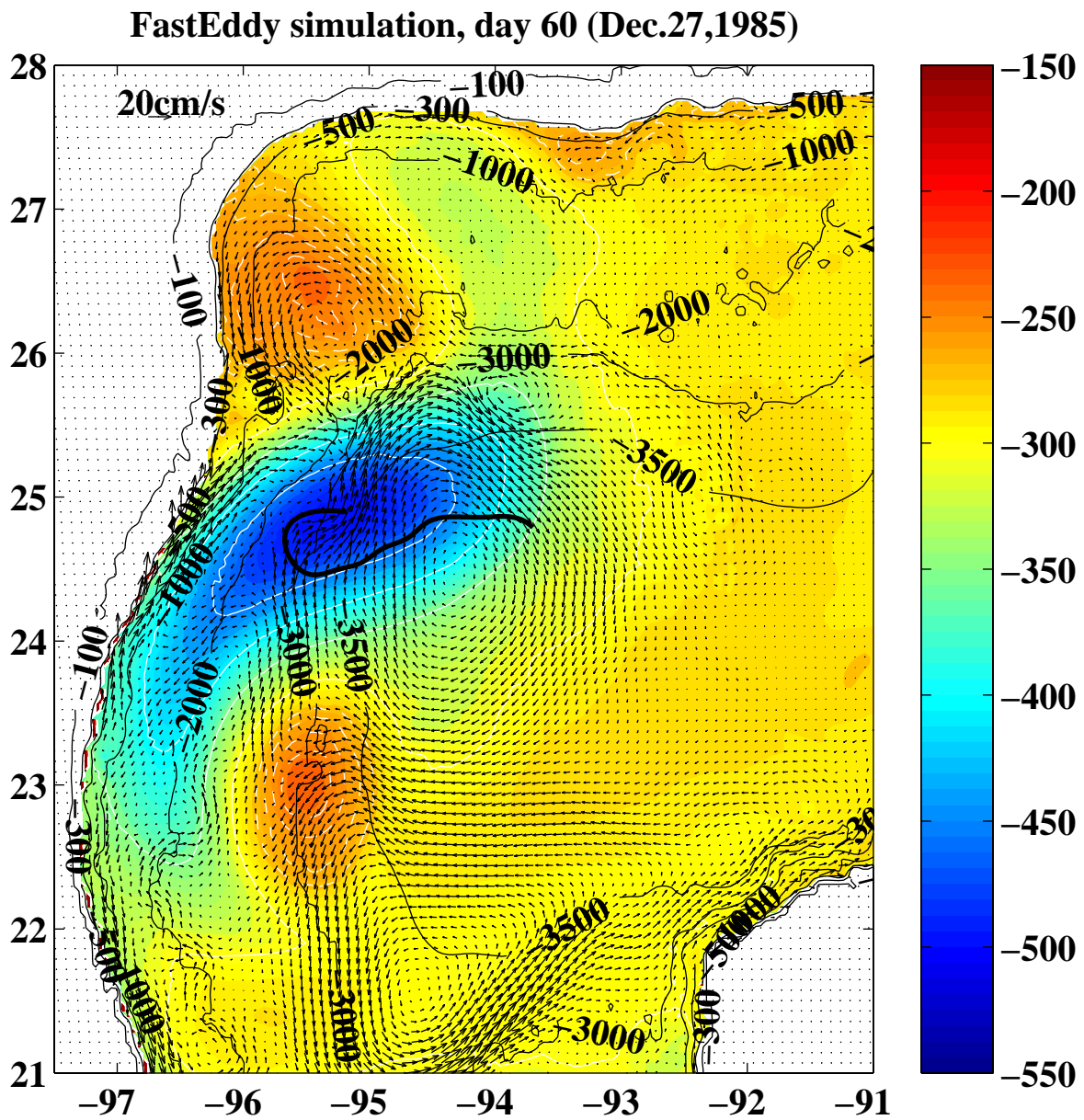


Figure 4.37. Same as Figure 4.36 but 60 days of integration.

5. DYNAMICAL EFFECTS OF DESOTO CANYON

5.1 Introduction

The DeSoto Canyon region is a site for a large number of oil and gas drilling operations. The threat of a spill contacting land in the northeastern GOM is of great concern to the MMS. Information and analysis which expands the understanding of physical oceanographic conditions and processes in this region will support an enhanced basis for developing sound, rationally based environmental assessments. The goal of this study was to improve understanding of physical oceanographic conditions and processes within, and in the vicinity of, the DeSoto canyon through using numerical models as a tool for dynamical reanalysis of available data. The principal source of data for the reanalysis was the DeSoto Canyon Eddy Intrusion study (Hamilton et al. 2000) funded by MMS to assemble the oceanographic climatological database for oil spill trajectory calculations.

The DeSoto Canyon Eddy Intrusion study produced two complete years of field observations that included moored current meter measurements collected from 13 locations, satellite temperature and altimeter data, and 9 hydrographic surveys. In the course of the field program a number of strong current events were observed in the vicinity of the Canyon. The available data allowed the investigators to identify the circulation patterns associated with several of these events and to hypothesize dynamical mechanisms responsible for their existence. As a result several conceptual models were formulated. The conceptual models consisted of schematic descriptions of observed circulation patterns and physical processes hypothesized to be associated with them.

The data collected during the DeSoto Canyon Eddy Intrusion study were used in previous numerical modeling studies for data assimilating simulations of the circulation in the DeSoto Canyon region (Wang et al. 2003). These simulations were focused primarily on statistical characteristics of the regional circulation. Two dominant models of low frequency fluctuations were identified in both modeled and observed currents: a “single-eddy” mode, in which currents are concentrated at the foot of the canyon, and an “eddy-pair” mode, in which one eddy is at the foot of the canyon and the other, a counter-rotating eddy, is over the head of the canyon. The numerical model was shown to reproduce well the observed means and variances of the circulation.

The present study focuses on specific events observed during the DeSoto Canyon Eddy Intrusion study rather than the statistical characteristics of the flow. The “bottom-up” investigation methodology applied previously to studying the LCE-topography interaction is used to identify dynamical mechanisms responsible for the observed events. The investigation is structured upon the conceptual models of circulation in the DeSoto Canyon proposed by Hamilton et al. (2000) on the basis of their data analysis. A high resolution primitive equations model is used to simulate the events described by the conceptual models in isolation from the surrounding circulation in the GOM. The observational data is used to construct the initial conditions for each of the events and to verify the results of the numerical simulations. This approach allows to rigorously test the dynamical hypotheses formulated in conceptual models and, in some cases, to formulate alternative conceptual models.

In particular, three conceptual models are analyzed: direct interaction of an anticyclone with the canyon, remotely generated eastward jets west of the canyon, and the interaction with Loop Current frontal eddies. The first two models, i.e. direct interaction of an anticyclone with the canyon, remotely generated eastward jets west of the canyon, involve dynamical mechanisms very similar to those previously analyzed mechanisms which were associated with LCE-topography

interactions. Because of this, we skip the IE and IE+ classes of experiments in our experiment hierarchy proceeding right away with idealized PE experiments and realistic simulations. The third conceptual model, however, involves a set of new dynamical processes associated with stability properties of the Loop Current, which require developing of initial understanding and dynamical intuition. Thus, the investigation of the DeSoto Canyon interaction with Loop Current frontal eddies begins with idealized IE model experiments.

5.2 Direct Interaction with Anticyclones

Direct interaction of anticyclones with the DeSoto Canyon was identified by Hamilton et al. (2000) as one of the conceptual models describing circulation patterns in the canyon. The investigation of this conceptual model which consisted of three steps. During the first step we analyze the available observational data with the main goal of identifying the structure of anticyclones typically found at the mouth of the canyon. As the second step we investigate potential physical mechanisms that can lead to propagation of anticyclones towards the mouth of the canyon where they directly affect the circulation in the canyon. And finally, we study the circulation in the canyon induced by the direct interaction with anticyclones and identified one of the principal physical mechanisms involved in this interaction. We discuss these three steps in turn.

5.2.1 Structure of the Anticyclonic Circulation

As the first step in our investigation of direct interaction of anticyclones with the DeSoto Canyon, we analyze the available observational data with the main goal of identifying the structure of anticyclonic circulation typically found at the mouth of the canyon. The observed anticyclones were classified by the depth of the PV anomaly associated with them. Three idealized PV-based feature models, one for each of the observed eddy types, were created to represent .

The principal data source used in our analysis were nine high resolution hydrographic surveys conducted as a part of the DeSoto Canyon Eddy Intrusion Study (1997-1999). The analysis revealed a very high variability of anticyclonic circulation in the DeSoto Canyon region. The two major types of anticyclonic circulation are 1) the warm streamers and 2) the remnant warm-core rings. Currents associated with the warm streamers are typically confined to the upper 300 meters and tend to have complex shapes, while the currents associated with the remnant warm-core rings extend deeper than 500 meters and tend to be more circular. The remnant warm-core rings can be further subdivided into two classes depending upon the amount of vertical shear in the circulation of the ring. The rings with low vertical shear have their warm core confined to the lower thermocline while the rings with high vertical shear have their warm core extending throughout the entire depth of the thermocline. The horizontal size of the anticyclonic features found in the DeSoto Canyon region is also highly variable, however, a 100 km horizontal scale is the most common.

The anticyclonic features identified in the hydrographic surveys were classified by the depth of the PV anomaly associated with them. Since the anticyclones found in the vicinity of the DeSoto Canyon are typically weak, the negative PV anomaly associated with them is dominated by the isopycnal layer thickness anomaly. Thus, the depth of the PV anomaly is closely related to the depth of the warm core of the anticyclones. For instance, the warm streamers are associated with the warm water core in the upper 300 meters, consequently, their PV anomaly is also confined to the upper 300 meters. In contrast, the low shear remnant rings have the warm water core confined

between 300 and 500 meters, consequently, their PV anomaly is also confined to those depths. According to this classification three types of warm-core eddies were found:

- *Shallow eddies*: the PV anomaly is localized to the upper thermocline.
- *Deep eddies*: the PV anomaly is localized to the lower thermocline.
- *Full eddies*: the PV anomaly is distributed throughout the entire depth of the thermocline.

The PV-based eddy feature model used in our previous experiments was calibrated to represent each anticyclonic eddy type. A detailed description of the feature model can be found in Section 4.2.2, here we only briefly outline its basic design. The model is formulated in isopycnal layers and consists of a stack of slab-like PV anomalies in each layer. The PV anomaly in each layer is defined by its radius, amplitude, and the width of the transition zone between the center of the anomaly and the ambient PV in the layer; the form of the transition is prescribed by an analytic function. Thus, the feature model has three free parameters per layer that can be adjusted.

The calibration procedure is the same that was used in our simulations of the Fast Eddy (Section 4.4.6.2). The basic idea behind the calibration is to find the free parameters of the feature model that provide the best fit (in the least squares sense) to the density structure described by the set of observed density profiles. In this particular case we selected three hydrographic surveys which captured a warm-core eddy representative for each eddy type identified above. The feature model was then calibrated to represent the warm-core eddies in those surveys. Since we want our feature model to be representative of each anticyclonic eddy type found in the DeSoto Canyon region, the three calibrations were scaled to produce 100 km diameter eddies, which is the most common eddy size for each eddy type.

5.2.2 Eastward Propagation of Anticyclones

5.2.2.1 Introduction

According to observations (Hamilton et al. 2000) anticyclones are often advected towards the mouth of the DeSoto Canyon by LC frontal cyclones which generally propagate westward, captured in the circulation of the LC. However, anticyclones were observed to interact with the canyon even with the LC in its southern position and no frontal cyclones present in the vicinity of the canyon. It is not clear in this case how anticyclones can propagate eastward and remain at the mouth of the canyon for the interaction to occur. The natural tendency for anticyclonic eddies with no background currents and no topographic interaction is to propagate west-southwest due to the β -effect. Thus, some mechanism must exist which is capable of overcoming the westward β -drift and transporting warm eddies eastward to the mouth of the canyon in the absence of LC and its frontal eddies.

We hypothesize that the interaction with the northern shelf break may be responsible for propagating anticyclonic eddies eastward towards the mouth of the canyon in the absence of the LC. It is well known that the interaction of a vortex with a free-slip horizontal boundary can be described by the so-called image effect. One of the most relevant examples of this effect is the interaction of an LCE with a western boundary represented by a vertical wall with a free-slip boundary condition. It was demonstrated that in this case the image effect leads to northward eddy propagation (Shi and Nof 1994). A similar image effect can control an eddy interaction with a sloping bottom. It was demonstrated both analytically and numerically that the interaction of a baroclinic point

vortex (a vortex associated with a PV anomaly described with a delta function) with a topographic slope is identical to an interaction with another point vortex (its image) obtained by reflecting the original vortex relative to the bottom (Pankratov 1994). For the configuration relevant to the DeSoto Canyon region, i.e., an anticyclonic vortex interacting with a northern zonal bottom slope, this effect should produce an eastward eddy motion. Thus, the mechanism transporting warm eddies eastward could be the “image effect” created by the eddy interaction with the northern shelf break.

5.2.2.2 Experiment Design

In order to verify this hypothesis we designed a series of numerical experiments simulating the interaction of somewhat idealized anticyclonic eddies, representative of warm-core eddies near the DeSoto Canyon (see Section 5.2.1), with an idealized representation of the northern topography. The σ -coordinate primitive equations model (Section 3.3) was configured for a rectangular domain with 4 km uniform horizontal resolution and 50 σ -levels in the vertical. The model domain was rotated $\sim 18^\circ$ counterclockwise from the zonal direction. A uniform (along the model domain) bottom slope was specified to represent the northern topography in the GOM west of the DeSoto Canyon (see Figure 5.1). The slope profile was derived from the ETOPO5 bathymetry data set by averaging the ocean depth along the shelf break around 88°W . Closed boundary conditions were specified with a 15 grid point damping layer along the western boundary. All three types of anticyclonic eddies were initialized south of the slope and allowed to evolve.

5.2.2.3 Results

The experiments showed that all three types of warm-core eddies identified in Section 5.2.1 can propagate *eastward* as the result of interactions with the northern shelf under two conditions. The first condition is the proximity of an eddy to the shelf break. The image effect overtakes the westward β -drift and produces an eastward eddy propagation only when an eddy is forced close to the shelf by some external forcing, a cyclonic eddy in this case (see below). The second condition is the orientation of the shelf itself. The tilt of the shelf break line relative to the zonal direction is crucial for maintaining the proximity of an eddy to the shelf after the initial external forcing is gone.

Figure 5.1 illustrates the first type of experiment, where an isolated anticyclonic eddy is initialized south of the topographic slope. The thick contours on the plot indicate the eddy’s shallow water PV anomaly in the thermocline. The PV is calculated using velocities vertically averaged throughout the main thermocline. The main thermocline is defined by the $\sigma = 27 \text{ kg/m}^3$ isopycnal surface. The figure shows several positions of the eddy during the course of the integration with a time interval of 20 days. (The color of PV contours indicate the time; red contours indicate earlier times while blue contours indicate later times). In this case the eddy is a “deep” anticyclonic eddy; the results of experiments with other types of eddies are nearly identical. The eddy first moves westward under the influence of the beta-drift. After reaching the shelf it proceeds to move south-west following the shelf break. Thus, the image effect in this case is not strong enough to overpower the westward beta-drift.

In contrast to the results of the first type of experiment, the direction of the anticyclone propagation becomes eastward if it is initially forced against the shelf by a background current. This is consistent with our interpretation of an eastward eddy propagation as a result of the image effect. Since the strength of the image effect is proportional to the proximity of the eddy to its image, i.e., to the boundary which in this case is the shelf break, the image effect becomes dominant when the eddy comes closer to the shelf. This result is illustrated in Figure 5.2 which shows the second type

of experiment. In this experiment a cyclone was initialized 150 km south-west of the anticyclone in the beginning of the integration. The PV structure and size of the cyclone were modeled after the structure of the LC frontal cyclones captured in the hydrographic surveys from the DeSoto Canyon Eddy Intrusion Study. The technique of PV feature modeling used to initialize the cyclone was the same technique that was used previously to construct the idealized anticyclones. The anticyclone in this case is a “deep” anticyclone; the experiments with other types of anticyclones are very similar. The cyclone-anticyclone pair self-advect towards the shelf where the circulation of the cyclone forces the anticyclone against the shelf break. After this initial forcing the anticyclone proceeds northeast along the shelf while the cyclone moves south-west.

The orientation of the shelf break, in particular its tilt relative to the zonal direction, appears to be critical for eastward propagation of the anticyclones. The same experiment as described above, but now with a purely zonally oriented shelf, shows that even after the initial forcing onto the shelf the anticyclones quickly move back to the deeper region where they proceed to move westward. When a northward topographic tilt is present, the beta-drift acts to push the anticyclones against the shelf, which prevents them from moving off to the deeper continental slope, thus keeping the image effect active and supporting the eastward propagation.

5.2.3 Circulation Within the Canyon

The numerical model configuration used for the experiments described in Section 5.2.2 was applied for simulations of direct interaction of anticyclones with the DeSoto Canyon. For these simulations the idealized bottom topography was replaced with realistic topography from the ETOPO5 database. The eastward eddy propagation mechanism was used to transport the anticyclonic eddies to the mouth of the DeSoto Canyon. To trigger the eastward propagation the anticyclones were forced initially against the shelf in the vicinity of 88°W by a cyclone, employing the same technique that was used in the idealized experiments.

Warm-core eddies at the mouth of the DeSoto Canyon were shown to generate cyclonic circulation in the canyon. An example of this circulation is shown in Figure 5.3. In this simulation a “deep” anticyclonic eddy was initialized; other types of anticyclones produce similar results. Color coded in the figure is the shallow water PV in the main thermocline as previously defined, and arrows indicate the velocities vertically averaged throughout the thermocline. As the anticyclone moves along the shelf towards the DeSoto Canyon, a stream of high PV water is advected into the canyon forming into a cyclone which fills the deep portion of the canyon (deeper than ~ 300 meters). By the time the anticyclone comes to the mouth of the canyon a counter-rotating circulation pattern develops. This pattern consists of a relatively large anticyclonic circulation at the mouth of the DeSoto Canyon and a counter-rotating cyclonic circulation at the head of the canyon. This circulation pattern is consistent with the mode 2 circulation in the DeSoto Canyon identified by Wang et al. (2003) in their statistical analysis of surface current observations. Thus, our numerical simulations identify a link between a conceptual model of eddy interaction with the DeSoto Canyon proposed by Hamilton et al. (2000) and a statistical circulation mode derived by Wang et al. (2003).

Our analysis of the numerical simulations allows us to identify the off-shelf PV advection process as the primary physical mechanism responsible for the generation of the cyclonic circulation. The process consists of high PV shelf water advection into deeper regions, i.e., the regions with lower ambient PV, by the circulation induced by the anticyclone. The PV anomaly produced as a result of this process spins up the cyclonic circulation. The same mechanism was identified in our

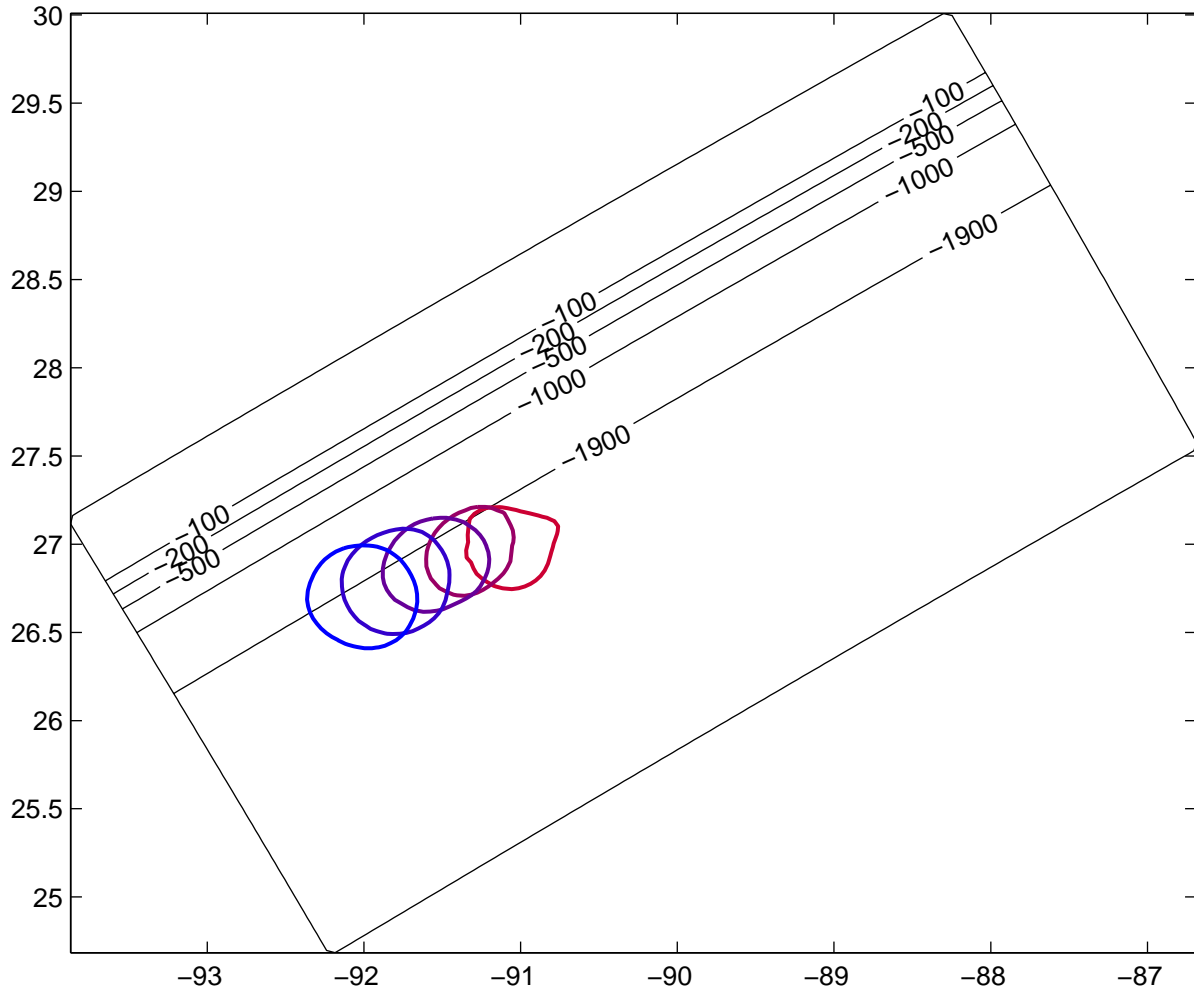


Figure 5.1. Interaction of "deep" anticyclonic eddy with the northern shelf west of DeSoto Canyon. Isolated deep (see Section 5.2.1) anticyclonic eddy is initialized south of the topographic slope shown with thin contours. The thick contours on the plot show the shallow water PV anomaly in the thermocline and indicate positions of the eddy at different times of integration. The PV is calculated using velocities vertically averaged throughout the main thermocline, where the main thermocline is defined by the 27 kg/m^3 isopycnal surface. The figure shows several positions of the eddy in the course of the integration with a time interval of 20 days; the color of PV contours indicate the time, red contours indicate earlier times while blue contours indicate later times.

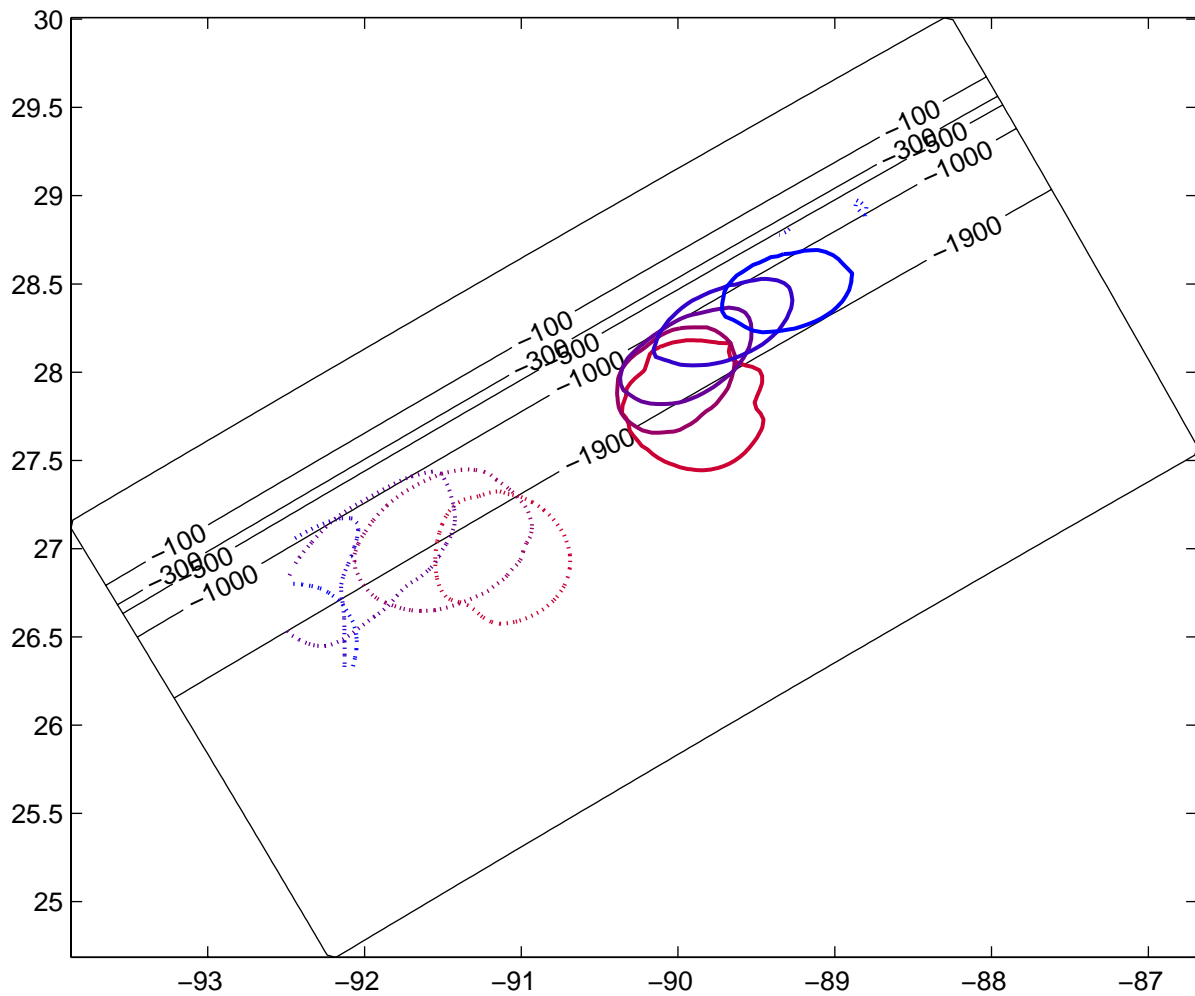


Figure 5.2. Same as in Figure 5.1 but forced with a cyclone. "Deep" anticyclonic eddy (solid contours) forced against the shelf by a cyclone (dotted contours) initially located to the south-west. The meaning of the contour lines is the same as in Figure 5.1.

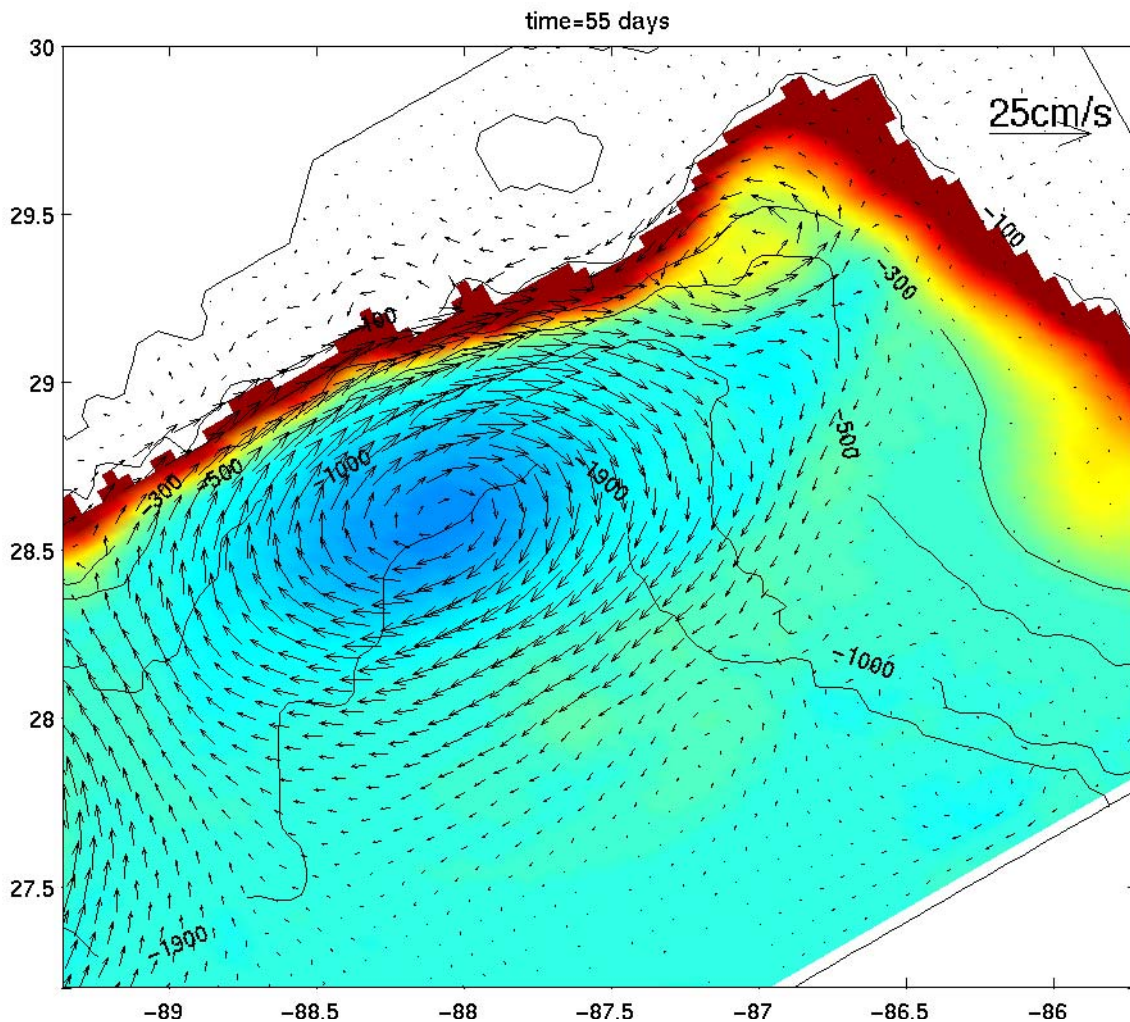


Figure 5.3. Realistic simulation of the "deep" anticyclonic eddy interacting with the DeSoto Canyon. Color coded in the figure is the shallow water PV in the main thermocline defined as previously, and arrows indicate the velocities vertically averaged throughout the thermocline.

previous experiments to be responsible for generation of cyclones during LCE interaction with the GOM coastal topography (Section 4.3.3).

A passive tracer analysis technique was developed to identify the mechanism of off-shelf advection in the numerical simulations. In the beginning of each simulation a passive tracer was distributed throughout the model domain. The initial tracer concentration is proportional to the total depth at each particular point and uniform throughout the water column. The tracer is then tracked along isopycnal surfaces. Thus, the low tracer concentrations represent the water from shallower regions and high concentrations represent the water from deeper regions. Figure 5.4 shows the tracer distribution after 55 days of the simulation along the 15°C isotherm. The color represents the tracer concentration and the arrows indicate the velocity field vertically averaged in the thermocline. By the time shown the cyclonic circulation has already developed at the head of the DeSoto Canyon. It can be clearly seen that the core of the cyclonic circulation is composed of water with lower tracer concentration, which means that it was advected from shallower regions.

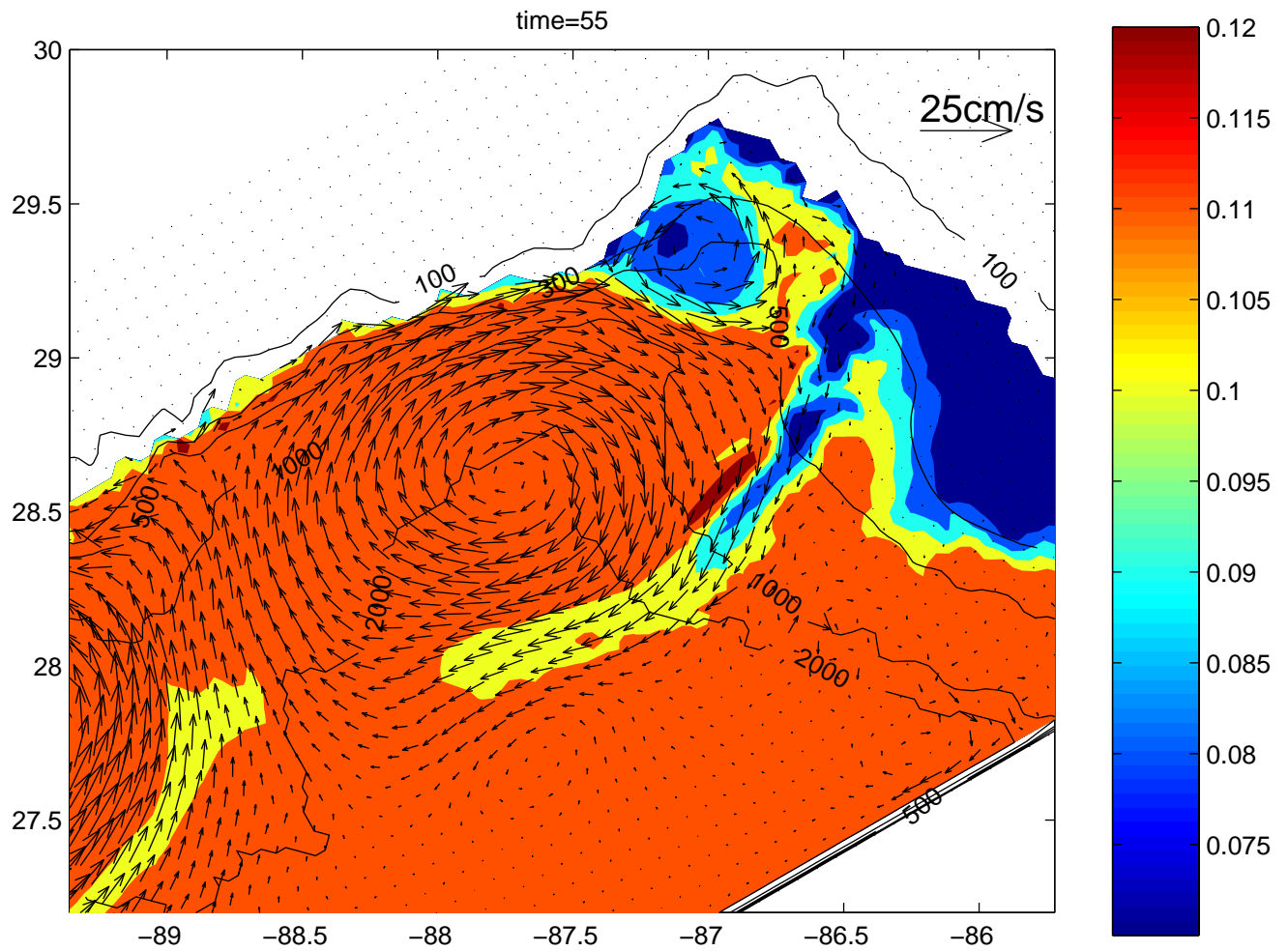


Figure 5.4. Same as in Figure 5.3 but color code indicates passive tracer concentration.

5.3 Remote Generation of an Eastward Along-Shelf Current

According to this conceptual model a remote LCE interacting with the coastal topography west of the Mississippi River delta generates a warm eastward jet along the shelf break that reaches the DeSoto canyon region producing eastward currents. Numerical simulations conducted using a set of initial conditions consistent with the scenario suggested by the conceptual model failed to reproduce the observed eastward jet. This negative result suggests that the physical processes, which were hypothesized to be responsible for the observed eastward jet, are not dynamically feasible. An alternative conceptual model, consistent with the observed events, was formulated and tested in numerical simulations. The numerical simulations constructed on the basis of the new conceptual model showed good agreement with observations.

5.3.1 Remote Generation of an Eastward Along-Shelf Current by an LCE

The conceptual model of the remote generation of an eastward along-shelf current by an LCE is shown schematically in Figure 5.5 (from Hamilton et al. (2000)). The strong eastward flow within the LCE is impinging onto the topographic slope setting up a negative along slope pressure gradient. The pressure gradient is trapped over the steep slope thus driving an eastward jet.

The observational basis for this conceptual model is shown in Figure 5.6 (from Hamilton et al. (2000)). In the figure Eldorado eddy can be identified by its SST signature west of Mississippi Canyon (its eastern boundary is labeled in the figure as “Loop Current Ring Boundary”). Eldorado eddy detached from the LC in October 1997 and moved westward along approximately 26°N . By early December 1997 the eddy can be identified around 91°W the eastern edge of the eddy is located around 90°W just west of the Mississippi canyon. A streamer of cold shelf water can be seen wrapped around the eastern side of the eddy indicating its interaction with the northern shelf. At the same time an eastward jet along the shelf break west of DeSoto canyon was measured by the array of current meters deployed as a part of DeSoto Canyon Eddy Intrusion Study. This observed sequence of events lead to a hypothesis that the eastward along-shelf jet west of DeSoto canyon was produced by the LCE interaction with the northern shelf west of Mississippi River delta.

The sequence of events suggested by the above conceptual model was simulated using the high resolution PE model. The experiment design and the PE model configuration used for this simulation were adopted, with very minor modifications, from our previous experiments simulating a LCE interacting with realistic northern GOM topography (Section 4.4.5). The initial location and size of the LCE were specified on the basis of sea-surface height data observed on October 1, 1997, approximately 1.5 months prior to the jet generation event (Figure 5.7). The initial PV structure of the LCE was that of a “generic” LCE derived in Section 4.4.3.1.

The size and the location of Eldorado Eddy determined from the SSH data have some degree of uncertainty associated with them. Moreover, the exact path of the eddy between October 1 and the moment when it interacted with the northern shelf is unknown. It is quite possible that the eddy drifted away from the nearly westward trajectory predicted by the β -drift alone due to interactions with other eddies. Also, the structure of the eddy can differ from the “generic” structure derived by averaging the structure of previously observed LCE’s. Because of these uncertainties, about 10 different simulations were performed with the initial eddy position, size, and PV structure varying within 20% intervals.

A typical result of these simulations is shown in Figure 5.8. Color coded in the figure is the layer PV field calculated using the thermocline thickness and vertically averaged velocities (shown with arrows). Variations in the initial conditions did not produce any qualitative changes, and the

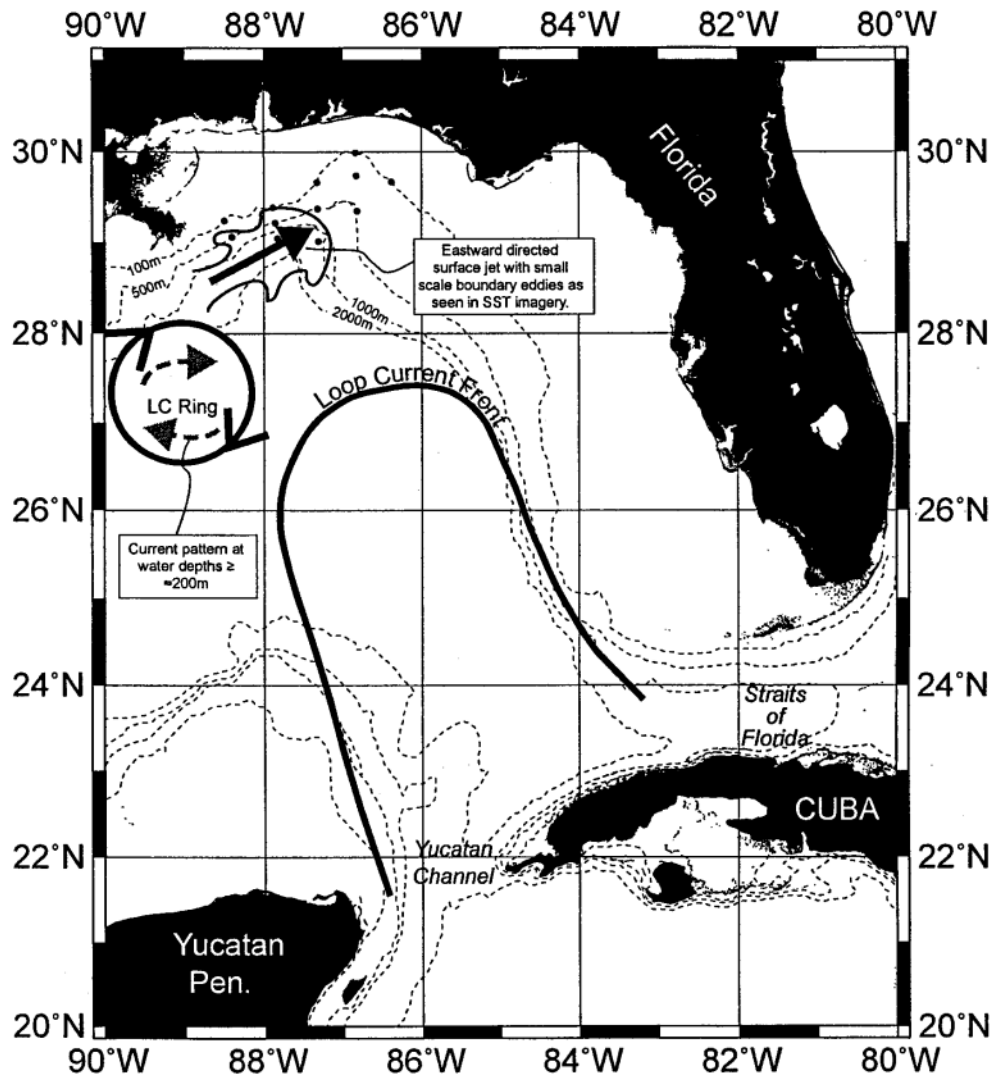


Figure 5.5. Schematic diagram of the eastward along-shelf jet generated by a remote LCE interaction with the shelf; from Hamilton et al. (2000).

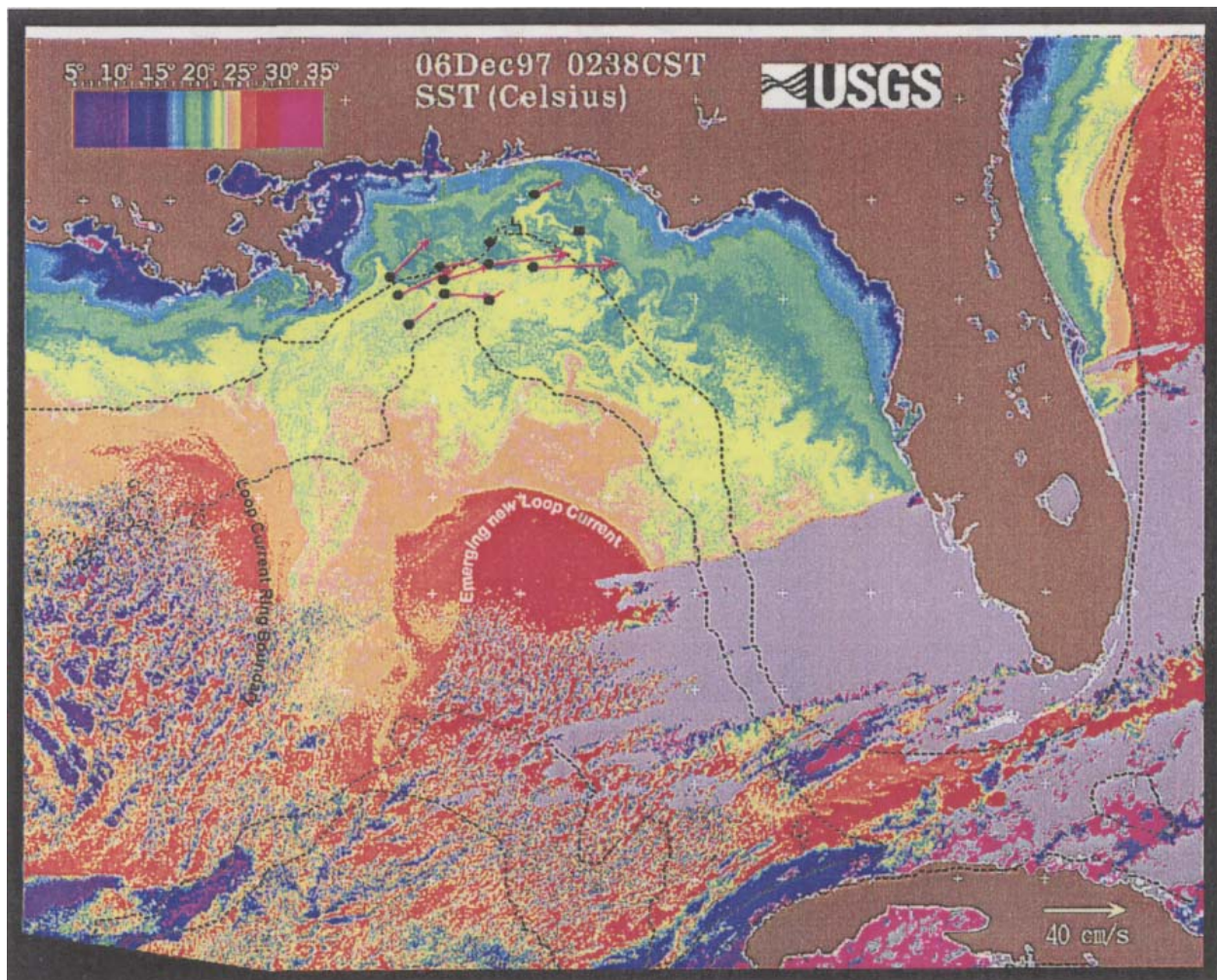


Figure 5.6. SST image for December 6, 1997. Measured near surface currents have been overlaid on the image. The eastward along-shelf jet can be clearly seen in the current measurement field. A warm-core ring appears to be interacting with the northern shelf west of Mississippi River.

simulation shown in the figure is representative of all the simulations. LCE interaction with the northern shelf fails to produce an eastward along-shelf jet. Instead a cyclone is generated due to the process of off-shelf PV advection, which is consistent with our previous results. This negative result motivated us to reevaluate the conceptual model and consider some alternative models also consistent with observations.

5.3.2 Remote Generation of an Eastward Along-Shelf Current by a Cyclone: Conceptual Model

An alternative mechanism for a remote generation of an eastward along-shelf current west of DeSoto Canyon was hypothesized. The mechanism consists of a “shielded” cyclonic eddy interacting with the northern shelf producing an eastward along-shelf jet east of it. The term “shielded” cyclonic eddy refers to a cyclone which has a negative PV anomaly wrapped around the positive PV core. The negative PV anomaly reduces the lateral extent of the eddy circulation, thus “shielding” it from interacting with surrounding features. Such PV anomaly can develop around a cyclone due to warm water being trapped in its circulation or due to lateral friction.

The alternative conceptual model is illustrated by a diagram shown in Figure 5.9. The low PV band initially wrapped around the cyclone is being stripped off in the process of interaction with the shelf break creating a negative PV anomaly trapped over the steep slope. The negative PV anomaly self-advects eastward along the shelf break due to the “image” effect (Pankratov 1994) extending east. The negative PV anomaly is associated with an eastward along-shelf current extending all the way to DeSoto canyon. The idea of a negative PV band “stripping” off an eddy during its interaction with topography comes from the work of Shi and Nof (1993). In their experiments an anticyclonic eddy with a negative PV core and “shielded” by a positive PV anomaly wrapped around it interacted with the western shelf break. This interaction led to stripping of the outer PV anomaly, which produced a “jet” effect propelling the eddy northward.

This alternative conceptual model is also consistent with observations. A cyclonic eddy can be identified in the SSH field on October 1, 1997 around 28°N , 87.5°W . A natural tendency for a cyclone on the β -plane is to drift northwest (see the simulations below) pushing it against the northern shelf. It is reasonable to assume that this cyclone has a band of warm water, i.e. negative PV anomaly, wrapped around it due to its interaction with the Loop Current or Eldorado Eddy. The interaction of this cyclone with the northern shelf would produce an eastward current to the east of it and an off-shelf flux of cold water to the west. This cold water would be captured into the circulation of Eldorado eddy creating the cold tongue seen on the SST image (Figure 5.6).

5.3.3 Remote Generation of an Eastward Along-Shelf Current by a Cyclone: Numerical Simulations

The conceptual model formulated in Section 5.3.2 was tested in a realistic numerical simulation. The PE model configured similar to the previous experiment (Section 5.3.1) was initialized with an isolated “shielded” cyclone. The cyclone was initialized using the same PV-based initialization technique used in our experiments simulating small cyclones over the northern continental slope (Section 6.1.1). The parameters of the PV feature model for the cyclone were adjusted to produce a cyclone approximately 100 km in diameter and 30 cm/s maximum swirl speed, which is consistent with the SSH anomaly observed on October 1 (see Figure 5.7). The negative PV anomaly along the perimeter of the cyclone was created using the same technique that was applied for constructing a Loop Current stream structure with narrow cyclonic side (see Section 5.4.1).

Gulf of Mexico Sea Surface Height

TOPEX/ERS-2 sea surface height anomaly
plus 10-year climatological model mean

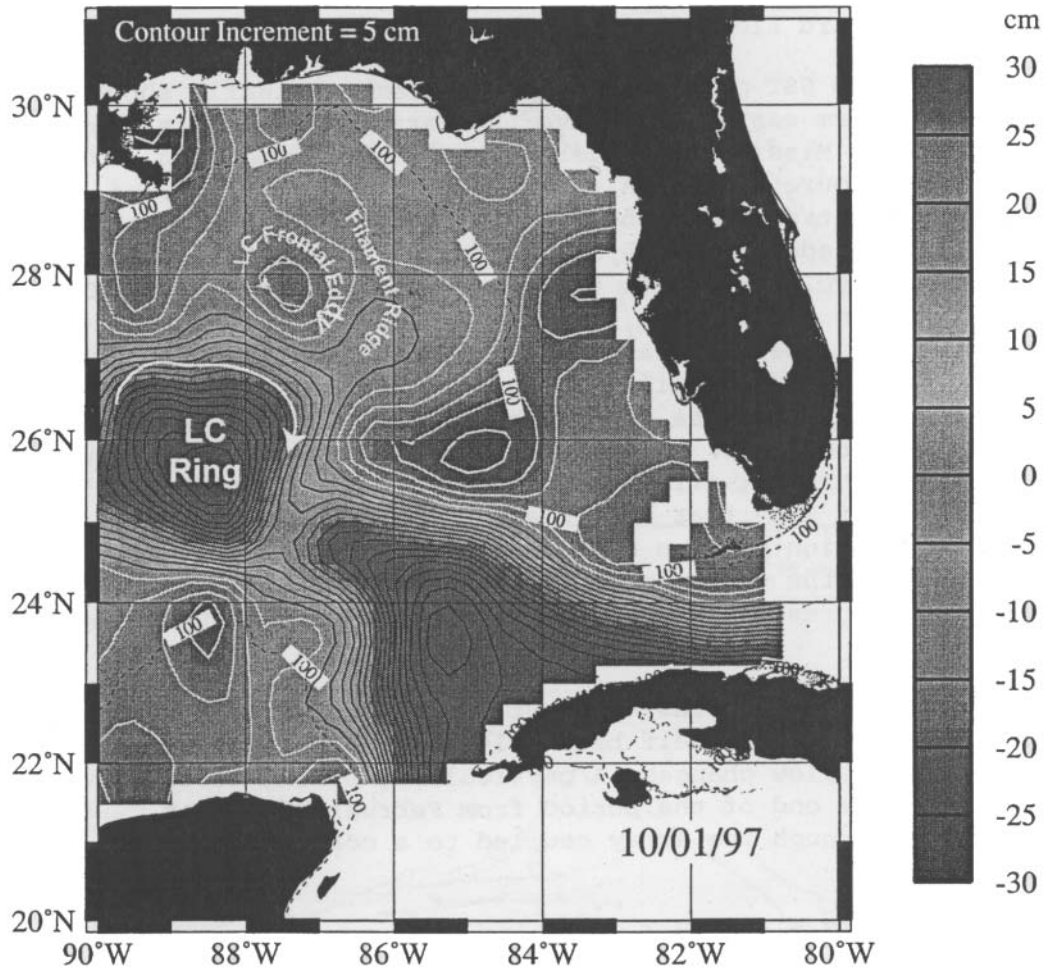


Figure 5.7. SSH for October 1, 1997, derived from TOPEX/ERS-2 plus model mean. Dark contours are for SSHs that are greater than zero; white contours are for SSHs less than zero; from Hamilton et al. (2000).

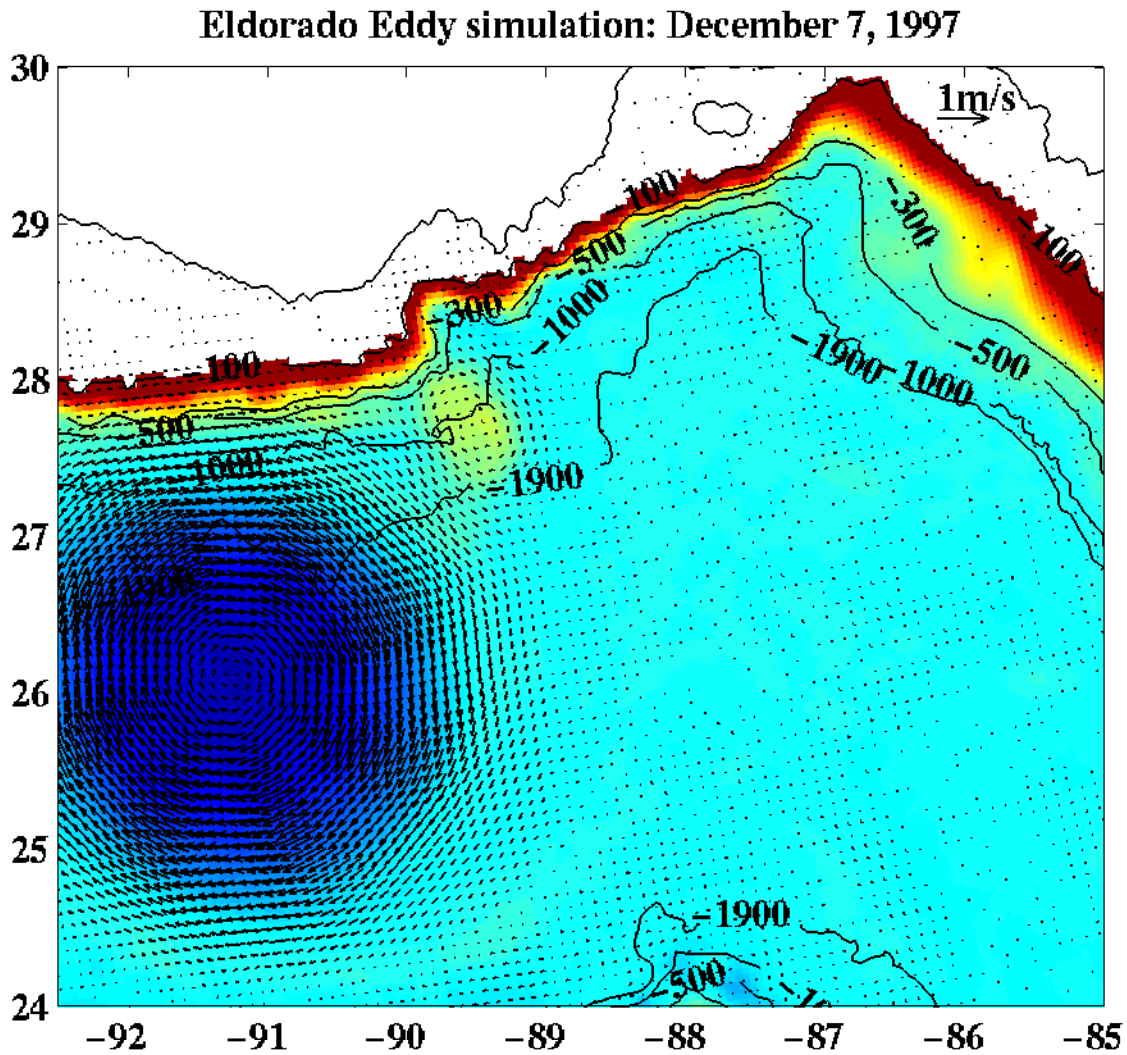


Figure 5.8. Simulation of Eldorado Eddy interacting with the northern shelf. Consistent with the previous experiments; the LCE produces a cyclone and does not generate an eastward along-shelf jet. Vectors indicate velocities vertically averaged over the thermocline depth; color coded is PV field in the thermocline.

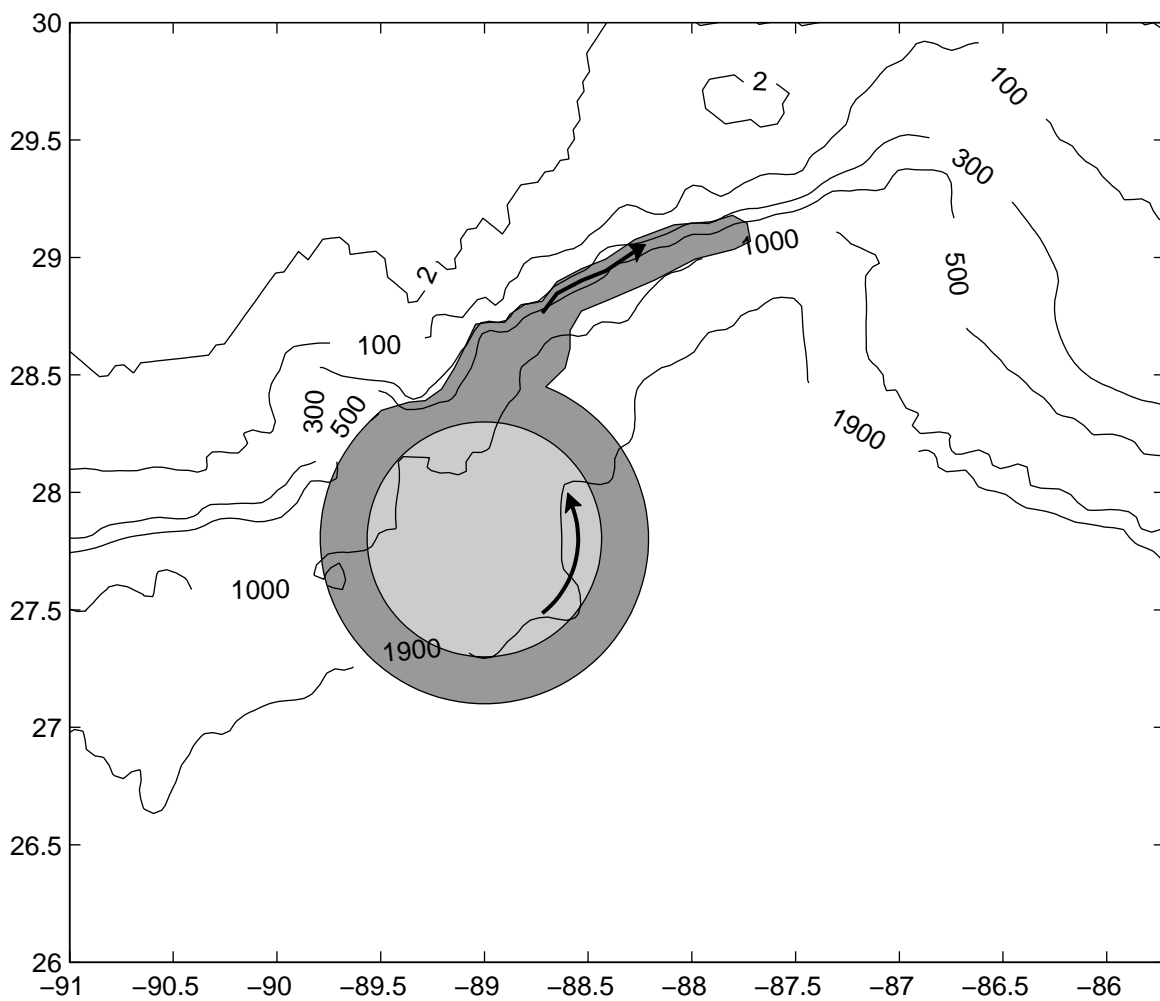


Figure 5.9. Schematic illustrating the conceptual model of an eastward along-shelf current by a cyclone. Darker shading indicates the negative PV anomaly wrapped around the cyclone.

The stability of the constructed “shielded” cyclone was first tested by allowing the cyclone to evolve freely without any interaction with topography. The same high resolution PE model configured with realistic northeast topography was used but the cyclone was initialized far away from the coastal topography around 26°N , 86°W . In this experiment the cyclone remained stable and retained its initial structure for the entire duration of the simulation (3 month), indicating that the prescribed cyclonic structure is dynamically self-consistent.

For the final experiment the cyclone was initialized at the position where it was observed on October 1 and allowed to evolve freely. The result of the experiment after 20 days of simulation is shown in Figure 5.10. Color coded in the figure is the PV in the thermocline calculated as previously. The band of low PV water wrapped around the cyclone can be clearly seen. The low PV water strips off the cyclone as it impinges onto the shelf and propagates eastward along the shelf just as suggested by the conceptual model. The velocity field produced in the simulation in the vicinity of DeSoto Canyon is shown in Figure 5.11. The velocity is shown at two depth levels: 15 meters (upper panel) and 300 meters (lower panel) after 1 month of the simulation (early November 1997). This velocity can be compared with the velocity observed during the event on November 11 (Figure 5.12). The observed velocity was derived through geostrophic calculation from the high resolution hydrographic survey conducted during the event. The calculated geostrophic velocities were reported to agree well with moored current meter measurements (Hamilton et al. 2000). The comparison indicates that all of the key features of the observed circulation are reproduced by the simulation. The eastward along-shelf current produced by the negative PV anomaly stripped off the cyclone reaches the canyon and turns south following the topography as observed. The current intensification and direction change observed at the western side of the moored array are also reproduced in the simulation, where they are caused by the circulation of the cyclone itself.

5.4 Interaction with Loop Current Frontal Eddies

This part of the investigation was concerned with conceptual models related to circulation induced in DeSoto Canyon by Loop Current Frontal Eddies (LCFE’s). LCFE’s are small (20-100 km in diameter) cyclones that are frequently observed along the cyclonic side of the LC (Vukovich and Maul 1985) and represent the most common source of the observed variability in the DeSoto Canyon region (Hamilton et al. 2000). They typically form along the western part of the LC and amplify in an unstable manner as they propagate downstream along the LC. Several previous studies (Maul 1977; Hurlburt 1986) suggested that LCFE’s are generated as the result of an instability process in the LC. The observational data presented in the Eddy Intrusion Study also support this hypothesis. One of the typical circulation patterns induced by LCFE’s in the DeSoto Canyon region is depicted by a conceptual model from the Eddy Intrusion Study report (Figure 5.13). According to this model, the cyclonic circulation of LCFE’s entrains warm LC water around their cold cores. As LCFE’s move to the east around the LC they produce a warm streamer that extends into the DeSoto Canyon region. This generates an eastward flow along the shelf break in the upper 100 m. Below that depth, the cyclonic circulation in the LCFE causes strong westward flow. The numerical simulations described in this section were designed to investigate the dynamical mechanisms leading to this circulation pattern.

The unstable nature of the LCFE’s makes them difficult to simulate in numerical models. While isolated eddies, both cyclones and anticyclones, have relatively well defined structures and, therefore, can be implanted into initial fields using feature models, LCFE’s do not have such a structure. Instead, LCFE’s are an inseparable part of the instability process of the LC and, therefore, the

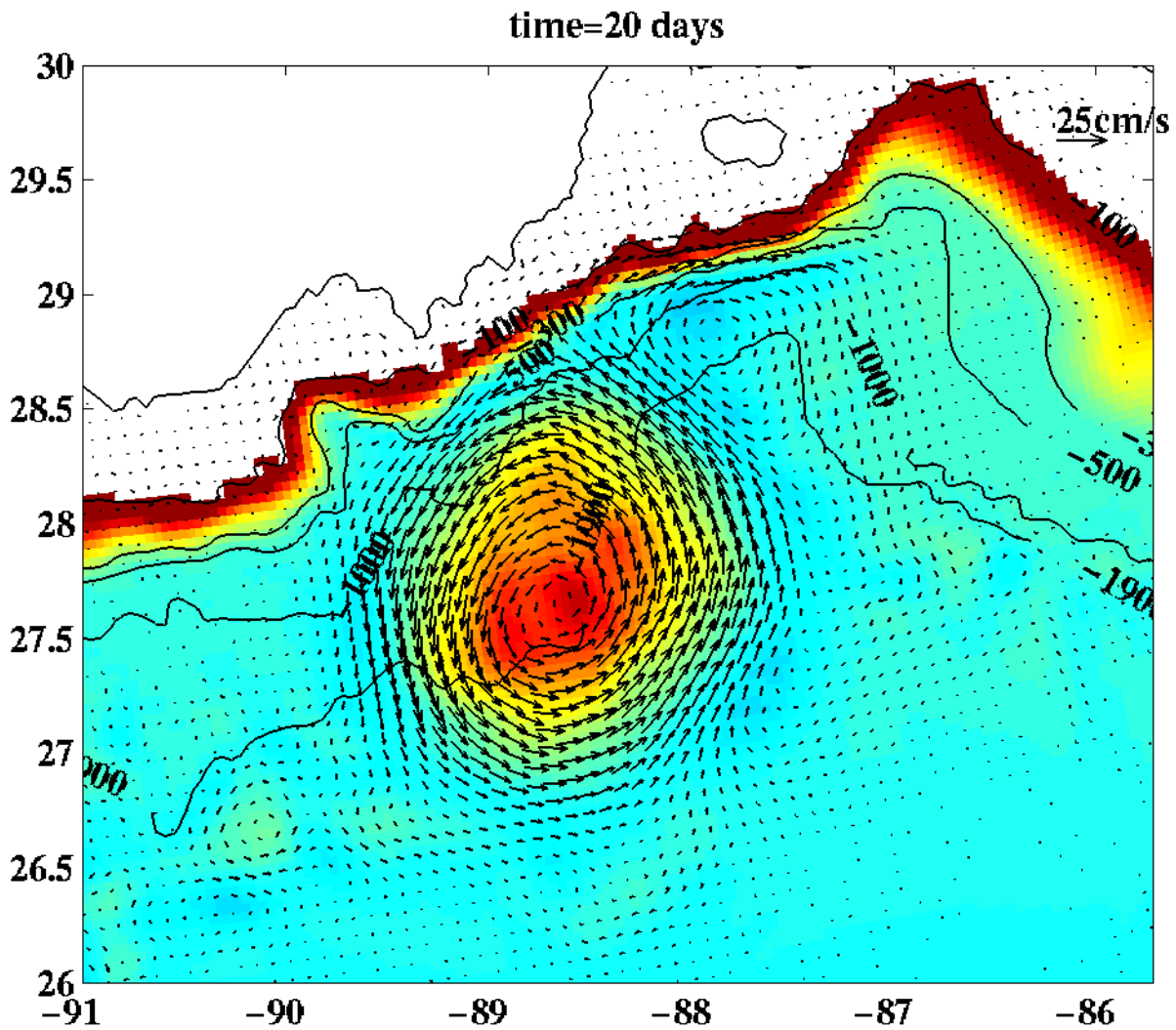


Figure 5.10. Simulation of a "shielded" cyclone interacting with the northern shelf west of DeSoto Canyon. Vectors indicate velocities vertically averaged over the thermocline depth; color coded is PV field in the thermocline. Simulation produces an eastward along-shelf jet extending all the way to DeSoto Canyon.

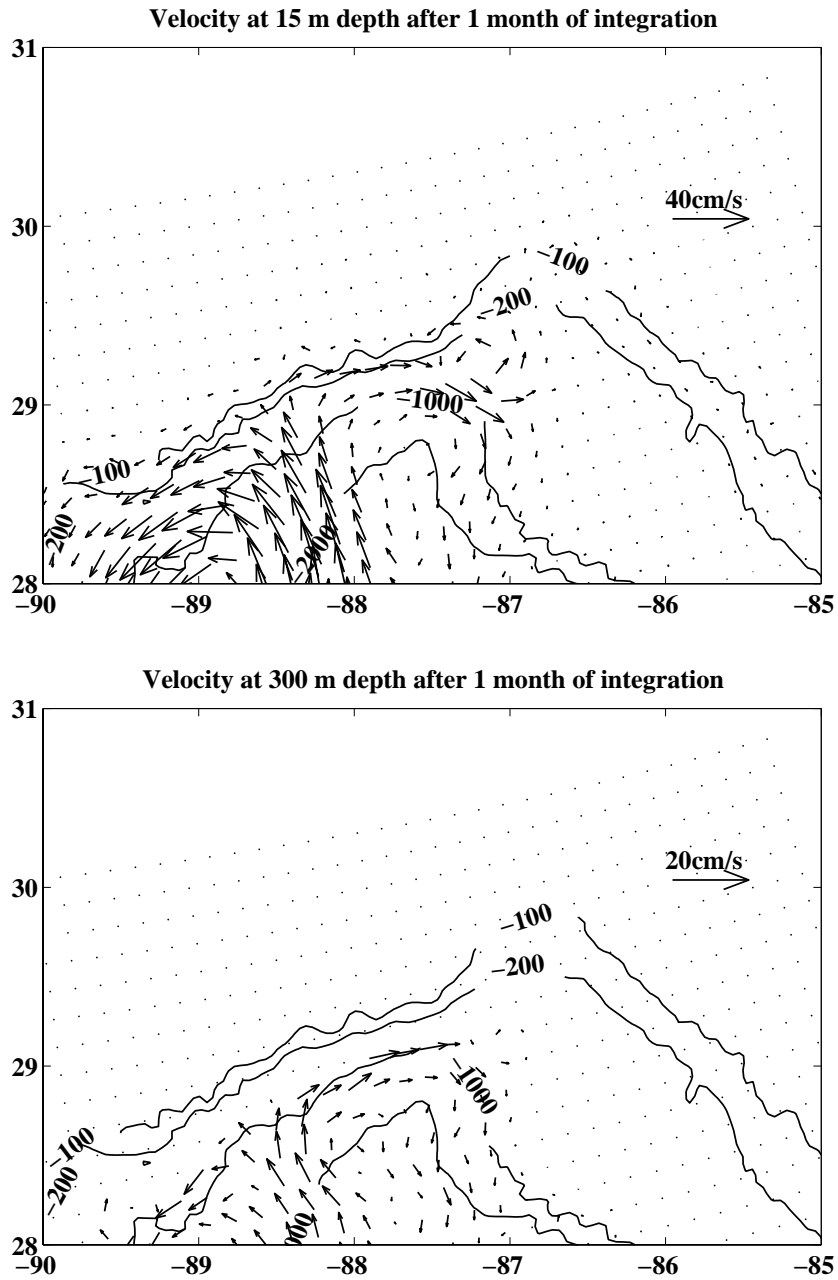


Figure 5.11. Simulated velocity field at 15- (upper panel) and 300- (lower panel) meter depth.

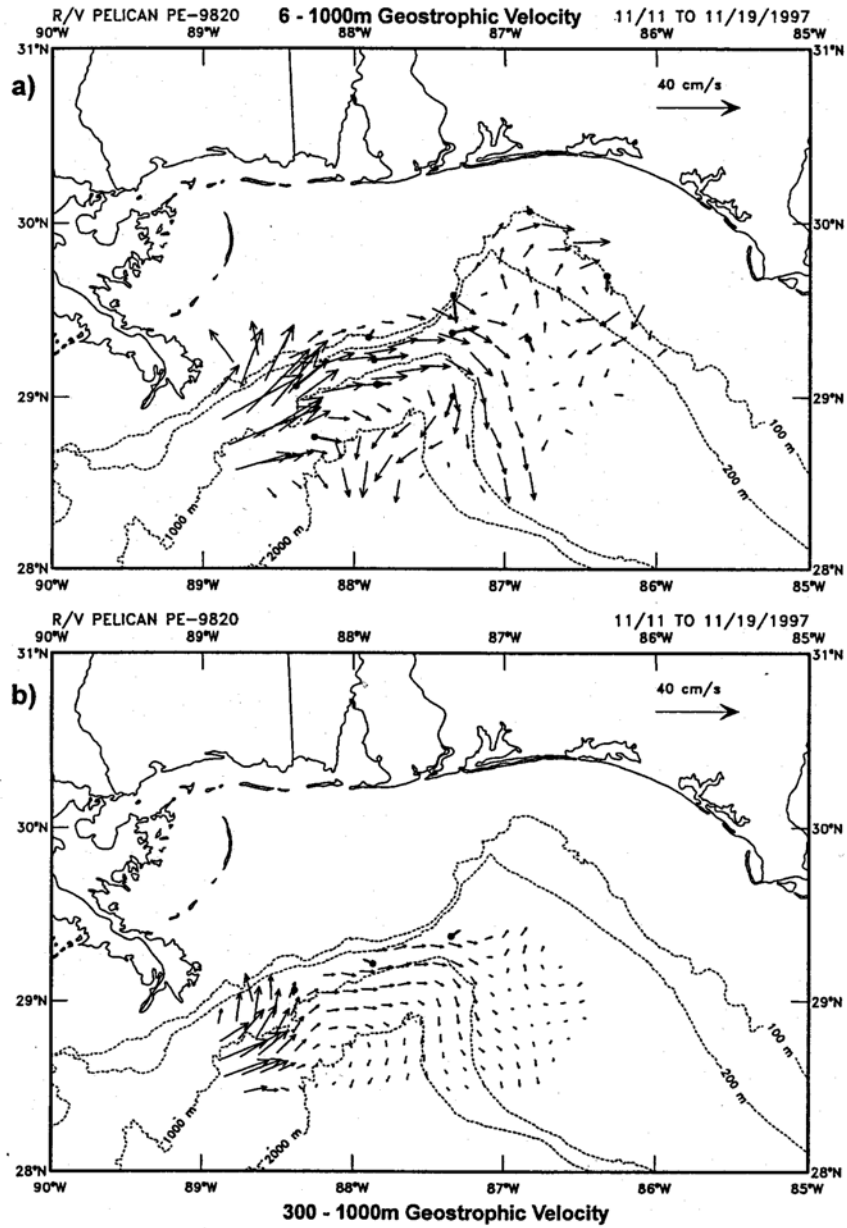


Figure 5.12. Velocities at 6- and 300-meter depth observed during the “eastward jet” event in the vicinity of DeSoto Canyon.

entire instability process has to be recreated in a numerical model in order to properly simulate LCFE's. Furthermore, the properties of this instability process have to be well understood if we are to be able to control it. Such control is necessary for producing LCFE's at a specified location and with specified characteristics.

Thus, numerical investigation of LCFE interactions with the DeSoto Canyon started with an investigation of the LCFE formation mechanism. First, through a series of zonal channel experiments conducted using our multi-layer Intermediate Equations (IE) model, we identified the stream structure which leads to the formation of frontal cyclones with spatial and temporal scales consistent with observations of LCFE's. The results of the zonal channel experiments were then used to introduce an LC with realistic stability properties into a regional, high resolution Primitive Equations (PE) model with realistic topography, and the formation of LCFE's was simulated within this realistic setting. Finally, the interactions of LCFE's with the DeSoto Canyon topography were simulated and compared against observations. The simulation allowed us to investigate, in some detail, the effect LCFE's have on the water mass exchanges between the DeSoto Canyon and surrounding regions.

5.4.1 Stability Properties of the Loop Current

As a part of our investigation of the LCFE formation mechanism we studied numerically the stability properties of the Loop Current in a series of idealized experiments. The principal objective of these experiments was to identify a LC stream structure that can lead to formation of LCFE-like features as a result of an evolution of a small initial disturbance over distances shorter than the distance between the northern tip of the Yucatan shelf and the maximum northward penetration of the LC (~ 400 km). This objective is based upon the assumption that LCFE's are formed as a result of an instability process on the cyclonic side of the LC triggered by disturbances originating from LC interactions with the Yucatan Peninsula topography. For LCFE's to reach the size of up to 100 km near the DeSoto Canyon, as it was observed, the stability properties of the LC have to be such as to allow an initial disturbance of 10-20 km in diameter, formed at the northern tip of the Yucatan, to grow 5-10 times as it propagates downstream.

The experiments were conducted using our IE model configured with 10 isopycnal layers and 3 km horizontal resolution. In these experiments the LC is represented as a zonal jet in a channel with open inflow/outflow boundary conditions. A small perturbation is initially specified close to the inflow boundary. In a typical experiment the initial perturbation generates a packet of meanders consisting of a superposition of several unstable modes that propagate downstream and amplify due to the instability process. As growing meanders reach the saturation stage, cyclonic features resembling those of the observed LCFE's, develop in the meander troughs. With this approach, the wavelength of the most unstable mode, its growth rate and (most importantly) the along-stream distance required for the initial disturbance to reach the saturation stage, i.e. form the cyclonic features resembling the LCFE's, can be determined from a single experiment. The LC stream structure in these experiments was specified by introducing small variations around the baseline structure derived from observed cross-sections of the LC. The variations were based on several hypotheses about the natural variability of the LC structure.

5.4.1.1 Experiment Design

The stability properties of the LC were analyzed using a series of numerical experiments with an unstable zonal jet. The experiment design was similar to the design that was used by Sutyrin

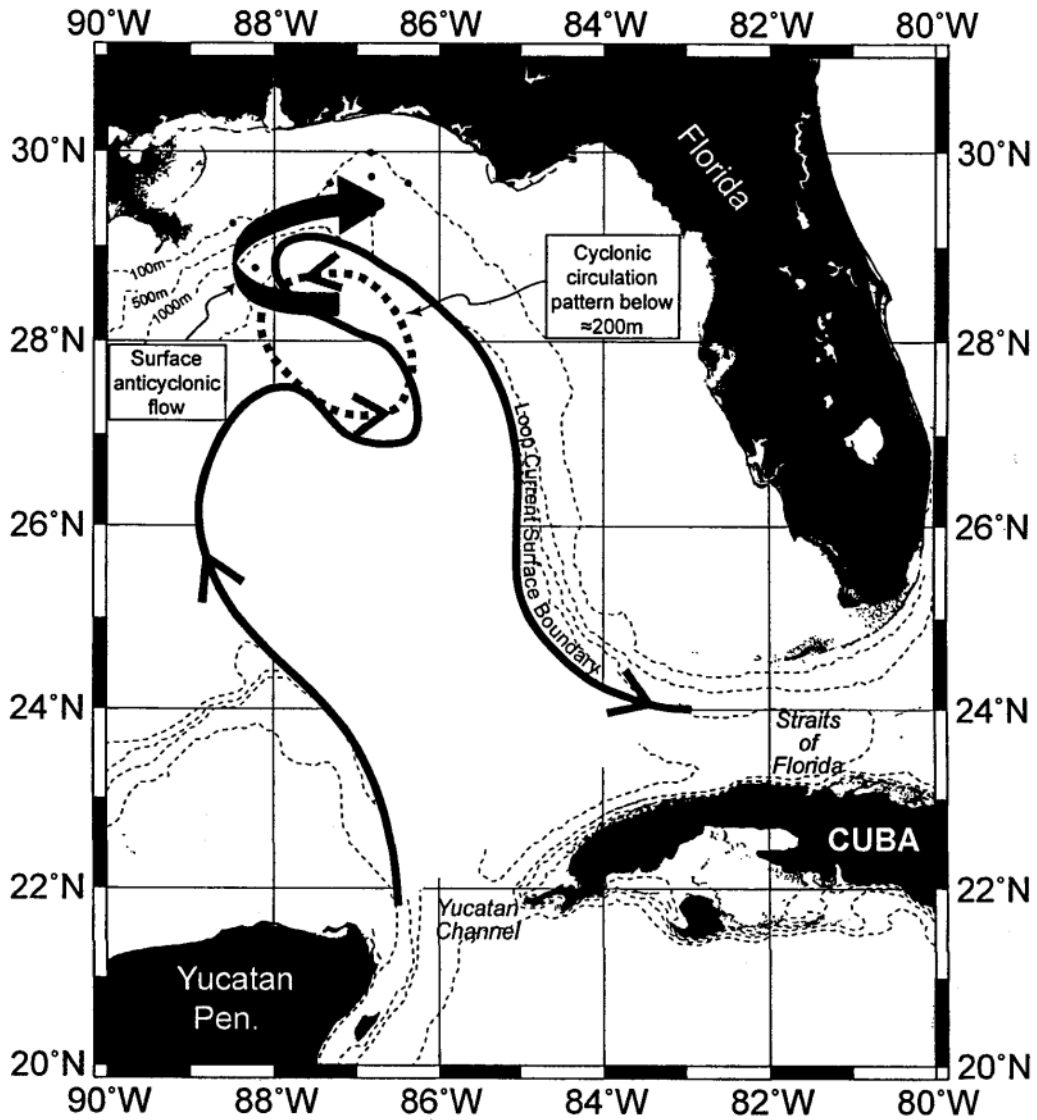


Figure 5.13. Conceptual model of a LCFE flow interaction with the slope in the DeSoto Canyon region; from Hamilton et al. (2000).

et al. (2001) to study the stability properties of a Gulf Stream-type jet. In this type of numerical experiment an unstable, initially straight jet is introduced into a zonal channel. A small perturbation of the jet trajectory is initially specified near the upstream side of the channel. In a typical experiment the initial perturbation triggers a packet of meanders that propagate downstream and amplify due to the instability process. The meander packet evolution in time can be described in four stages. During the first stage the initial disturbance restructures itself into a packet consisting of a superposition of several unstable modes. During the next stage the unstable modes start growing exponentially. This exponential growth is typically well described by the linear stability theory and, therefore, this stage is called the linear stage. As unstable modes continue to amplify the linear theory becomes no longer applicable; accordingly, this stage of meander growth is called the nonlinear stage. During the nonlinear stage the meander growth rate gradually decreases and finally stops as the packet evolution enters the so-called saturation stage. In our experiments the saturation stage is characterized with a formation of cyclonic features resembling observed LCFE's.

This experiment design allows us to efficiently explore the stream stability properties, since for each specified stream structure a single experiment allows us to determine the wavelength of the most unstable mode, its growth rate and the along-stream distance required for the initial disturbance to reach its saturation stage. A typical experiment is illustrated in Figure 5.14. The upper panel shows the initial conditions that consist of a straight zonal jet and an initial disturbance near the inflow boundary. The second panel shows the second stage of the experiment (15 days after initialization) when the initial perturbation has just restructured itself into a packet consisting of a superposition of several unstable modes. The lower panel shows the saturation stage during which the meander growth stops and cyclonic features resembling the LCFE's develop.

Instead of the 3-dimensional PE model used by Sutyrin et al. (2001) we conducted the experiments using our IE model (see Section 4.2). The IE model was selected for these experiments since it allows for a more transparent dynamical analysis due to its simpler physical formulation; it also allowed us to conduct a large number of experiments (for exploring parameter space) due to its computational efficiency. Both the f -plane and the β -plane approximations were used in the model formulation. For these experiments the IE model was configured with 10 isopycnal layers and 3 km horizontal resolution. The model domain was a zonal channel with open inflow/outflow boundary conditions along zonal boundaries and closed boundary conditions along meridional boundaries. A sponge layer 400 km wide, which is the typical spatial scale of simulated meanders, was applied at the outflow boundary to allow the meanders to leave the domain. The bottom topography was configured as a linear slope in the cross-stream direction designed to represent the continental slope in the eastern GOM. The presence of the bottom slope is crucial for blocking bottom-intensified eddies thus eliminating the baroclinic instability associated with the PV gradient inversion in the lower layer (Sutyrin et al. 2001).

A wide variety of plausible LC stream structures were explored in these experiments by introducing small variations around the baseline structure derived from observed cross-sections of the LC. Currently available observations of the LC stream structure downstream of Yucatan are limited to a number of instantaneous ADCP and hydrographic cross-sections through the LC. Since the LC constantly undergoes the process of meandering and frontal cyclone formation it is nearly impossible to derive a representative unperturbed structure of the stream from available snapshot-like observations. In order to construct an unperturbed stream structure representative of the LC we use the available observations to derive a baseline stream structure, which incorporates only the most robust observed characteristics of the stream. The robust characteristics of the stream include the stream width and the spatially averaged stratification on the cold and on the warm sides of the stream away from the transition zone. The term robust does not imply that the above

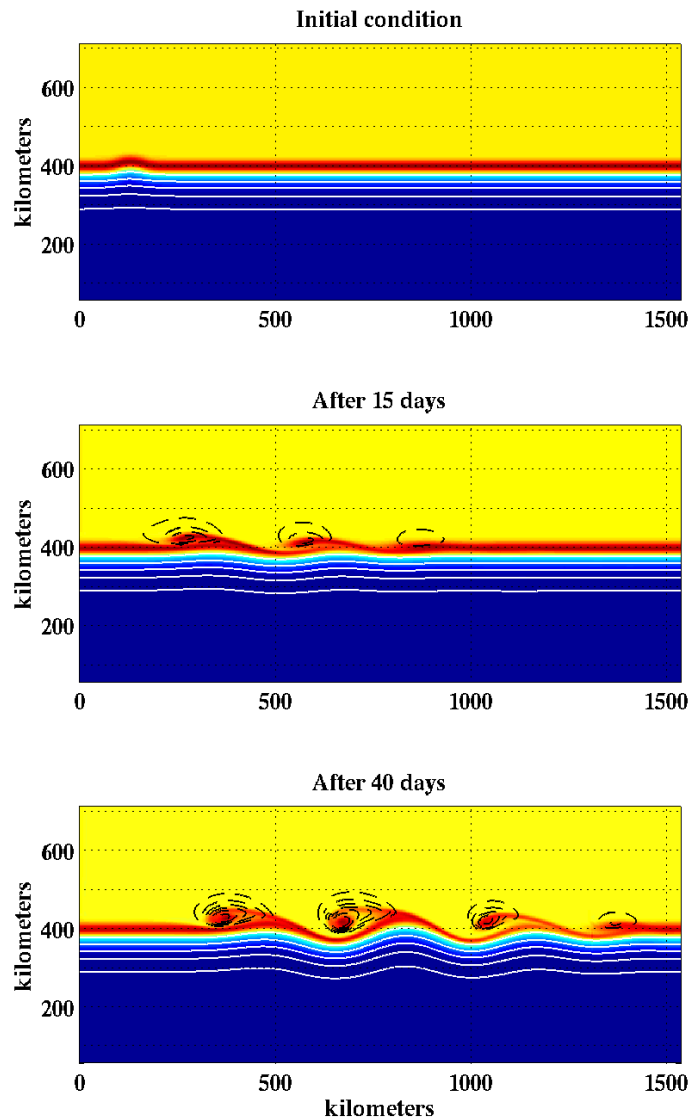


Figure 5.14. Example of a zonal channel stability experiment leading to the formation of frontal cyclones resembling observed LCFE's.

mentioned characteristics remain constant. Instead, it means that these characteristics experience the least variability between different observed cross-sections and vertical density profiles. The baseline stream-structure represents only the bulk stream characteristics; the finer details of the stream structure cannot be derived from the limited number of instantaneous cross-sections and have to be reconstructed on the basis of hypotheses about the natural variability of the LC and its observed stability properties. On the basis of the observed behavior of the LC we selected several stream characteristics that can vary in the process of the LC evolution and affect its stability properties. Small variations of the selected stream characteristics were then introduced into the baseline stream structure and the stability properties of the resulting stream were then explored.

The baseline LC structure was constructed using the PV-based technique of Logutov et al. (2001). Logutov et al. demonstrated that the Gulf Stream structure downstream of Cape Hatteras can be reasonably well reproduced by assuming a monotonic PV variation in cross-stream direction. On the basis of this assumption they constructed a 5-layer PV model of the Gulf Stream

structure, which can be used to calculate the stream density and velocity structures. The PV-based technique of Logutov et al. was modified to construct the baseline stream structure of the LC. In this case we used a 10-layer PV model to increase the vertical resolution. The PV in each layer is prescribed as

$$q_i = Q_i + A_i \times \tanh(W_i y),$$

where y is the cross-stream distance, index i refers to the layer number, and Q , A , W are constant parameters determining the amplitude and the width of PV front in each layer. The values of the free parameters are determined from the observed stream width and the spatially averaged stratification on the cold and on the warm sides of the stream away from the transition zone. Figure 5.15 shows the resulting baseline stream structure and compares it to one of the observed instantaneous LC structures. The upper panel in the figure shows the hydrographic cross-section of the LC from (Vukovich and Maul 1985) taken at approximately 26°N. The middle panel shows the positions of layer interfaces and corresponding along-stream velocity in the constructed baseline section. The lower panel shows the PV structure used to construct this section.

The LC stream structures used in the stability experiments were obtained by introducing small variations based upon several hypotheses about the natural variability of the LC to the baseline structure. One of the observed patterns of the LC variability is its interaction with the eastern shelf of the Yucatan Peninsula prior to its entering the deep eastern GOM. As the LC flows along the shelf-break its cyclonic side becomes narrower, presumably due to lateral friction with the shelf-break. The evidence of that can be found in Sheinbaum et al. (2002) if one compares their average LC cross-section derived from long-term LC mooring array observations in the Yucatan Channel to the baseline cross-section in Figure 5.15. It is reasonable to assume that the elevated cyclonic vorticity associated with the narrow cyclonic side is carried downstream north of the Yucatan contributing to the LC stability properties in the deep GOM. In order to incorporate this elevated cyclonic vorticity into the baseline section, the cyclonic side of the baseline velocity profile in each layer was replaced with an analytically prescribed profile:

$$u_i = Umax_i \times \exp(-y^\alpha/w_i) \quad y > 0$$

where y is the cross-stream distance, with $y = 0$ at the location of the maximum velocity in each layer and $y > 0$ at the cyclonic side of the stream. $Umax$ is the maximum velocity in each layer, and α and w_i are constants determining the resulting width of the cyclonic side. The transport in each layer is determined by the stratification change across the stream which is assumed to remain constant. Therefore, once α is selected w_i is calculated to preserve the transport. The choice of this particular analytical form of the velocity structure on the cyclonic side of the stream was based primarily upon simplicity of implementation. Our experiments with alternative forms of velocity structure show that specifics of the velocity profile have little effect on the stream stability. The key parameter affecting the stream stability is the cyclonic side width, and the above choice of the velocity profile provides a convenient way of controlling this parameter.

The LC stream structure with a narrow cyclonic side is shown in the upper panel of Figure 5.16. The baseline stream-structure is shown in the lower panel of the figure for comparison. Figure 5.17 shows the corresponding PV stream structures. The velocity of the stream structure with a narrow cyclonic side results from a PV structure with a local maximum in the upper layers. The presence of this local maximum creates an inversion of the PV gradient in the upper layers leading to a more unstable stream (see below).

Another observed LC behavior pattern is its expansions to the north which typically leads to the formation of LCE's. It is reasonable to assume that a rapid expansion to the north can lead

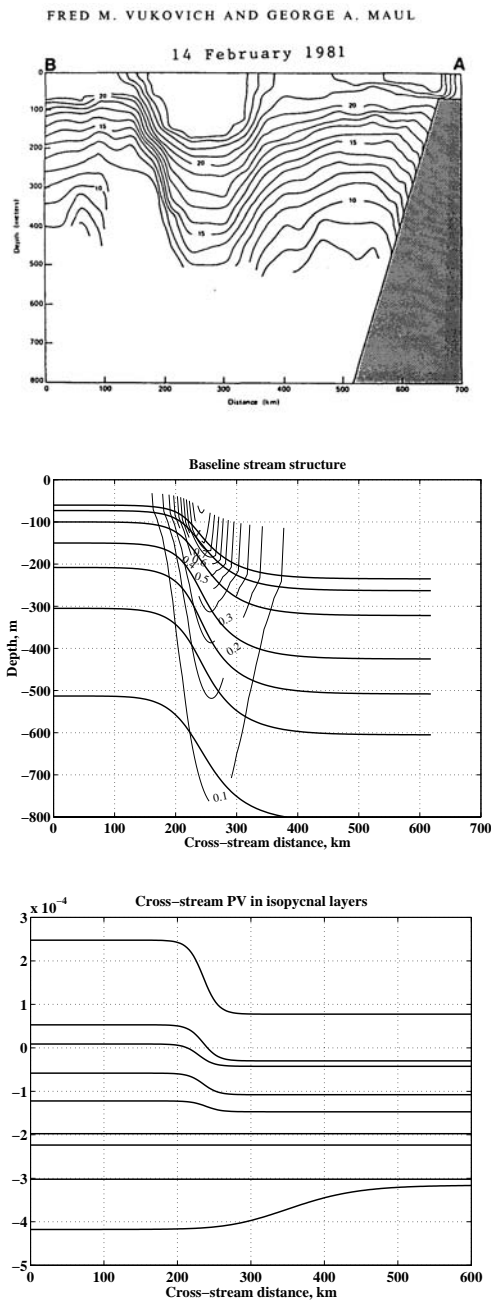


Figure 5.15. Observed LC cross-section compared to the constructed baseline stream structure. Observed LC cross-section from Vukovich and Maul (1985) is shown in the upper panel). Velocity cross-section and interface positions of constructed baseline stream structure are shown in the middle panel, the corresponding PV structure is shown as cross-stream profiles in each layer in the lower panel.

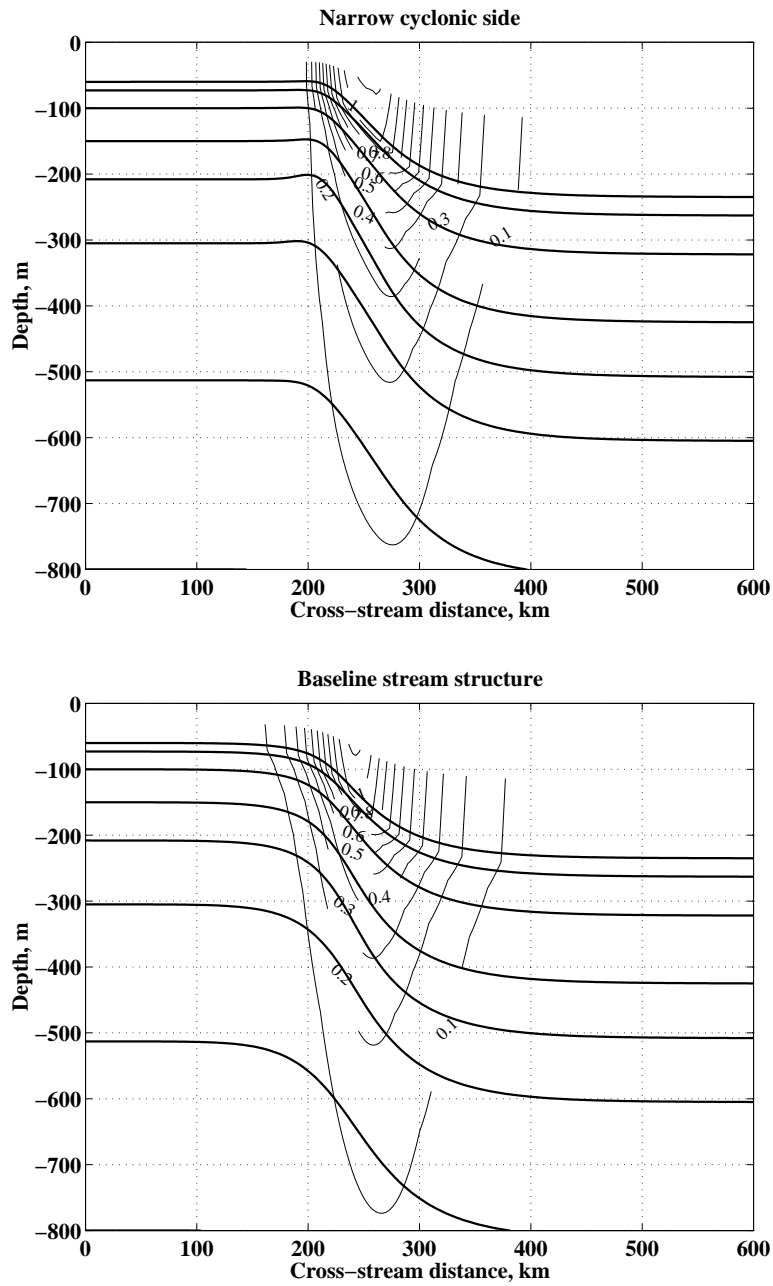


Figure 5.16. LC stream structure with a narrow cyclonic side (upper panel) compared to the baseline LC stream structure (lower panel). Colored lines indicate positions of density layer interfaces.

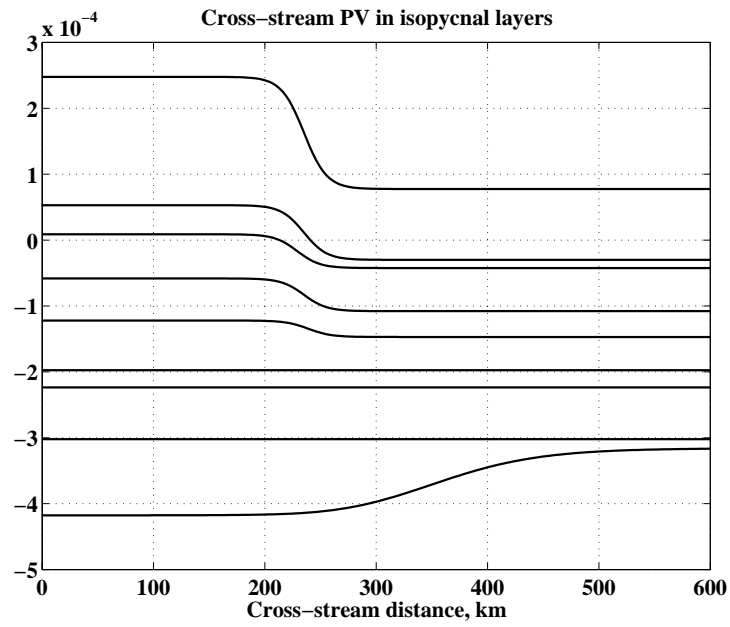
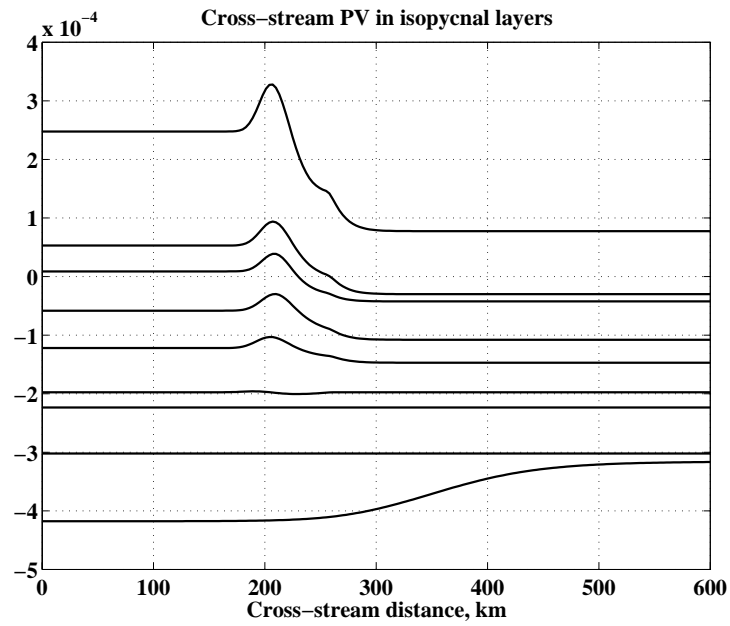


Figure 5.17. Cross-stream PV profiles in each density layer corresponding to the LC stream structure with a narrow cyclonic side (upper panel) and to the baseline stream structure (lower panel).

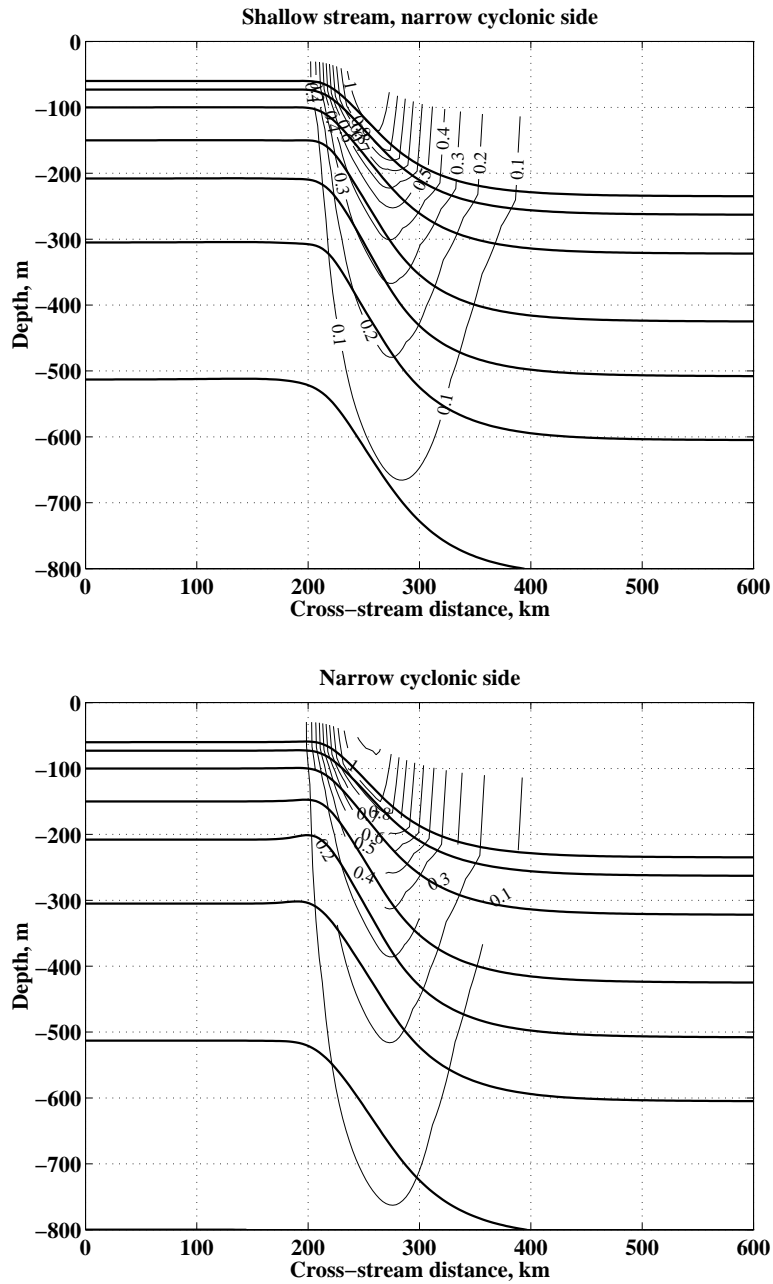


Figure 5.18. Shallow stream structure with a narrow cyclonic side (upper panel) compared to the regular depth stream structure with a narrow cyclonic side (lower panel).

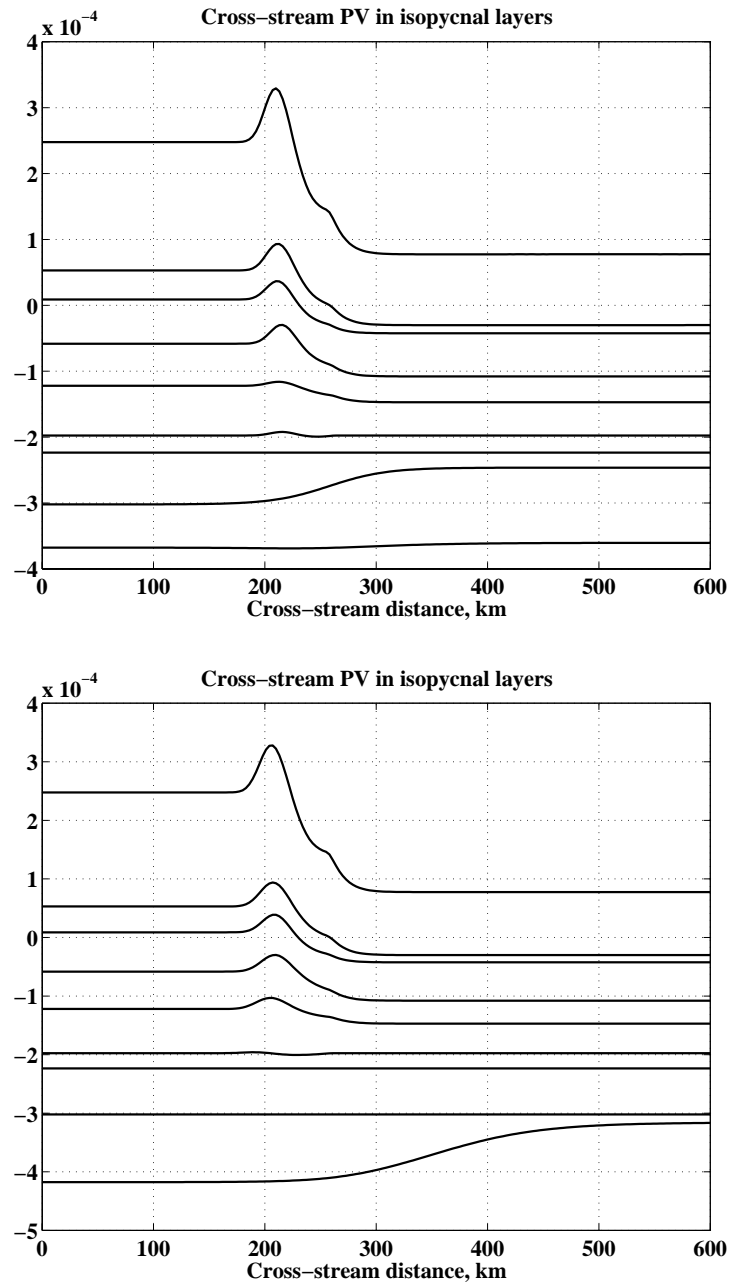


Figure 5.19. Cross-stream PV profiles in each density layer for the shallow LC stream structure (upper panel) and for the same LC stream structure with a regular depth (lower panel). Both stream structures have narrow cyclonic sides, which can be seen as several vertically aligned local extrema in PV profiles.

to the stream losing its deep component and becoming shallower. This type of stream structure variability can be easily incorporated into the baseline stream structure by changing the depth of the level of no-motion. Figure 5.18 compares the shallow stream structure to the stream structure with a regular depth. In both cases the stream structure with an incorporated narrow cyclonic side was used. Figure 5.19 shows the corresponding PV structure. As one can see, the key difference between the two sections is the depth of the layer with an inverted PV gradient. In the case of the shallow stream the PV gradient inversion occurs in the 8-th layer, while in the baseline stream structure the inversion occurs in the 9-th layer.

5.4.1.2 Results

The LC stability experiments demonstrate that cyclones resembling the observed LCFE's can form on the cyclonic side of the stream as a result of an instability process in a zonal LC-type jet triggered by a small disturbance. The experiments also revealed the key features of the LC stream structure controlling the intensity and the growth rate of these cyclones. The latter result is important for controlled simulations of LCFE's in realistic settings.

The experiment shown in Figure 5.14 illustrates how an instability process leads to formation of cyclones resembling the observed LCFE's. This particular experiment was conducted with the shallow LC stream structure and with a narrow cyclonic side. Color coded in the figure is the PV in the upper layer; the red band of high PV indicates the PV extremum associated with a narrow cyclonic side. Dashed black contours indicate negative pressure anomalies in the upper layer that are associated with cyclonic circulation. The small initial disturbance (upper panel) triggers a packet of meanders (unstable modes), which amplify as they propagate downstream (middle panel). By day 40 of the integration one can observe cyclones forming in the meander troughs (lower panel). When fully developed those cyclones are roughly 100 km in diameter with a typical swirl speed of 20 cm/s and a vertical extent of about 800 km. The cyclones become fully developed approximately 400 km downstream of the initial disturbance and propagate with a typical speed of 10 km/day. All the above characteristics are consistent with the LCFE properties observed by Hamilton et al. (2000).

The series of stability experiments with different LC stream structures allowed us to identify the stream structures capable of forming these cyclones. The cyclones were shown to form only by streams with a positive PV extremum on the cyclonic side, i.e., the narrow cyclonic side. Moreover, the intensity of the cyclones was found to be proportional to the magnitude of the extremum. Figure 5.14 provides an intuitive explanation to this result. One can see that the core of the LCFE resembling cyclones is composed of the high PV water stripped off the cyclonic side of the stream suggesting a direct link between the amount of positive PV and the cyclone intensity.

The presence of PV extremum, however, is not sufficient for cyclone development. Given that the characteristic horizontal scale of the LC loop in its fully extended state is 400-500 km, a small initial disturbance must amplify fast enough to form frontal cyclones over this relatively short distance. In other words, the stream has to be unstable enough to allow rapid meander growth. Our experiments indicate that the stream stability, as defined by the rate of meander growth, is linked to the stream vertical extent. The LC with a shallower stream structure was shown to be significantly more unstable.

Figure 5.20 provides a summary of all zonal channel stability experiments on the f-plane and the β -plane. The upper panel shows time evolution of cyclone intensity in different experiments, while the lower panel shows time evolution of the maximum meander amplitude. The meander amplitude is related to the size of the cyclones. As one can see from Figure 5.14, it is roughly

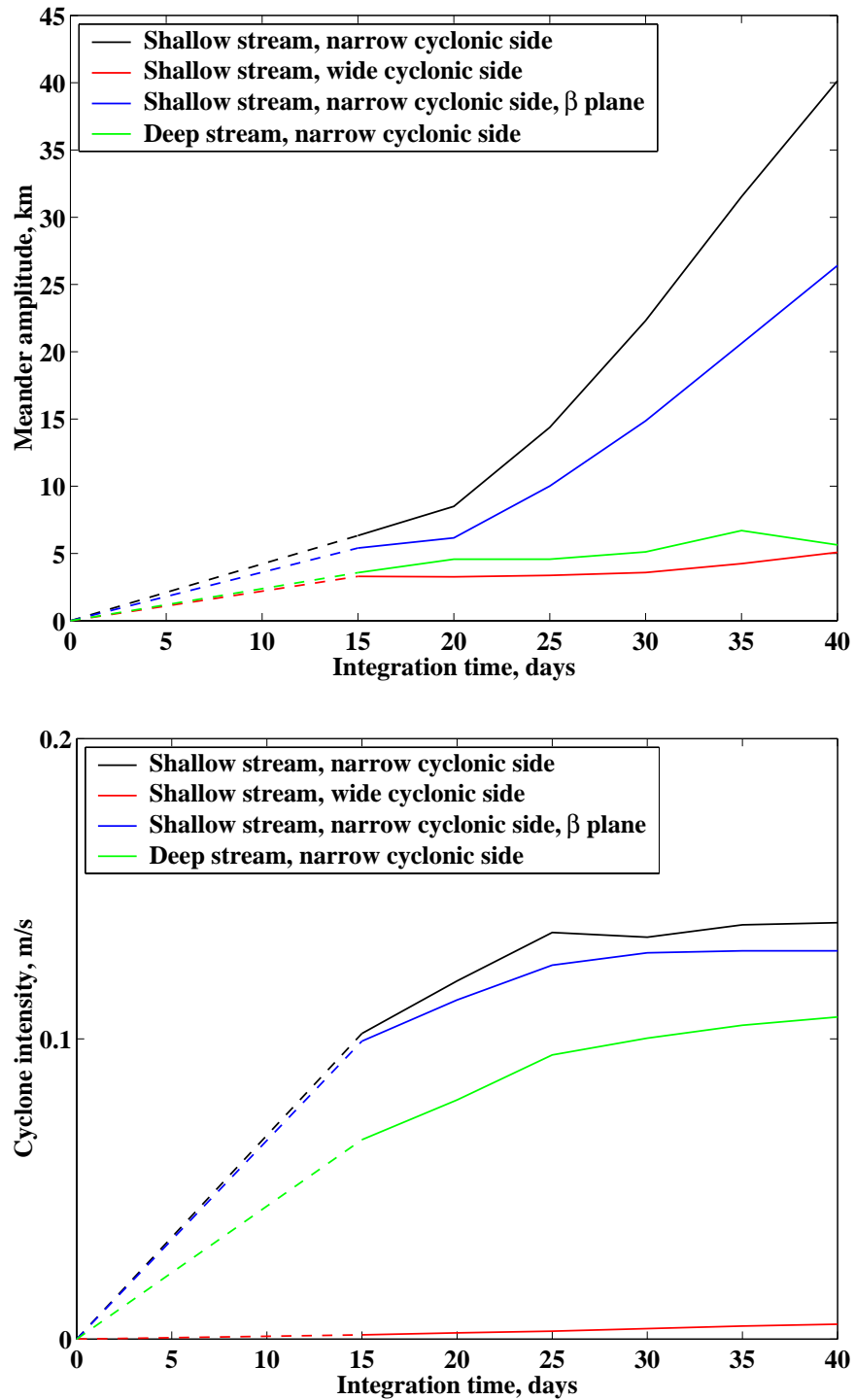


Figure 5.20. Summary of zonal channel stability experiments. Upper panel shows time evolution of frontal cyclone intensity. Lower panel shows maximum meander amplitude.

equal to the half radius of LCFE's. Color represents different experiments; the color mapping is shown in the legend. Experiments shown in the legend are referred to by key features of the corresponding stream structure, which were discussed in the previous section. Unless otherwise noted, all of the experiments were conducted on the f-plane. During the first 15 days the initial disturbance undergoes the process of restructuring during which the meander amplitude and the cyclone intensity are not well defined, consequently, this time period is designated with dashed lines. In addition to varying the stream structure both the f-plane and the β -plane approximations were tested.

As one can see in the upper panel of Figure 5.20, the LC with a wide cyclonic side, i.e., without a PV extremum on the cyclonic side, shows no significant frontal cyclone development. We only show the experiment with a shallow PV structure since it is more likely to produce frontal cyclones due to a more unstable stream. The experiment with a deep stream structure also does not develop frontal cyclones. However, as soon as the PV extremum is introduced (narrow cyclonic side), frontal cyclones start developing even for an LC with a deep stream structure which should be more stable (green curve). The alternative view of the same experiment that is presented in the lower panel shows that these cyclones are small, only about 20 km in diameter (4 times the meander amplitude). When a shallow stream structure is introduced along with the PV extremum, the size of the cyclones increases up to 150 km (black line). The cyclone intensity also increases up to 14 cm/s (upper panel). Introduction of the β -plane approximation has notable but relatively small effect on the stream stability (blue line). The size of the cyclone decreases to about 100 km (lower panel), however their intensity remains almost the same (upper panel).

5.4.2 Realistic Simulations of LCFE's

The understanding of the mechanisms that drive the LCFE growth, developed as a result of the zonal stability experiments of Section 5.4.1, was then applied to simulate LCFE's in the PE model experiments with fully realistic topography. As the first step in transition to the PE framework we repeated the key zonal stability experiments initially conducted with the IE model but now using the PE model. This step is necessary to ensure that the introduction of the new physics associated with the more complete set of primitive equations does not substantially change the results obtained within the framework of the intermediate equations.

The next step in our modeling hierarchy was to configure a regional PE model for simulating LCFE's in a realistic setting. This new regional configuration incorporated a stream trajectory representative of the real LC and a bottom topography that together allow realistic simulations of LCFE-topography interactions while, at the same time, retaining control over the LC stream structure. A new form of the initial disturbance capable of triggering LCFE development in this realistic setting was also developed. The simulated LCFE's were compared against observations and the effect of LCFE's on the circulation within the DeSoto Canyon was then analyzed.

5.4.2.1 PE Model Stability Experiments

The key results of the zonal channel stability experiments described in the previous section were verified using a PE model. This verification was accomplished by repeating the key zonal channel experiments within the PE model. The PE model used in these experiments is the same model that we employed in our previous work (Section 3.3). In this case the model had 50 σ -levels with 4 km horizontal resolution and was configured for the same zonal channel described in the previous section with. The horizontal resolution of the PE model is slightly coarser than

the resolution of the IE model (3 km), however since the PE model employs a C type grid, which effectively increases the horizontal resolution, small horizontal scales are equally well resolved in both models. Another notable difference between the PE and IE model configurations is the 10-grid point sponge layer at the inflow boundary added to the PE model. The sponge layer was introduced to prevent secondary disturbances from forming at the inflow boundary due to boundary condition formulations in the PE model. This additional sponge layer did not have any notable influence on the formation of the frontal cyclones.

Figure 5.21 shows the zonal channel stability experiment with a shallow stream structure that has a PV extremum on the cyclonic side. The initial fields in the PE model were specified by transferring the initial conditions from the corresponding IE model experiment. The technique of this transfer has been previously used for PE model initialization in our eddy-topography interaction experiments (Section 4.4.1). Color coded in the figure is the PV in the thermocline defined as the layer above 27 kg/m^3 isopycnal surface. In the initial PV field (upper panel) one can clearly see the PV extremum associated with the narrow cyclonic side stream structure as well as the PV front associated with the stream. The initial disturbance restructures itself into a packet of growing meanders (middle panel) that is very similar to the IE model experiments. After 30 days of integration frontal cyclones are formed in the meander troughs (lower panel). Just like in the IE model experiment the cyclone cores are associated with high PV regions being stripped off the cyclonic side of the stream.

The experiment with the baseline stream-structure, i.e. without PV extremum, has also been repeated in the PE framework. Just like the corresponding IE model experiment it did not result in the formation of frontal cyclones. Thus, the PE model experiments confirm the key IE model result: the stream has to have a PV extremum on the cyclonic side for frontal cyclones to develop. The PE experiments do show some differences from the IE experiments. The meander growth rate seems to be faster in the PE framework; frontal cyclones already fully develop after 30 days compared to 40 days within the IE dynamical framework. The shape of the unstable modes (meanders) also seems to be slightly different. These minor differences are to be expected due to the significant differences in model formulations, however, the key results seem to be robust enough and independent of the numerical model being used.

5.4.2.2 Model Configuration for LCFE Simulations

LCFE simulations were conducted with the same PE model described above. For these simulations the model was configured for the domain shown in Figure 5.22. The vertical and the horizontal resolutions of the model are the same that were used in the zonal channel experiments. A fully realistic Coriolis parameter is prescribed. The western boundary of the domain is closed. The southern boundary is opened with a 25-grid point sponge layer applied along the boundary. The sponge layer performs the same function as the inflow and outflow sponge layers in the zonal channel experiments. The LC is initialized along a hypothetical trajectory designed to simulate the LC in its extended state. The trajectory is circular at its northern end with the center and the radius of the circle adjustable to control its northern extent. South of the circle center the trajectory is purely meridional. The bottom topography is taken from the ETOPO5 database and is fully realistic north of 25°N . South of this latitude the topography is modified by blending the real topography with a flat bottom that is 1500 m deep. This blending is accomplished by applying a weighting function which is equal to 1 at the southern boundary, i.e. the blend consists entirely of the uniform depth topography, and decreases exponentially in the northward direction reaching $1/e$ of the value 500 km away from the boundary. The weighting function effectively becomes

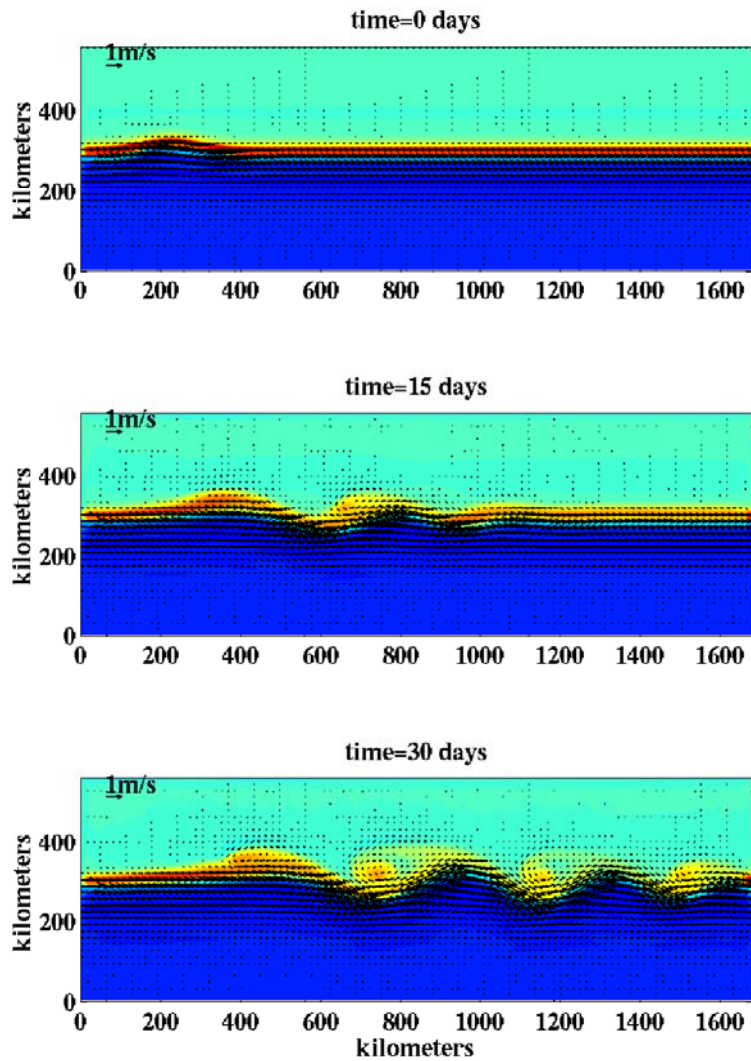


Figure 5.21. Zonal channel stability experiment conducted using a PE model. Color coded is the PV in the thermocline. Arrows indicate velocities vertically averaged through the thermocline.

0 around 25°N at which point the blend consists entirely of realistic ETOPO5 topography. The main purpose of the topography modification is to remove the Yucatan Peninsula and to introduce uniform-depth topography along the southern inflow/outflow boundary. The former allows control of the stream structure by eliminating the stream-topography interaction at the inflow boundary that can potentially seriously modify the stream. The latter is done to simplify the mass balance conditions in the model domain.

Typical initial conditions for a realistic LCFE simulation with a PE model are shown in Figure 5.22. As before, color coded in the figure is the PV in the thermocline. A small initial disturbance is specified near the southern end of the inflow LC branch similar to the zonal channel experiments. The initial density and velocity fields are specified by transporting them from the IE model as was configured for the same domain. This is accomplished using the same technique of PE model initialization that we previously used in our PE experiments.

5.4.2.3 Realistic LCFE Simulations

An important result of the LCFE simulation experiments was the failure of the initial disturbance produced by a shift in the stream trajectory to generate frontal cyclones similar to those generated in the zonal channel stability experiments. The experiment indicated that initial perturbations of the stream trajectory either dissipate or form large-scale meanders which do not produce frontal cyclones. The exact dynamical explanation of this result requires further in-depth analysis of the instability process. Our preliminary hypothesis attributes this result to the orientation of the stream relative to the direction of the environmental β . The baroclinic instability process can be viewed as a process of vertical coupling of the upper level stream meanders with deeper cyclones and anticyclones, e.g. Sutyrin et al. (2001). This process can be briefly described as follows. A downstream propagating meander causes stretching and compression of the isopycnal layer underneath which produce cyclonic and anticyclonic circulations that are coupled with the meander due to PV conservation in this layer. These circulations underneath the meander extend vertically into the upper layer generating the cross-stream velocity that leads to meander growth. According to our hypothesis the environmental β will produce a tendency for the circulations underneath the meander to move westward thus disrupting the vertical coupling crucial for the meander growth.

A growing LCFE consistent with observations is generated if the structure of the initial disturbance is modified. An initial disturbance capable of generating an LCFE is shown in Figure 5.23. The principal difference between this disturbance and the disturbance previously used in our zonal channel experiments is the positive PV anomaly at the trough of the disturbance. The positive PV anomaly is associated with a cyclonic circulation and is equivalent to specifying a small cyclone on the cyclonic side of the stream. We hypothesize that such a cyclone can be created in reality via the process of LC interaction with the Yucatan Peninsula topography. As we demonstrated in our previous eddy-topography studies, a baroclinic current intersecting a topographic slope can generate PV anomalies by advecting high PV water from shallow regions into deeper regions. The LC, which is known to meander as it flows along the Yucatan shelf (Sheinbaum et al. 2002), can generate positive PV anomalies by advecting high PV water off the Yucatan shelf.

The initial disturbance shown in Figure 5.23 generates an LCFE which is very similar to the observed LCFE's. The result of 1 month of integration is shown in Figure 5.24. As one can see the initial disturbance propagated north along the stream and grew to a considerable size (approximately 150 km in diameter). At the stage shown in the figure the warm tongue (low PV region) leading the LCFE interacts with the DeSoto Canyon region. The LCFE produced in this particular experiment is among the largest that we were able to simulate using this approach. In general, the

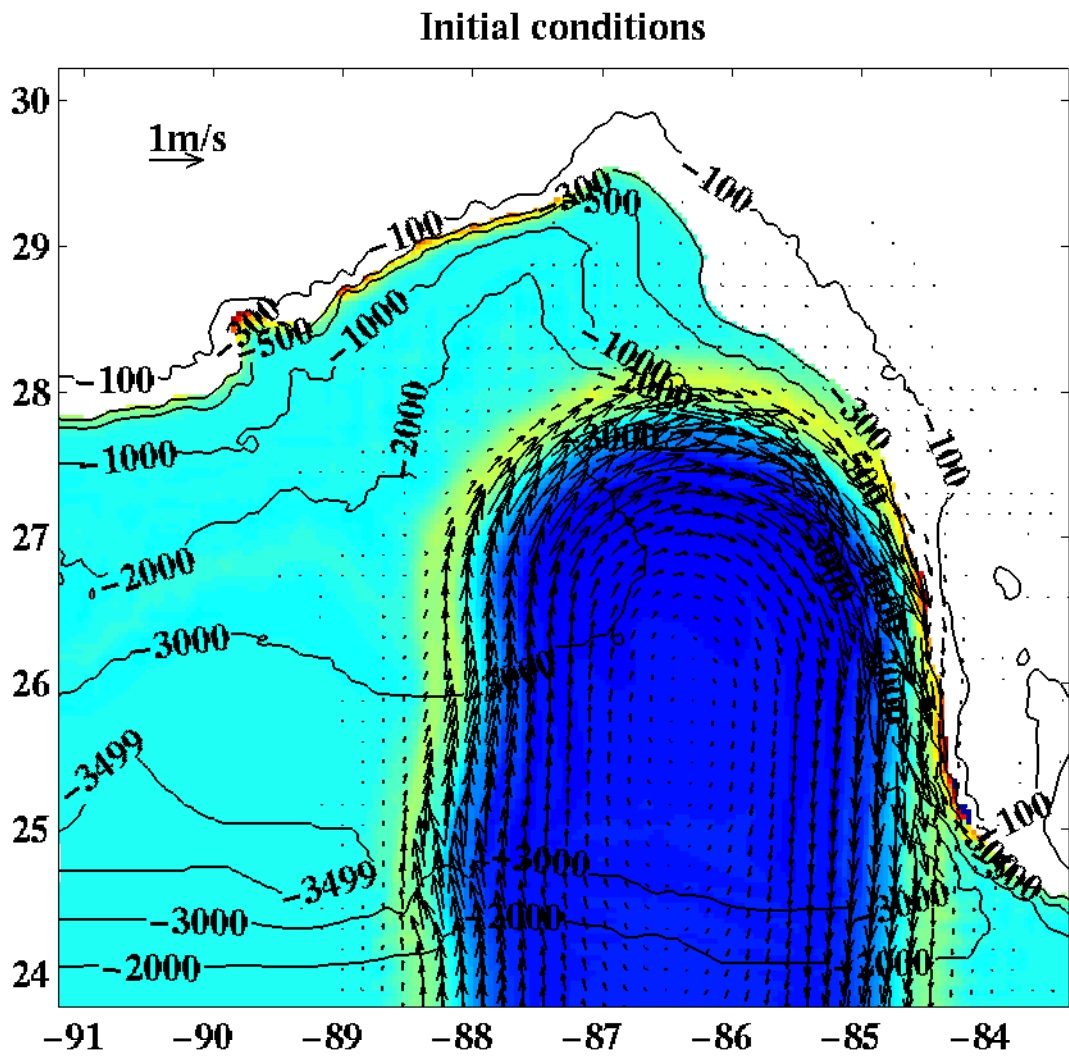


Figure 5.22. PE model configuration and typical initial conditions designed for realistic LCFE simulations. Color coded is PV in the thermocline; vectors indicate the velocity vertically averaged throughout the thermocline.

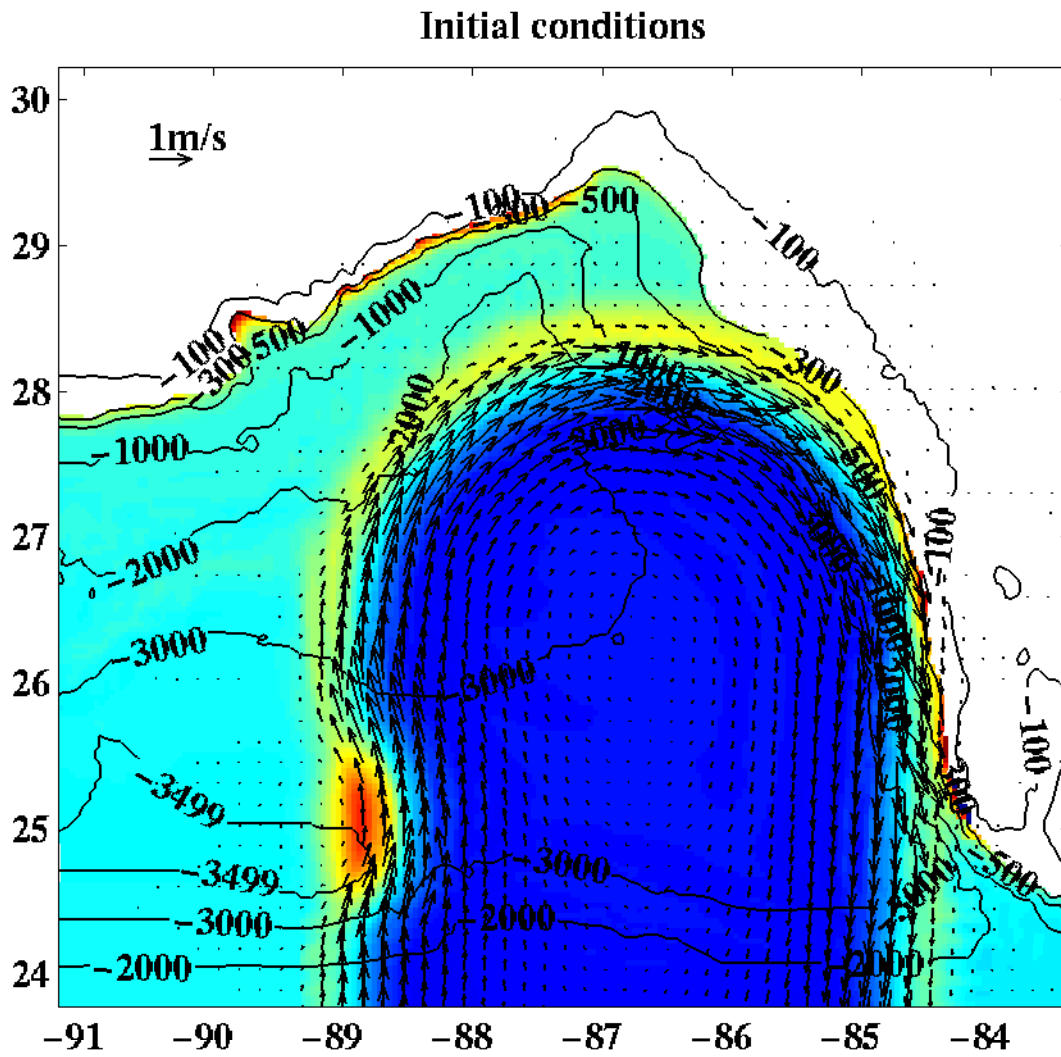


Figure 5.23. Same as in Figure 5.22 but with the initial disturbance capable of developing an LCFE.

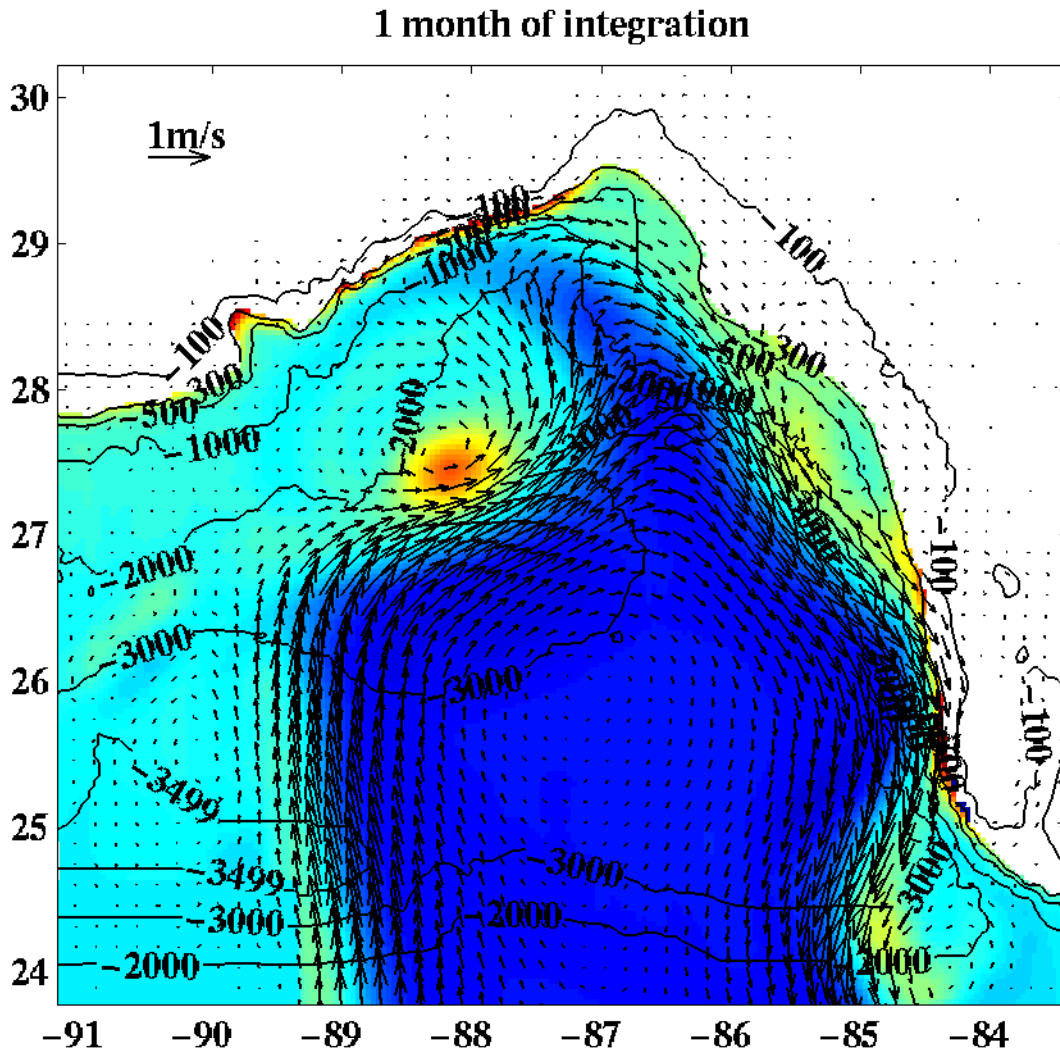


Figure 5.24. Same as in Figure 5.23 but after 1 month of integration.

resulting LCFE size can be controlled by varying the size of the initial disturbance and by changing the stream stability characteristics. In the experiment shown these parameters were adjusted to produce an LCFE similar to the one observed during the DeSoto Canyon Eddy Intrusion Study (Hamilton et al. 2000).

Figure 5.25, Figures 5.26, and Figure 5.27 show comparisons of the simulated LCFE with observations. Figure 5.25 compares the sea surface height and Figures 5.26 and 5.27 compare the velocity at two depth levels. Both comparisons are quite favorable. Even though the simulation does not reproduce the finer details present in observations, which is not surprising given the unstable nature of the LCFE evolution, the key features are well represented. The trough that is seen in the observed SSH field around 87°W , 28°N corresponds to the simulated LCFE; the ridge that is located north of the trough in the observed SSH field corresponds to the positive SSH anomaly in the simulation associated with the LC meander (warm tongue leading the LCFE). The lack of a positive anomaly in the observed SSH field east of the LCFE is likely due to a gap between TOPEX tracks at this location. The simulation reproduces the eastward along-shelf current near the surface that can be seen in the observed velocity field west of the DeSoto Canyon (Figure 5.27).

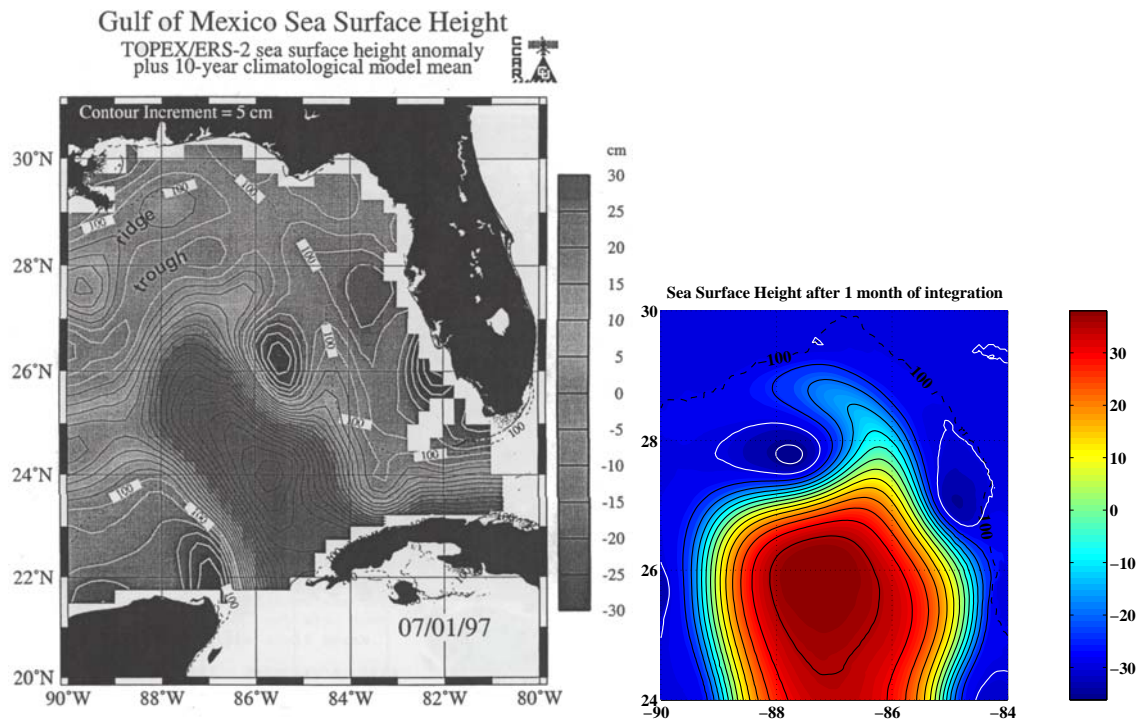


Figure 5.25. SSH from the realistic LCFE simulation (lower panel) compared to observed SSH (upper panel). The image of observed SSH is taken from Hamilton et al. (2000).

Further off-shore the direction of the current reverses similar to observations. The cyclone that is clearly seen in the observations at 300 m depth is also well reproduced. The simulated circulation pattern is also in a very good agreement with the conceptual model of Hamilton et al. (2000) (Figure 5.13).

After developing the LCFE simulation technique described above we were able to investigate the process of LCFE interaction with the DeSoto canyon. By introducing a passive tracer into the model we were able to visualize the water exchange between the DeSoto Canyon and the surrounding GOM generated by the LCFE. The passive tracer was introduced using the same technique that we used in our previous simulations of eddy interaction with the DeSoto Canyon (Section 5.2.3). The tracer concentration is initially proportional to the total water depth and is uniform throughout the water column. Thus, high concentration of the tracer represents the water from the deep GOM while the low concentration represents the water from the shallower regions. Figure 5.28 shows the tracer distribution at 50 m depth resulting from 1 month of integration after the moment the tracer was introduced. The tracer was introduced at the time step shown in Figure 5.25.

As one can see the result of LCFE interaction with the DeSoto Canyon in this particular case was the generation of an anticyclonic circulation at the mouth of the canyon. The circulation was produced as a result of the warm tongue leading the LCFE being clipped by the deep eastern wall of the canyon. The anticyclonic circulation, in turn, produced a cyclonic circulation within the canyon itself via the mechanism of off-shelf PV advection. The resulting cyclone-anticyclone pair produces intensive water exchange between the canyon and the deep GOM as can be seen from the tracer distribution. We believe that this circulation pattern is a typical result of an LCFE interaction with the DeSoto Canyon.

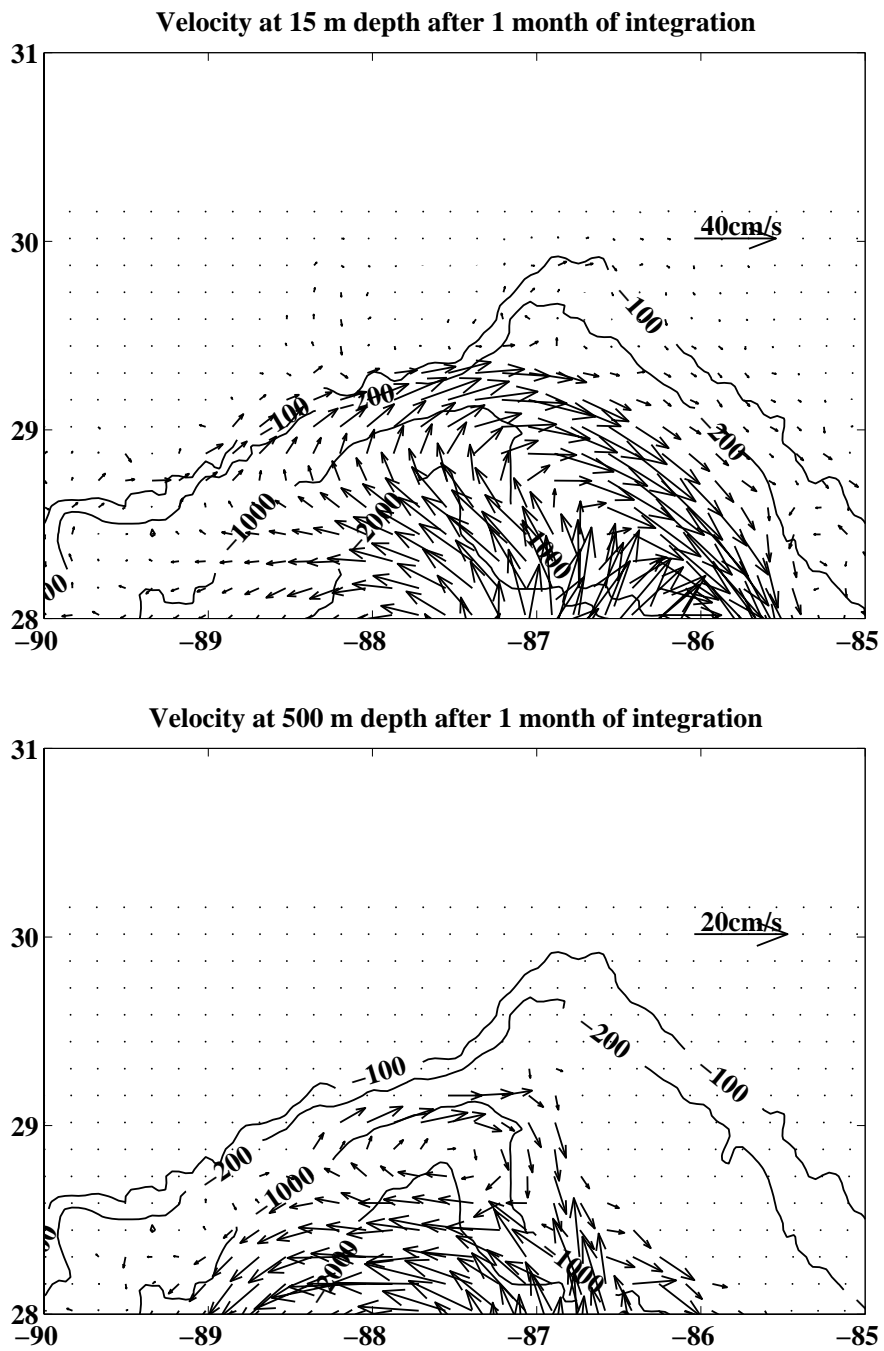


Figure 5.26. Velocities produced by the realistic LCFE simulation. Upper panel shows velocities near the surface, lower panel shows velocities at 500 meters.

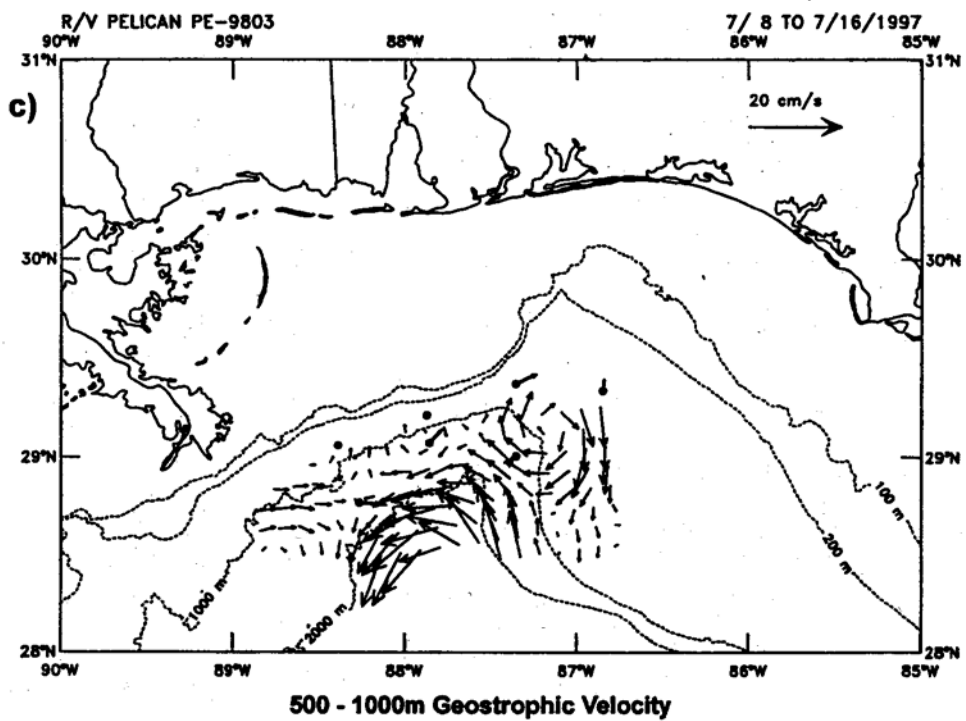
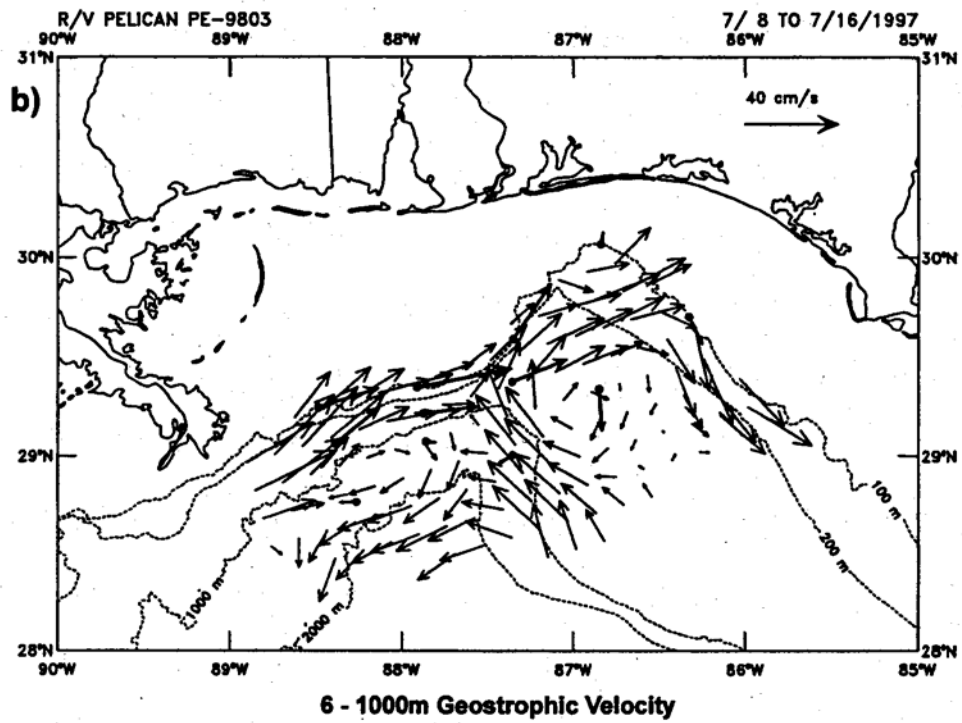


Figure 5.27. Observed geostrophic velocities corresponding to simulated simulated velocities in Figure 5.26.

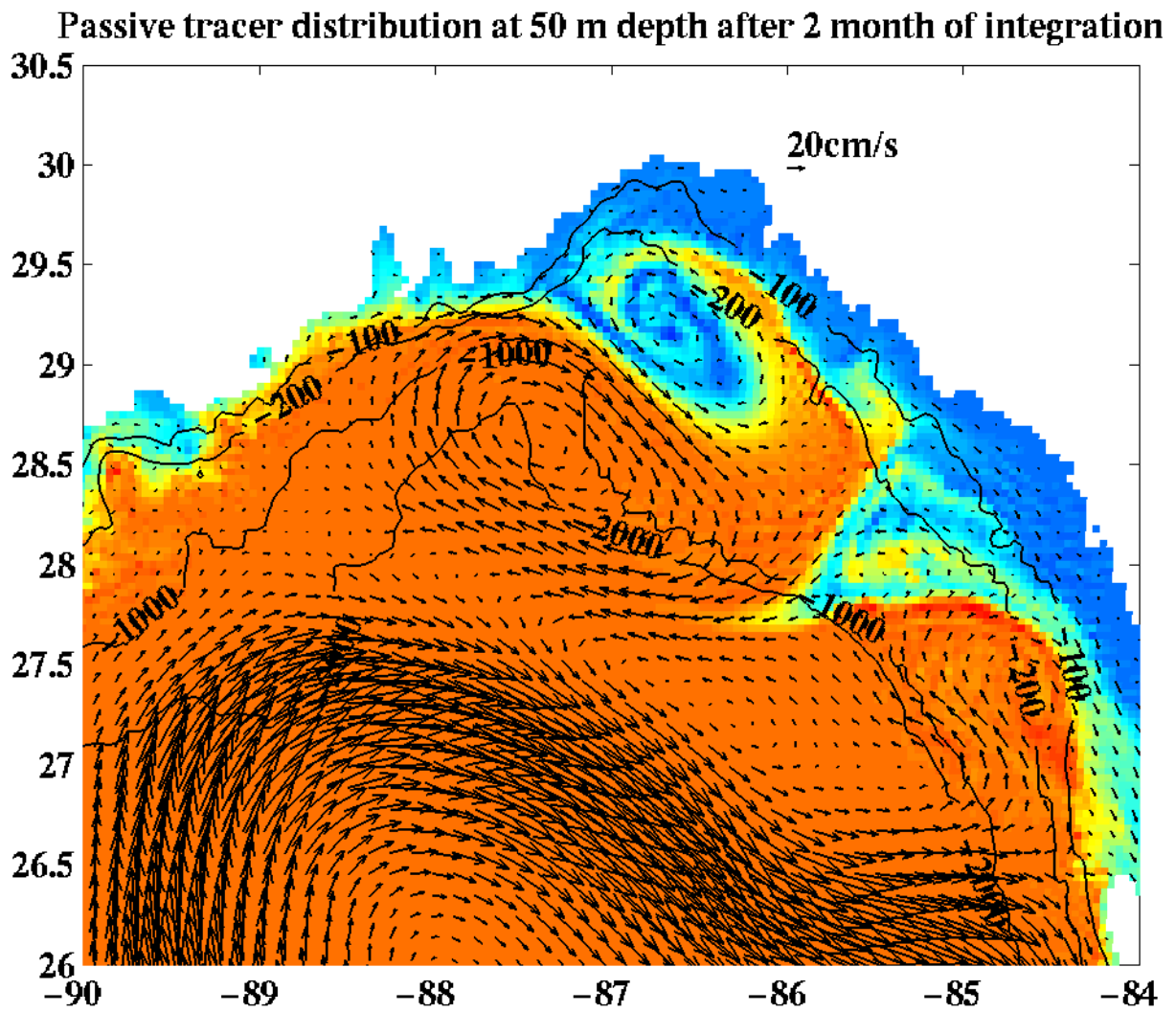


Figure 5.28. Passive tracer distribution at 50-m depth after 2 months of model integration.

6. MIDWATER-COLUMN JETS

A brief investigation of the physical processes associated with the evolution of small-scale cyclones over the northern continental slope in the GOM was conducted. The goal of this investigation was to identify potential mechanisms that can lead to the formation of high-intensity midwater-column-intensified currents, which will be further referred to as midwater-column jets. The investigation consisted of three phases. The first phase was concerned with studying the evolution of small-scale cyclones in the northern GOM, while the second phase was concerned with identifying physical processes leading to their formation. The last phase consisted of formulating hypotheses for additional mechanisms of midwater-column jet generation. Our study of the evolution of small-scale cyclones in the northern GOM conducted during the first phase is described in Section 6.1. The investigation of physical processes potentially leading to the formation of the midwater-column jets is presented in Section 6.2. An alternative hypothesis for midwater-column jet generation is described in Section 6.3.

6.1 Small-Scale Cyclones over Northern Slope Topography

Two regimes of small-scale cyclone evolution were studied. In the first regime an isolated cyclonic eddy is allowed to evolve on the β -plane with no background circulation over realistic northern GOM topography. The key questions that we were seeking to answer in this case are:

- Can our numerical model adequately describe those eddies?
- What is the evolution pattern of those eddies and how is it dependent on the eddy size?

In the second regime a small-scale cyclone is interacting with a larger LCE. In this case the questions that we seek to answer are:

- What is the effect of the LCE on the cyclone evolution?
- How does the presence of a small-scale cyclone affect the evolution of the LCE?

6.1.1 Isolated Cyclones

6.1.1.1 Experiment Design and Model Setup

Evolution of isolated cyclones was simulated with a high-resolution, σ -coordinate PE model (see Section 3.3). Isolated cyclones were initialized using the same procedure that was used for initializing LCE's (Section 4.4.1). The procedure consists of calculating the initial density and velocity structure of an eddy in an isopycnal-layer intermediate equation (IE) model from a given potential vorticity (potential thickness) structure and then interpolating it into the σ -coordinate system of the PE model. The potential vorticity structure of an eddy used for its initialization was calibrated every time to obtain the desired initial eddy characteristics, i.e., size, swirl speed, etc.

Cyclones of two different sizes were simulated. The diameter of the larger cyclone was ~ 100 km while the diameter of the smaller cyclone was ~ 50 km. The structure of the larger cyclone was modeled after cyclone *C2* surveyed during November 1994 over the lower northern slope (Berger et al. 1996). The characteristic features of the cyclone include peak swirl speed

of ~ 40 cm/s, currents penetrating down to ~ 800 m, and nearly constant currents in the upper ~ 300 m. The structure of the smaller cyclone was modeled after the cyclone surveyed in August 1992 over the lower northern slope and tracked by drifter 07837 (Berger et al. 1996). The smaller cyclone has structure similar to *C2* but with weaker swirl speed of ~ 20 cm/s.

The model was configured with 50 σ -layers, providing a maximum of 35 m vertical resolution in the thermocline. Boundary conditions are closed along the northern boundary and opened along all the other boundaries. A weak sponge-layer is applied along all boundaries; the western boundary has a stronger sponge-layer to suppress reflection of topographic Rossby waves. For the larger cyclone simulation the model was configured with uniform 4 km horizontal resolution, while for the smaller cyclone simulation the horizontal resolution was increased to 2.7 km.

6.1.1.2 Results

The results of two typical simulations are shown in Figure 6.1, the upper panel showing the small cyclone simulation while the lower panel showing the large cyclone simulation. The color code indicates the potential vorticity in the thermocline which is defined as an isopycnal layer potential vorticity within the layer above $\sigma = 27$ kg/m³; the vectors indicate velocity vertically averaged over the thermocline depth (above $\sigma = 27$ kg/m³). The trajectory of the cyclone propagation is shown with the thick black line, and the time interval between the marks is 10 days.

The simulations were run for 120 days. During this period of time the eddy intensity decreased only slightly, indicating that without external forcing the life period of small-scale cyclones over the northern slope is at least several months, which is consistent with observational data (Berger et al. 1996). In both cases cyclones propagate northwest with a speed slightly over 1 km/day. The propagation speed of the larger cyclone is ~ 1.2 km/day, while the propagation speed of the smaller cyclone is ~ 1.1 km/day. In contrast to LCE's, small-scale cyclones do not induce any significant cross topographic flow; after encountering the northern shelf break they continue to propagate westward along the shelf without any significant increase in their decay rate. The trajectories become more zonal as the cyclones move onshore, indicating that the direction of propagation is probably weakly depth dependent. Additional analysis are necessary, however, to establish the nature of this effect more conclusively.

6.1.1.3 Conclusions

Numerical experiments demonstrated that the high-resolution PE model is capable of adequately describing the evolution of cyclones as small as 50 km in diameter over realistic topography. The cyclones were shown to retain their initial structure for periods of time of several months, which is consistent with observational data. The isolated small-scale cyclones were shown to have a general tendency to propagate northwest with a typical speed of slightly over 1 km/day. Our preliminary results indicate that the exact direction of propagation seems to be affected by the underlying topography. After encountering the northern shelf break cyclones continue to propagate westward along the shelf without any significant increase in their decay rate; no significant cross topographic flow is generated.

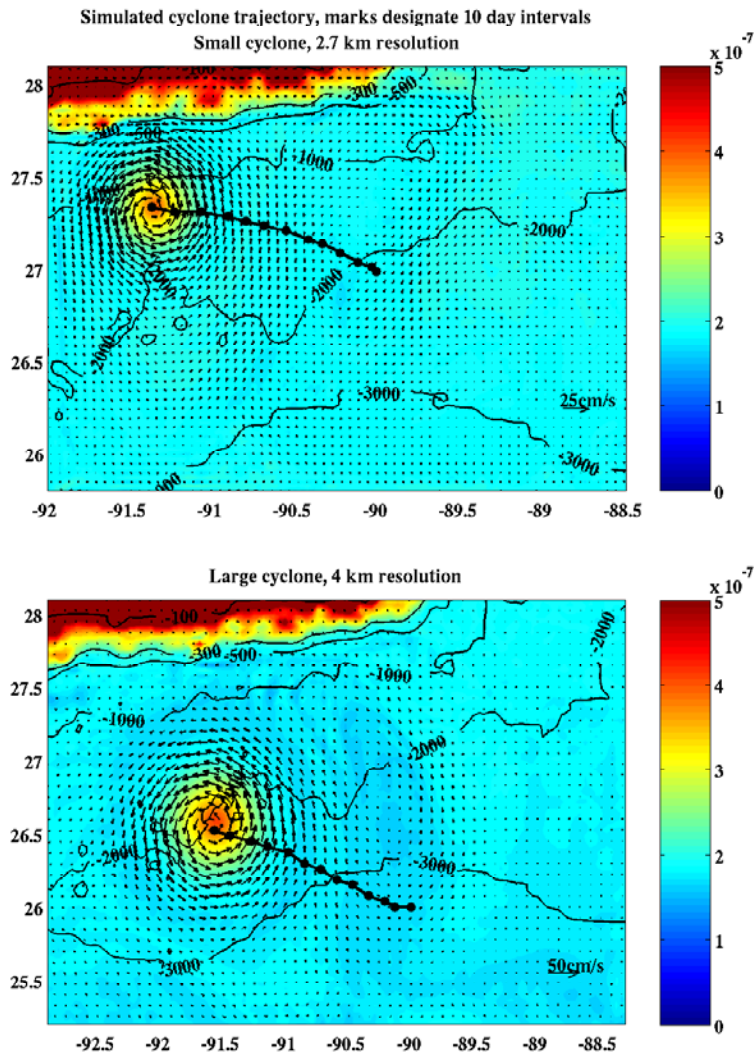


Figure 6.1. PE model simulations of a small (upper panel) and a large (lower panel) isolated cyclones over realistic northern GOM topography. Potential vorticity in the upper layer is color coded, where the upper layer is defined as the layer above 27 kg/m^3 density surface.

6.1.2 Cyclones Coupled with LCE's

6.1.2.1 Experiment Design

The PV-based eddy initialization scheme used previously to initialize isolated cyclones was extended to include the ability to initialize multiple eddies. The advantage of using a PV-based initialization procedure over a density or streamfunction-based procedure is illustrated in Figure 6.2. The upper panel of the figure shows the depth of the $\sigma = 27 \text{ kg/m}^3$ isopycnal surface corresponding to an elliptic LCE coupled with a small-scale cyclone. One can clearly see that the density (and the streamfunction) structures of the two eddies are overlapping, making it difficult or even impossible to apply a density-based feature model in this case since the density field between the eddies is an undetermined combination of the two features. The lower panel of the figure shows the PV field for the same eddy dipole. The PV fields of the cyclone and the LCE are clearly separated enabling a clean application of a feature model.

The extended initialization procedure was used to initialize an elliptic LCE coupled with a small-scale cyclone west of it. The structure of the LCE is modeled after loop current eddy *Y* surveyed in November, 1994 (Berger et al. 1996). The structure of the cyclone was modeled after cyclone *C2* surveyed at the same time as the LCE (Berger et al. 1996). The same model configuration that was used for the isolated larger cyclone simulation is applied here.

6.1.2.2 Results

The initial condition is shown in the upper panel of Figure 6.3; the lower panel shows the result after 80 days of integration. The simulation indicates that the cyclone was caught in the circulation of the LCE and advected around with an average speed of $\sim 10 \text{ km/day}$. During the entire period of integration the LCE remains elliptic and coupled with the cyclone. As the result of the interaction with the cyclone, the LCE trajectory was shifted substantially southward.

In order to illustrate the effect of the coupling on the LCE, the same experiment was repeated without the cyclone. The initial condition and the result after 80 days of integration of this experiment are shown in Figure 6.4. As one can see, without the coupling the LCE quickly loses its initial ellipticity and moves westward with constant speed driven by the β -drift.

6.1.2.3 Conclusions

The small-scale cyclones appear to play a key role in maintaining the ellipticity of LCE's and determining their trajectory over the northern slope. Isolated LCE's over the topographic slope, initially specified to have an elliptic shape were shown to quickly lose their initial ellipticity and propagate westward driven by the β -drift. The same initially elliptic LCE's coupled with a small-scale cyclone retain their ellipticity for several months during which time the interaction with the cyclone introduces a significant meridional component into LCE trajectories, sometimes pushing it off the northern slope into the central GOM. Since the observational data indicate that LCE's typically have an elliptic shape, this implies that the evolution of the majority of LCE's over the northern slope is strongly influenced by small-scale cyclones.

6.2 Mechanisms of Midwater-Column Jet Formation

Two potential generation mechanisms for midwater-column jets were studied. The first mechanism can potentially generate strong middepth-intensified currents via the process of violent in-

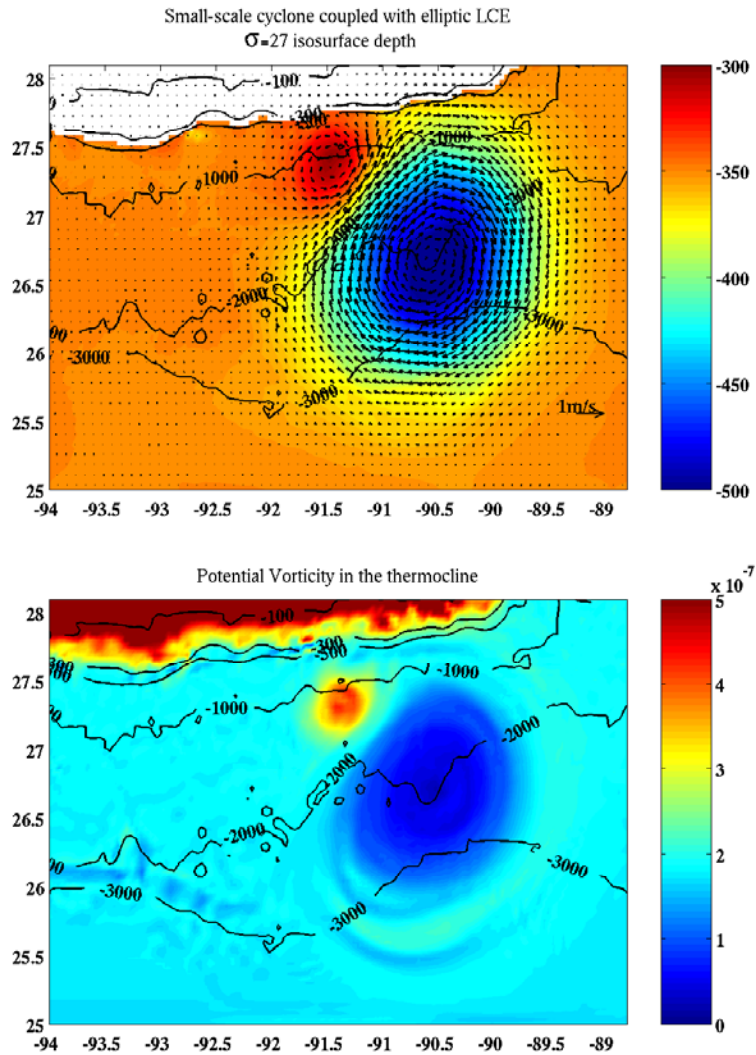


Figure 6.2. Illustration of advantages of the PV-based initialization scheme. The upper panel shows the depth of the 27 kg/m^3 density surface and velocity vertically averaged in the thermocline; the lower panel shows the corresponding PV.

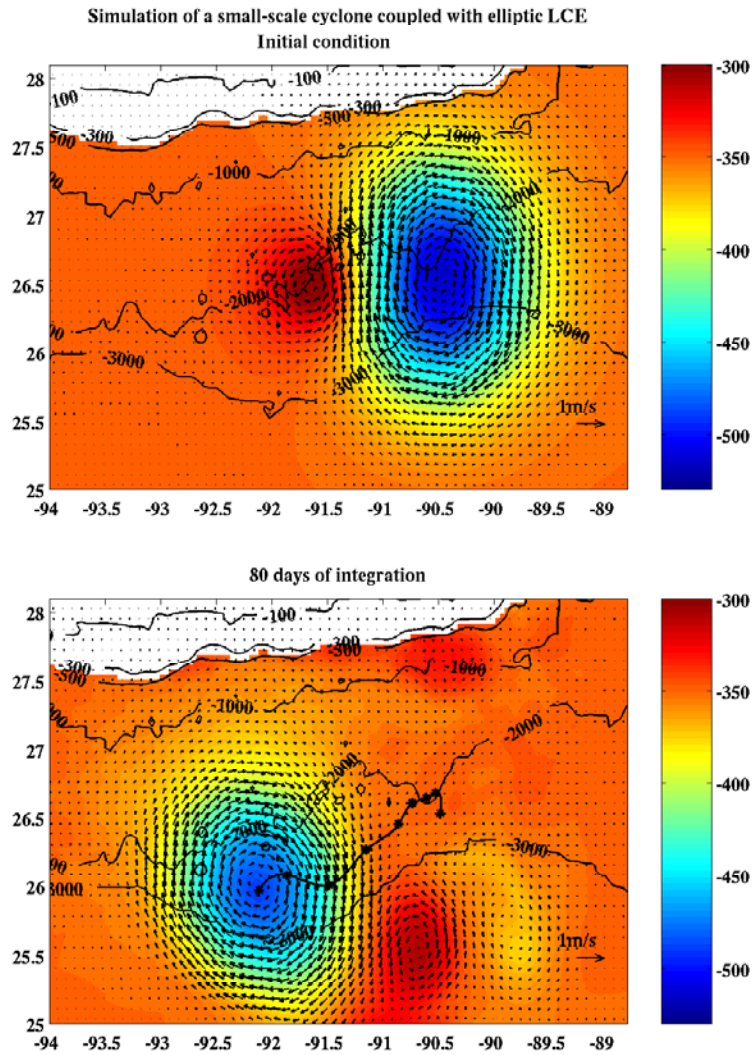


Figure 6.3. PE model simulation of an elliptic LCE interacting with a small-scale cyclone. The depth of 27 kg/m^3 density surface in meters is color coded. Vectors show the velocity vertically averaged in the thermocline. The initial condition is shown on the upper panel; the lower panel shows the 80-th day of the simulation.

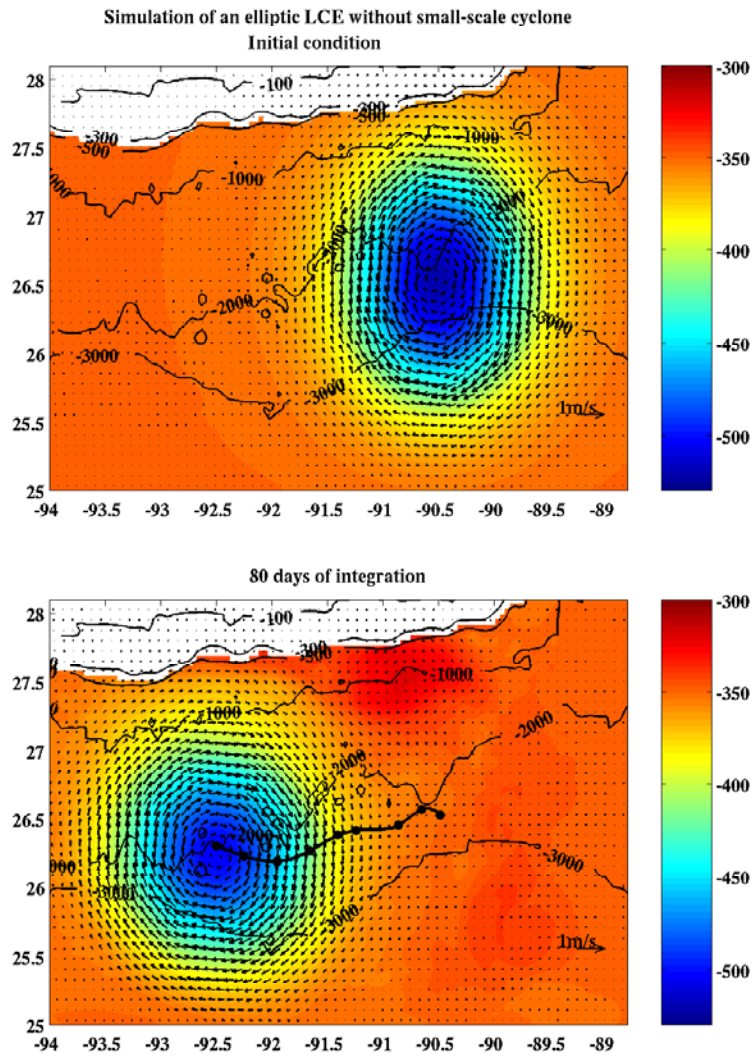


Figure 6.4. Same as in Figure 6.3 but for the isolated elliptic LCE simulation.

interactions of preexisting small-scale eddies with rough topography. The violent interactions of small-scale eddies with topography is produced by an LCE/small-scale cyclone pair. A cyclone captured in the circulation of an LCE is squeezed between the LCE and the northern shelf-break. During this process the energy associated with the cyclone, initially distributed over a relatively large area, is forced by the currents of the larger LCE into a narrow channel, which can potentially lead to current amplification and the generation of strong intermittent currents at middepth. The second mechanism generates strong middepth-intensified currents via the process of baroclinic instability in preexisting larger-scale features. The baroclinic instability process converts available potential energy into kinetic energy, accelerating quickly evolving currents in the vicinity of the unstable mesoscale feature.

6.2.1 Topography Interactions

Scientific question: Can midwater-column jets be generated during the violent interaction of small-scale cyclones and LCE's with rough topography within the *hydrostatic* framework?

6.2.1.1 Experiment Design and Numerical Models

The numerical experiment setup in this case is very similar to the coupled cyclone-LCE experiment described above. A small cyclone (~ 100 km in diameter) is initialized next to a larger anticyclone (~ 350 km in diameter) over the continental slope in the northern GOM. The centers of the eddies are initially 200 km apart with the cyclonic eddy located west of the anticyclone. The horizontal resolution of the model was increased to 2.6 km for this experiment. Accordingly, the bottom topography resolution was also increased. A high resolution hydrographic survey database, extended by the ETOPO5 data, was used to generate the northern GOM topography on a regular grid with 2 km resolution.

6.2.1.2 Results

Figure 6.5 shows simulated temperature and velocity fields at 260 meters after a month of model integration. At the moment shown the cyclone captured in the circulation of the LCE is squeezed between the LCE and the northern shelf. The instantaneous velocity field does not show any indication of current amplification due to interaction of the cyclone with the topography. East of the LCE one can see another cyclone forming, which is generated by the off-shelf PV advection mechanism. After another month of integration (not shown), the cyclone clears the area between the LCE and the shelf and merges with the cyclone formed behind the LCE by the process of off-shelf PV advection. As the result of interactions with topography, the intensity of the cyclone decreases indicating a significant loss of energy. The energy loss is most likely due to radiation of long gravity waves.

6.2.1.3 Conclusions

High resolution hydrostatic simulations of violent cyclone-topography interaction has shown no significant current amplification at midwater depth. The energy of the cyclone appears to be radiated away by long gravity waves. Further experiments within the nonhydrostatic context are necessary to obtain more conclusive results, since the hydrostatic approximation is likely to be violated during the process of interaction with rough topography at this scale.

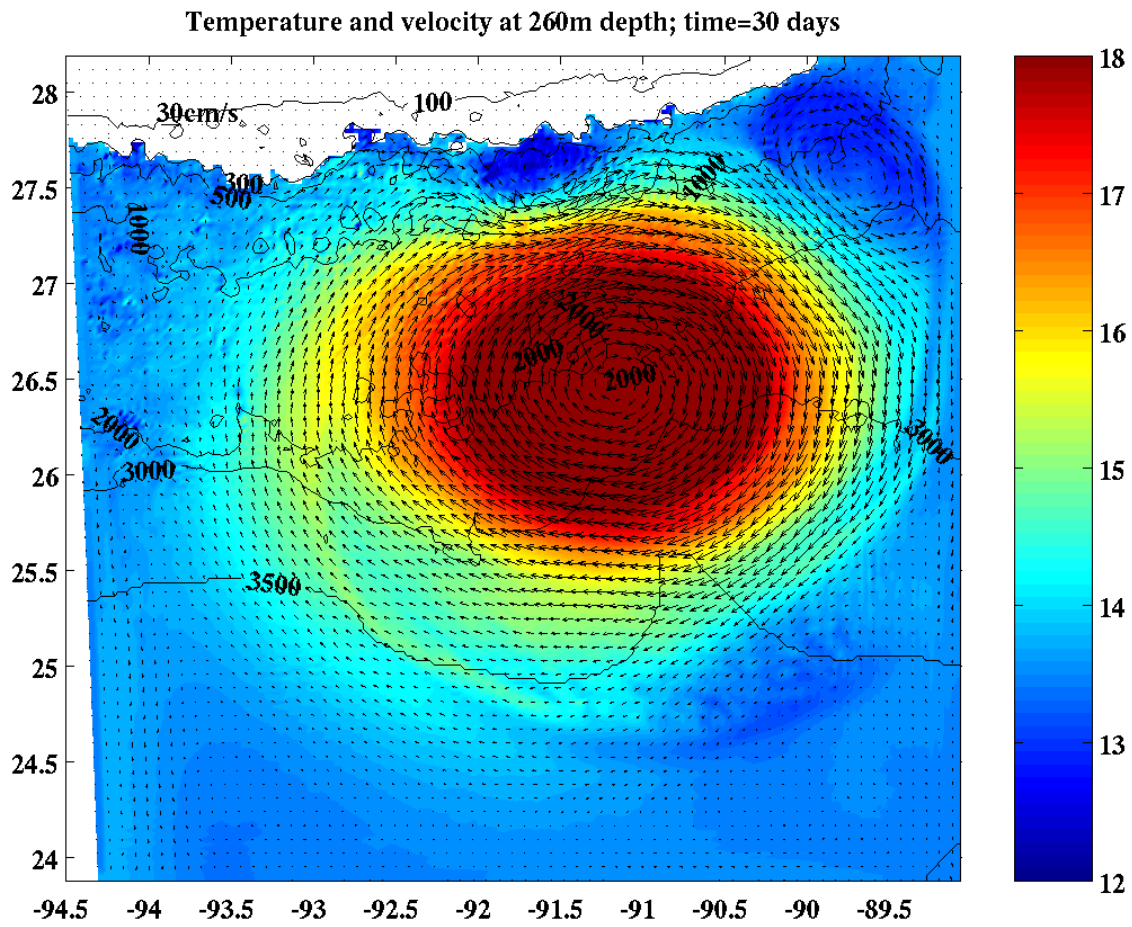


Figure 6.5. Simulation of a cyclone being squeezed between an LCE and topography. Shown are the simulated temperature and velocity fields at 260 meters depth after 1 month of integration, the center of the cyclone is located approximately at 91.7°W , 27.6°N .

6.2.2 Baroclinic Instability

The goal of this part of our research was to identify mesoscale features that can be baroclinically unstable over a sloping bottom and determine whether those features can produce currents with characteristics resembling midwater-column jets. Two frontal structures that are baroclinically unstable over the sloping bottom were identified. These two frontal structures correspond to two different potential scenarios of midwater-column jet generation. The first structure is surface-intensified, which corresponds to the scenario where the energy initially confined to the upper ocean is being transformed into kinetic energy of the intermediate layer via the process of stretching/squashing by rapid horizontal displacements of the layer interface. The second structure is initially midwater-column-intensified, which corresponds to the scenario where the energy initially confined to the intermediate layer is being redistributed and focused into high intensity jets via the process of sharpening of initially broad fronts. These structures were tuned to produce zonal fronts with the most intense and fastest growing baroclinic instability. These “optimized” structures were then used to construct baroclinically unstable cyclonic and anticyclonic eddies. Finally, the stability properties of these constructed eddies were studied.

6.2.2.1 Identifying Baroclinically Unstable Frontal Structures

The properties of the currents that we are expecting to be generated by the instability present a number of limitations on the unstable frontal structure that we are looking for. Since the midwater-column jets were observed over the northern slope, we expect the instability to be able to develop over a sloping bottom. The topographic slope of the northern GOM effectively blocks any large-scale (horizontal) motions in the unstratified layer below the main thermocline. Consequently, the development of a baroclinic instability with vertical scale comparable to the thermocline depth is suppressed, since it requires strong horizontal motions in the lower layer. Features (fronts and eddies) with large vertical scale, i.e., comparable to the depth of the main thermocline, which are baroclinically unstable over flat bottom, are stabilized in the presence of the bottom slope. Thus, only baroclinic instability with vertical scale smaller than the main thermocline depth can amplify in this situation. The midwater-column jets are characterized by high intensity currents on a very short time scale. Consequently, the instability capable of generating those currents should have the fastest possible growth rate and the highest level of energy released. The available potential energy and, therefore, the released kinetic energy is generally proportional to the vertical scale of the unstable feature, hence, we are looking for baroclinically unstable features with maximum possible vertical scale. The growth rate is generally proportional to the cross-frontal PV gradient, therefore the desired frontal structure should have the highest possible PV gradient.

Our general approach to selecting appropriate unstable frontal structures consists of two steps. First we select structures within a certain parameter¹ range which satisfy the general requirement of being baroclinically unstable over the bottom slope. Then, the selected structures are “tuned” to produce zonal fronts with the most intense and fastest growing baroclinic instability within the specified parameter range. The “tuning” consists of varying the frontal structure within the specified parameter range to achieve the desired stability properties. The stability properties of a zonal front with a specified structure are investigated by simulating the development of a small disturbance on the front initialized upstream (similar to (Sutyrin et al. 2001)). A small disturbance (much smaller than the spatial scale of the instability) on a baroclinically unstable front typically

¹A frontal structure is characterized by a set of parameters which determine the width, the horizontal location and the amplitude of PV transition within each layer.

evolves into a packet of growing meanders propagating downstream. Analyzing the properties of the packet allows determination of the spatial and temporal characteristics of the instability (Sutyrin et al. 2001).

The simulations of the instability development on a zonal front were conducted using the multi-layer IE model (Section 3.1). This model is perfectly suited for this type of experiments since it allows for clear PV analysis in isopycnal layers, which is the key to describing the process of baroclinic instability. In addition to that, the model computational efficiency permits the exploration of a wide parameter range necessary for “tuning” of the unstable frontal structure. The model was used extensively for LCE-topography interaction studies and performs well compared to the PE model. The model was configured with 8 isopycnal layers representing the typical GOM stratification (Section 4.4.3.1). A 2 km horizontal resolution was specified. The model domain was a zonal channel with constant linear bottom slope and inflow/outflow boundary conditions along the eastern and western boundaries. A strong sponge-layer was specified at the outflow boundary to suppress the reflection of meanders. The f -plane approximation was used for all of these experiments.

6.2.2.2 Baroclinic Instability Confined to the Upper Water Column

The unstable surface-intensified frontal structure identified by the process described above is shown in the upper panel of Figure 6.6. The necessary condition for baroclinic instability is satisfied due to the PV gradient inversion between the second and the fourth layers with average (unperturbed) depth of 30 and 120 meters respectively. The maximum current speed reaches 1 m/s near the surface (in the upper layer). The characteristic front width is 100 km, and the characteristic vertical scale is less than 200 m. The exponential growth rate for a zonal front with this structure is ~ 5 days, the wavelength of the most unstable wave (spatial scale of the instability) is ~ 130 km.

This unstable frontal structure was used to construct an anticyclone with 150 km radius. The stability properties of the anticyclone were investigated using the IE model. For this investigation the IE model was configured in the same manner as for the experiment with zonal fronts. The shape of the anticyclone was slightly perturbed to create an initial disturbance similar to the one in the zonal front experiment. The initial disturbance evolves into a series of undulations along the anticyclone boundary which eventually pinch off and form small anticyclones.

The lower panel in Figure 6.6 shows the PV and velocity fields in the midwater column (170-350 m layer) after 30 days of model integration. At this time the instability is in a fully nonlinear stage. The undulations along the anticyclone boundary cause stretching/squashing of the intermediate layer which results in generation of cyclonic and anticyclonic vortices. The currents in the intermediate layer reach a peak intensity of 20 cm/s within cyclonic vortices. The characteristic spatial scale of those currents is ~ 100 km while the characteristic temporal scale is ~ 10 days.

6.2.2.3 Baroclinic Instability Confined to the Midwater Column

The unstable midwater-intensified frontal structure is shown in the upper panel of Figure 6.7. The necessary condition for baroclinic instability is satisfied due to the PV gradient inversion between the fifth and sixth layers with average (unperturbed) depths of 280 and 525 meters, respectively. The maximum current speed reaches 40 cm/s at 110 meters depth (in the fourth layer). The characteristic front width is 60 km, and the characteristic vertical scale is 400 m. The exponential growth rate for a zonal front with this structure is ~ 10 days; the wavelength of the most unstable wave (spatial scale of the instability) is ~ 120 km.

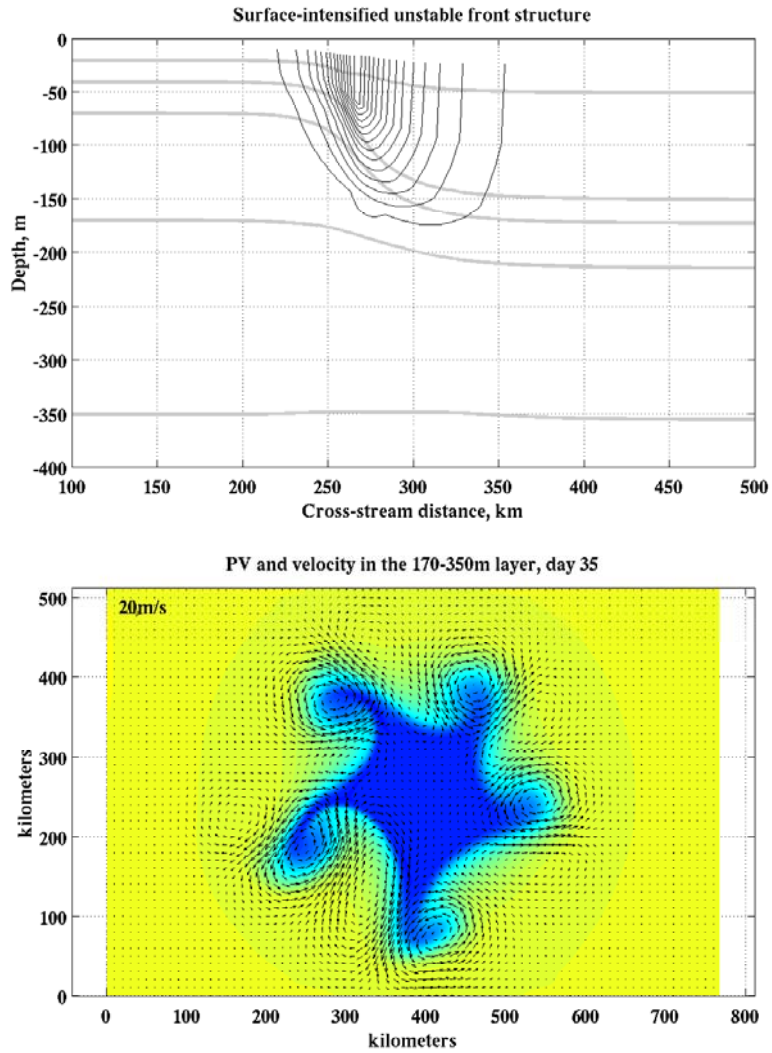


Figure 6.6. Unstable surface-intensified frontal structure (upper panel) and the PV and velocity fields in the midwater column (170-350m layer) after 30 days of model integration (lower panel).

This unstable frontal structure was used to construct a cyclone with 50 km radius. The stability properties of the cyclone were investigated in a manner similar to the previous case. The lower panel in Figure 6.7 shows the PV and velocity fields in the midwater column (170-350 m layer), respectively, after 60 days of integration. At the time shown the instability along the cyclone boundary reaches the fully nonlinear stage and three smaller cyclones pinch off. As the result of this process the currents in the intermediate layer intensify by ~ 5 cm/s reaching a peak intensity of 45 cm/s. The characteristic spatial scale of these currents is ~ 50 km while the characteristic temporal scale is ~ 20 days.

6.2.2.4 Conclusions

Neither of the baroclinically unstable frontal structures that we identified as candidates for generating strong middepth currents produced currents with characteristics similar to the observed midwater-column jets. The currents thus produced typically have weaker amplitude, larger spatial scales, and longer temporal scale than that of the observed midwater-column jets. (One important caveat here; the observational basis for any of this is quite limited). Nevertheless, baroclinic instability was shown to be an efficient mechanism for channeling kinetic energy into the intermediate layer. Therefore, it is still very likely to play an important role in generating/maintaining midwater-column jets.

6.3 Other Hypothesis for Midwater-Column Jets

In addition to investigating the mechanisms for midwater-column jet generation based upon the hypotheses formulated above, a considerable effort was also made to formulate alternative hypotheses. The result of this effort was a hypothesis which relates the observed midwater-column-intensified currents to internal solitary waves. Internal solitary waves have been observed in many regions of the world ocean including the Western Equatorial Pacific (Pinkel 2000), the Sulu Sea (Apel et al. 1985), and the Mediterranean (Vlasenko 2000). There are also a number of theoretical studies that analyze the structure and physical mechanisms controlling these waves (Vlasenko 1994). Internal solitary waves are characterized by spatial scales of approximately 1 km and temporal scales of approximately 15 minute. These waves typically have current speeds exceeding 1 m/s in both the horizontal and vertical directions.

Large vertical velocity and short time scale are two of the major characteristics of internal solitary waves that match those of midwater-column jets observed in the northern GOM. However, in contrast to the midwater-column jets, those internal solitary waves that have been observed and studied so far are surface-intensified (Vlasenko 2000). In addition to this last discrepancy, the time scale of 15 minute is somewhat too short for completely explaining the midwater-column jets, which were observed to persist for several hours.

Vlasenko (1994) derived a general analytical solution of an internal solitary wave. Even though the solution consists of multiple vertical modes, only the first baroclinic mode solution has been analyzed in detail due to the fact that the observed waves consist predominantly of the first mode. However, internal solitary waves consisting of higher vertical modes can theoretically exist. These waves have roughly the same spatial and temporal characteristics, but the currents associated with them are middepth-intensified.

Even though the time scale of an isolated internal solitary wave is fairly short, observations indicate that solitary waves are typically generated in trains (Apel et al. 1985). Close to the

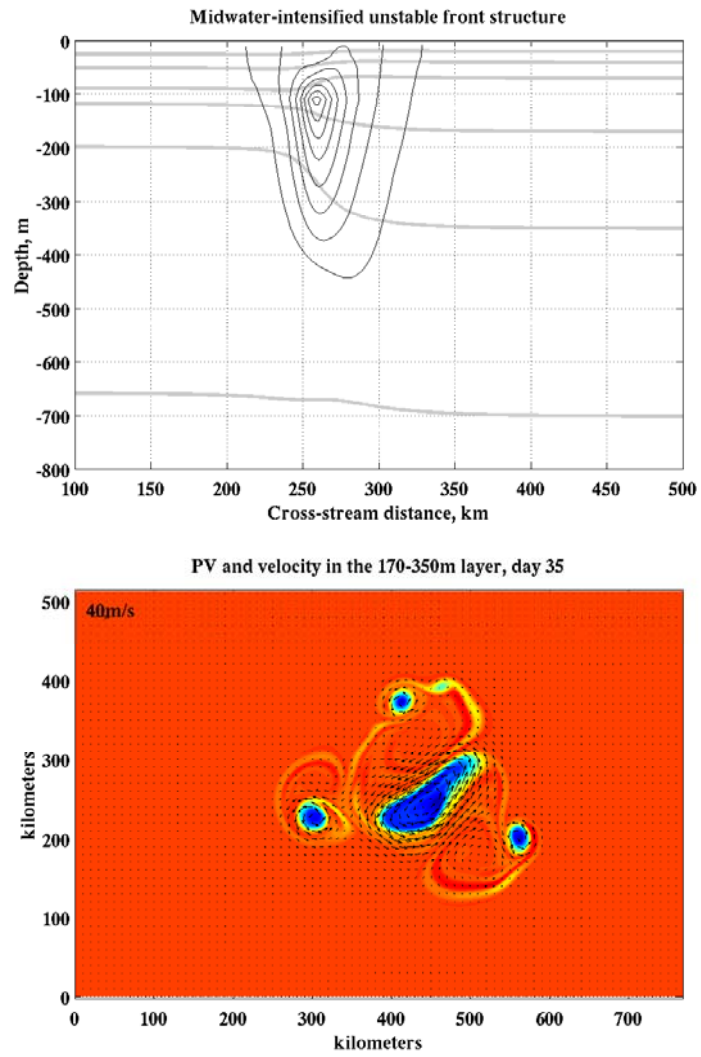


Figure 6.7. Same as in Figure 6.6 but for midwater-intensified front structure after 60 days of integration.

generation source a train of internal solitary waves can look to a point observer as a single strong current event with the duration of several hours (Apel et al. 1985).

Thus the midwater-column jets can potentially be explained as trains of second-mode internal solitary waves generated in the vicinity of the observation point by strong current-topography interactions. A nonhydrostatic model is clearly needed to verify this hypothesis.

7. SUMMARY

7.1 Loop Current Eddies

A methodology of gradually increasing realism was applied to investigating physical processes associated with LCE interactions with topography in various regions of the GOM. Several new dynamical mechanisms controlling LCE interactions with topography were identified, and other more familiar mechanisms were clarified. Most importantly, potential scenarios describing the evolution of an isolated LCE interacting with bottom topography in various regions of the GOM were identified. Clearly, in reality the behavior of each particular LCE is affected by the history of evolution of earlier LCE's and by LCE's present in the GOM at the same time. However, identifying possible scenarios of evolution of an isolated LCE is critical for understanding the complex patterns of real LCE interactions. Finally, a real event of an LCE interacting with coastal topography was simulated and the results were compared directly with observations. The previously developed understanding of dynamical processes involved in LCE-topography interactions obtained from our more process-oriented experiments enabled a much clearer dynamical interpretation of the observed events.

7.1.1 Dynamical Mechanisms

The investigation of physical mechanisms associated with LCE's and LCE-topography interactions in various regions of the GOM resulted in the conclusion that LCE evolution in each region is governed by a common set of interacting dynamical processes: planetary β -drift, deep circulation driven by the LCE itself, cyclone formation due to off-shore advection of high potential vorticity (PV) water, and interaction with midwater-column currents that can be generated underneath a LCE moving on-shore. These processes combine in different ways to produce specific outcomes in different areas of the GOM.

As the β -effect drives LCE's westward, the accompanying vortex tube stretching in the ocean beneath the LCE leads to the development of deep eddy features that play a critical role in LCE propagation over the relatively flat regions in the central GOM. The bottom-intensified eddies can significantly affect LCE behavior even when it is interacting with a shelf. In this case the bottom-intensified eddies are typically generated when a portion of a LCE is forced by some other dynamical process off the continental slope and over the flat topography. As a portion of the LCE moves over flat topography the process of water column compression (stretching) in the lower layer generates anticyclonic (cyclonic) relative vorticity. The same process works over the continental slope as well, however the topographic slope leads to radiation of the lower layer relative vorticity as topographic Rossby waves. On the other hand, the lower layer relative vorticity generated over flat topography forms bottom-intensified eddies which couple with the LCE, significantly affecting its trajectory.

The process of cyclone formation during LCE interactions with the coastal shelf is very robust and can be identified in all simulations that include a thermocline-penetrating shelf. When a LCE encounters a shelf, the circulation of the LCE penetrates onto the deeper part of the shelf advecting the shelf water onto the continental slope. As this water mass moves offshore, cyclonic vortices are formed, presumably due to stretching of vortex tubes as the shelf water moves across topographic contours. The cyclones generated by this process can reach considerable strength depending upon

the exact shape of the bathymetry and the motion of the LCE. The currents associated with these cyclones typically have a significant effect on LCE propagation.

As a LCE moves onto the continental slope crossing topographic contours an accelerated current (15-20 cm/s) is generated in the midwater column region underneath the eddy. The current is directed along the topography and to the right of the direction of eddy propagation and accelerates in the onshore direction. A slow, broad current recirculating behind the LCE in the opposite direction is generated. We have demonstrated that the generation mechanism for these currents underneath the eddy is related to water column squashing as the eddy advances onto the topographic slope. The current generation, however, can only occur if stratification exists below the main thermocline. In the absence of stratification the relative vorticity generated by thermocline motions is radiated away as topographic Rossby waves. The stratification enables cross-topographic flow underneath the thermocline, i.e. via the JEBAR mechanism (Mertz and Wright 1992), allowing the along-shore northward current to recirculate around the eddy. The net effect of the midwater-column currents on the LCE is to deflect its trajectory to the right.

7.1.2 Interaction of an Isolated LCE with Topography in Various Regions of the GOM

Each of the processes described in Section 7.1.1 is strongly affected by the specifics of the bathymetric configuration and the positioning of the LCE. Consequently, multiple scenarios of LCE interaction with coastal topography can occur. Using a series of idealized experiments, accompanied by several realistic experiments, we have identified a number of such scenarios. The central, the western, and the northern regions of the GOM were studied in isolation. In each region we considered several scenarios of LCE evolution and for each scenario we identified the effect of each particular mechanism and their relative importance.

In the central region of the GOM a LCE moves westward over the relatively flat topography driven by the β -effect; the accompanying vortex tube stretching in the ocean beneath the LCE leads to the development of deep eddy features. The deep eddies interact with the LCE creating a strong southerly component to its motion. This result is consistent with two-layer PE simulations of Chassignet and Cushman-Roisin (1991). Formation of deep eddies in this case is a radiative process, which means that the eddies eventually separate from the LCE producing a characteristic "wake" of deep motions behind it. This wake of deep motions produced behind an LCE moving over flat topography is likely to be an important source of energy for the deep circulation in the GOM.

As a LCE driven westward by the β -drift encounters the western GOM coastal topography, the following sequence of events typically occurs. As the LCE moves onto the continental slope, midwater-column currents are generated underneath it. The effect of these currents is to deflect the eddy trajectory northward. Soon the westward LCE propagation is halted when it encounters the shelf break. As soon as the onshore motion of the eddy stops, its northward motion stops as well since midwater-column currents are no longer generated. It is important to note here that the presence of the shelf prevents the LCE from coming close to the western boundary, therefore the so-called "image effect," identified to play an important role in advecting LCE's northward in experiments without a realistic shelf (Shi and Nof 1993; Shi and Nof 1994), is inactive. Thus, in the absence of the image effect, the interaction with midwater-column currents is the only mechanism identified thus far which produces northward LCE propagation. The behavior of the LCE after encountering the shelf break is largely determined by the structure of the coastal topography.

At 25°N in the western GOM, the coastal topography is characterized by a wide shelf and an adjacent narrow continental slope. This specific topographic configuration allows for the generation of a deep circulation beneath the LCE, since the narrow continental slope forces a large portion of the eddy to remain over flat topography during its interaction with the shelf. When the LCE first encounters the shelf, shelf water is advected offshore on the northern side of the LCE. As this water mass moves offshore, cyclonic vortices are formed, presumably due to stretching of vortex tubes as the shelf water moves over the slope. The cyclonic vortices in close proximity to the LCE cause it to become slightly elliptic. This ellipticity generates the deep circulation beneath the LCE over flat topography east of the continental slope. The effect of the deep circulation is to push the LCE off-shore and southward. As the deep circulation disperses as topographic Rossby waves, the β -effect takes over and propels the LCE back on to the shelf. The above sequence of events repeats again, producing an oscillatory motion of the LCE. This LCE behavior pattern has been observed in "Fast Eddy" in 1985-86 during its interaction with the western shelf.

At 23°N in the western GOM, the coastal topography in the GOM is characterized with a narrow shelf and wide continental slope, just the opposite of the configuration at 25°N . This topographic configuration locks the deep circulation beneath the LCE, thus eliminating the mechanism of interaction with bottom-intensified eddies. Cyclonic vortices are produced north of the LCE similar to the 25°N case; however they are unable to generate strong, deep circulation feedback. The vortices are quickly swept around the LCE periphery and dispersed as topographic Rossby waves when they encounter the shelf on the LCE's southern side. Subsequent LCE interaction with small cyclonic vortices produces the oscillatory motion similar to that of 25°N case; however the amplitude of this motion is much smaller.

In the northwest corner of the GOM, the presence of both the northern and the southern continental slopes isolates the LCE from the flat topographic region in the central GOM preventing deep eddy formation. The presence of the northern shelf blocks the northward eddy propagation produced by the interaction with mid-water column currents generated beneath an LCE. Off-shelf PV advection and associated cyclone generation are the only remaining mechanisms affecting the LCE behavior in the northwest corner. The mean effect of LCE interaction with off-shelf advected cyclones appears to be a slow southward drift. It is suggested, however, that an anticyclonic background circulation and/or anticyclones east of the LCE can counteract this southward drift thus trapping LCE's in the northwest corner.

Also, due to the specific shelf configuration in the Perdido Escarpment region ($\sim 25.5^{\circ}\text{N}$), which forms a corner protruding into the interior of the GOM, LCE interaction with off-shelf advected cyclones seems to result in a mass ejection from the LCE and an associated high LCE dissipation rate. Our preliminary analysis indicates that cyclones advected around the LCE periphery pinch the elongated end of the elliptic LCE against the protruding Perdido Escarpment, which clips the end of the LCE off. This process seems to produce very strong on-shelf mass flux and along-shelf currents that extend far south of the LCE.

Even though the same dynamical processes control the LCE interaction with the northern GOM topography their interplay results in quite different patterns of LCE behavior. The difference comes from the fact that in the northern GOM the topographic slope is oriented along the preferred direction of eddy propagation, i.e., in the zonal direction. Several different regimes of LCE interaction with the northern GOM topography, depending upon the LCE latitude, were identified.

An LCE initially located north of approximately 26.5°N (the exact latitude depends upon the size of the LCE) and east of roughly 90°W moves westward driven by the β -drift and encounters the northern shelf, similar to the western shelf situation. In this case, however, the shelf break is oriented at a sharp angle to the direction of eddy propagation. Because of this, the effect of the

midwater-column currents formed beneath the LCE as it moves onshore is to push it eastward. The strength of this effect is proportional to the geometric fraction of the LCE that encounters the shelf. Consequently, for the LCE's that are located further north, the midwater-column currents are strong enough to overpower the β -drift and deflect LCE's eastward. For the LCE's that are located further south, the midwater-column currents are only strong enough to slow down the eddy's westward propagation.

After the LCE encounters the shelf it creates off-shelf PV advection. The off-shelf PV advection mechanism in the northern GOM produces small-scale cyclones very similar to the western shelf setting. However, in the northern GOM eddies are typically propagating westward driven by the β -drift. The dispersion property of the β -drift (the speed of β -drift is roughly proportional to eddy size) leads to separation of LCE's and off-shelf advected cyclones that limits their interaction. This is in contrast to the western GOM where the westward eddy propagation is stalled by the western shelf allowing all eddy scales to stay together and interact for prolonged periods of time. A typical effect of LCE interaction with off-shelf advected cyclones in the northern GOM setting is to deflect the LCE trajectory southward.

Thus the overall behavior pattern of LCE's encountering the northern GOM bathymetry north of approximately 26.5°N is the following. The LCE approaches the shelf and either deflects south-east or slows down depending upon the initial LCE latitude. A cyclone is formed north of the LCE due to off-shelf advection. The cyclone pushes the LCE trajectory southward and typically stays behind as the LCE proceeds to move westward over the continental slope in a nearly zonal direction.

A LCE which encounters the northern continental slope at approximately 25.5°N (the exact latitude depends upon the size of the LCE) remains partially over the deep flat portion of the GOM. This allows deep eddies to form underneath the LCE similar to the western GOM (i.e. with a narrow continental slope). However, the effect of these eddies on the surface anticyclone is quite different from the western GOM. The orientation of the topographic slope adjacent to the western shelf creates a tendency for bottom-intensified eddies to radiate southward, from beneath the LCE, as Rossby waves. This limits the LCE interaction with bottom-intensified eddies in the western GOM. In the northern GOM, however, the preferential direction of deep eddy propagation coincides with the preferential direction of LCE propagation, making a prolonged interaction possible. We have demonstrated that LCE's moving along the southern edge of the northern continental slope can form solitary, quasi-stationary configurations with bottom-intensified anticyclones. These configurations propagate westward with about twice the speed of the β -drift.

7.1.3 Fast Eddy Simulation

As the final stage of the investigation an actual event of an LCE interacting with the western shelf of the GOM was simulated. The event selected for the simulation was the interaction of Fast Eddy with the western shelf at 25°N which started during December 1985 and continued for several months. To our knowledge this event is the best-documented example of LCE interaction with the western shelf, which makes it ideal for a numerical simulation.

The primitive equations model was configured for a regional simulation in the western GOM with a uniform 4 km horizontal resolution. The model was initialized using our previously developed PV-based feature model technology. The structure and location of Fast Eddy, as well as key features of the background circulation, were determined from hydrographic surveys and drifter tra-

jectory data collected during the event (SAIC 1988). The numerical simulation started on October 28, 1985, when Fast Eddy was approaching the shelf, and continued for six months.

The simulation showed considerable skill in reproducing the observed evolution of Fast Eddy and surrounding mesoscale features. The skill of the model was evaluated by visually comparing the model produced density and velocity fields with the observed fields. For the first 15-20 days of the simulation, the predicted positions and the structure of the LCE and key mesoscale features were very close to those observed. For times beyond one month, the observed evolution is qualitatively reproduced. The fact that the model was capable of qualitatively reproducing the actual sequence of events during the interaction of Fast Eddy with the shelf demonstrates that the physical mechanisms controlling the eddy-shelf interaction are well represented. This enables us to make conclusions about the dynamics controlling the evolution of the temperature and velocity field during the event, which are well understood from the dynamical basis provided by our previously conducted idealized studies.

In addition to an improved understanding of the dynamics governing Fast Eddy's interaction with the western shelf, our simulation also enhanced our knowledge of the fate of some smaller mesoscale features involved in the event. In particular, three elements of the observed event sequence can be noted:

- the northward shift of the eddy track as it approached the western shelf,
- the development of a cyclone north of the eddy after its interaction with the shelf
- the abrupt off-shore motion of the eddy after interacting with the shelf.

These are discussed next, in turn.

As Fast Eddy moved onshore during December 1985, there was a noticeable northward shift in its track as indicated by the drifter trajectories. This shift was reproduced in the numerical simulation and is attributed to the interaction of the eddy with northward currents generated in the mid-water column beneath the eddy as the result of its on-slope motion.

In January-February 1986 Fast Eddy was interacting with the western shelf. During this time a cyclone of increasing amplitude was observed north of the eddy. It was hypothesized that this cyclone was the same cyclone that was observed west of Fast Eddy as it was approaching the shelf, and its amplification was attributed to topographic interactions. Our simulation indicates that it is unlikely that the cyclone observed initially west of Fast Eddy would move westward and amplify. In the simulation this cyclone was caught in the circulation of Fast Eddy and advected off-shore. The cyclone that was subsequently formed north of Fast Eddy was the result of off-shelf PV advection, similar to the idealized experiments.

Finally, by the end of February 1986 Fast Eddy was observed to move off-shore and southward, returning back to the shelf around April. The same event was reproduced in the simulation and is attributed to the interaction with a deep anticyclone that formed beneath the eddy as it rotated over the flat topography adjacent to the western continental slope. The off-shore eddy motion in the simulation occurred approximately two months earlier than it was observed. We attribute the error in timing to deficiencies of deep circulation initialization in the model caused by the lack of appropriate observational data.

7.2 Dynamical Effects of DeSoto Canyon

Physical processes controlling the circulation within, and in the vicinity of, the DeSoto Canyon were studied. Our investigation focused on the conceptual models of circulation in the DeSoto

Canyon proposed by Hamilton et al. (2000) on the basis of their analysis of the data collected during the DeSoto Canyon Eddy Intrusion Study (1997-1999). In particular, three of their conceptual models were analyzed: 1) the direct interaction of an anticyclone with the canyon; 2) remotely generated eastward jets west of the canyon; and 3) the interaction with Loop Current frontal eddies. The results of our analysis were conclusions about the dynamical feasibility of the proposed models and identifying the physical mechanisms involved. For each of the conceptual models the observed events were simulated, and the results compared with observations.

7.2.1 Direct Interaction of an Anticyclone with the DeSoto Canyon

This conceptual model (mode 1a in Hamilton et al. (2000)) represents direct interaction of a remnant warm-core ring south of the canyon. This mode of interaction occurs when the LC is positioned far south and, thus, the LC should not have any direct effect on the circulation in the canyon (the role of the LC is still important for formation of the warm-core rings and their propagation towards the DeSoto Canyon).

The structure of warm eddies typically found at the mouth of the canyon was first identified. The typical structure of the warm eddies was derived from analysis of nine detailed hydrographic surveys of the DeSoto Canyon region conducted as a part of the Eddy Intrusion Study (1997-1999). The eddies were classified by the depth of their potential vorticity (PV) anomaly. According to this classification three types of warm-core eddies were found:

- Shallow eddies: the PV anomaly is localized to the upper thermocline.
- Deep eddies: the PV anomaly is localized to the lower thermocline.
- Full eddies: the PV anomaly is distributed throughout the entire depth of the thermocline.

Our numerical experiments demonstrate that despite their natural tendency to propagate westward due to the β -effect, all three types of warm-core eddies can propagate eastward as the result of interactions with the northern shelf break. This effect might be responsible for transporting warm eddies towards the mouth of the canyon in the absence of the LC and its frontal eddies. The orientation of the shelf break was shown to be critical for the existence of this effect. It is also demonstrated that warm-core eddies need to be initially forced against the shelf in order to trigger the eastward propagation. This initial forcing is likely to be provided by LC frontal cyclones.

Warm-core eddies at the mouth of the DeSoto Canyon were shown to generate cyclonic circulation in the Canyon. This circulation pattern is consistent with the mode 2 circulation in the Canyon identified by Wang et al. (2003) from surface current observations. Thus, our numerical simulations identify a link between a conceptual model of eddy interaction within the DeSoto Canyon proposed by Hamilton et al. (2000) and a statistical circulation mode derived by Wang et al. (2003). Off-shelf PV advection is identified as the primary physical mechanism responsible for the generation of the cyclonic circulation. This mechanism is identified using a passive tracer technique developed specifically for the analysis of our numerical experiments.

7.2.2 Remote Generation of Eastward Jets

According to this conceptual model a remote LC ring interacting with the coastal topography west of the Mississippi River delta generates a warm eastward jet along the shelf break that reaches

the DeSoto Canyon region producing eastward currents. This model was based upon analysis of the hydrographic survey combined with current meter data and satellite SST observations during one particular event; the so-called Eldorado Eddy interacting with the northern GOM slope just west of the Mississippi Canyon.

Using all available information about the event, and our experience in simulating LCE interactions with coastal topography, we conducted a series of realistic simulations of the Eldorado Eddy interacting with the northern slope. Simulations with several different eddy structures and locations within the observational uncertainty range failed to reproduce the eastward shelf-break jet observed at the foot of the canyon in November-December 1997. Even though this result cannot be regarded as conclusive evidence, it suggests that some other processes may be responsible for the eastward shelf-break jet observed at the foot of DeSoto Canyon.

Observational data from this time period, in particular the sea surface height fields derived from the TOPEX satellite data, suggest the presence of a large cyclone centered just east of the Mississippi River delta. We propose that it is the interaction of this cyclone with the shelf break east of the Mississippi River delta that produces the eastward jet along the shelf. The jet is generated as a result of low PV water, which is initially wrapped around the cyclone in the upper thermocline, stripping off the perimeter of the cyclone when its core approaches the shelf break. Numerical simulations of this process showed the generation of a topography-following eastward jet similar to the one observed.

7.2.3 Interaction with Loop Current Frontal Eddies

This part of our investigation was concerned with conceptual models related to the circulation induced within the DeSoto Canyon by Loop Current Frontal Eddies (LCFE's). LCFE's are small (20-100 km in diameter) cyclones that are frequently observed along the cyclonic side of the LC (Maul 1977; Vukovich et al. 1979; Vukovich and Maul 1985) and represent the most common source of the observed variability in the DeSoto Canyon region Hamilton et al. (2000). They typically form along the western part of the LC and amplify in an unstable manner as they propagate downstream along the LC. Several previous studies (Maul 1977; Hurlburt 1986) suggested that LCFE's are generated as the result of an instability process in the LC. The observational data presented in the Eddy Intrusion Study report also support this hypothesis. One of the more typical circulation patterns induced by LCFE's in the DeSoto Canyon region is depicted by a conceptual model from the Eddy Intrusion Study report (Figure 5.13). According to the model, the cyclonic circulation of LCFE's entrains warm LC water around their cold cores. As the eddies move to the east around the LC they leave a warm streamer that extends into the DeSoto Canyon region. This produces an eastward flow along the shelf break in the upper 100 m. Below that depth, the cyclonic circulation in the LCFE causes strong westward flow. The numerical simulations that we conducted were designed to investigate the dynamical mechanisms leading to this circulation pattern.

The unstable nature of the LCFE's makes them difficult to simulate in numerical models. While isolated eddies, both cyclones and anticyclones, have relatively well defined structure and, therefore, can be implanted into initial fields using feature models, LCFE's do not have such a structure. Instead, LCFE's are an inseparable part of an instability process in the LC and, therefore, the entire instability process must be recreated in a numerical model in order to accurately simulate LCFE's. Furthermore, the properties of this instability process have to be well understood if one is to be able to control it. Such control is necessary for producing LCFE's at a specified location and with specified characteristics.

Thus, numerical investigation of LCFE interaction with DeSoto Canyon has to start with the investigation of the LCFE formation mechanism itself, i.e., one needs to understand the conditions necessary for initial formation and subsequent growth of LCFE's as well as the properties of the LC itself which lead to this growth. Our investigation was structured accordingly. First, through a series of zonal channel experiments conducted using our multi-layer IE model, we identified the stream structure which leads to formation of frontal cyclones with spatial and temporal scales consistent with those of LCFE's. Then, the results of these zonal channel experiments were applied to introduce a LC, with desirable stability properties, into a regional high resolution PE model with realistic topography. This allowed us to simulate the formation of LCFE's in a realistic setting. Finally, the interaction of LCFE's with DeSoto Canyon topography was simulated and compared against observations. The simulation allowed us to investigate, in some detail, the effect LCFE's have on the water mass exchange between the DeSoto Canyon and surrounding regions.

The stream structure that leads to formation of frontal cyclones with spatial and temporal scales consistent with those of LCFE's was identified using a series of numerical experiments similar to Sutyrin et al. (2001). The experiments were conducted using our IE model configured with 10 isopycnal layers and 3 km horizontal resolution. In these experiments the LC is represented as a zonal jet in a channel with open inflow/outflow boundary conditions. A small perturbation is initially specified close to the inflow boundary. In a typical experiment the initial perturbation generates a packet of meanders consisting of a superposition of several unstable modes that propagates downstream and amplifies due to the process of instability. As growing meanders reach the saturation stage, cyclonic features resembling the LCFE's develop in the meander troughs. With this approach, the wavelength of the most unstable mode, its growth rate and, most importantly, the along-stream distance required for the initial disturbance to reach the saturation stage (i.e. form the cyclonic features resembling the LCFE's) can be determined from a single experiment.

A wide variety of plausible LC stream structures were explored in these experiments by introducing small variations around the baseline structure derived from observed cross-sections of LC (Vukovich and Maul 1985). The baseline LC structure was constructed using a 10-layer PV model with free parameters adjusted to match the most robust characteristics of the LC. Variations around the baseline structure were derived from two hypotheses about the natural variability of the LC. According to one hypothesis the width of the cyclonic side of the stream can vary as a result of LC interaction with the Yucatan Peninsula. As the LC meanders westward, the lateral friction along the Yucatan Peninsula shelf break can reduce the width of the stream's cyclonic side, thus producing a positive extremum in the cross-stream PV structure. The other hypothesis assumes that the vertical extent of the stream can decrease as the stream extends rapidly northward resulting in a shallower stream structure.

The LC stability experiments demonstrate that cyclones resembling the observed LCFE's can form on the cyclonic side of the stream as a result of an instability process in a zonal LC-type jet triggered by a small disturbance. The cyclones were shown to form only by streams with a positive PV extremum on the narrow cyclonic side. Moreover, the intensity of the cyclones was found to be proportional to the magnitude of the extremum. The experiments also indicated that the stream stability, as defined by the rate of meander growth, is linked to the stream vertical extent. The LC with shallower stream structure was shown to be significantly more unstable producing larger frontal cyclones over shorter distances. The β -effect was found to have only minor influence on the stream stability.

The understanding of the mechanisms that drive the LCFE growth developed as a result of the zonal stability experiments used to simulate LCFE's in the PE model with fully realistic topography. As the first step in the transition to the PE model experiments we repeated the key

zonal stability experiments (initially conducted with the IE model) using the PE model. The PE model experiments reproduced the results of the IE model experiments with only minor quantitative differences, indicating that the key physics controlling the development of frontal cyclones is accounted for by the IE model. The LC with the unstable stream structure (identified in the zonal channel experiments) was then introduced into a regional, high-resolution PE model with realistic topography. The PE model here is the same model that was used in our previous eddy-topography interaction experiments configured for the region in the GOM extending from $\sim 24^{\circ}\text{N}$ to $\sim 30^{\circ}\text{N}$ in the meridional direction and from $\sim 83^{\circ}\text{W}$ to $\sim 91^{\circ}\text{W}$ in the zonal direction. In a typical experiment the LC is initialized along an idealized trajectory designed to imitate the LC in the fully extended northward position. Development of LCFE's was triggered by a disturbance introduced initially near the southern boundary of the domain along the inflow LC branch.

An important result of these simulations was establishing additional conditions necessary for a LCFE to grow, or even maintain itself, as it propagates along the western branch of the LC, which is a characteristic LCFE behavior according to observations. These conditions, in turn, provide some insight into the processes leading to formation of LCFE's. It was established that a small disturbance, which was used in the zonal channel experiment to trigger formation of LCFE's, is insufficient for a LCFE to develop in the situation where the LC is oriented meridionally. While an in-depth dynamical explanation of the instability of a meridional jet requires further study, we hypothesize that the vertical coupling between the upper stream meander and underlying cyclones, which is driving the LCFE growth in the zonal channel experiments, is disrupted by the stream crossing the environmental vorticity gradient, thus preventing the initial disturbance from growing. Modifying the structure of the initial disturbance can produce a growing LCFE consistent with observations. The key feature of the disturbance capable of producing LCFE's is a positive PV anomaly at the trough of the disturbance. The positive PV anomaly is associated with a cyclonic circulation and is equivalent to specifying a small cyclone on the cyclonic side of the stream. We hypothesize that such a cyclone can be created in reality via the process of LC interaction with the Yucatan Peninsula topography. As we demonstrated in our previous eddy-topography studies, a baroclinic current intersecting a topographic slope can generate PV anomalies by advecting high PV water from shallow regions into deeper regions. It is very possible that the LC, which is known to meander as it flows along the Yucatan shelf (Sheinbaum et al. 2002), can generate positive PV anomalies by advecting high PV water off the Yucatan shelf.

The characteristics of the LCFE generated using the above technique can be controlled by varying the size of the initial disturbance and by changing the stream stability characteristics. In our simulations these parameters were adjusted to produce a LCFE similar to one of the LCFE's observed during the DeSoto Canyon Eddy Intrusion Study (Hamilton et al. 2000). Comparisons of the observed and simulated sea surface height and geostrophic velocities at two depth levels show very good agreement. This result suggests that our approach to simulating LCFE's is valid, and the simulated LCFE is realistic. It also suggests that the conceptual model of LCFE-DeSoto Canyon interaction proposed by Hamilton et al. (2000) is valid and consistent with LCFE dynamics.

The LCFE simulation technique described above was applied for investigating the process of LCFE interaction with the DeSoto Canyon. By introducing a passive tracer into the model we were able to visualize the water exchange between the DeSoto Canyon and the surrounding GOM that was generated by the LCFE. Our simulations indicated that a result of LCFE interaction with the DeSoto Canyon can be the generation of an anticyclonic circulation at the mouth of the canyon. The circulation was produced as a result of the tongue of warm LC water that leads the LCFE, being clipped by the deep eastern wall of the canyon. The anticyclonic circulation, in turn, produced a cyclonic circulation within the canyon itself via the mechanism of off-shelf PV advection. The

resulting cyclone-anticyclone pair produces extensive water exchange between the canyon and the deep GOM, as can be seen from the tracer distribution. We believe that this circulation pattern is a typical result of LCFE interaction with the DeSoto Canyon.

7.3 Small Cyclones in the Northern GOM

This part of the investigation was concerned with the physical processes associated with the evolution of small-scale cyclones over the northern continental slope in the GOM. The goal of this investigation was to identify potential mechanisms that can lead to the formation of high-intensity, midwater-column-intensified currents, which will be further referred to as midwater-column jets. The investigation consisted of three phases. The first phase was concerned with studying the evolution of small-scale cyclones in the northern GOM, while the second phase was concerned with identifying the physical processes that lead to their formation. The last phase consisted of formulating hypotheses for testing additional mechanisms of midwater-column jet generation.

During the first phase the behavior of pre-existing isolated cyclones of different sizes, and their interaction with LCE's in the northern GOM, was studied numerically using a high-resolution PE model with realistic topography. An 8-layer potential vorticity model of a typical cyclone was constructed on the basis of available hydrographic and direct current observations of small-scale cyclones in the northern GOM (Berger et al. 1996). This model, in conjunction with the previously developed initialization procedures (Section 4.4.1), allowed us to initialize dynamically balanced cyclones in the PE model. The PE model experiments demonstrated that the resolution of the model is adequate for describing the evolution of cyclones as small as 50 km in diameter over realistic topography. The cyclones were shown to retain their initial structure for time periods of at least several months, which is consistent with observational data. The isolated small-scale cyclones were shown to have a general tendency to propagate northwest with a typical speed of slightly over 1 km/day. Our preliminary results indicate that the exact direction of propagation is affected by the underlying topography. After encountering the northern shelf-break, cyclones continue to propagate westward along the shelf without any significant increase in their decay rate; no significant cross topographic flow is generated.

A procedure was developed to initialize multiple mesoscale features in the primitive equation model using a potential vorticity approach. This procedure was applied to initialize and simulate small-scale cyclones coupled with LCE's. One of the most important results of these simulations is that the small-scale cyclones appear to play a key role in maintaining the ellipticity of the LCE's and determining their trajectory over the northern slope. Isolated LCE's over the topographic slope, initially specified to have an elliptic shape, were shown to quickly lose their initial ellipticity and propagate westward driven by the β -drift. The same initially elliptic LCE's coupled with a small-scale cyclone retain their ellipticity for several months during which the interaction with the cyclone introduces a significant meridional component into the trajectory of a LCE, sometimes pushing it off the northern slope into the central GOM. Since the observational data indicate that LCE's typically have an elliptic shape, it implies that the evolution of the majority of LCE's over the northern slope is strongly influenced by small-scale cyclones. We believe this to be a significant result.

The goal of the second phase of the investigation was to analyze potential generation mechanisms for midwater-column jets. Two potential mechanisms were studied. The first mechanism generates strong middepth-intensified currents via the process of violent interactions of pre-existing small-scale eddies with rough topography. The violent interactions of small-scale eddies

with topography can be produced, for example, by a paired LCE and small-scale cyclone. A cyclone captured in the circulation of an LCE can be squeezed between the LCE and the northern shelf break. During this process the energy associated with the cyclone, initially distributed over a relatively large area, is forced by the currents of the larger LCE into a narrow channel, which can potentially lead to current amplification and generation of strong intermittent currents at middepth.

The second mechanism generates strong middepth-intensified currents via the process of baroclinic instability in pre-existing larger-scale features. The baroclinic instability process converts available potential energy into kinetic energy, accelerating quickly evolving currents in the vicinity of the unstable mesoscale feature. Aside from generating strong horizontal currents with relatively short time scales, the process of baroclinic instability is characterized by relatively large vertical velocities. Since the available observational data indicate that midwater-column current events are typically associated with large vertical velocities, the baroclinic instability mechanism appears to be a very plausible source of these currents.

The scenario of a small-scale cyclone being squeezed between a large LCE and the northern shelf break was simulated with a hydrostatic, high-resolution PE model at 2.6 km horizontal and approximately 50 m vertical resolution. There was no significant current amplification at midwater depth. The energy of the cyclone appears to be radiated away by long gravity waves. This result, however, is insufficient to make a definitive conclusion about the role of cyclone-topography interaction in generating the midwater-column jets. This is because the hydrostatic approximation employed by the model is likely to be violated during the process of interaction with rough topography at this scale. Therefore, additional simulations with a nonhydrostatic model are necessary to obtain more conclusive results. This is beyond the scope of the re-directed work.

Two potential scenarios of midwater-column jet generation associated with baroclinic instability were investigated. In the first scenario the energy initially confined to the upper ocean is transformed into kinetic energy in the intermediate layer via the process of stretching/squashing of the intermediate layer by rapid horizontal displacements of the upper layer features. In the second scenario, the energy initially confined to the intermediate layer is redistributed and focused into high intensity jets via the process of sharpening of initially broad fronts. For both scenarios the unstable front structures were first identified using 8-layer IE model experiments simulating a zonal front over a uniform linear slope. Cyclonic and anticyclonic eddies, with the identified unstable structure, were then simulated with both IE and PE models. The simulations failed to produce midwater-column currents of the desired intensity. The speed of currents generated at the middepth in the first scenario, i.e., downward transport of kinetic energy by a surface-intensified feature, did not exceed 20 cm/s, even though the speed of the initial surface current was in excess of 1 m/s. The simulations of the second scenario, i.e., intensifications of currents initially confined to middepth, did not produce any substantial current amplification. Even though baroclinic instability alone appears to be incapable of generating midwater-column jets, it is still likely to play an important role in supplying the energy into the midwater column and to smaller scales.

As the third phase of the investigation, a considerable effort was made to formulate alternative hypotheses of midwater-column jet generation. The result of this effort was a hypothesis that relates the observed midwater-column-intensified currents to internal solitary waves. Large vertical velocities and short time scale are the two characteristics of internal solitary waves that match the characteristics of midwater-column jets.

8. LITERATURE CITED

- Allen, J., J. Barth, and P. Newberger, 1990. On intermediate models for barotropic continental shelf and slope flow fields. Part I: Formulation and comparison of exact solutions. *J. Phys. Oceanogr.* 20:1017–1042.
- Apel, J., J. Holbrook, A. Liu, and J. Tsai, 1985. The Sulu Sea internal soliton experiment. *J. Phys. Oceanogr.* 15:1625–1651.
- Berger, T., P. Hamilton, J. Singer, R. Leben, G. Born, and C. Fox, 1996. Louisiana/Texas shelf physical oceanography program: Eddy circulation study; final synthesis report. Volume I: Technical report. U.S. Department of the Interior, Minerals Management Service, Gulf of Mexico OCS Region, New Orleans, LA. OCS Study MMS 96-0051. 294pp.
- Blumberg, A. and G. Mellor, 1987. A description of a three-dimensional coastal ocean circulation model. In: Three-dimensional coastal ocean models, Volume 4. American Geophysical Union, Washington, D.C., Heaps, N., ed. 1–16.
- Chassignet, E. and B. Cushman-Roisin, 1991. On the influence of a lower-layer on the propagation of nonlinear ocean eddies. *J. Phys. Oceanogr.* 21:939–957.
- Cooper, C., G. Forristall, and T. Joyce, 1990. Velocity and hydrographic structure of two Gulf of Mexico warm-core rings. *J. Geophys. Res.* 95:1663–1679.
- Glenn, S. and C. Ebbesmeyer, 1993. Drifting buoy observations of a Loop Current anticyclonic eddy. *J. Geophys. Res.* 98:20,105–20,119.
- Grimshaw, R., D. Broutman, X. He, and P. Sun, 1994. Analytical and numerical study of a barotropic eddy on a topographic slope. *J. Phys. Oceanogr.* 24:1587–1607.
- Hamilton, P., B. Fargion, and D. Biggs, 1999. Loop Current eddy paths in the western Gulf of Mexico. *J. Phys. Oceanogr.* 29:1180–1207.
- Hamilton, P., T. Berger, J. Singer, E. Waddell, J. Churchill, R. Leben, T. Lee, and W. Sturges, 2000. DeSoto Canyon eddy intrusion study: final report. Volume II: Technical report. U.S. Department of the Interior, Minerals Management Service, Gulf of Mexico OCS Region, New Orleans, LA. OCS Study MMS 2000-080. 275pp.
- Hurlburt, H., 1986. Dynamic transfer of simulated altimeter data into subsurface information by a numerical ocean model. *J. Geophys. Res.* 91:2372–2400.
- Kirwan, A., J. Lewis, P. Reinersman, and I. Quintero, 1988. Observed and simulated kinematic properties of Loop Current rings. *J. Geophys. Res.* 93:1189–1198.
- Lewis, J., A. Kirwan, Jr., and G. Forristall, 1989. Evolution of a warm-core ring in the Gulf of Mexico: Lagrangian observations. *J. Geophys. Res.* 94:8163–8178.
- Logoutov, O., G. Sutyrin, and D. Watts, 2001. Potential vorticity structure across the Gulf Stream: Observations and a PV-Gradient model. *J. Phys. Oceanogr.* 31(2):637–644.
- Maul, G., 1977. The annual cycle of the Loop Current. Part I: Observations during a one-year time series. *J. Mar. Res.* 35:29–47.
- Mellor, G., 1998. User's guide for a three-dimensional, primitive equation, numerical ocean model. Atmospheric and Oceanic Sciences Program. Princeton University.
- Mellor, G. and T. Yamada, 1982. Development of turbulent closure model for geophysical fluid problem. *Rev. Geophys. Space Phys.* 20:851–875.

- Mertz, G. and D. Wright, 1992. Interpretations of the JEBAR term. *J. Phys. Oceanogr.* 22:301–305.
- Nof, D., 1983. On the migration of isolated eddies with application to Gulf Stream rings. *J. Mar. Sci.* 41:413–425.
- Nowlin, W., A. Jochens, S. DiMarco, R. Reid, and M. Howard, 2001. Deepwater physical oceanography reanalysis and synthesis of historical data: Synthesis report. U.S. Department of the Interior, Minerals Management Service, Gulf of Mexico OCS Region, New Orleans, LA. OCS Study MMS 2001-064. 528pp.
- Nycander, J. and G. Sutyrin, 1992. On the structure of stationary translating anticyclones on the β -plane. *Dyn. Atmos. Oceans* 16:473–498.
- Pankratov, K., 1994. Influence of topography on the dynamics of baroclinic oceanic eddies. Ph.D. thesis, MIT/WHOI.
- Pinkel, R., 2000. Internal solitary waves in the warm pool of the western equatorial Pacific. *J. Phys. Oceanogr.* 30:2906–2926.
- SAIC, 1988. Gulf of Mexico physical oceanography program: Year 3; final report. Volume II: Technical report. U.S. Department of the Interior, Minerals Management Service, Gulf of Mexico OCS Region, New Orleans, LA. OCS Study MMS 88-0046. 241pp.
- Sheinbaum, J., J. Candela, A. Badan, and J. Ochoa, 2002. Flow structure and transports in the Yucatan Channel. *Geophys. Res. Lett.* 29:1029–1035.
- Shi, C. and D. Nof, 1993. The splitting of eddies along boundaries. *J. Mar. Res.* 51:771–795.
- Shi, C. and D. Nof, 1994. The destruction of lenses and generation of wadons. *J. Phys. Oceanogr.* 24:1120–1136.
- Smagorinsky, J., 1963. General circulation experiments with primitive equations: I. the basic experiments. *Mon. Wea. Rev.* 91:291–304.
- Smith, D., 1986. A numerical study of Loop Current eddy interaction with topography in the western Gulf of Mexico. *J. Phys. Oceanogr.* 16:1260–1272.
- Smith, D. and J. O'Brien, 1983. The interaction of a two-layer isolated mesoscale eddy with bottom topography. *J. Phys. Oceanogr.* 13:1681–1697.
- Sutyrin, G., 1994. Long-lived planetary vortices and their evolution: Conservative intermediate geostrophic model. *Chaos* 4:203–212.
- Sutyrin, G., 2001. Effects of topography on the β -drift of a baroclinic vortex. *J. Mar. Res.* 59:977–989.
- Sutyrin, G. and I. Yushina, 1989. Numerical modelling of the formation, evolution, interaction and decay of isolated vortices. In: *Mesoscale/Synoptic Coherent Structures in Geophysical Turbulence*, Volume 50. Elsevier Oceanogr. Series, 721–736.
- Sutyrin, G., I. Ginis, and S. Frolov, 2001. Equilibration of baroclinic meanders and deep eddies in a Gulf Stream-type jet over a sloping bottom. *J. Phys. Oceanogr.* 31:2049–2065.
- Theirry, V. and Y. Morel, 1999. Influence of a strong slope on the evolution of a surface-intensified vortex. *J. Phys. Oceanogr.* 29:911–924.
- Vidal, V., F. Vidal, and J. Pérez-Molero, 1992. Collision of a Loop Current anticyclonic ring against the continental shelf slope of the western Gulf of Mexico. *J. Geophys. Res.* 97:2155–2172.

- Vlasenko, V., 1994. Multi-modal soliton of internal waves. *Atmos. Oceanic Phys.* 30:161–169.
- Vlasenko, V., 2000. Structure of large-amplitude internal solitary waves. *J. Phys. Oceanogr.* 30:2172–2185.
- Vukovich, F. and G. Maul, 1985. Cyclonic eddies in the eastern Gulf of Mexico. *J. Phys. Oceanogr.* 15:105–117.
- Vukovich, F. and B. Crissman, 1986. Aspects of warm rings in the Gulf of Mexico. *J. Geophys. Res.* 91:2645–2660.
- Vukovich, F. and E. Waddel, 1991. Interaction of a warm ring with the western slope in the Gulf of Mexico. *J. Phys. Oceanogr.* 21:1062–1074.
- Vukovich, F., B. Crissman, M. Bushnell, and W. King, 1979. Some aspects of the oceanography of the Gulf of Mexico using satellite and in-situ data. *J. Geophys. Res.* 84:7749–7768.
- Wang, D., L. Oey, T. Ezer, and P. Hamilton, 2003. Nearsurface currents in DeSoto Canyon (1997-1999): Comparison of current meters, satellite observations and model simulation. *J. Phys. Oceanogr.* 33:313–326.
- Welsh, S. and M. Inoue, 2000. Loop Current rings and the deep circulation in the Gulf of Mexico. *J. Geophys. Res.* 105:16,951–16,959.



The Department of the Interior Mission

As the Nation's principal conservation agency, the Department of the Interior has responsibility for most of our nationally owned public lands and natural resources. This includes fostering sound use of our land and water resources; protecting our fish, wildlife, and biological diversity; preserving the environmental and cultural values of our national parks and historical places; and providing for the enjoyment of life through outdoor recreation. The Department assesses our energy and mineral resources and works to ensure that their development is in the best interests of all our people by encouraging stewardship and citizen participation in their care. The Department also has a major responsibility for American Indian reservation communities and for people who live in island territories under U.S. administration.



The Minerals Management Service Mission

As a bureau of the Department of the Interior, the Minerals Management Service's (MMS) primary responsibilities are to manage the mineral resources located on the Nation's Outer Continental Shelf (OCS), collect revenue from the Federal OCS and onshore Federal and Indian lands, and distribute those revenues.

Moreover, in working to meet its responsibilities, the **Offshore Minerals Management Program** administers the OCS competitive leasing program and oversees the safe and environmentally sound exploration and production of our Nation's offshore natural gas, oil and other mineral resources. The MMS **Minerals Revenue Management** meets its responsibilities by ensuring the efficient, timely and accurate collection and disbursement of revenue from mineral leasing and production due to Indian tribes and allottees, States and the U.S. Treasury.

The MMS strives to fulfill its responsibilities through the general guiding principles of: (1) being responsive to the public's concerns and interests by maintaining a dialogue with all potentially affected parties and (2) carrying out its programs with an emphasis on working to enhance the quality of life for all Americans by lending MMS assistance and expertise to economic development and environmental protection.